

Florida State University Libraries

2015

Synthesis of Oxide and Spinel Nanocrystals for Use in Solid State Lighting

Megan Elizabeth Foley



FLORIDA STATE UNIVERSITY
COLLEGE OF ARTS AND SCIENCES

SYNTHESIS OF OXIDE AND SPINEL NANOCRYSTALS
FOR USE IN SOLID STATE LIGHTING

By

MEGAN ELIZABETH FOLEY

A Dissertation submitted to the
Department of Chemistry and Biochemistry
in partial fulfillment of the
requirements for the degree of
Doctor of Philosophy

2015

Megan Foley defended this dissertation on October 28, 2015.

The members of the supervisory committee were:

Geoffrey F. Strouse
Professor Directing Dissertation

William M. Landing
University Representative

Albert E. Stiegman
Committee Member

Gregory B. Dudley
Committee Member

The Graduate School has verified and approved the above-named committee members, and certifies that the dissertation has been approved in accordance with university requirements.

To my fantastic husband Timmy, you mean the world to me, I love you very much sweetheart.
You were always there to keep me going and keep me laughing, not to mention your unending
patience, you are the best, around.

To my Dad, thank you for all the inspiration you gave me and the push I needed to finish
undergrad, as well as the encouragement to pursue my doctorate, love you dearly.

To my Mom, I love you, thank you for being there for me, and you know, making me so
awesome, love you mom.

To my sister Melissa, thank you for always being there when I needed someone to chat with,
play games with, or just be a bum with, you're the best sister ever, love you always.

To my stepmonster Jeanne, you have filled our family home with lots of love and joy, and so
glad that you joined our family, I love you stepmonster.

ACKNOWLEDGMENTS

The journey to getting my PhD would have never happened if I was not surrounded by so many awesome and supportive people. The people around me have encouraged me, challenged me, and help me to grow into the person I am today.

First of course, thank you Dr. Strouse for always pushing me to do my best, and then finally pushing me out of the door. Thank you for also accepting me as a student despite my last second request to join your group, that had to have made you nervous. You're a great chemist, and have helped me immensely in honing my own knowledge and skill.

I would also like to thank all of my committee members for taking the time to help me along my path, offering really excellent advice and insight.

Additionally, I would also like to thank the following people:

- My family, who are the best ever! Whenever I'm feeling lazy and don't want to keep working, I think of them, and they keep me going.
- My group members for putting up with me despite all my mess. You guys have helped me with my science and knowledge.
- Carley, Nandita, and Virginia. We started this journey together, and now, we are all just about done. I'm not sure if I would have been able to make it through the stress of grad school without you guys. Tricia too, though she wasn't part of the original posse.
- Muroska, I always had a blast hanging out with you, and you always helped me through encouragement and with time management.
- Dr. Lovingood, you helped me so much when I first started. You taught me ssNMR and synthesis, two skills that have become so important for me to get my PhD.
- Dr. Washington, because you're awesome. You were an inspiration throughout my time in grad school, and though I don't know you well, you have helped me immensely.
- Kate, for your up beat attitude, which always made my day better, thanks for being such a nice and cheerful person, and a good friend.
- Ryan, you always questioned everything, and though at times annoying, you always made me think deeper about my science. Plus, you and Crystal are just awesome.
- Breshike, for doing 5 billion TEM images for me, and Dave, for taking up the mantle after him.

TABLE OF CONTENTS

List of Tables	viii
List of Figures	ix
List of Abbreviations	xvi
Abstract.....	xvii
1. INTRODUCTION	1
1.1 General Introduction	1
1.2 Light Emitting Diodes (LEDs).....	2
1.2.1 History of the LED.....	2
1.2.2 LED Design.....	3
1.2.3 State-of-the-Art	5
1.2.4 The Future of Solid State Lighting.....	7
1.3 Nanoscience and Nanotechnology	9
1.3.1 Quantum Confinement and Size Effects	11
1.3.2 Metal Oxide Nanoparticles	14
1.4 Synthesis of Nanophosphors.....	15
1.4.1 Methods of NP Synthesis	15
1.4.2 Nucleation Theory.....	17
1.4.3 Microwaves	21
1.4.4 Microwave Heating.....	21
1.4.5 Nanoparticles.....	25
1.4.6 Lanthanide Doped Nanoparticles	27
1.5 Lanthanide Luminescence	27
1.5.1 Selection Rules.....	28
1.5.2 Lanthanide Absorption.....	31
1.5.3 Ligand/Molecular Antenna Effect.....	31
1.5.4 Dexter Energy Transfer.....	32
1.5.5 Lanthanide Emission.....	34
1.6 Characterization Methods	40
1.6.1 UV-Vis and Fluorescence	40
1.6.2 Powder X-Ray Diffraction (pXRD)	41
1.6.3 Transmission Electron Microscopy (TEM)	44
1.6.4 Nuclear Magnetic Resonance (NMR)	45
2. LIGAND-PASSIVATED EU:Y ₂ O ₃ NANOCRYSTALS AS A PHOSPHOR FOR WHITE LIGHT EMITTING DIODES.....	48
2.1 Introduction.....	48
2.2 Experimental Section	51
2.2.1 Synthesis of Eu:Y ₂ O ₃ (0%, 2%, 9%, 11%, 18%) Nanocrystals	51
2.2.2 Measurements	52
2.3 Results.....	54

2.3.1	Characterization of Eu:Y ₂ O ₃	54
2.3.2	Surface Passivation Layer of Eu:Y ₂ O ₃	58
2.3.3	Optical Properties of Eu:Y ₂ O ₃	65
2.3.4	Evidence of the Presence of Surface and Core Eu(III) Sites in the Eu:Y ₂ O ₃ Nanocrystal	72
2.3.5	Structural Evolution of Nanocrystals Following Thermal Treatment.....	74
2.3.6	Application of acac-Eu:Y ₂ O ₃ as a Solid-State Phosphor	76
2.4	Conclusion	80
3.	MICROWAVE SYNTHESIS AND LIGAND MODIFICATION OF OXIDE AND SULFIDE NANOSPINELS	82
3.1	Introduction.....	82
3.2	Experimental Section.....	84
3.2.1	Materials.....	84
3.2.2	Synthesis of ZnB ₂ O ₄ (B = Al ³⁺ or Ga ³⁺)	84
3.2.3	Synthesis of MgB ₂ O ₄ (B = Al ³⁺ or Ga ³⁺)	85
3.2.4	Synthesis of ZnGa ₂ S ₄	85
3.2.5	Ligand Exchange.....	86
3.2.6	Measurements	86
3.3	Results.....	87
3.3.1	Synthesis of AB ₂ O ₄ and ZnGa ₂ S ₄ (A = Mg or Zn; B = Al or Ga)	87
3.3.2	Reaction Phase Space for Formation of ZnB ₂ O ₄ (B = Al or Ga).....	95
3.3.3	Nanospinel Ligand Exchange	98
3.3.4	Optical Properties of AB ₂ O ₄ (A = Mg or Zn; B = Al or Ga) and ZnGa ₂ S ₄ Nanospinels	105
3.4	Conclusion	106
4.	EU ³⁺ DOPED ZNM ₂ O ₄ (M = AL ³⁺ , GA ³⁺) NANOSPINELS, AN EFFICIENT RED PHOSPHOR	107
4.1	Introduction.....	107
4.2	Experimental Section.....	109
4.2.1	Materials.....	109
4.2.2	Synthesis of Eu:ZnB ₂ O ₄ (B = Al ³⁺ or Ga ³⁺ , 1%, 2.5%, 5%, 7.5%, 10%, 12.5% Eu) Nanocrystals.....	109
4.2.3	Ligand Exchange Protocol	110
4.2.4	X-ray Powder Diffraction	110
4.2.5	Transmission Electron Microscopy.	111
4.2.6	X-ray Absorption Near Edge (XANES) and X-ray Absorption Fine Structure (XAFS).....	111
4.2.7	Optical Measurements.....	111
4.3	Results.....	112
4.3.1	Synthesis of Eu:ZnB ₂ O ₄ (B = Al, Ga).....	112
4.3.2	Optical Properties of Eu:ZnB ₂ O ₄ (B = Al, Ga).....	120
4.3.3	Molecular Energy Sensitization of Eu(III) Centers	129

4.3.4 CIE Coordinantes	132
4.4 Conclusion	134
5. MOLECULAR SENSITIZATION OF RARE EARTH PHOSPHOR EMISSION IN METAL OXIDE NANOCRYSTALS	136
5.1 Introduction.....	136
5.2 Experimental section.....	138
5.2.1 Materials.....	138
5.2.2 Synthesis of Nanocrystals.	139
5.2.3 Ligand Exchange Protocol	139
5.2.4 Measurements	140
5.3 Results.....	141
5.3.1 Nanoparticle Structure	141
5.3.2 Nanophosphor Ligand Passivation.....	143
5.3.3 Optical Properties.....	148
5.3.4 Color Purity.....	155
5.4 Conclusion	157
References	158
Biographical Sketch	172

LIST OF TABLES

Table 1.1: Material and wavelength (nm) of LEDs of specific colors.....	5
Table 1.2: Dielectric constants ($\tan \delta$) for many common solvents, divided by those with high $\tan \delta$'s, medium $\tan \delta$'s, and low $\tan \delta$'s. The higher the $\tan \delta$, the more the material absorbs microwave radiation.....	24
Table 1.3: 4f electron configurations, term symbol for the ground state, and solid color for the trivalent lanthanide series	29
Table 1.4: Ground state (G), main emissive state (I), and final state (F) of the f-f transitions in trivalent lanthanide ions, energy difference between the emissive state and highest energy receiving state, as well as the radiative lifetime calculated for the aqua ions	37
Table 2.1: Experimental FT-IR data and assignments for samples collected in KBr pellets	63
Table 3.1: Structural characteristics of the nanospinels, including sizes, d-spacing, space group, and $M^{2+}:M^{3+}$ ratios	95
Table 3.2: IR assignments of samples as prepared and after exchange with tta	103
Table 3.3: Optical properties of the nanospinels, including theoretical band gap, the singlet of acac, and vacancies	104
Table 4.1: EXAFS fitting results for 12.7% Eu:ZnAl ₂ O ₄ and 15.6% Eu:ZnAl ₂ O ₄	119
Table 4.2: The sensitization efficiency and QEs (Φ) in solution, in a PMMA matrix, and intrinsic	125
Table 4.3: Intrinsic QEs ($\Phi_{\text{intrinsic}}$), sensitization, R/O Ratios, and intensity ratio of Eu ³⁺ /tta	130
Table 4.4: CIE coordinates for tta exchanged Eu:ZnAl ₂ O ₄ and Eu:ZnGa ₂ O ₄	134
Table 5.1: Lifetimes, quantum efficiencies, and CIE coordinates of the ligand exchanged nanophosphors	147
Table 5.2: Ligand structures and electronic properties	150

LIST OF FIGURES

Figure 1.1: A p-n junction diode with forward bias being applied.....	3
Figure 1.2: A typical 5mm LED design.....	4
Figure 1.3: Typical designs for a pc-LED for generation of white light through either a blue LED.pumping a yellow or yellow and red phosphor, or a UV LED pumping a combination of blue, green, and red phosphors	5
Figure 1.4: A pictorial depiction of the energy levels for a bulk semiconductor verses that of a quantum dot. As is shown, as the size of the QD gets smaller, the energy levels become more discreet, and the band gap widens, causing a shift in the absorption of the particle to higher energy.....	10
Figure 1.5: CdSe/ZnS quatum dots relating the size of the nanoparticle (shown above) with the color of the QDs (shown below).....	13
Figure 1.6: A flow chart illustrating all the methods for nanoparticle synthesis through either a top-down or bottom-up approach.....	17
Figure 1.7: Free energy diagram of a spherical particle, showing both the critical free energy required for nanoparticle formation as well as the critical radius size to avoid redissolving of the particle.....	19
Figure 1.8: LaMer diagram showing how concentration of precursors change throughout the nucleation and growth process. C_m is the concentration of monomers (red line), C_{min} is the minimum monomer concentration required for nucleation, and C_{max} is the supersaturation concentration.....	20
Figure 1.9: Graph theorizing the difference in time to achieve nucleation in MW reactions (blue line) and reactions using conventional heating (red line)	22
Figure 1.10: Electromagnetic spectrum which includes wavelength, frequency, and interactions with molecules in the different energy areas of the spectrum	23
Figure 1.11: Heat transfer is conventional heating versus microwave heating. As heat is transferred from the outside in in a conventional heating system, there is generally a temperature gradient, where the inside is significantly cooler than the outside. In MW heating, dipolar or ionic molecules within the reaction batch are becoming superheated, then transferring the heat to the solvent molecules in the vicinity, resulting in less of a temperature gradient as all the molecules are being heated simultaneously.....	26
Figure 1.12: Diagram showing the difference between gerade (even) symmetry versus ungerade (odd) symmetry	28

Figure 1.13: Orbital projection diagram of the s, d, d, and f orbitals. Color differences in p, d, and f orbitals represents differences in symmetry (gerade vs ungerade)	30
Figure 1.14: Molecular antenna approach to sensitization of lanthanide emission. DET stands for Dexter energy transfer, the mechanism by which energy transfer occurs in a ligand sensitization.....	32
Figure 1.15: Crystal structures of nanoparticles of Eu ³⁺ doped ZnAl ₂ O ₄ sensitized by thenoyltrifluoroacetone (tta) and Tb ³⁺ doped Y ₂ O ₃ sensitized by hexafluoroacetylacetone (hfacac)	33
Figure 1.16: Location of the 4f electrons in lanthanide molecules.....	35
Figure 1.17: Configurational coordinate diagram for an organic ligand, left, vs a Ln ³⁺ ion, right	36
Figure 1.18: Splitting of the 4f orbitals as a result of electron repulsion, spin-orbit coupling, and crystal field effects	38
Figure 1.19: Emission spectra for Eu ³⁺ and Tb ³⁺ doped into ZnAl ₂ O ₄ nanospinels.....	39
Figure 1.20: X-rays interacting with lattice planes within a crystalline material. As the x-rays hit an appropriate Θ corresponding to a lattice plane as defined by Bragg's law, the x-rays are in phase with each other and through constructive interference, an XRD signal is seen	42
Figure 1.21: Peak in a pXRD spectra, where peak position and the full width half max (FWHM) can be used to determine particle size.....	43
Figure 1.22: Splitting of the spin states induced by an applied magnetic field, the basis behind Nuclear Magnetic Resonance (NMR).....	46
Figure 2.1: (top) TEM micrograph of 6.4 ± 1.5 nm Eu (2%):Y ₂ O ₃ imaged at 200 keV (250 000×) on a 400 mesh amorphous carbon grid (scale bar 100 nm). Inset: image of a single Eu:Y ₂ O ₃ nanocrystal at 1 500 000× magnification. (bottom) Size distribution of Eu(2%):Y ₂ O ₃ measured over 433 particles in the TEM	55
Figure 2.2: Selected TEM micrograph area showing the dominant features observed for the solvent dispersion of Eu(2%):Y ₂ O ₃ on 400 mesh amorphous carbon grid operating at 250keV	56
Figure 2.3: Selected TEM micrograph area showing the larger nanoparticles observed for the solvent dispersion of Eu(2%):Y ₂ O ₃ on 400 mesh amorphous carbon grid operating at 250keV	57
Figure 2.4: Selected TEM micrograph area exhibiting 15 nm particles in the solvent dispersion of Eu(2%):Y ₂ O ₃ on 400 mesh amorphous carbon grid operating at 250keV	58

Figure 2.5: pXRD spectra of Eu(2%):Y ₂ O ₃ in comparison to the standard card for the cubic phase of Y ₂ O ₃ (JCPDS 43.1036). Inset: TEM -electron diffraction pattern with plane assignments for the Eu:Y ₂ O ₃ nanocrystal	59
Figure 2.6: (A) Type A bridging bidentate coordination of acac to yttrium. The numbers in parentheses label the carbons as a reference. (B) Proposed octahedral coordination of acac to the (222) lattice plane of Eu:Y ₂ O ₃ in the cubic crystal structure (JCPDS card 43.1036).....	60
Figure 2.7: Surface passivation layer characterization data for 6.4 ± 1.5 nm acac-passivated Eu:Y ₂ O ₃ nanocrystals: (A) FT-IR spectra of Eu:Y ₂ O ₃ illustrating mid-frequency IR data and (in the inset) low-frequency IR data; (B) ¹³ C ¹ H} CP-MAS spectra for Y(acac) ₃ (black), acac-Eu:Y ₂ O ₃ (red), and acac-Y ₂ O ₃ (blue).....	61
Figure 2.8: FT-IR spectra of KBr pellets containing Y(acac) ₃ , Eu(acac) ₃ , HDA, and Eu(2%):Y ₂ O ₃	62
Figure 2.9: The wavelength dependent powder PL spectra of 0%, 2%, 5%, 10%, and 15% Eu:Y ₂ O ₃ excited at A) $\lambda_{\text{ex}}=270$ nm, and B) $\lambda_{\text{ex}}=370$ nm	66
Figure 2.10: Wavelength dependent powder PLE spectra monitored at A) $\lambda_{\text{em}}=611$ nm, B) $\lambda_{\text{em}}=520$ nm, and C) $\lambda_{\text{em}}=430$ nm for 0%, 2%, 5%, 10%, and 15% doped Eu:Y ₂ O ₃	67
Figure 2.11: (A) Solution UV-vis absorption spectra in CH ₃ CN of acac–Eu:Y ₂ O ₃ , Eu(acac) ₃ , and Y(acac) ₃ . (B) Solid-state photoluminescence (PL) spectra (298 K, λ_{ex} 250, 270, 370, and 394 nm) of acac–Eu:Y ₂ O ₃ . (C) Solid-state photoluminescence excitation (PLE) spectra (295 K, λ_{em} 430, 520, 611, 704 nm) of acac–Eu:Y ₂ O ₃	68
Figure 2.12: Photoluminescence measurement at $\lambda_{\text{ex}} = 270$ nm showing spectral broadening of the ⁵ D ₀ → ⁷ F ₂ transition in bulk and nanocrystal Eu(2%):Y ₂ O ₃	69
Figure 2.13: (A) Schematic energy level diagram and (B) relaxation pathways for efficient downconversion to the Eu(III) J-O transitions and Y ₂ O ₃ defect levels in the acac–Eu:Y ₂ O ₃ nanocrystals.....	72
Figure 2.14: High-resolution PLE spectra for Eu (2%):Y ₂ O ₃ and bulk Eu:Y ₂ O ₃ sample monitored at λ_{em} 611 nm in order to probe the ⁷ F ₀ → ⁵ D ₀ J-O transition for the Eu(III) C ₂ symmetry occupation in the Y ₂ O ₃ host lattice	73
Figure 2.15: Thermal response for the Eu(2%):Y ₂ O ₃ nanocrystal during thermolysis from 20 to 1000 °C: (A) thermogravimetric analysis (TGA) data and first differential of TGA experimental data; (B) temperature-dependent FT-IR spectra; (C) temperature-dependent pXRD spectra.....	74
Figure 2.16: Temperature-dependent changes in the optical properties of Eu (2%):Y ₂ O ₃ nanocrystals during thermolysis from 20 to 1000 °C: (A) solid-state photoluminescence	

excitation spectra monitored at $\lambda_{\text{em}} = 611$ nm; (B) solid-state photoluminescence spectra, $\lambda_{\text{ex}} = 270$ nm	76
Figure 2.17: (A) CIE coordinates for Eu:Y ₂ O ₃ doped at (A) 0%, (B) 2%, (C) 9%, (D) 11%, and (E) 18% plotted on the CIE1931 chromaticity chart. (B) Images of a LED phosphor assembled from deposition of Eu (9%):Y ₂ O ₃ onto a 370 nm LED operating at 3.0 V	78
Figure 2.18: Plot of the relative intensity of the white light phosphor versus the applied voltage to the 370 nm LED. The relative intensity is calculated by normalizing the spectra from 400 – 750 nm by the intensity of the LED PL at 370 nm	79
Figure 3.1: Proposed decomposition mechanism for formation of the AB ₂ X ₄ nanospinels form solvent induced thermal de-composition of molecular precursors for A) ZnAl ₂ O ₄ from Zn(UND) ₂ and AlCl ₃ and B) ZnGa ₂ S ₄ from ZDC and GaCl ₃ . The proposed mechanism is believed to be applicable to the analogous AB ₂ O ₄ and AB ₂ S ₄ spinel families.....	88
Figure 3.2: pXRD spectra of (A) ZnAl ₂ O ₄ (JCPDS 82.1043), (B) ZnGa ₂ O ₄ (JCPDS 86-0415), (C) MgAl ₂ O ₄ (JCPDS 82.2424), (D) MgGa ₂ O ₄ (JCPDS 89-3082), and (E) ZnGa ₂ S ₄ (JCPDS 40-1462).....	89
Figure 3.3: pXRD spectra A) ZnGa ₂ O ₄ and B) MgGa ₂ O ₄ made using MCl ₃ and Zn(UND) ₂	90
Figure 3.4: Transmission electron microscopy images with indexing of the major facet and size dispersity of A) ZnAl ₂ O ₄ , B) ZnGa ₂ O ₄ , C) MgAl ₂ O ₄ , D) MgGa ₂ O ₄ , and E) ZnGa ₂ S ₄ . A complete size dispersity graph is not shown for MgAl ₂ O ₄ due to the low TEM cross-section for the sample.....	92
Figure 3.5: High resolution TEM image of A) ZnAl ₂ O ₄ , B) ZnGa ₂ O ₄ , C) MgAl ₂ O ₄ , D) MgGa ₂ O ₄ , and E) ZnGa ₂ S ₄	93
Figure 3.6: Low resolution TEM image of acac grown A) ZnAl ₂ O ₄ , B) ZnGa ₂ O ₄ , C) MgAl ₂ O ₄ , D) MgGa ₂ O ₄ , (E) and ZnGa ₂ S ₄	94
Figure 3.7: pXRD of A) ZnAl ₂ O ₄ and B) ZnGa ₂ O ₄ with different ratios of Zn ²⁺ and B ³⁺ as well as the XRD diffraction patterns The inserted XRD diffraction patterns are ZnO (JPCDS 079-0208), ZnAl ₂ O ₄ (JPCDS 82.1043), Al ₂ O ₃ (JPCDS 050-0741), ZnGa ₂ O ₄ (JPCDS 86-0415), and Ga ₂ O ₃ (JPCDS 020-0426)	96
Figure 3.8: (440) peak position shift as a function of Zn ²⁺ concentration. The black triangles are ZnAl ₂ O ₄ and the blue squares are the ZnGa ₂ O ₄ . The (103) peak for ZnO which is in the same area as the (440) peak is also plotted (red circle).....	97
Figure 3.9: NOBF ₄ exchange mechanism to replace acac groups passivating the as prepared nanospinels	98

Figure 3.10: ZnAl ₂ O ₄ ¹ H NMR spectra of nanocrystals (A) before exchange and (B) after tta exchange. ZnGa ₂ S ₄ ¹ H NMR of nanocrystals (C) before exchange and (D) after tta exchange. Samples were dissolved in deuterated acetonitrile	99
Figure 3.11: ¹ H NMR spectra of tta and the starting materials in deuterated acetonitrile at 298K. A) 2.thenoyl trifluoroacetone, B) Zinc diethyldithiocarbamate, and C) Zinc undecylenate ..	100
Figure 3.12: IR spectra of A) ZnAl ₂ O ₄ and B) ZnGa ₂ S ₄ . As prepared is in blue and after tta exchange in red. The IR was performed on powdered samples using an attenuated total reflectance sample chamber equipped with a ZnSe crystal over coated with diamond.....	101
Figure 3.13: IR of tta solid. The IR was performed using an attenuated total reflectance (ATR) sample chamber	102
Figure 3.14: Absorption spectra of the nanospinels in toluene. ZnAl ₂ O ₄ is in black, ZnGa ₂ O ₄ is in blue, MgAl ₂ O ₄ in red, MgGa ₂ O ₄ in dark red, and ZnGa ₂ S ₄ in green	102
Figure 3.15: Excitation (black) monitored at 420 nm and emission (red) spectra excited at 350 nm in toluene before and after tta exchange. As prepared A) ZnAl ₂ O ₄ , C) ZnGa ₂ O ₄ , C) ZnGa ₂ S ₄ , and tta exchanged D) ZnAl ₂ O ₄ , E) ZnGa ₂ O ₄ , and ZnGa ₂ S ₄	105
Figure 4.1: pXRDs of A) 12.7% Eu(III) ZnAl ₂ O ₄ (inset: TEM image of a single particle with lattice spacing of 0.285 nm corresponding to the (220) lattice plane) and B) 15.6% Eu(III) ZnGa ₂ O ₄ (inset: TEM image of a single particle with lattice spacing of 0.295 nm corresponding to the (220) lattice plane). TEM scale bar is 2.5 nm. C) Eu L3.edge XANES data for 12.7% Eu:ZnAl ₂ O ₄ (blue) and 15.6% Eu:ZnGa ₂ O ₄ (red). The inset expands the region of the white line to make the spectral shift between samples more observable. EXAFS data (Zn in red and Eu in black) for D) 12.7% Eu:ZnAl ₂ O ₄ and E) 15.6% Eu:ZnGa ₂ O ₄ . For both (D) and (E) the open circles represent the data points and the solid lines are the 1 st coordination shell fit	113
Figure 4.2: pXRD at different Eu(III) concentrations in A) ZnAl ₂ O ₄ and B) ZnGa ₂ O ₄	114
Figure 4.3: High resolution TEM of 12.5% Eu ZnAl ₂ O ₄ . The samples were dissolved in toluene and deposited on a graphene grids. The samples were baked under high vacuum at 130°C for at least 8 hours. The TEMs were obtained using a Tecnai Osiris operating at 200 kV. The size distribution plot is included as an inset.....	115
Figure 4.4: High resolution TEM of 15.6% Eu ZnGa ₂ O ₄ . The samples were dissolved in toluene and deposited on a Ted Pella carbon type A (300 mesh) Cu grid with removable Formvar. The samples were baked under high vacuum at 130°C for at least 8 hours. The images were obtained using a Tecnai Osiris operating at 200 kV. The size distribution plot is included as an inset	116

Figure 4.5: TEM-EDS of 12.7% (measured by ICP-MS) Eu ZnAl ₂ O ₄ . The TEM-EDS was obtained using a Tecnai Osiris operating at 200 kV. The measured amounts results in a structure of ZnAl _{1.5} Eu _{0.25} O ₄	117
Figure 4.6: TEM-EDS of 15.6% (measured by ICP-MS) Eu ZnGa ₂ O ₄ . The TEM-EDS was obtained using a Tecnai Osiris operating at 200 kV. The measured amounts results in a structure of ZnGa _{1.2} Eu _{0.27} O ₄	118
Figure 4.7: XANES of Eu(III) doped ZnAl ₂ O ₄ and ZnGa ₂ O ₄ at the (A) Zn and (B) Ga K-edges	119
Figure 4.8: Normalized IR spectra of A) 12.7% Eu:ZnAl ₂ O ₄ and B) 15.6% Eu:ZnGa ₂ O ₄ (blue = acac, black = NOBF ₄ , red = tta). PL spectra of doped nanospinels before (blue) and after (red) tta exchange, C) 12.7% Eu:ZnAl ₂ O ₄ and D) 15.6% Eu:ZnGa ₂ O ₄ . E) Luminescence of 1 x 10 ⁻⁹ M Eu _{0.20} ZnAl _{1.80} O ₄ in toluene under 364 nm excitation when passivated by i) acac, ii) DMF, and iii) tta	120
Figure 4.9: Absorption spectra of tta exchanged Eu(III) doped A) ZnAl ₂ O ₄ (1% in black, 2.5% in purple, 4.7% in blue, 7.5% in green, 9.7% in red, and 12.7% in dark red) and B) ZnGa ₂ O ₄ (1% in black, 2.5% in purple, 5% in blue, 8.7% in green, 12.4% in red, and 15.6% in dark red)	121
Figure 4.10: Photoluminescence spectra of tta passivated samples with different concentrations of Eu(III) doped in A) ZnAl ₂ O ₄ (1% in black, 2.5% in purple, 4.7% in blue, 7.5% in green, 9.7% in red, and 12.7% in dark red) and B) ZnGa ₂ O ₄ (1% in black, 2.5% in purple, 5% in blue, 8.7% in green, 12.4% in red, and 15.6% in dark red). The samples were dissolved in toluene and the PL spectra collected at room temperature	122
Figure 4.11: Ratio of the integrated intensities of the ⁵ D ₁ → ⁷ F ₁ line to the ⁵ D ₀ → ⁷ F ₃ . Higher ratios generally indicate that there are longer Eu-Eu distances	124
Figure 4.12: A) tta passivated Eu(III) doped ZnB ₂ O ₄ crystal lattice (3 nm) showing the approximate range of the quenching spheres according to a Dexter mechanism. B) Energy level diagram indicating the singlet and triplet levels for tta relative to the Judd-Olfelt allowed transition in Eu(III) and the spinel band gaps. Perrin plot of A) ZnAl ₂ O ₄ (radius of quenching = 0.48 ± 0.02 nm) and B) ZnGa ₂ O ₄ (radius of quenching = 0.54 ± 0.03 nm).....	126
Figure 4.13: A) Ratio Eu ³⁺ emission versus tta emission (I _{612nm} /I _{420nm}) Eu ³⁺ doped ZnAl ₂ O ₄ and ZnGa ₂ O ₄ as a function of concentration. B) Intrinsic QE of the Eu ³⁺ emission in the spinels as a function of Eu ³⁺ concentration. C) Red orange (I _{612nm} /I _{580nm}) ratio of Eu ³⁺ doped ZnAl ₂ O ₄ and ZnGa ₂ O ₄ as a function of concentration. ZnAl ₂ O ₄ is in black and ZnGa ₂ O ₄ in red	128
Figure 4.14: CIE diagram above for all the doped spinel samples with the solids excited at 364 nm embedded in a PMMA below. Eu doped ZnAl ₂ O ₄ are represented by letters A-F, where A	

is 1% Eu:ZnAl₂O₄ and F is 12.7% Eu:ZnAl₂O₄. Eu:ZnGa₂O₄ are represented by G-L where G is 1.2% Eu:ZnGa₂O₄, and L is 15.6% Eu:ZnGa₂O₄.....133

Figure 5.1: A) Lattice structure of lanthanide doped ZnAl₂O₄ and Y₂O₃ with a surface passivation layer of tta and acac respectively. B) Energy level diagram showing the bandgaps of Y₂O₃ and ZnAl₂O₄ (in light blue), the energies of the J-O levels of the Eu³⁺ (in red) and Tb³⁺ (in green) ions, and the singlet and triplet levels of the ligands used in this study (in dark blue)142

Figure 5.2: IR spectra of A) 10% Eu:Y₂O₃, and B) 10% Tb:Y₂O₃. Ligands are colored the same in each graph (before exchange in grey, NOBF₄ in yellow, tfacac in black, acac in purple, tmhd in blue, fod in green, hfacac in red, and tta in dark red)144

Figure 5.3: PL spectra of ligand passivated, doped nanophosphors A) 10% Eu:ZnAl₂O₄, B) 10% Tb:ZnAl₂O₄, C) 10% Eu:Y₂O₃, and D) 10% Tb:Y₂O₃. Eu(III) doped nanophosphors $\lambda_{\text{ems}} = 614 \text{ nm}$, Tb(III) doped nanophosphors $\lambda_{\text{ems}} = 544 \text{ nm}$ Ligands are colored the same in each graph (tfacac in black, acac in purple, tmhd in blue, fod in green, hfacac in red, and tta in dark red). All samples were dissolved in toluene with the exception of samples passivated by hfacac, which were dissolved in acetone145

Figure 5.4: Excitation spectra of ligand passivated, doped nanophosphors A) 10% Eu:ZnAl₂O₄, B) 10% Tb:ZnAl₂O₄, C) 10% Eu:Y₂O₃, and D) 10% Tb:Y₂O₃. Ligands are colored the same in each graph (tfacac in black, acac in purple, tmhd in blue, fod in green, hfacac in red, and tta in dark red). Acac, tfacac, and tmhd $\lambda_{\text{exc}} = 315 \text{ nm}$, tta, fod, and hfacac $\lambda_{\text{exc}} = 340 \text{ nm}$. All samples were dissolved in toluene with the exception of samples passivated by hfacac, which were dissolved in acetone146

Figure 5.5: Quantum yield of the samples versus the energy difference between the singlet of the ligand and the lowest J-O level (⁵D₀ in Eu(III) and ⁵D₄ in Tb(III)). A) 10% Eu:ZnAl₂O₄, B) 10% Tb:ZnAl₂O₄, C) 10% Eu:Y₂O₃, and D) 10% Tb:Y₂O₃.....152

Figure 5.6: CIE coordinate diagram of ligand passivated, doped nanophosphors A) 10% Eu:ZnAl₂O₄, B) 10% Tb:ZnAl₂O₄, C) 10% Eu:Y₂O₃, and D) 10% Tb:Y₂O₃. Eu(III) doped nanophosphors $\lambda_{\text{ems}} = 614 \text{ nm}$, Tb(III) doped nanophosphors $\lambda_{\text{ems}} = 544 \text{ nm}$ Ligands are colored the same in each graph (tfacac in black, acac in purple, tmhd in blue, fod in green, hfacac in red, and tta in dark red)154

LIST OF ABBREVIATIONS

Abs	Absorption
acac	Acetylacetone
a.u.	Arbitrary Units
CFL	Compact fluorescent lamp
CP-MAS.....	Cross-polarization magic angle spinning
CT	Charge transfer
CVD	Chemical vapor deposition
DET	Dexter energy transfer
EXAFS	Extended x-ray absorption fine structure
FTIR	Fourier transform infrared
FWHM	Full Width Half Maximum
J-O.....	Judd Ofelt
HDA.....	Hexadecylamine
LED.....	Light emitting diode
Ln	Lanthanide
LMCT	Ligand to metal charge transfer
MW	Microwave
NMR	Nuclear magnetic resonance
NP	Nanoparticle
OLED.....	Organic light emitting diode
pc-LED.....	Phosphor converted light emitting diode
PL	Photoluminescence
PLE	Photoluminescence excitation
PLQY	Photoluminescence quantum yield
PVD.....	Physical vapor deposition
pXRD	Powder x-ray diffraction
QDs	Quantum dots
RE	Rare earth
S/P	Scotopic-to-photopic
SSL.....	Solid state lighting
ssNMR	Solid state nuclear magnetic resonance
TEM	Transmission electron microscopy
TGA	Thermogravimetric analysis
tta	Thenoyltrifluoroacetone
UV	Ultraviolet
XANES	X-ray absorption near edge structure

ABSTRACT

In this dissertation, microwave chemistry is employed to synthesize a variety of different crystalline nanoparticles (NPs). This introduction will describe the structures, properties and applications of the NPs studied within the dissertation, with a main focus being on ligand sensitization for the goal of enhanced luminescence. The use of metal acetylacetonate complexes to make Europium (III) doped Yttrium (Y_2O_3) NPs is explored, where the acetylacetonate acts both as a source of oxygen for the synthesis of Y_2O_3 , as well as an organic chromophore acting as an “antenna” for the absorption of light and subsequent excitation transfer to the incorporated Europium (III) (Chapter 2). Other host materials are investigated by method of metal acetylacetonate decomposition to synthesize a variety of different nanospinels, having the general formula AB_2X_4 , with sulfide variants made by decomposition of diethyldithiocarbamate, (Chapter 3). The antenna ligand thenoyltrifluoroacetone (tta), which is known to undergo a Dexter energy transfer (DET) mechanism to efficiently sensitize Europium (III) emission, is used to determine the distance of energy transfer in Europium (III) doped nanospinels by passivating the surface of the nanospinel with a tta (Chapter 4). A variety of ligands are explored in order to optimize the sensitization efficiency in relation to the difference in energy between the singlet and triplet levels of the ligands versus the $^5\text{D}_0$ and $^5\text{D}_4$ energy levels of Europium (III) and Terbium (III) respectively (Chapter 5).

CHAPTER 1

INTRODUCTION

1.1 General Introduction

Solid state lighting (SSL) utilizes phosphors, including nanophosphors, as the luminescence source when light emitting diodes (LEDs) are used as the light source. A nanophosphor is a nanomaterial (under 10 nm in diameter) which is optically luminescent. Nanophosphors are useful as lighting sources due to their high quantum efficiencies, ease of synthesis, and versatile tunability.¹ SSL is highly efficient, up to ten times more efficient than incandescent bulbs and two times more efficient than fluorescent lighting.² The latter two types of lighting lose significant amounts of energy to heat - especially in the case of incandescent bulbs. SSL is also far less toxic than fluorescent lighting, as LED light sources contain no mercury. Lighting accounts for around 18% of all electricity use in the United States, a number which has been steadily decreasing since the introduction of LED lightbulbs.³ Through the use of SSL, lighting energy consumption is projected to decrease 40% by 2030 resulting in an overall energy savings in the US of 7%.³ This would result in substantial greenhouse gas reduction from the production of electricity, resulting in noteworthy positive environmental effects. Investigation into SSL research has the potential to significantly improve the quality of life and the overall health of the planet. As SSL is an expanding technology which is projected to replace all other lighting technologies within the next few decades, research into understanding and improving the materials involved is an important undertaking.

By improving the components of LEDs to make the embedded phosphor or phosphors, more efficient, great strides can be made toward the successful global implementation of SSL. The introduction will be concerned with presenting the topics that will be later discussed within the dissertation. The main focus of the dissertation is improving synthesis methods and efficiencies of phosphors for SSL, therefore the first topic to be covered LEDs, looking at the history, design, and state-of-the-art of the technology. Next will be an overview of nanomaterials and nanotechnology. Afterwards, the synthesis method of the materials will then be presented. Lastly, the methods of characterization of the materials will be discussed, with particular emphasis on structural and optical characterization methods.

1.2 Light Emitting Diodes (LEDs)

Light emitting diodes, LEDs, are a common light source used in SSL. LEDs contain a phosphor material within the diode or embedded in a polymer above the diode of the LED. Excitation of the phosphor is achieved either electrically or by UV/blue excitation for phosphors embedded within the diode or polymer layer, respectively. The phosphor pumped by the UV or blue LED achieves emission through a down conversion process, and is known as a phosphor converted LED. The synthesis and characterization of NPs to be used in down conversion phosphors is the focus of this dissertation, therefore, an understanding of LEDs and solid state lighting is imperative.

1.2.1 History of the LED

The first evidence of electroluminescence – the key property that allows LED's to work - came about in 1907.⁴ Henry Round and other researchers found that certain crystals, used in radio receivers, fluoresced after exposure to electricity, leading to the term “electroluminescence”. Other discoveries were made to further LED technology, however, the next most significant came from Nick Holongale of General Electric. His discovery of the first red LED that was bright enough to be utilized in commercial applications, leading to him being deemed the “father of the LED.”⁵ By 1968, the red LED was being mass produced, appearing in indicator lights produced by Monsanto as well as calculators made by Hewlett Packard. Sufficiently bright yellow and green LEDs soon followed suit when George Craford investigated a different type of crystal semiconductor in 1972. By the 1980s, red, yellow, orange and green LEDs had been fabricated to be 10 times brighter than the previous generation of LEDs.⁶ This allowed for the construction of LED traffic signals for the first time in 1989. The next big breakthrough came in 1993 when Shuji Nakamura demonstrated the first efficient blue light-emitting diode made from GaN, a feat that later resulted in him receiving the Nobel prize for physics.⁷ With an efficient blue light source, white light generation became possible, opening up the future for SSL.⁴

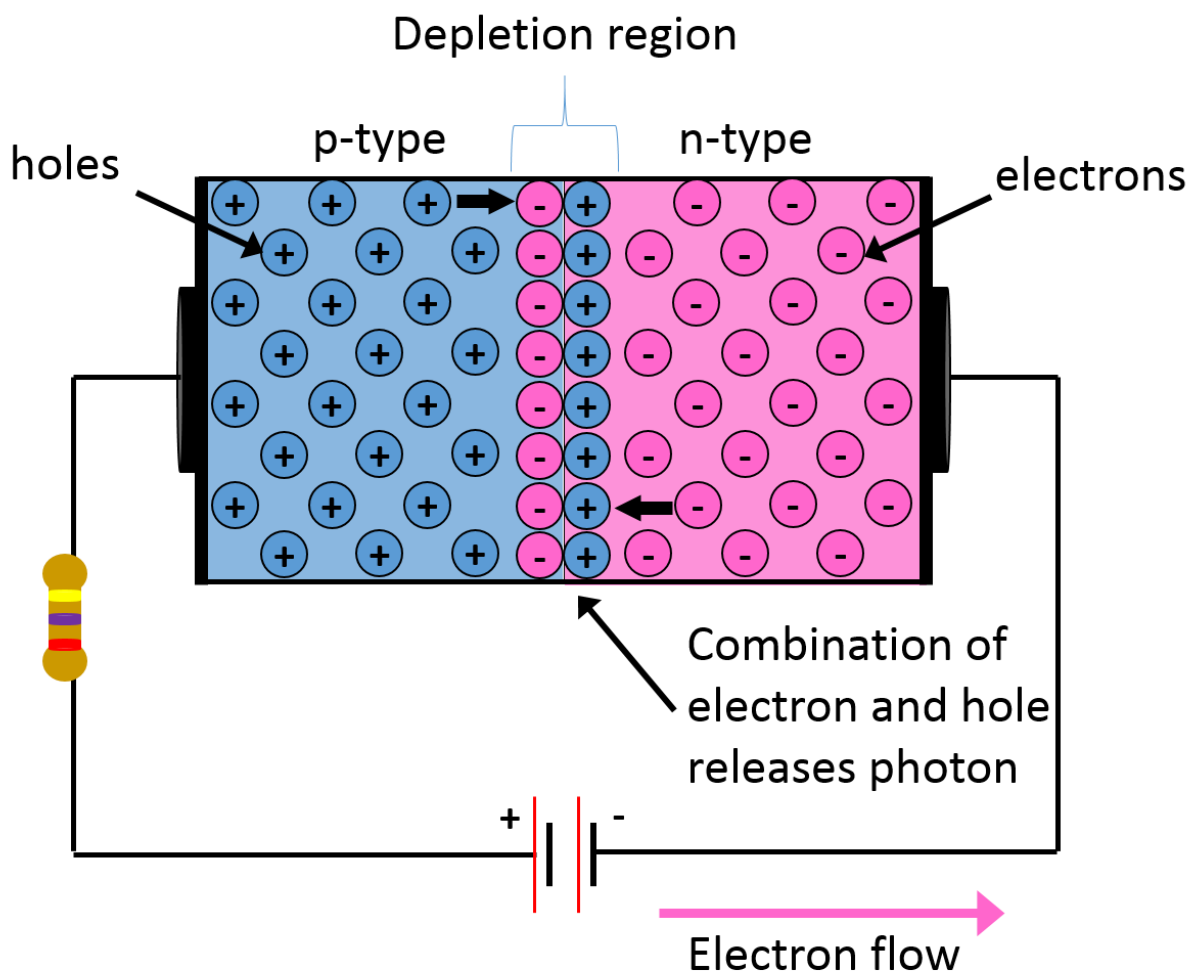


Figure 1.1: A p-n junction diode with forward bias being applied.

1.2.2 LED Design

Light emitting diodes consist of a p-n junction diode, shown in Figure 1.1, containing an n-type and p-type semiconductor. A diode works on the principle of electroluminescence where light is emitted as electricity is passed through the diode. In essence, as a forward electrical bias is applied to the diode, electrons diffuse into the depletion region formed at the junction between the two semiconductors from the n-type semiconductor. Simultaneously, holes are pushed into the junction due to the repulsion from the positive voltage applied as a result of the forward bias. The current design for a basic 5 mm LED is shown in Figure 1.2.⁸ The color of the LED is determined by the semiconductor dye that is electrically pumped via the electrical leads.

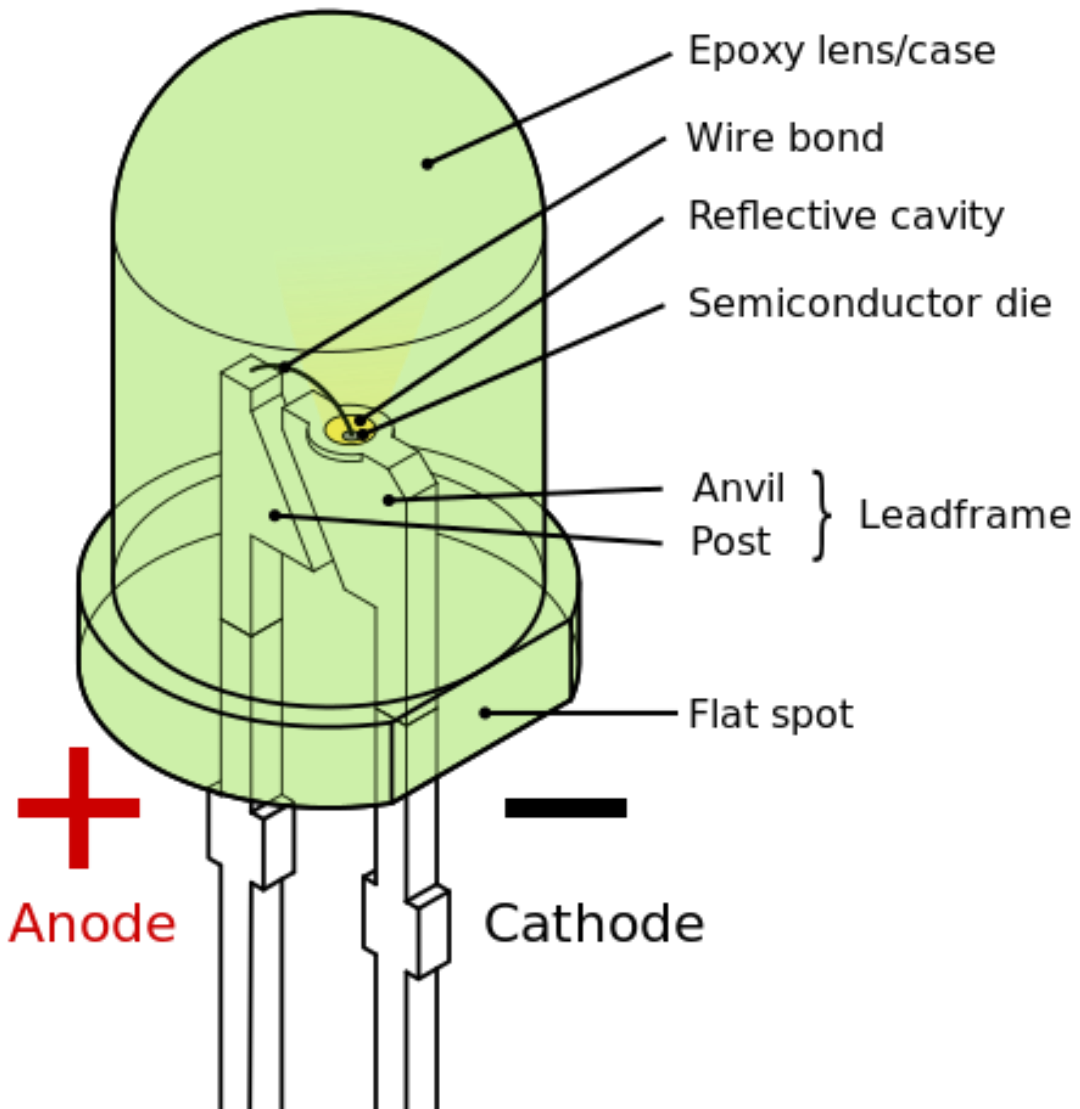


Figure 1.2: A typical 5mm LED design.

The LED colors that are generally used are listed in Table 1.1, noting their wavelength range and the semiconductor used to produce the color. Commercially available LEDs are composed of bulk semiconductors which have fairly high quantum efficiencies.

For the production of white light in a phosphor converted LED (pc-LED), there are a variety of different methods, shown in Figure 1.3. A pc-LED generates white light through a UV or blue electrically pumped diode overcoated with a phosphor that can be excited by the light given off by the diode. This can be done with a blue LED pumping either a yellow phosphor or a

Table 1.1: Material and wavelength (nm) of LEDs of specific colors.

LED Color	Wavelength Range	Semiconductor
Violet	390-455	InGaN
Blue	455-492	ZnSe
Green	492-577	GaN
Yellow	577-600	AlGaInP
Orange	600-625	GaAsP
Red	625-760	AlGaAs

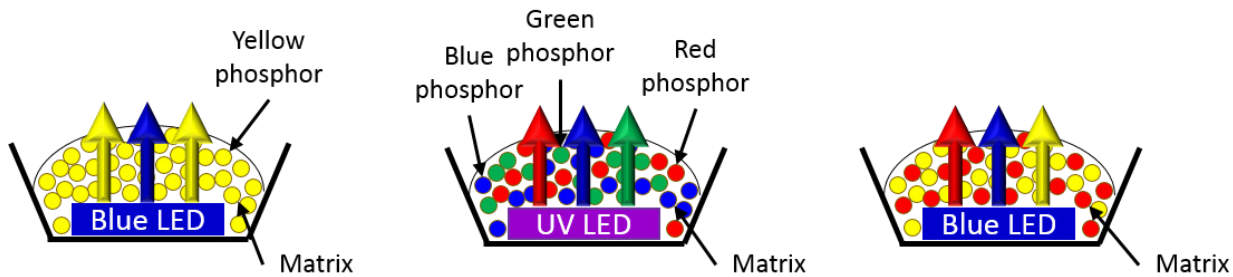


Figure 1.3: Typical designs for a pc-LED for generation of white light through either a blue LED pumping a yellow or yellow and red phosphor, or a UV LED pumping a combination of blue, green, and red phosphors.

combination of green and blue. Alternatively, white light can be obtained through red, green, and blue phosphors pumped by a UV LED. The color quality of pc-LED is greatly dependent upon the individual components' emission. Sharp emission lines, along with high molar absorption coefficients, are required in order to efficiently absorb the blue or UV LED light, which increase energy efficiency while also avoiding either light that is too cool or UV leakage, respectively.

1.2.3 State-of-the-Art

The state of the art in solid state lighting is still Ce:YAG for performance, but the Color Rendering Index (CRI) is poor. Phillips currently sells a high performance white light LED based upon this technology, their Luxeon T LED's, with a lumens per watt (lm/W) output as

high as 143 lm/W for cool white (5000K-6500K), 140 lm/W for neutral white (4000K) and 123 lm/W for warm white (3000K).² Attempts to tune the control by the incorporation of sulfur have shown improvement of color quality, but at the expense of host stability. More recently, quantum dots have been proposed as likely replacement technology, and as such are already appearing in devices and are commercially available through QDvision and Nanoco. Unfortunately, most quantum based devices rely on heavy metal or toxic binary components that will limit their application downstream and require significant encapsulation to lower the environmental risk. Furthermore the success of producing reproducible quantum dots that meet the desired technical criteria in high quantities remains challenging. While kg batches are being produced (Nanoco), failure rates, often > 30%, still exceed the requirements for cost-effective production. Difficulties that are appearing in the QD approach include thermal degradation, photo induced color shifting, and long term stability in the devices. The recent development of a single source route to doped oxides, has shown that Eu³⁺ can be incorporated into yttria producing a temperature and humidity stable phosphor. Unlike traditional CdSe or InGaP quantum dot based nanoscale phosphors, the nanospinels are not considered a health risk and can achieve the CIE targets for white light.^{9, 10} While lanthanide doping of oxides has been demonstrated in nano-yttria, the color quality and performance is below future DOE targets.¹¹

SSL platforms based upon down conversion phosphors rely either on a single component broad band emitter, of which Ce:YAG is an example or multi-component blends to simulate white light. Clear limitations such as scattering, re-absorption, thermal and humidity stability, and active control over color have suggested the development of nanoscale phosphors and new hosts may allow DOE targets to be achieved. To date, the effort on nanoscale down conversion phosphors has focused on producing materials by bulk ball-milling or solvothermal routes that lead to large micron scale aggregates or poorly formed materials with a distribution of emitting sites leading to loss of color quality in the packaged LED phosphor. While breakthroughs have appeared through the use of Eu²⁺ broad band emitters in nitrides and silicates, the difficulty in actively tuning the CRI, relegates these material advances to the “simple” solid state lighting approaches.^{12, 13} Extensive synthetic efforts in oxides, notably yttria have shown the practicality of doping lanthanides into the host lattice, but performance has been moderate due to disorder and high scattering properties of the reported materials.¹⁴⁻¹⁷ Furthermore, yttria is a critical material due to low supply. Many of the current phosphors do not produce true white light, nor

are they easily processed due to insolubility of the solid state phosphors that are utilized commercially.¹⁸

Classical rare earth (RE) phosphors doped into oxide, nitride, sulfide, and oxysulfide host lattices are effective but excess rare earth compounds are required to promote high quantum efficiencies. Each of these phosphors are susceptible to charging effects due to photon-traps, degradation under UV excitation, and in the case of Cd based lighting environmental toxicity. Classical phosphors employed in compact fluorescence lights (CFLs) are not directly compatible with LEDs and are typically single color (Ce doped YAG) exhibiting poor color rendition and are insoluble in polymer cladding.

1.2.4 The Future of Solid State Lighting

The future of LED technology is the PC-LED (Phosphor Converted Light Emitting Diode), where a blue LED down-converts a yellow or green phosphor material resulting in white light. The InGaN blue LED has a higher than 80% power-conversion leading to a wall plug efficiency of 40% (direct electroluminescent pumping). The blue LED then pumps the yellow phosphor material, and the resulting efficiency is only 22% (another issue with this design is poor color rendering.) Though this approach is inefficient, this technology is still the most reliable and cost effective white LED fabrication method that achieves a reasonable luminosity.

Many different approaches are being investigated to further solid-state (ss)-lighting technology. One approach is to improve the phosphors used in PC-LED's, allowing established technology to advance further. Another way of improving SSL is to forgo down-conversion completely, relying instead on the mixing of three or four electrically pumped LED's (RGB or RYGB) to produce white light. Both methods have their advantages and challenges.

Phosphor development and improvement is arguably the easiest method of SSL advancement. The phosphor could either be pumped with a blue LED (InGaN) or an UV-LED, depending upon the absorption profile of the phosphor. The most advantageous, of course, would be pumping by the blue LED, as this would allow for lower energy costs. In addition, the down-converters need to have a high Quantum Efficiency (QE), a narrow emission linewidth (5.25 nm), tunability, thermal stability, and low cost.^{2, 3, 19} The lifetime of the LED source needs to be at least 50,000 hours at normal operating conditions, taking into account temperature, UV and blue light exposure, as well as moist and dry environments. The phosphors are expected to

operate at high temperatures, and it is important that at those temperatures the phosphor is stable and still emissive. It is also important that the phosphors don't suffer from color shifts, so they need to have color stability, reliability, and long lifetimes. Issues with color shifts can cause long term warranty liability consequences.¹⁹ Additionally, there is a push for reducing rare-earth concentrations, as well as avoiding heavy metal or toxic phosphors.²

The purpose of the work included in this dissertation is the synthesis of phosphor materials in order to improve the existing SSL technology. The phosphors consist of host lattices of either Ln:Y₂O₃ or earth abundant Ln:AB₂O₄ spinel host lattices (ZnAl₂O₄ or ZnGa₂O₄) in the 3.6 nm diameter range that are passivated by molecular antenna that exhibit enhanced down conversion efficiency through energy transfer from the antenna molecule to the embedded lanthanide ions (Ln(III) = Eu or Tb).

The basic operating principle to enhance performance of the molecular antenna passivated nano down conversion phosphor is enhanced Dexter energy transfer in the system.²⁰ The use of a molecular antenna enhances efficiency by light harvesting to improve photon capture and improved energy transport to the emitter. The efficiency of down conversion from a molecular antenna to the Ln(III) emitter in a host lattice is directly dependent on the energy transfer pathways to the desired emissive state and the distance between the absorber and emitter. The strategy not only improves conversion efficiencies, it is anticipated to result in lower Ln(III) ion loading and allows for lower energy excitation due to the molecular antenna absorption. The molecular antennae are β -diketone derivatives that have energy overlap of the triplet levels with the $f-f$ levels in the lanthanide. The nanophosphor's improvement in efficiency reflects the increased cross section for absorption (photon capture), improved triplet to $f-f$ Ln(III) energy transfer, and more efficient Ln(II) incorporation at the Dexter critical distance for energy coupling.²¹ The NPs are small in size to allow for enhanced conversion efficiency from the molecular antenna to the Ln(III) ion based on predictions from the Dexter energy transfer mechanism. In addition, the small size of the particles in comparison to bulk crystals that are currently used in LEDs, have less loss from scattering, which should improve efficiency, as well as make them more soluble, allowing them to be embedded in the LED cladding.

1.3 Nanoscience and Nanotechnology

The term “nano” is the Greek prefix that refers to a unit of measurement that is 10^{-9} which translates into one billionth of the suffix unit. Nanoscience is the study of structures and materials at the nanometer scale. Though nature has been producing compounds at the nanometer scale for billions of years (such as DNA which has a width of approximately 3 nm), scientists only began to explore the possibility of synthesis on the nanoscale about 60 years ago. Back in 1959, Richard Feynman expressed the idea that there was potential to synthesize smaller structures through the direct manipulation of atoms.²² This idea resulted in the term nanotechnology, first coined by Norio Taniguchi in 1974, then later by Eric Drexler in 1986.²³ The first proof of this concept came in 1983 when L.E. Brus found evidence of changing band gap energies of aqueous CdS crystallites, which he determined to be representative of the change in size of the CdS particles. A year later, Brus published on the quantum confinement effects of CdS as a three dimensional particle in a box.²⁴ This watershed event led to the explosion of nanoscience, both industrially and academically. The next year, in 1985, a further leap forward in nanoscience was made when Harold Kroto, Richard Smalley, and Robert Curl discovered fullerene, a 1 nm spherical lattice of interconnected carbon atoms.²⁵ This was followed by the discovery of graphene (flat monolayers of connected carbon atoms) and carbon nanotubes (cylindrical tubes of single or multi-walled carbon atoms that have nanometer scale widths and lengths upwards of micrometer). Since that time, the synthesis and characterization of materials on the nanometer scale, also known as NPs, have been explored extensively.²⁶⁻³² The main focus of this dissertation is the synthesis and characterization of nanomaterials for use in solid state lighting.

Quantum dots (QDs) and other NP types are of great interest owing to the unique properties they exhibit at the nanometer scale. They are crystalline materials possessing both metal and nonmetal elements, and therefore have a characteristic bandgap. QDs are based on semiconductor materials with small band gaps (0.1-3.9 eV), while metal oxide and sulfide NPs are generally wide band gap semiconductors or insulators (4.0+ eV). The size range of QDs is usually confined to 1.10 nm, while metal oxides and sulfide NPs can be anywhere from 1 nm to 100s of nanometers. The QD size regime results in what is known as quantum confinement, a phenomena that results in the band gap being dependent upon the size of the material. This will be explained in more detail later in this text, but briefly, the phenomenon results from the size of

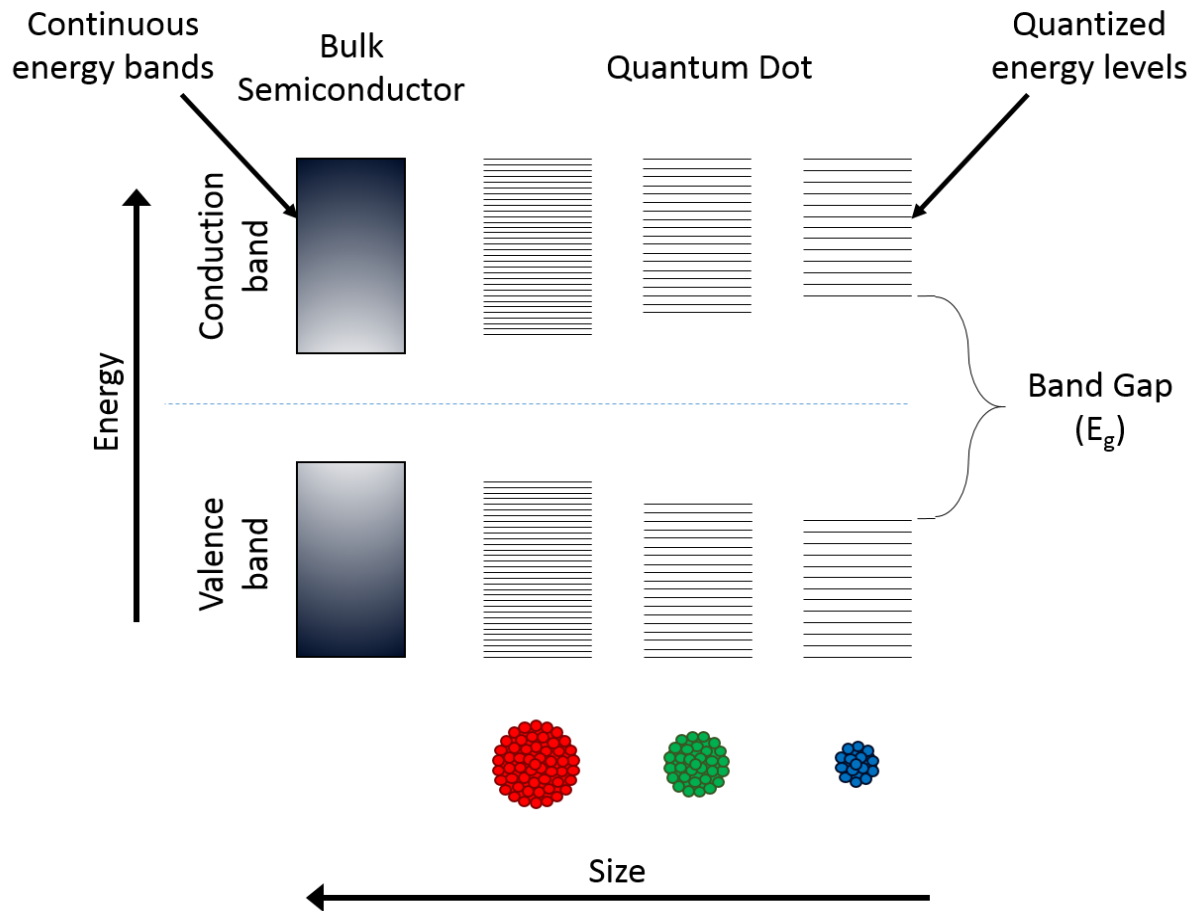


Figure 1.4: A pictorial depiction of the energy levels for a bulk semiconductor versus that of a quantum dot. As is shown, as the size of the QD gets smaller, the energy levels become more discrete, and the band gap widens, causing a shift in the absorption of the particle to higher energy.

the nanomaterial becoming smaller than the Bohr radius of the exciton in the bulk semiconductor, thus the particle undergoes a process known as quantum confinement. The exciton is an electron hole pair, where the electron and hole are coupled to each other via coulombic attractive forces. Quantum confinement, or the confinement of the electron's movement due to the reduced particle size, results in quantized energy levels that allow for widening of the band gap, which in turn allows for the electronic and optical properties to be tunable with material size.

Nano-oxides may also feel the effects of quantum confinement, though tunability is limited by a smaller exciton Bohr radii and larger band gaps in these materials. For metal oxides

to exhibit quantum confinement effects, they often have to be on the order of 1.2 nm. For example, Y_2O_3 has a Bohr radius of 1 nm,¹ which is too small for even weak confinement to occur. Despite this, there has been reports of luminescence enhancement in lanthanide doped Y_2O_3 nanoparticles.^{17, 33, 34} The enhancement in nano-oxides systems stems from high surface area and changes in oscillator strength. Additionally, confinement of an atom in a single nanoparticle results in increased interaction with the host material compared to bulk.¹

1.3.1 Quantum Confinement and Size Effects

NP Quantum confinement is defined as the confinement of the wavefunction of a material as a result of decreasing size. In effect, the motion of the electrons is confined to a volume smaller than the wavelength of the electron, which causes a loss of the ability to move freely, as in a bulk material. In response the electron forms an electron-hole pair, also known as an exciton, which is at a discrete energy level. This in turn causes the properties of the material to be between that of a bulk material and a molecule. As shown in Figure 1.4, the band gap of a material can be altered by decreasing the size of the material. This is a result of reducing the number of atoms within the crystal. When comparing a semiconducting material at the bulk scale to that of a NP, there are infinitely more atoms in the bulk compared to the NP, each with associated energy levels. In bulk materials, the massive amount of overlapping energy levels results in bands of energy as opposed to discrete levels, which are seen in molecules and nanomaterials. These bands known as the valence band (where all the ground state electrons are located) and the conduction band (the empty orbitals where conducting electrons go after excitation) have a gap of energy between them, devoid of any energy states. This gap is known as the band gap, and it is dependent upon the composition of the material. As the material is reduced in size, there are fewer and fewer energy levels contributing to the energy bands of the materials, which allows for a widening of the band gap. The equation that dictates the relationship between the bulk band gap and the band gap at a given size is the Brus equation, shown below.

$$E_{np} = E_g + \frac{\hbar^2}{8r^2} \left(\frac{1}{m_e^*} + \frac{1}{m_h^*} \right) - \left(\frac{1.8e^2}{4\pi\epsilon\epsilon_0 r} \right) \quad (1.1)$$

In this equation, E_{np} is the expected bandgap of a NP at a radius r , shown to be the first exciton peak. E_g , m_e^* , m_h^* , and ϵ are all values relating to the specific material that is under investigation, and represent the band gap of the material, the effective mass of the electron, the

effective mass of the hole, and ϵ is the dielectric constant of the material, respectively. The remaining values are the charge on the electron, e , and the vacuum permittivity, ϵ_0 . In addition to the increase in band gap at decreased sizes, the energy levels themselves become discrete. This is the reason for the ability to see the absorption features instead of just a band gap edge. Additionally, as the material becomes smaller, the absorption coefficient of the material becomes larger, as a result of a higher phonon density in a nanomaterial.

The size of a semiconductor greatly affects the electronic properties of the material. In a semiconductor crystallite with a radius smaller than the size of its exciton Bohr radius, the excitons are compressed, leading to quantum confinement. The energy levels can then be modeled using the particle in a box model in which the energy of different states is dependent on the length of the box. The confinement of the particle can either be strong or weak, depending on both the size of the particle as well as the composition of the material. NPs which possess sizes that are on the same order as the exciton Bohr radius are said to be in the 'weak confinement regime' while those smaller in size are considered to be 'strongly confined.' If the size of the quantum dot is small enough for the quantum confinement effects to dominate (typically less than 10 nm in diameter), then the electronic and optical properties will be highly tunable. The optical properties of a material are usually determined by electronic transitions within the material and light scattering effects. As a result, when the electronic transitions within a material are altered, so are the optical properties that it exhibits.

QDs show the most prevalent effects from confinement within the scope of semiconductors. All semiconducting NPs can be confined when at an appropriate size, though only QDs have small enough band gaps and large enough Bohr radii to show strong confinement. Although not studied in this dissertation, QDs are an important material within the field of nanoscience, and the strong confinement shown in QDs will better explain the effects of confinement that can be applied to the materials studied hereafter that show weak confinement effects.

Quantum structures (dots, wires, and wells) show very interesting properties as a result of directional confinement. The most apparent size effect in Quantum structures is the difference

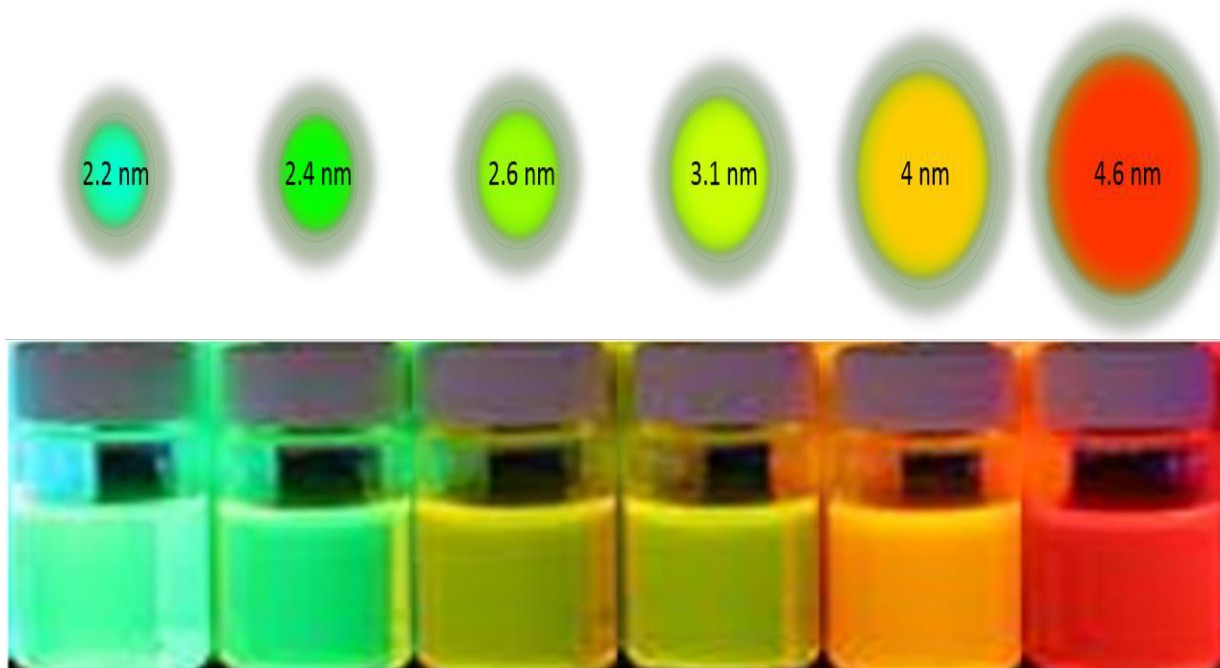


Figure 1.5: CdSe/ZnS quantum dots relating the size of the nanoparticle (shown above) with the emitted color of the QDs (shown below).

in optical properties. Figure 1.5 shows how the size of the QD directly relates to the color of the QD (absorbance and emission spectra). As the size is decreased, the color of absorption of the material goes from red to yellow to blue, with other colors seen in between. In addition, quantum structures, unlike their bulk semiconductor counterpart, efficiently absorb and emit light. The wavelength of that light depends on the composition of the material and the size of the particle. As a result, quantum dots in particular are being investigated for lighting, display technologies, and biological imaging. QDs and other <10 nm NPs, are small enough for probing intracellular events. In addition, NPs possess highly functional surfaces with large surface to volume ratios which allow for appendage of various biologically relevant molecules, such as peptides, DNA, and small molecule therapeutics to be attached for cellular targeting, delivery and simultaneous tracking.

The effect of decreased size on the properties of the material varies. In a metal NP, which has no band gap, a pseudo-semiconductor is formed as a result of a band gap forming. As a result, the material forms a surface plasmon which can be tuned by size. In addition, the color of the material changes dramatically. For example, gold is characteristically yellow in color, yet at

the nanoscale, colloidal gold is purple in color. Many metals also show significantly different properties at the nanoscale. Unlike bulk gold which is relatively inert, NPs of gold, as well as other noble metals, have been found to be great catalysts.³⁵

Another material that is interesting at the nanoscale is carbon. Graphite, the material you find in a pencil, is composed of billions of sp^2 hybridized carbon atoms arranged in ring patterns. Graphite naturally has a high electrical conductivity as a result of the delocalized electrons throughout the structure, however, it is a fairly soft material as it is composed of sheets of carbons which are only weakly associated with each other. At the nanoscale, for instance, one layer of graphite, also known as graphene, has a significantly larger mechanical strength, with a hardness similar to diamond.³⁶ In addition, graphene sheets show very high thermal conductivity and an ability to absorb molecules onto the surface of the sheet. Nanodiamond has also been investigated, and it is shown to possess higher chemical and biological activity, yet retain many of bulk diamond's fundamental properties, such as hardness.³⁶ Other interesting carbon nanostructures include fullerene, a spherical lattice composed of 60-70 carbon atoms which is soluble in organic solvents³⁷ and can absorb molecules and metal ions on the surface or inside the carbon ball. Additionally, carbon nanotubes are long tubes of carbon atoms which have remarkably high tensile strength, elasticity, and conductivity.³⁸

1.3.2 Metal Oxide Nanoparticles

Both semiconducting and insulating NPs are studied in this dissertation. They are used as host materials for a variety of lanthanide ions and their photophysical properties are investigated. Metal oxide NPs have very small Bohr radii, small enough that extremely small sizes are needed to achieve confinement, and even so are usually only weakly confined. As such, metal oxide NPs are only weakly confined and therefore do not show quantized energy levels as QDs do. Though many of them are semiconductors, their band gaps are too large to allow for great tunability, only shifting energy in both absorption and emission few nanometers upon a decrease in size. These types of materials make good host lattices for dopants, as they are generally more robust than their QD counterparts, and the desired properties are often a result of the dopant incorporation rather than the semiconductor itself, making dopant induced defects favorable instead of detrimental to the optical properties, such as quenching of the emission in transition metal doped QDs.³⁹ The band gaps for these materials are generally pumped in the UV, making them ideal

hosts for lanthanides as their bandgaps will often overlap with the f-f transitions of the lanthanides, acting as a sensitizer for emission. Insulating NPs, such as Y_2O_3 , do not have bandgaps at low enough energies to overlap with the energy of the lanthanide f-f transitions, making them unable to directly energize the lanthanide ions.

1.4 Synthesis of Nanoparticles

The NPs in this dissertation were prepared using Microwave (MW) heating. MW heating is a thermal heating technique which utilizes MW radiation with centimeter wavelength electromagnetic waves in order to heat molecules. This method of heating selectively heats specific molecules by taking advantage of a molecule's dipole. By using MWs to couple with the molecule's dipole moment, and through alignment of the static dipole of the reactants with oscillations of the MW field, heat is produced through friction. That heat can then be transferred to the surrounding atoms, thoroughly heating the reaction batch. By doing this, the efficiency of the reaction increases dramatically, as well as the reproducibility. By use of MW heating, NPs can be produced at small sizes with good size distribution. In addition, doping is possible with a range of concentrations of ions to a desired molar quantity, further opening up the applications of the NPs in question.

1.4.1 Methods of NP Synthesis

Quantum dots and oxide NPs have been synthesized in a variety of different ways which can be characterized into two different groups: the top-down approach, and the bottom-up approach. Thus NPs can be synthesized by either breaking down products mechanically, to form smaller subunits, or building up the products from atomic and molecular precursors. The synthesis methods have been summarized in Figure 1.6.⁴⁰ The top-down approach is divided into dry and wet grinding. It is the crudest method, and therefore the least successful in making high quality NPs. In dry grinding, bulk materials are reduced in size by grinding the material using a mill, such as a ball mill, resulting in grinding through shock, compression, or friction. This method in general, will not make nanoscale materials with much homogeneity. Wet grinding is accomplished through use of a fast-rotating liquid-phase agitator in a grinding mill. Though this method is more useful for NP synthesis than the dry grinding approach, the method is still lacking in the ability to make highly uniform, < 100 nm particles.

The bottom-up approach is the most highly investigated and successful method for synthesizing NPs. The method can be further divided into solid phase and liquid phase methods. In solid phase bottom-up methods, the precursors are generally solid compounds heated to high enough temperatures that they sublime. The two main approaches are the chemical vapor deposition method (CVD) and the physical vapor deposition method (PVD), where in CVD the reaction occurs in the gaseous phase, and in PVD, the materials are evaporated then rapidly cooled to form NPs. CVD has been successfully employed to synthesize carbon nanotubes and NPs of silicon, titanium, and zirconium oxide.^{35, 41} The synthesis of NPs using PVD is less studied, though groups have reported synthesis of titanium dioxide. These methods can be used to make <100 nm particles, though very small sizes cannot be achieved.⁴² Through these methods, oxide and metal NPs have been the most successfully made, and industrially, CVD and PVD are the most widely used for these materials.

The other bottom-up approach is in the liquid phase, either through sedimentation methods or liquid/liquid. This approach has recently become the most investigated method as it is capable of making < 10 nm particles with favorable size distributions as well as the easiest to execute and manipulate. Different shapes, sizes, and compositions can easily be achieved using the liquid phase method. These methods are also generally the cheapest, as expensive equipment is not necessary, though the reactions are more difficult to scale up.

The liquid phase method can be subdivided into the sedimentation method and the liquid/liquid method. There are several different sedimentation methods, though the most studied and successful is the sol-gel method. The sol-gel method has been used to make a whole host of different NP types, including silica NPs and various metal oxide NPs.⁴³ The liquid/liquid technique can also be divided into many more group as well, including the reduction method, which includes chemical and photo-reduction, and the solvothermal method, including lyothermal and hydrothermal. The chemical reduction technique has been highly successful in the synthesis of gold NPs, as well as other types of metal NPs.^{31, 44}

Within the liquid/liquid techniques, MW chemistry can be found. Most of the techniques within the liquid/liquid regime have been attempted using MW heating.^{40, 45-49} MW heating adds the advantage of short reaction times, scalability, and reproducibility not found with other thermal heating methods for liquid/liquid techniques.^{29, 47, 48, 50}

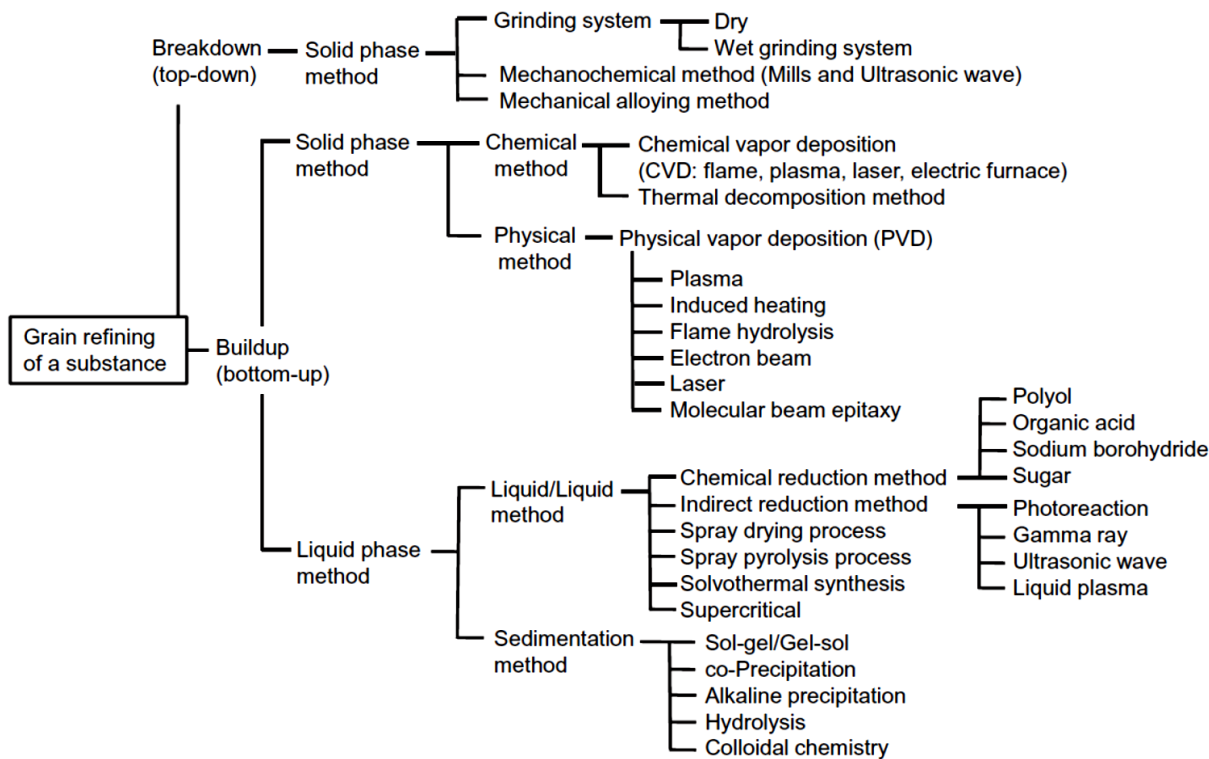


Figure 1.6: A flow chart illustrating all the methods for nanoparticle synthesis through either a top-down or bottom-up approach.

1.4.2 Nucleation Theory

The nucleation theory is the proposed mechanism by which nanocrystal nuclei ‘seeds’ form, acting as the base unit for crystal growth. Nucleation can be considered either homogeneous or heterogeneous depending on the reaction conditions. Homogeneous nucleation occurs as a burst of nuclei that form simultaneously within the solution, while heterogeneous nucleation is a more stochastic process. A reaction undergoes random nucleation as a result of temperature gradients within the reaction or as a consequence of point nucleation due to an impurity or container surface. In order to obtain highly crystalline, uniform NPs, homogeneous nucleation is essential.⁵¹

In order to achieve nucleation and crystal growth, nuclei of a critical size must be formed. The critical nuclei size must be large enough to be stable within the solution without redissolving. When considering the critical nuclei size for a spherical particle, it is essential to

first look at the total free energy as a function of the surface free energy, γ , and the bulk crystal's free energy, ΔG_v . The equation for the total free energy of a spherical particle of radius r is defined by equation 1.2, while the bulk crystal free energy, ΔG_v is then given by equation 1.3.

$$\Delta G = 4\pi r^2 \gamma + \frac{4}{3}r^3 \Delta G_v \quad (1.2)$$

$$\Delta G_v = \frac{-k_B T \ln(S)}{v} \quad (1.3)$$

Here T is the temperature, k_B is the Boltzmann constant, S is the supersaturation of the solution, and v is the molar volume of the solution. If ΔG is differentiated with respects to the radius of the particle and the set to zero ($d\Delta G/dr = 0$), the critical nuclei size can be determined using equations 1.4 and 1.5.

$$\Delta G_{crit} = \frac{4}{3}\pi\gamma r_{crit} = \Delta G_{crit}^{homo} \quad (1.4)$$

$$r_{crit} = \frac{-2\gamma}{\Delta G_v} = \frac{2\gamma v}{k_B T \ln(S)} \quad (1.5)$$

The critical radius of the nuclei as well as the critical free energy to obtain the nuclei can be viewed pictorially in Figure 1.7.

In addition to the formation of a critical nuclei, other factors are considered in the nucleation theory, including the growth mechanism. One of the most accepted theories of crystal growth is the LaMer mechanism, which divides the nucleation into two steps, the formation of monomers, and then the monomers forming nuclei through what is considered a “burst nucleation” step. Following the nucleation, crystal growth occurs from the monomers adding to the nuclei or the nuclei attaching to each other. The LaMer diagram can be seen in Figure 1.8. It can be seen from the diagram that as time goes by, the monomer concentration increases to the point at which it reaches the minimum concentration needed for nucleation, at which point nuclei form. During nuclei formation, the monomer concentration decreases dramatically, resulting in no more nuclei forming, after which point the nuclei grow into NPs through diffusion of the monomers still left in solution. The growth of the NPs is then dictated by either Ostwald ripening, coalescence, or oriented addition.⁵¹

Though there are other theoretical mechanisms that describe the growth of particles, Ostwald ripening, coalescence, and oriented addition are the main schools of thought on the subject. In Ostwald ripening, large particles grow at the expense of smaller ones, by adsorbing their atomic mass as they redissolve into solution. In theory, the smaller particles are redissolved,

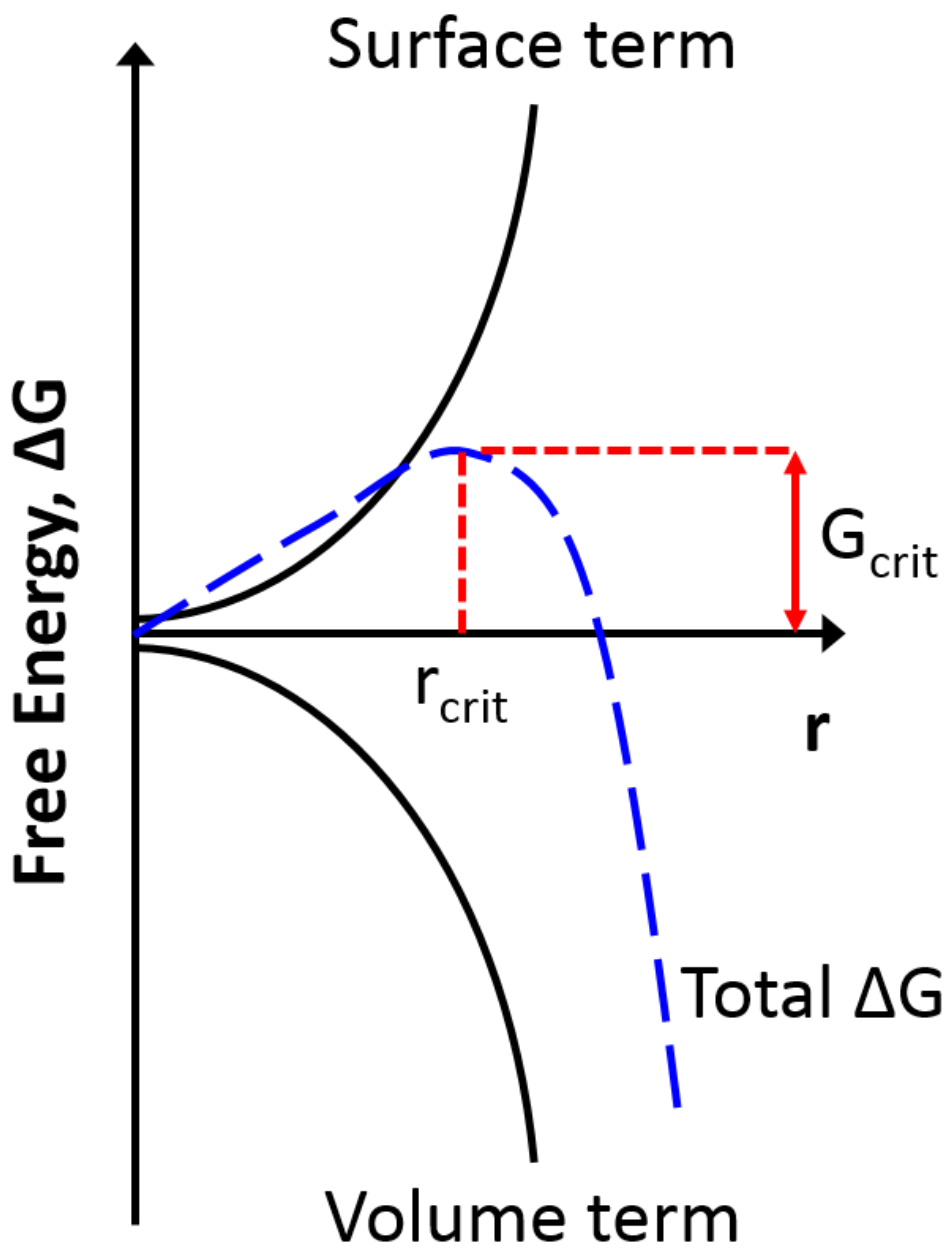


Figure 1.7: Free energy diagram of a spherical particle, showing both the critical free energy required for nanoparticle formation as well as the critical radius size to avoid redissolving of the particle.

and act as monomers for larger crystals to grow. Ostwald ripening is thought to occur because smaller particles are more soluble than the larger particles, and thus can be reintroduced into the

LaMer Burst Nucleation

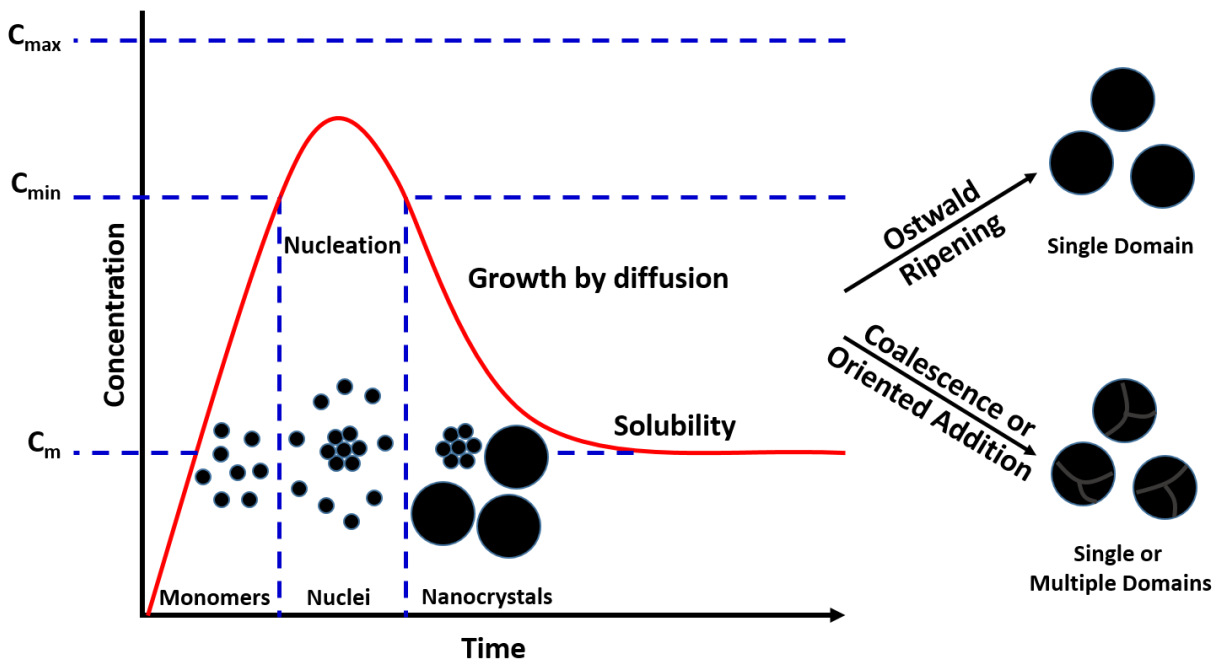


Figure 1.8: LaMer diagram showing how concentration of precursors change throughout the nucleation and growth process. C_m is the concentration of monomers (red line), C_{min} is the minimum monomer concentration required for nucleation, and C_{max} is the supersaturation concentration.

reaction medium. Ostwald ripening usually leads to single domain particles, though if left for too long in the ripening stage of crystal growth, larger sizes distributions will occur owing to the process of continual processes of dissolution and growth.²⁹ Unlike Ostwald ripening, coalescence and oriented addition do not rely on the addition of monomers for crystal growth. In both mechanisms, crystal growth is a result of nuclei or nanocrystals adding to each other in one of two ways: by random interactions which lead to coalescence, or by attaching at points where the lattice planes match the extended crystallographic planes, known as oriented addition. The two growth mechanisms are responsible for the unique shapes that can be seen in NPs, including nanowires, nanostars, and nanorods.^{52, 53} Generally, coalescence leads to many defects within the crystal structure, and therefore multiple domains. Oriented addition, on the other hand, results in relatively defect free crystals, and can lead to the NP having a single domain.

As stated above, homogeneous nucleation is the key to high quality NP synthesis. In this dissertation, microwave heating is used to synthesize all the materials. This has been shown by

many groups to help facilitate homogeneous nucleation by promoting faster nucleation times (Figure 1.9) through irradiating all the precursors simultaneously.^{54, 55} This leads to faster reaction times and smaller size distributions.

1.4.3 Microwaves

MWs are a type of electromagnetic radiation in the frequency range of 100 MHz to 3 GHz, corresponding to wavelengths of 300 cm to 10 cm. Prior to MW use as a heating source, they were predominantly used in radars during World War II. Heating using MWs was discovered accidentally by a man named Percy Spencer who found, while working on radar equipped with a high-powered microwave beam, a candy bar in his pocket melted. After testing that this was, in fact, due to MW radiation induced heating, a patent was filed by Raytheon, which was the company that employed Spencer, for a magnetron designed to heat food using MW energy.⁵⁶ More recently, MWs have been used in laboratories for organic and inorganic synthesis, extractions, and digestions (ref).⁴⁰ MWs work through dipole rotation, causing no ionization or changes in structures of reactants (Figure 1.10).

1.4.4 Microwave Heating

MW heating, also known as dielectric heating, utilizes an alternating electric field to polarize a dielectric material. Dielectric materials are insulators (poor conductors of electricity) which can be efficiently polarized using an external electric field. The dielectric constant ($\tan \delta$) of a material is determined by the ability of the material to insulate charges, and is usually proportional to the polarity of the material. A material with a large dielectric constant is able to easily orient with an electric field, such as a MW field, making it easier to polarize and therefore heat.

In a MW reaction, the heat generation in the sample that is obtained with microwave energy requires the presence of a material with mobile electronic charges, such as dielectric or ionic compounds. The rotation of the dipoles in the alternating field causes friction, which produces heat. More precisely, the applied microwave field causes the molecules, on average, to

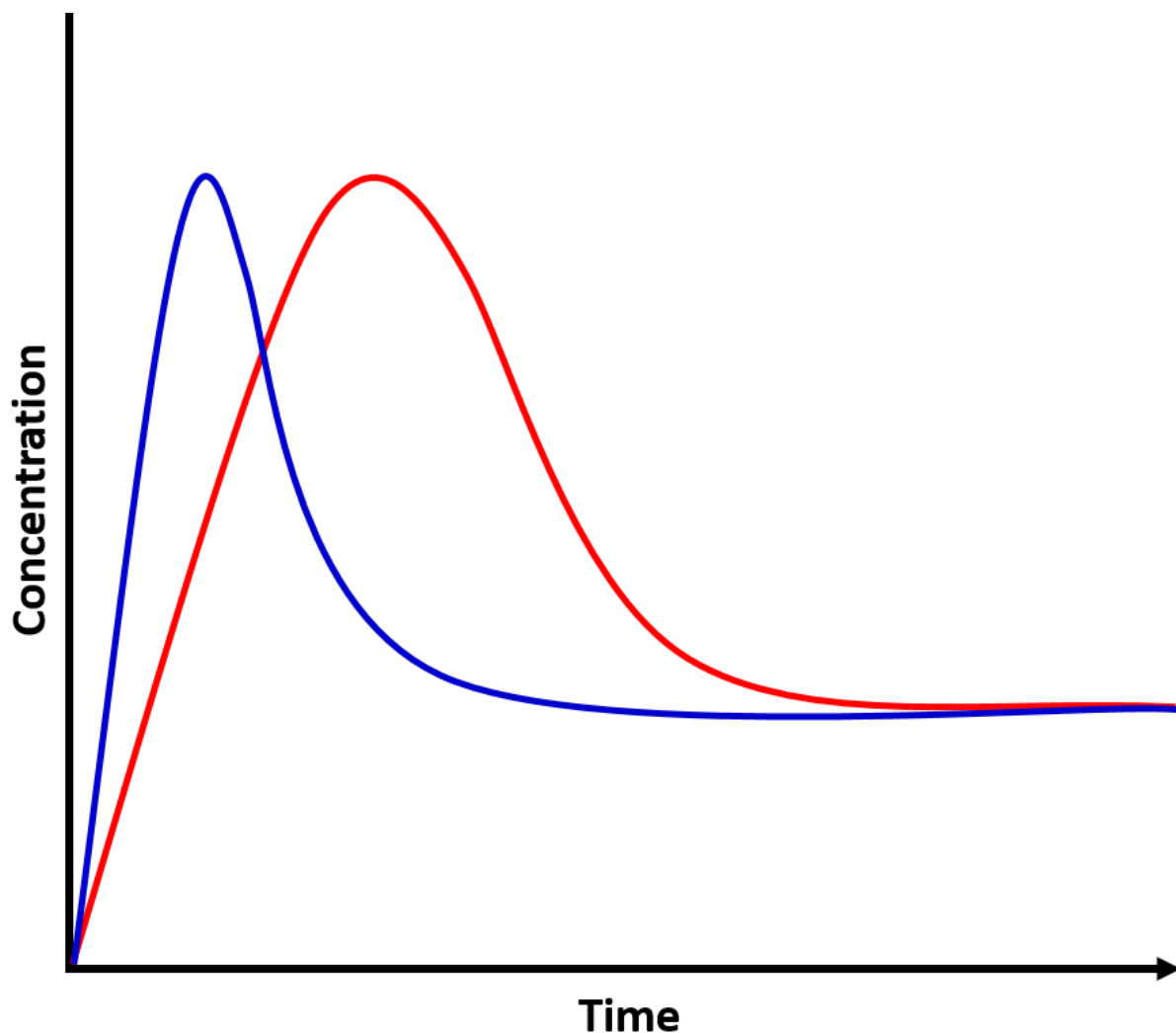


Figure 1.9: Graph theorizing the difference in time to achieve nucleation in MW reactions (blue line) and reactions using conventional heating (red line).

temporarily spend slightly more time orienting themselves in the direction of the electric field rather than in other directions. When the field is removed, thermal agitation returns the molecules to a disordered state in the relaxation time, and thermal energy is released. Thus, microwave heating results from the dissipation of the electromagnetic waves in the irradiated medium. The dissipated power in the medium depends on the MW's electric field strength and the complex permittivity ($\tan \delta$) of the material. Therefore, both the frequency of the MWs and the $\tan \delta$ of the material are very important. At low frequencies, oscillations with the field are slow and result in very little heat generation. At high frequencies, the molecules can't keep up

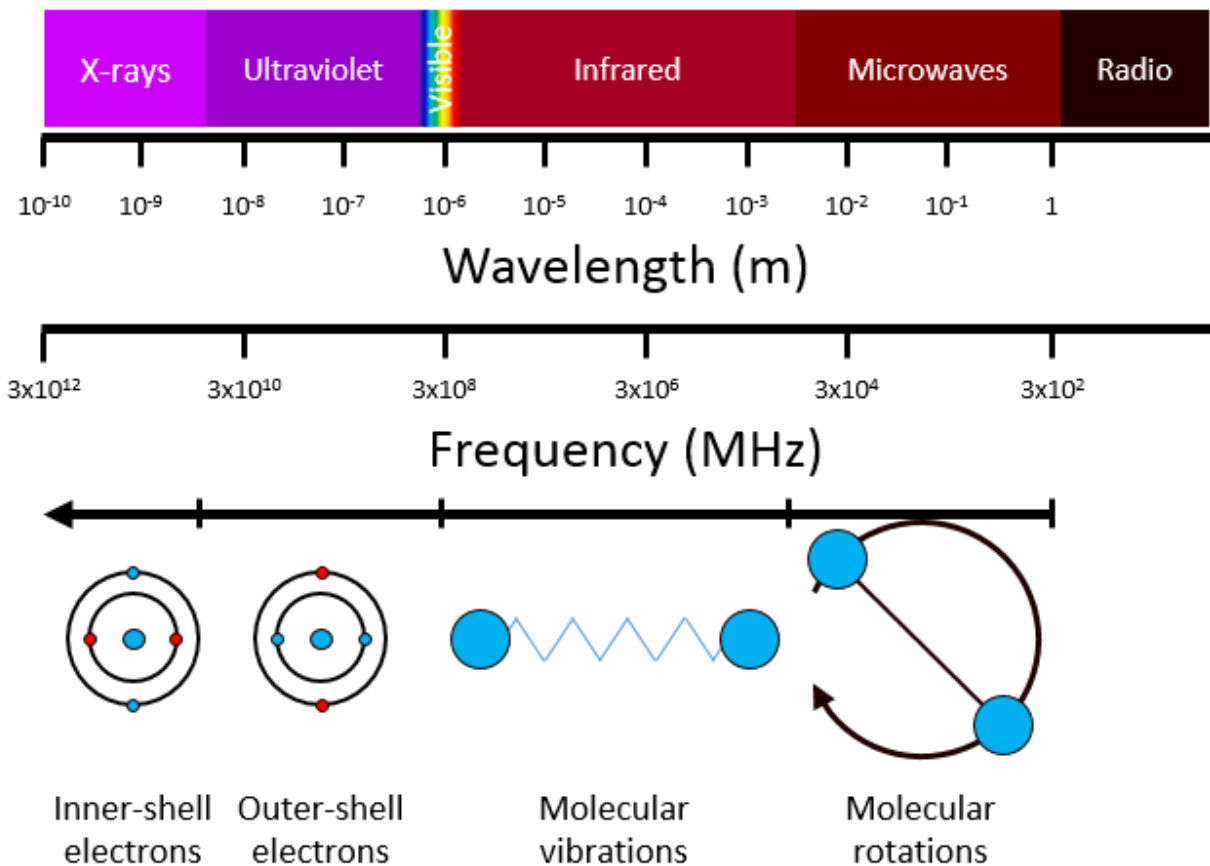


Figure 1.10: Electromagnetic spectrum which includes wavelength, frequency, and interactions with molecules in the different energy areas of the spectrum.

with the oscillations of the field, resulting in an inability for the molecules to orient with the field quickly enough, which also results in very small amounts of heat being produced. The most common MW frequency used is 2.54 GHz, though high powered MW reactors have frequencies upwards of 5.8 GHz, or even 22.1 GHz. The ability for a MW to heat a molecule depends on the $\tan \delta$ of the material. As a general rule, molecules with an overall dipole moment will have a larger $\tan \delta$ than those without a dipole moment. The $\tan \delta$ is dependent upon the material's dielectric constant, ϵ' , and dielectric loss, ϵ'' , and given by the equation:

$$\tan \delta = \epsilon' / \epsilon'' \quad (1.6)$$

A list of compounds and their corresponding $\tan \delta$'s are given in Table 1.2. As the table shows, hydrocarbons, which are commonly used as solvents in solvothermal MW reactions, have low $\tan \delta$'s, while alcohols have relatively high $\tan \delta$'s. By using this knowledge, reactions can be

Table 1.2: Dielectric constants ($\tan \delta$) for many common solvents, divided into those with high $\tan \delta$'s, medium $\tan \delta$'s, and low $\tan \delta$'s. The higher the $\tan \delta$, the more the material absorbs microwave radiation.

	Compound	$\tan \delta$
High $\tan \delta$ ($\tan \delta > 0.5$)	Ethylene glycol	1.350
	Ethanol	0.941
	DMSO	0.825
	2-Propanol	0.799
	Formic acid	0.722
	Methanol	0.659
	Nitrobenzene	0.589
	1-Butanol	0.571
Medium $\tan \delta$ ($0.1 - 0.5$)	2-Butanol	0.447
	Dichlorobenzene	0.280
	NMP	0.275
	Acetic acid	0.174
	DMF	0.161
	Dichloroethane	0.127
	Water	0.123
	Chlorobenzene	0.101
Low $\tan \delta$ ($\tan \delta < 0.1$)	Chloroform	0.091
	Acetonitrile	0.062
	Ethyl acetate	0.059
	Acetone	0.054
	THF	0.047
	Dichloromethane	0.042
	Toluene	0.040
	Hexane	0.020

tailored to selectively heat a specific compound in a reaction. An example of this is CdSe, which was synthesized in the MW using non-MW absorbing solvents, resulting in very quick reactions (~30 seconds) that produced high quality particles with low size distributions.⁴⁸ This is a result of selectively heating the precursors of the reaction and not the solvent, thereby increasing the efficiency of the reaction by making higher quality particles while reducing the energy output.

As a result of the direct heating that occurs using MW radiation, energy waste is greatly reduced. In conventional heating, heat transfers occur from the heating device to the medium, while in MW heating, heat transfers occurs from the irradiated molecules to the surrounding molecules. Another important difference between MW heating and conventional heating is that in MW heating, the heat is generated from all of the molecules within the reaction that possess a dipole, so there is very little in the way of a temperature gradient, especially when stirring. In contrast, the thermal energy in conventional heating techniques is coming from outside of the reaction, and therefore moves from the heat source, to the glass, to the solvent, and then finally to the reactants themselves. This results in not only a large loss of energy, but also a large temperature gradients within the solution. Conventional heating techniques have large lag times for the entire reaction to reach thermal equilibrium, on the order of minutes, in comparison to the seconds required for MW heating thermal equilibration. Figure 1.11 shows the difference in uniformity in heating in conventional heating compared to MW heating reaction systems.

1.4.5 Nanoparticles

Spinel NPs, also known as nanospinels, are the majority of the NPs studied in this dissertation, though Y_2O_3 is also investigated. Spinels have the form AB_2X_4 with the A denoting a divalent metal ion, B being a trivalent metal ion, and X representing O^{2-} or S^{2-} . Spinels have high chemical, thermal, and radiation stability, making them viable for use in optoelectronic devices. Certain spinel types exhibit interesting electric, mechanical, magnetic, and optical properties. Oxide and sulfide spinels are wide bandgap semiconductors with both tetrahedral (A^{2+}) and octahedral (B^{3+}) sites, which make them suitable for substitution by ions with a variety of different sizes and oxidation states. Bulk and nanospinels have been studied to a great extent for use as phosphors, owing to the existence of both divalent tetrahedral sites, as well as trivalent octahedral sites, which increases the ease of doping with a variety of transition and rare earth

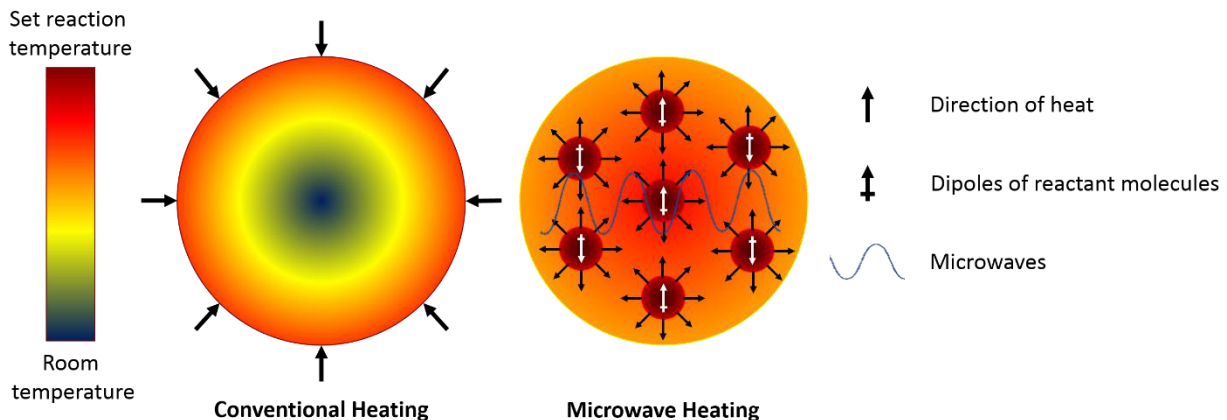


Figure 1.11: Heat transfer is conventional heating versus microwave heating. As heat is transferred from the outside in in a conventional heating system, there is generally a temperature gradient, where the inside is significantly cooler than the outside. In MW heating, dipolar or ionic molecules within the reaction batch are becoming superheated, then transferring the heat to the solvent molecules in the vicinity, resulting in less of a temperature gradient as all the molecules are being heated simultaneously.

metals. Along the same lines, recent interest has been sparked by the discovery of long persistent luminescence found in Cr^{3+} doped spinels. Nanospinels have been employed for use in a variety of applications including use as catalysts or catalyst supports, owing to their high surface area, thermal stability, low acidity, and hydrophobic behavior. Their visible transparency, high mechanical reliability, low dielectric constant and low dielectric loss, has caused bulk and nanospinel uses to include transparent conductors, dielectric materials, window applications, as well as inclusion in some ceramic tile glazes. Spinels have been made using a variety of techniques including solid state methods, sol-gel, citrate-gel, matrix-assisted calcination, hydrothermal, lyothermal, as well as MW and thermal combustion techniques. Solid state reactions have been employed to make sub-micron and bulk spinel oxides (AB_2O_4) with a good variability of A and B sites, as well as bulk thiospinels (AB_2S_4), however NPs are not currently obtainable using this technique. Sol-gel, hydrothermal, and lyothermal techniques have been employed to make nano-sized oxide spinels, completely ignoring the sulfides.⁵⁷⁻⁵⁹ Employing MW heating, both thio-spinels as well as oxide spinels can be synthesized on the nano-scale with a variety of A and B ions, as discussed later in this dissertation. Using the MW is a quick and efficient way to make either sulfur containing or oxygen containing nanospinels by a simple

precursor substitution. Though this synthetic method does have some limitations, a vast array of different spinels can be made using this technique. And using MW radiation, 3.4nm particles can be reliably produced, with reaction times of only 5 minutes.

1.4.6 Lanthanide Doped Nanoparticles

In order to achieve visible light emission, metal oxide hosts can be doped with 2+ and 3+ lanthanide ions. Lanthanides, which will be discussed in more detail in section 1.5, are good dopants for use in solid state lighting owing to their narrow emission bands (in the case of the 3+ ions) and long lifetimes. The different lanthanide ions' emission span the visible spectra with blue emission (from Ce³⁺ and Tm³⁺), green emission (Tb³⁺ and Er³⁺), and red emission (Eu³⁺, Sm³⁺, and Ho³⁺), as well as Eu²⁺ which can emit red, green, or blue depending on the lattice. By doping lanthanide ions into appropriate host lattices, the emission intensity can be increased by the relaxation of the selection rules governing emission. In addition, utilizing a host lattice spatially separates the lanthanide ions, decreasing self-quenching events and improving efficiency. Lastly, the host acts as a sensitizer for lanthanide emission by pumping the band gap of the host lattice which can transfer energy to the lanthanide if the band gap is at an appropriate wavelength. This dissertation focuses on Eu³⁺ and Tb³⁺ doping into oxide host lattices using MW heating, though the approach can be adapted to dope with any of the lanthanides, as well as transition metal ions, depending on the application.

1.5 Lanthanide Luminescence

Lanthanides possess unique electronic properties owing to the nature of the 4f electrons responsible for the lanthanide absorption and emission. Some physical properties of the 3+ ions in the lanthanide series are listed in Table 1.3, including the 4f electron configuration, the ground state term symbol, and the color of the solid. The Laporte's parity selection rule states that electric dipole transitions cannot have the same parity, resulting in f-f transitions being forbidden.⁶⁰ Because of this, the absorption bands of lanthanides in the 3+ oxidation state are sharp and weak which lead to low molar extinction coefficients that prohibit the direct excitation of the ions. Additionally, the 4f electrons of the lanthanide series are buried below the 5s and 5p electrons, equating to the electrons being shielded from the environment, making them more molecular in nature. This shielding translates into the emission spectra by forming bands that are

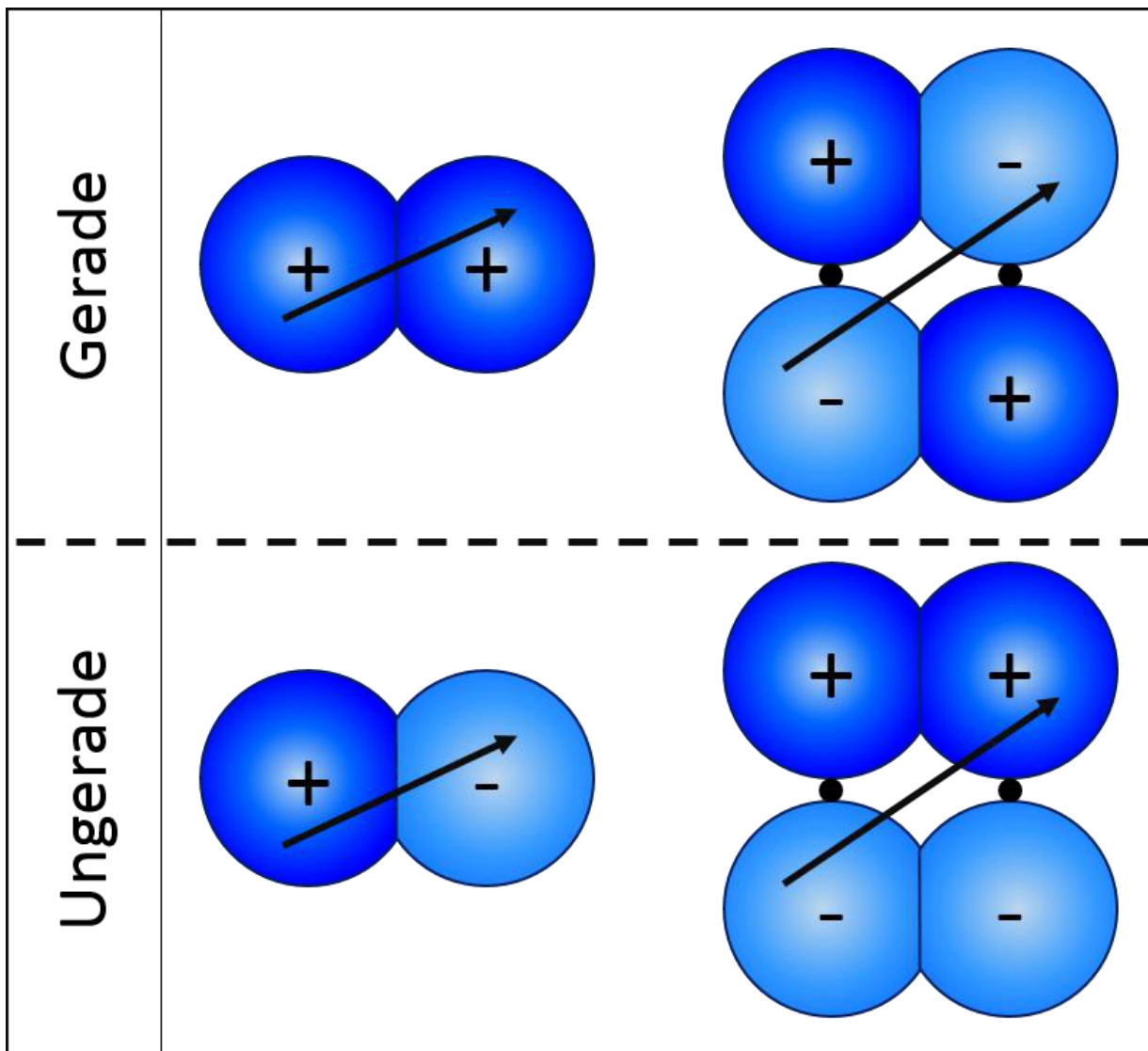


Figure 1.12: Diagram showing the difference between gerade (even) symmetry versus ungerade (odd) symmetry.

also very sharp, though not quite as narrow as the absorption bands, leading to the line-like emission spectra that is characteristic of the lanthanide series. Because of the low absorption cross-sections of the trivalent lanthanide ions, antenna ligands are often used in order to efficiently sensitize the lanthanide emission.⁶⁰

1.5.1 Selection Rules

Selection rules are the rules that govern the magnitude of the transitions of the 4f orbitals in optically active lanthanides.⁶⁰ These rules basically state which transitions within lanthanide

Table 1.3: 4f electron configurations, term symbol for the ground state, and solid color for the trivalent lanthanide series.

Lanthanide	4f electron configuration	Ground state term symbol	Color of the solid
Lanthanum (La ³⁺)	4f ⁰	¹ S ₀	Colorless
Cerium (Ce ³⁺)	4f ¹	² F _{5/2}	Colorless
Praseodymium (Pr ³⁺)	4f ²	³ H ₄	Green
Neodymium (Nd ³⁺)	4f ³	⁴ I _{9/2}	Lilac
Promethium (Pm ³⁺)	4f ⁴	⁵ I ₄	Pink
Samarium (Sm ³⁺)	4f ⁵	⁶ H _{5/2}	Pale yellow
Europium (Eu ³⁺)	4f ⁶	⁷ F ₀	Colorless
Gadolinium (Gd ³⁺)	4f ⁷	⁸ S _{7/2}	Colorless
Terbium (Tb ³⁺)	4f ⁸	⁷ F ₆	Very pale pink
Dysprosium (Dy ³⁺)	4f ⁹	⁶ H _{15/2}	Pale yellow
Holmium (Ho ³⁺)	4f ¹⁰	⁵ I ₈	Yellow
Erbium (Er ³⁺)	4f ¹¹	⁴ I _{15/2}	Pink
Thulium (Tm ³⁺)	4f ¹²	³ H ₆	Pale green
Ytterbium (Yb ³⁺)	4f ¹³	² F _{7/2}	Colorless
Lutetium (Lu ³⁺)	4f ¹⁴	¹ S ₀	Colorless

ions are forbidden or allowed. Though transition that are deemed “forbidden” are not actually impossible transitions, rather, those transitions are less likely to occur, and are often times weak emitters. The selection rules are derived from the quantum numbers S, L, and J, which are known as the spin angular momentum, orbital angular momentum, and the total angular momentum, respectively. The two most important selection rules in regards to lanthanides are the spin rule and the Laporte rule. The spin rule states that electronic transitions are only allowed when no change in spin occurs. The Laporte rule is a parity selection rule which forbids transitions that are not accompanied by a change in parity, *i.e.* going from gerade to ungerade.⁶¹

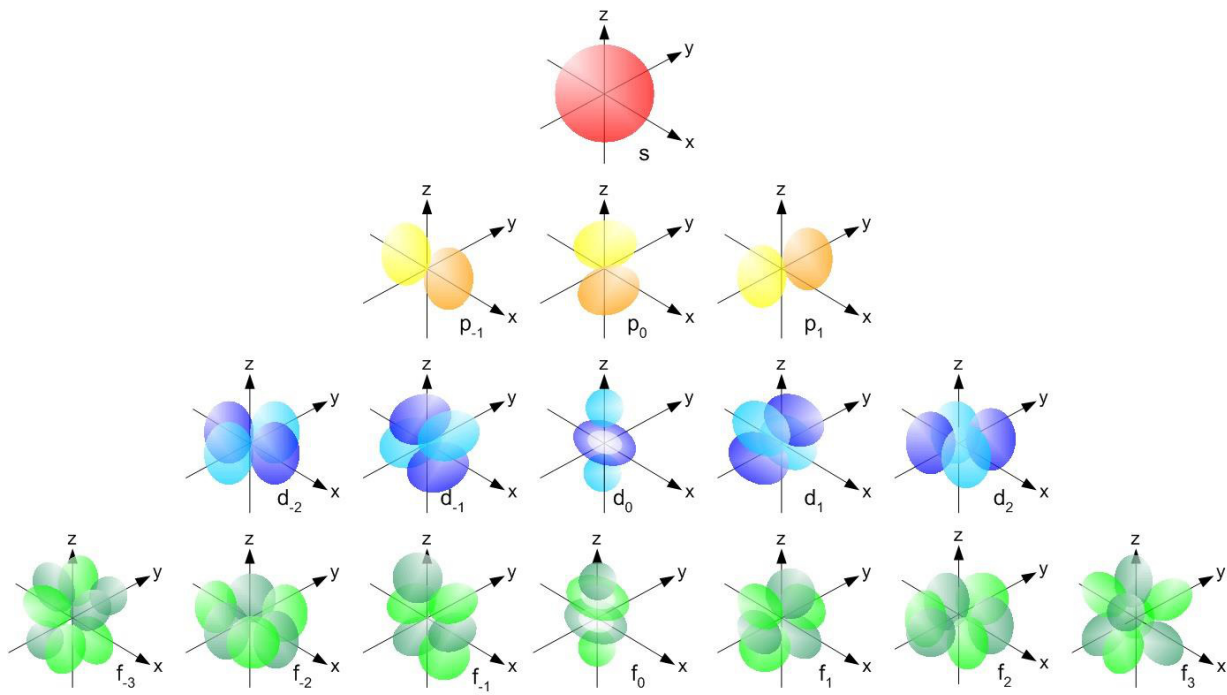


Figure 1.13: Orbital projection diagram of the s, p, d, d, and f orbitals. Color differences in p, d, and f orbitals represents differences in symmetry (gerade vs ungerade).

The Laporte selection rule is more complicated than the spin selection rule, and more important as it is the selection rule that forbids f-f transitions, so it will be discussed in more detail. The Laporte selection rule applies only to centrosymmetric molecules, those with a center of inversion. This is due to the fact that promotion of an electron in a site with a center of inversion will not result in a change in parity. The symmetry will not go from a gerade (even) symmetry to an ungerade (odd) symmetry as the ground and excited states of centrosymmetric atoms will have the same symmetry with respect to an inversion center, Figure 1.12. Transitions from f-d, on the other hand, are Laporte-allowed transitions as f-orbitals have an ungerade symmetry and d-orbitals have a gerade symmetry as seen in Figure 1.13.

The selection rules governing lanthanide transitions can be relaxed through a number of means. Spin-orbit coupling, the interaction with the particle's spin and motion, can result in weak spin forbidden bands arising. Since the lanthanides are so heavy, the spin-orbit coupling constant is generally large, so the interaction becomes much more prevalent than in lighter transition metal ions, which allows for a relaxation of the spin selection rule. Another situation

that gives rise to selection rule relaxation is vibronic coupling as a result of an unsymmetrical vibration, causing a loss of centrosymmetry, which overcomes the Laporte selection rule temporarily. This is possible as electronic transitions are much quicker than vibrational ones. Analogously to vibronic coupling, the breaking of site symmetry through disorder can allow the Laporte rule to be circumvented as well. Lastly, the Laporte selection rule can be overcome by mixing the electronic states from charge transfer bands or ligands with that of the 4f wavefunction from the lanthanides.

1.5.2 Lanthanide Absorption

Direct excitation into lanthanide 4f-4f transitions is extremely difficult due to the forbidden nature of those transitions which results in very low extinction coefficients. Besides direct excitation into those levels, other electronic transitions are allowed due to opposite parity conditions, including magnetic dipole transitions, 4f-5d transitions, charge transfer transitions, and induced or forced electric dipole transitions resulting from orbital mixing or symmetry breakage. In general, however, few of these transitions are actually viable for lanthanide excitation. 4f-5d transitions are usually very high energy, with only those of Ce³⁺ and Tb³⁺ being low enough in energy to allow for efficient pumping of those states. Forced dipole transitions and magnetic dipole transitions still only weakly absorb. Because of this, molecular antenna are often utilized to efficiently sensitize the lanthanide ions. The molecular antenna approach is symmetry allowed, and the compounds used in this method generally have very large extinction coefficients, resulting in very efficient light harvesting.^{61, 62}

1.5.3 Ligand/Molecular Antenna Effect

The molecular antenna effect utilizes the high extinction coefficients of the antenna ligand in combination with favorable energy overlap with lanthanide centers to allow for high efficiency energy transfer. In the molecular antenna approach, a ligand molecule is used to harvest light in the form of a photon, promoting an electron from a ground singlet state to an excited singlet state. After electron promotion, the electron undergoes intersystem crossing to the ligand's excited triplet state, and from there populates the excited states of the lanthanide ions. There are several important factors that dictate how efficient the energy transfer is in this method, including the differences in energy between the singlet excited state and the triplet

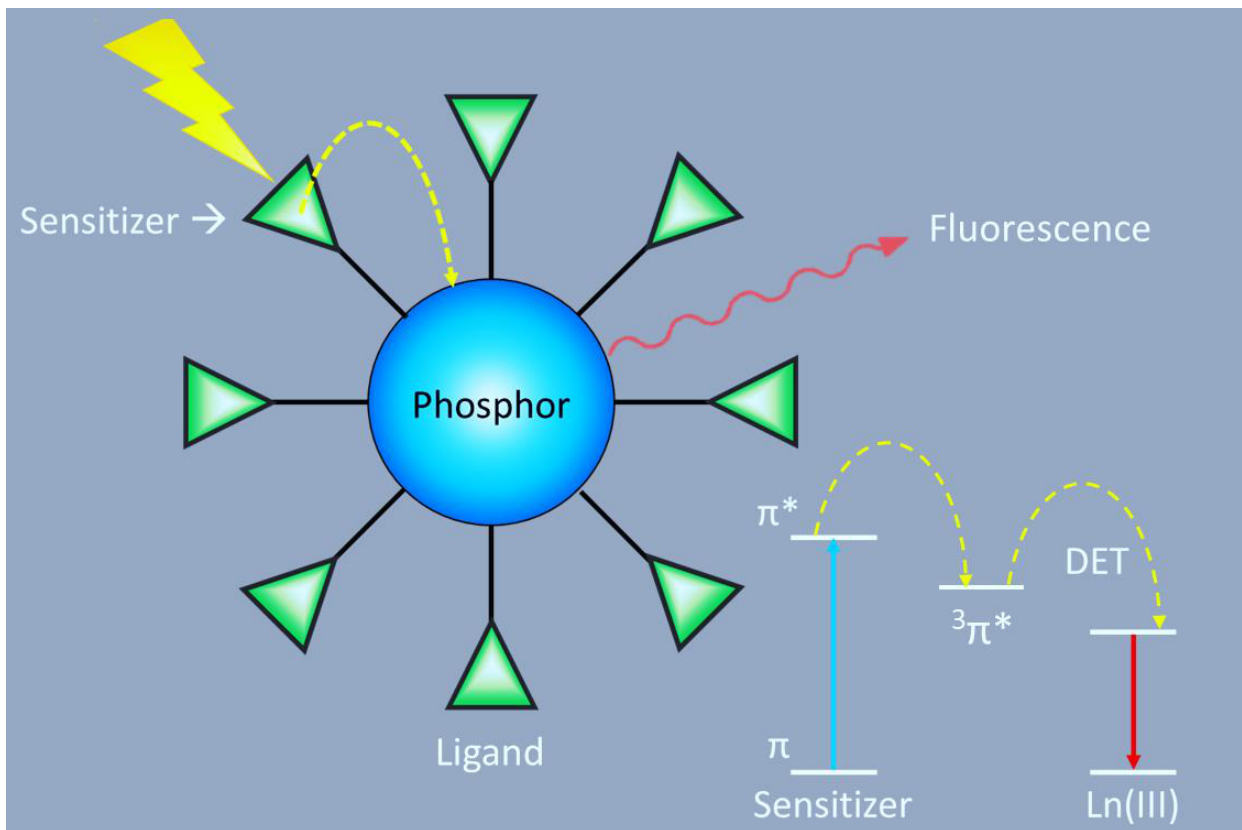


Figure 1.14: Molecular antenna approach to sensitization of lanthanide emission. DET stands for Dexter energy transfer, the mechanism by which energy transfer occurs in a ligand sensitization.

excited state in the ligand and the difference in energy between the triplet excited state of the ligand and the lanthanide emissive levels. The optimal energy difference between the singlet and triplet has been found to be 0.6 eV,⁶³ while the difference in energy between the triplet and lowest excited state for Eu³⁺ and Tb³⁺ is 0.3 eV and 0.25 eV respectively.⁶³ The reasoning for these energy differences stems from the need to have a small enough energy difference for efficient energy transfer while removing the effects of back transfer. Figure 1.14 shows a cartoon depicting a simplified view of the molecular antenna mechanism. The mechanism for energy transfer for a molecular antenna to a lanthanide center is widely believed to be Dexter energy transfer (DET).²⁰

1.5.4 Dexter Energy Transfer

Dexter energy transfer (DET) is a short range, electron exchange energy transfer mechanism. The length scale of the electron exchange is generally 2 nm and below, with energy

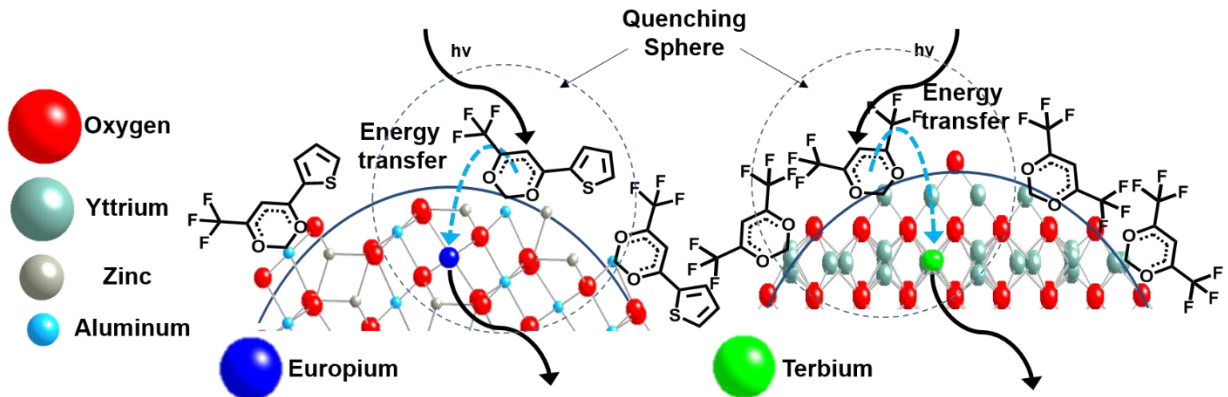


Figure 1.15: Crystal structures of nanoparticles of Eu³⁺ doped ZnAl₂O₄ sensitized by thenoyltrifluoroacetone (tta) and Tb³⁺ doped Y₂O₃ sensitized by hexafluoroacetylacetone (hfacac).

transfer rates decreasing above 0.5 nm. In order for transfer to occur, there must be an overlap of the wavefunctions of the donor and acceptor, *i.e.* there should be overlap between the emission spectra of the donor and absorption spectra of the acceptor. The rate of energy transfer (k_{DET}) scales as the exponential of the separation distance with the equation:

$$k_{DET} = K \langle J \rangle \exp\left(\frac{-2R_{DA}}{L}\right). \quad (1.7)$$

K is the pre-exponential factor describing the probability of electron state population, $\langle J \rangle$ is the spectral overlap integral, R_{DA} is the separation distance from the β-diketonate to the lanthanide ion, and L is the sum of the van der Waals radii for the donor and acceptor. The quenching sphere, also which can be used to calculate the critical radii for energy transfer, can be determined through the use of a Perrin model. The equation for a Perrin non-diffusional quenching model is given by:

$$\ln \frac{Q}{Q_0} = -VN_A[\text{Ln}^{3+}] \quad (1.8)$$

where Q is the QE of the sample, Q_0 is taken to be 1, V is the volume of the quenching sphere, N_A is Avogadro's number, and $[\text{Eu}]$ is the concentration of Eu(III) in mol/L.²¹ By plotting the intensity ratio $\ln(Q/Q_0)$ vs Eu(III) concentration, the slope, which is equal to $-N_A V$, can be used in conjunction with the equation for the volume of a sphere:

$$V = \frac{3}{4}\pi r^3 \quad (1.9)$$

to solve for the critical radii, r , for energy transfer. Figure 1.15 shows the quenching sphere in reference to Tb:Y₂O₃ NPs passivated by the molecular antenna hexafluoroacetylacetone (hfacac), and Eu:ZnAl₂O₄ NPs passivated by the molecular antenna thenoyltrifluoroacetone (tta).

1.5.5 Lanthanide Emission

Lanthanide ions have characteristically sharp emission lines which are generally insensitive to the environment around them. This is a result of the buried nature of the f-f transitions in the lanthanide series, Figure 1.16. The 4f electrons of the lanthanides are shielded by all the 6s, 5d, 5s, and 5d electrons, meaning that the 4f electrons are considered core electrons. As such, the 4f orbitals do not participate very much in ligand bonding, leading to only small perturbations in the orbitals upon excitation, and therefore very sharp lines. This can be seen in Figure 1.17. In addition to the shielding of the f orbitals resulting in sharp emission bands, it also results in long fluorescence lifetimes.⁶¹

Most lanthanide ions are luminescent with the exception of La³⁺ and Lu³⁺. The lanthanide ion emission spans the entire visible region, with some that also have emission in the UV and NIR. Table 1.4 summarizes the emission lines for all luminescent lanthanide 3+ ions, including their main emissive and final states. Upon inspection of Table 1.4, it is evident that many lanthanides have several emission lines within their spectra. This is a result of splitting of the 4f orbital, as seen in Figure 1.18 of Eu³⁺. The initial energy splitting is due to electron repulsion, resulting in a splitting of the f orbitals into two different levels. This is similar to what is seen in transition metal ions, where you get the e_g and t_{2g} levels. Unlike transition metals, the next cause of splitting is spin-orbit coupling, not crystal field. This is because of two reasons: 1) the f-orbitals are buried, and therefore don't interact with ligands like the d-orbitals of transition metal ions, 2) the lanthanides are larger. This results in less effects of the crystal field, only resulting in very small splitting of some of the J-levels into sublevels. Generally, the ligand's electric field, which generally restricts the motion of electrons of transition metal ions, results in the orbital angular momentum being reduced or quenched, causing the spin-orbit coupling in transition metals to be diminished. In lanthanides, where the f-orbitals are shielded from the ligand effects, spin-orbit coupling is a much larger contributor to the electronic properties in a lanthanide. Heavier transition metal ions also have significant spin-orbit coupling effects as a result of larger angular momenta.⁶⁰

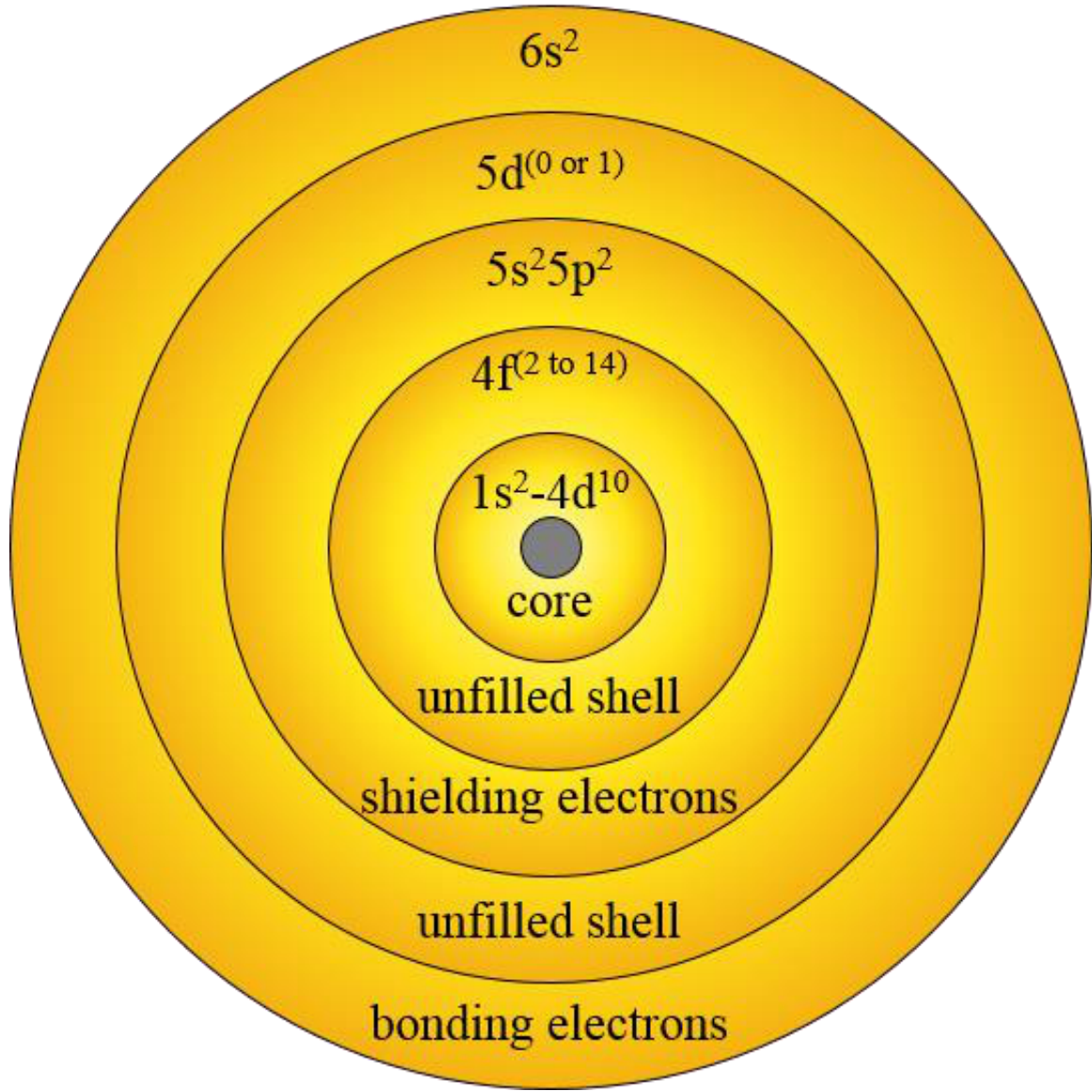


Figure 1.16: Location of the 4f electrons in lanthanide molecules.

The lanthanide ions that are investigated in this dissertation are Eu^{3+} and Tb^{3+} . The main emissive state in Eu^{3+} is the $^5\text{D}_0$ state, with the ground state $^4\text{F}_J$ ($J = 0 - 6$). For Tb^{3+} , the main emissive state is the $^5\text{D}_4$ state, with the ground state $^4\text{F}_J$ ($J = 6 - 0$). The term symbol for the lanthanides can be determined using Russel-Sauders (L-S) coupling, where the ground state follows Hund's rules. The three tenets of Hund's rules state that 1) the spin angular momentum (S) is equal to the maximum possible value, 2) the orbital angular momentum quantum number

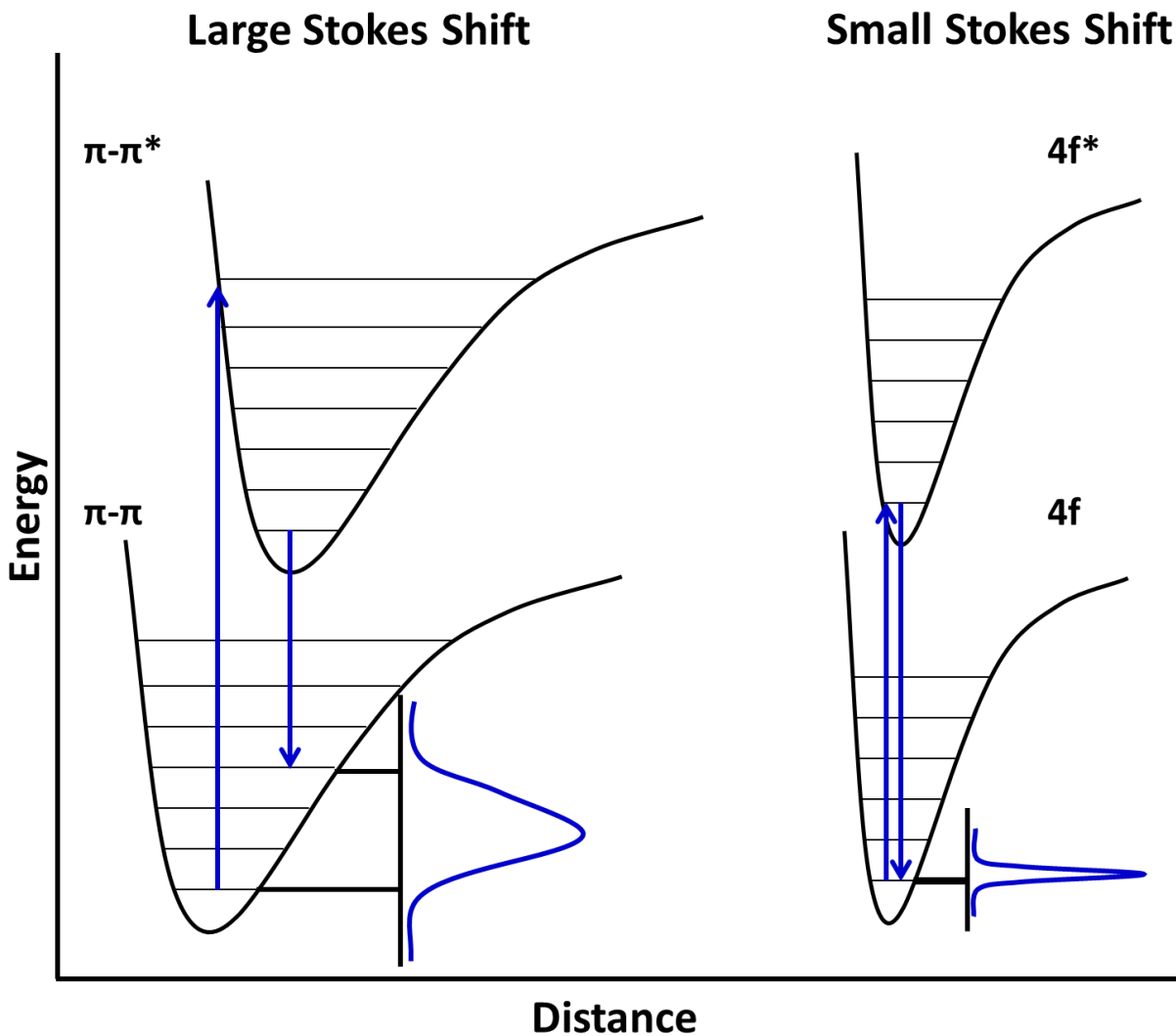


Figure 1.17: Configurational coordinate diagram for an organic ligand, left, vs a Ln^{3+} ion, right.

(L) is equal to the maximum possible value of L, and 3) total angular momentum quantum number (J) is equal to $L-S$ for orbitals that are less than half-filled shells, $J = L+S$ for more than a half-filled shell, and if the shell is half-full: $L = 0$ and $J = S$. The term symbol takes on the form $2S+1L_J$, where $2S + 1$ is the multiplicity, the value of L that is calculated will then be converted to a letter ($L = 0, 1, 2, 3 \dots$ gives $L = S, P, D, F \dots$), and $J = L \pm S$. Thus, taking Eu^{3+} as an example, which has a $4f^6$ electron configuration, the value for S will be 3, giving a multiplicity ($2S + 1$) of 7. The value of L, which only considers unpaired electrons, will be 3. Applying Hund's third rule,

Table 1.4: Ground state (G), main emissive state (I), and final state (F) of the f-f transitions in trivalent lanthanide ions, and the radiative lifetime calculated for the aquated ions.

Ln	G	I	F	λ (nm)	$\tau^{\text{rad}}/\text{ms}$
Cerium	$^2\text{F}_{5/2}$	5d	$^2\text{F}_{5/2}$	Tunable (300-450)	-
Praseodymium	$^3\text{H}_4$	$^1\text{D}_2$ $^3\text{P}_0$	$^3\text{F}_4, ^1\text{G}_4, ^3\text{H}_4, ^4\text{H}_5$ $^3\text{H}_J (J = 4-6)$ $^3\text{H}_J (J = 2-4)$	1000, 1440, 600, 690 490, 545, 615, 640 700, 725	0.05-0.35 0.003-0.02
Neodymium	$^4\text{I}_{9/2}$	$^4\text{F}_{3/2}$	$^4\text{I}_J (J = 9/2-13/2)$	900, 1060, 1350	0.42
Samarium	$^6\text{H}_{5/2}$	$^4\text{G}_{5/2}$	$^6\text{H}_J (J = 5/2-13/2)$ $^6\text{F}_J (J = 1/2-9/2)$ $^6\text{H}_{13/2} (J = 9/2-13/2)$	560, 595, 640, 700, 775 870, 887, 926, 1010, 1150 877	6.26
Europium	$^7\text{F}_0$	$^5\text{D}_0$	$^7\text{F}_J (J = 0-6)$	580, 590, 615, 650, 720, 750, 820	9.7
Gadolinium	$^8\text{S}_{7/2}$	$^6\text{P}_{7/2}$	$^8\text{S}_{7/2}$	315	10.9
Terbium	$^7\text{F}_6$	$^5\text{D}_4$	$^7\text{F}_J (J = 6-0)$	490, 540, 580, 652, 650, 660, 675	9.0
Dysprosium	$^6\text{H}_{15/2}$	$^4\text{F}_{9/2}$ $^4\text{I}_{15/2}$	$^6\text{H}_J (J = 15/2-9/2)$ $^6\text{H}_J (J = 15/2-9/2)$	475, 570, 660, 750 455, 540, 615, 695	1.85 3.22
Holmium	$^5\text{I}_8$	$^5\text{S}_2$ $^5\text{F}_5$	$^5\text{I}_J (J = 8, 7)$ $^5\text{I}_8$ $^5\text{I}_7$	545, 750 650 965	0.37 0.8
Erbium	$^4\text{I}_{15/2}$	$^4\text{S}_{3/2}$ $^4\text{F}_{9/2}$ $^4\text{I}_{9/2}$ $^4\text{I}_{13/2}$	$^4\text{I}_J (J = 15/2-13/2)$ $^4\text{I}_{15/2}$ $^4\text{I}_{15/2}$ $^4\text{I}_{15/2}$	545, 850 660 810 1540	0.7 0.6 4.5 0.66
Thulium	$^3\text{H}_6$	$^1\text{D}_2$ $^1\text{G}_4$ $^3\text{H}_4$	$^3\text{F}_4, ^3\text{H}_4, ^3\text{F}_3, ^3\text{F}_2$ $^3\text{H}_6, ^3\text{F}_4, ^3\text{H}_5$ $^3\text{H}_6$	450, 650, 740, 775 470, 650, 770 800	0.09 1.29 3.6
Ytterbium	$^2\text{F}_{7/2}$	$^2\text{F}_{5/2}$	$^2\text{F}_{7/2}$	980	1.3-2.0

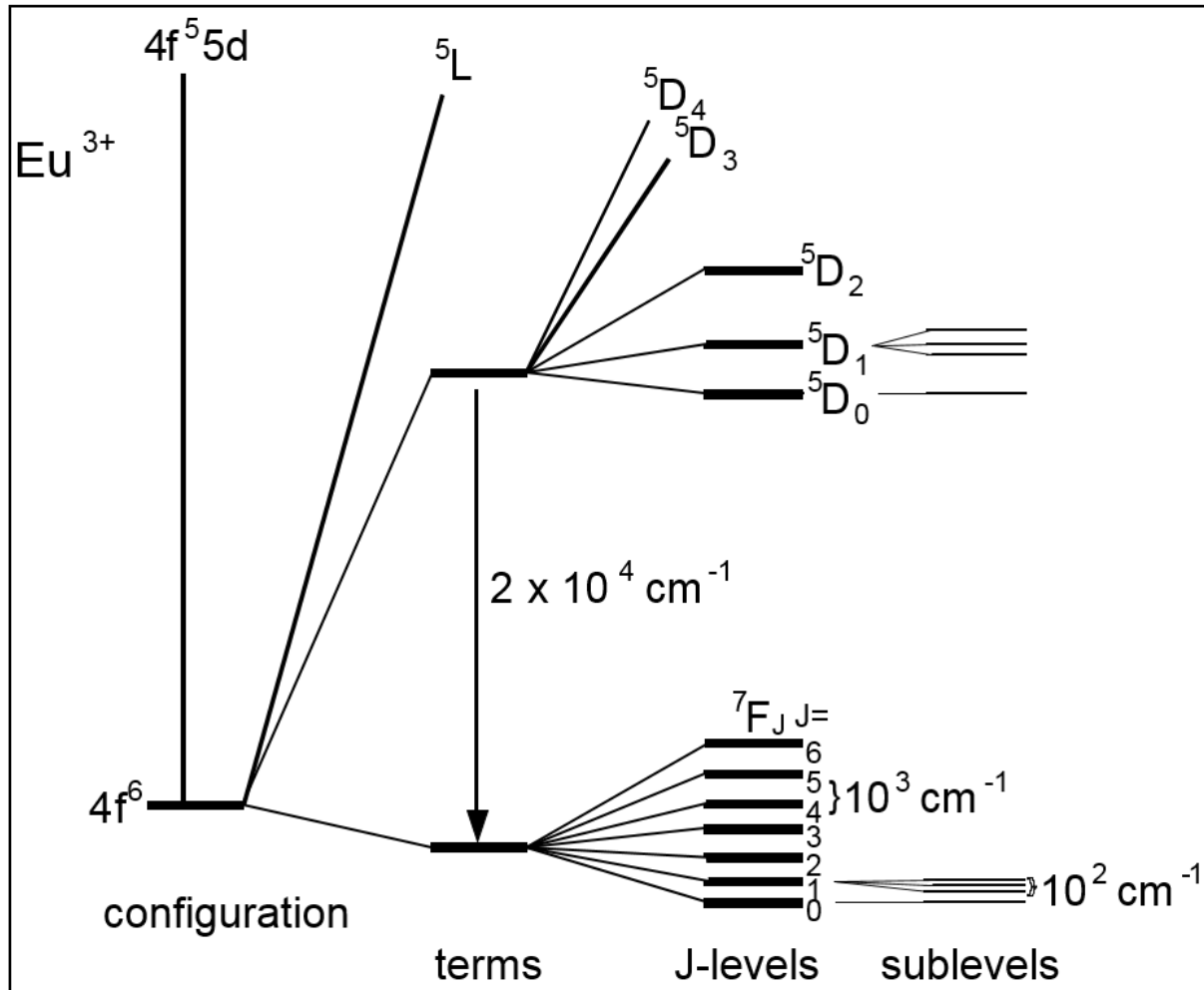


Figure 1.18: Splitting of the 4f orbitals as a result of electron repulsion, spin-orbit coupling, and crystal field effects.

Eu^{3+} is less than half filled, therefore $J = L - S$, so $J = 0$. Putting it all together, the ground state for Eu^{3+} is 7F_0 . In the same way, the ground state of Tb^{3+} can be found from its $4f^8$ electron configuration, since the f-orbital is more than half-filled, the value for J will be $L + S$, and the ground state for Tb^{3+} is 7F_6 .⁶⁰

The emission spectra for both of them are shown in Figure 1.19. The spectra contain contributions from both magnetically allowed transitions and forced electric dipole transitions. The intensities of the transitions in Eu^{3+} and Tb^{3+} can provide a lot of structural information about the sites where the ions are located in the crystal lattice. The ${}^5D_0 \rightarrow {}^7F_2$ transition in Eu^{3+} , and the ${}^5D_4 \rightarrow {}^7F_5$ are both sensitive to their coordination environment. The ${}^5D_0 \rightarrow {}^7F_2$ transition

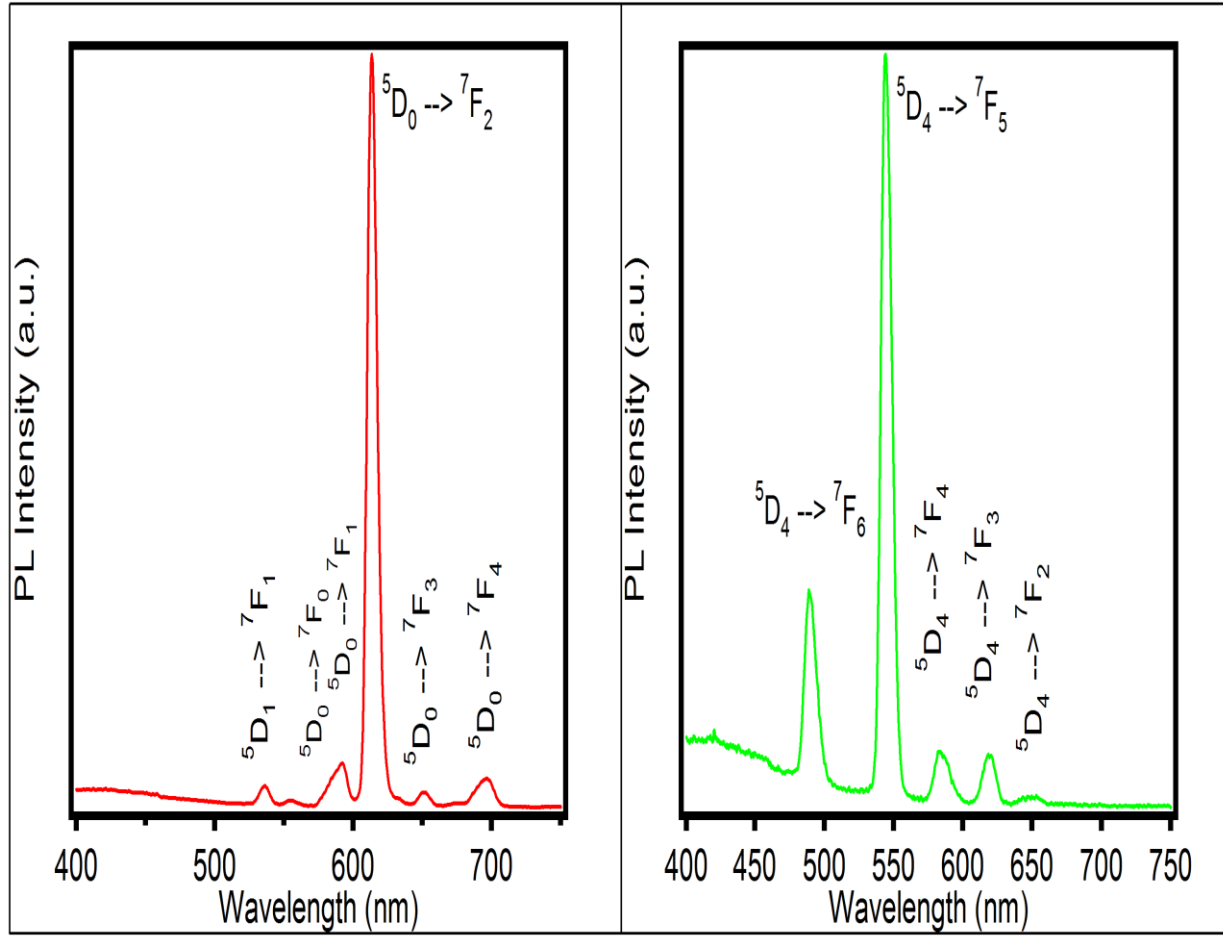


Figure 1.19: Emission spectra for Eu^{3+} and Tb^{3+} doped into ZnAl_2O_4 nanospinels.

is a forced electric dipole, which is hypersensitive and only partially allowed due to the selection rules, making it symmetry dependent. At lower symmetry sites, the ${}^5\text{D}_0 \rightarrow {}^7\text{F}_2$ transition becomes more intense, and results in the characteristic red emission found in Eu^{3+} . The ${}^5\text{D}_4 \rightarrow {}^7\text{F}_5$ transition in Tb^{3+} is also sensitive to the coordination environment of the Tb^{3+} ion. Because it is a magnetic dipole, it is allowed, though the peak position and intensity of the peak can change slightly as a result of site symmetry.^{27, 64} In a lower symmetry site, the peak is found to be a slightly higher in energy than higher symmetry sites.²⁷ There have also been claims that in lower symmetry sites, the ${}^5\text{D}_4 \rightarrow {}^7\text{F}_5$ transition increases in intensity very slightly, so that changes can be observed by comparing the ${}^5\text{D}_4 \rightarrow {}^7\text{F}_5$ to the ${}^5\text{D}_4 \rightarrow {}^7\text{F}_6$ transition, which is another magnetic dipole transition. This site, however, is completely insensitive to the environment.⁶⁰

1.6 Characterization Methods

1.6.1 UV-Vis and Fluorescence

Ultraviolet-visible spectroscopy (UV-Vis) is a spectroscopic technique that records the light absorption properties of materials in the UV and visible regions of the electromagnetic spectrum. As a material undergoes an electronic transition via the promotion of an electron from the ground state to an excited state, that transition occurs at a specific wavelength of light. It is that wavelength or wavelengths that are recorded in UV-Vis spectroscopy. Materials which have either band gaps, π -electrons, or non-bonding electrons generally have a characteristic absorption spectrum. The absorbance of a material is defined by the Beer-Lambert law:

$$(A = \varepsilon lc) \quad (1.10)$$

which relates the absorption, A, to the molar absorptivity of the material, ε , the path length of the cell, l, and the concentration of the material. This relationship is useful for determining the concentration of a given solute.⁶⁵

Fluorescence spectroscopy is complementary to UV-Vis. While UV-Vis gives information about what wavelengths of light a given material absorbs, fluorescence spectroscopy gives information about what wavelengths a material reemits after absorption of light at a specific excitation wavelength. After the absorption of a photon of light at a specific wavelength, promotion of an electron into an excited state will occur. As the excited material loses vibrational energy, the electron will fall back down to the ground state, resulting in the emission of a photon of lower energy than what was absorbed, alternatively the electron may undergo relaxation back to ground state via a non-radiative pathway, and give off the excited state energy as heat, etc. The efficiency of the conversion of the absorbed photons into emitted photons is known as the quantum efficiency, Φ , defined as:

$$\Phi = \frac{(\# \text{ of photons emitted})}{(\# \text{ of photons absorbed})} \quad (1.11)$$

In a perfect system, every absorbed photon would be converted to a photon of a different energy. However, since non-radiative pathways occur, quantum efficiencies are generally less than 1. Non-radiative pathways include loss of energy through the dissipation of heat, energy transfer to another molecule, or intersystem crossing (from the excited singlet state to the lowest excited triplet state).

Calculation of the quantum efficiency can be done in a number of ways, including using an integrating sphere, which can accurately determine both the amount of photons emitted as well as the amount of photons absorbed by the material, as well as through the use of a standard with a known quantum efficiency. In the latter case, the Φ of the standard is usually measured in an integrating sphere. Using such a standard, the relative quantum efficiency can be calculated using equation 8.

$$\frac{\Phi_S}{\Phi_R} = \frac{I_S}{I_R} \times \frac{1-10^{-A_R}}{1-10^{-A_S}} \times \frac{\eta_S^2}{\eta_R^2} \quad (1.12)$$

Here, the integrated intensity of emission at a given excitation wavelength is represented by I , (S is the sample and R is the reference or standard), A denotes the absorbance at the wavelength of excitation for both the sample and the reference, and η is the refractive index of the solvent used.⁶⁶ In the field of solid state lighting, the quantum efficiency of the material is of the utmost importance, with the goal being to increase LED efficiency through increased phosphor efficiency. The absorption, emission, and quantum efficiencies are therefore important properties, indicative of the level of quality for each synthesized nanophosphors.

1.6.2 Powder X-Ray Diffraction (pXRD)

Powder X-ray diffraction is a powerful technique that provides considerable information about the structure and quality of a material. Data from a pXRD measurement can elucidate the crystal structure for a given crystalline material, as well as provide information about disorder, evidence of impurities, and in the case of NPs, can allow for fairly accurate estimates of the average size of the material according to the Scherrer equation (discussed later in this section).

In crystalline materials which are composed of a regular array of atoms, lattice planes exist, which are parallel planes of atoms equally spaced from each other. Lattice planes are given by a set of Miller indices, hkl , which denote where in the unit cell the planes intersect with the main crystallographic axes, x , y , and z . By using x-rays, which are scattered upon contact with an atom, information about the distance between the lattice planes can be determined. As an incoming beam of x-rays at a set incident angle (Θ) scatters elastically off of the atoms of a crystal, a spherical wave is created. In most cases, the waves cancel each other through destructive interference, however at some Θ wavelengths, these waves happen to be in phase

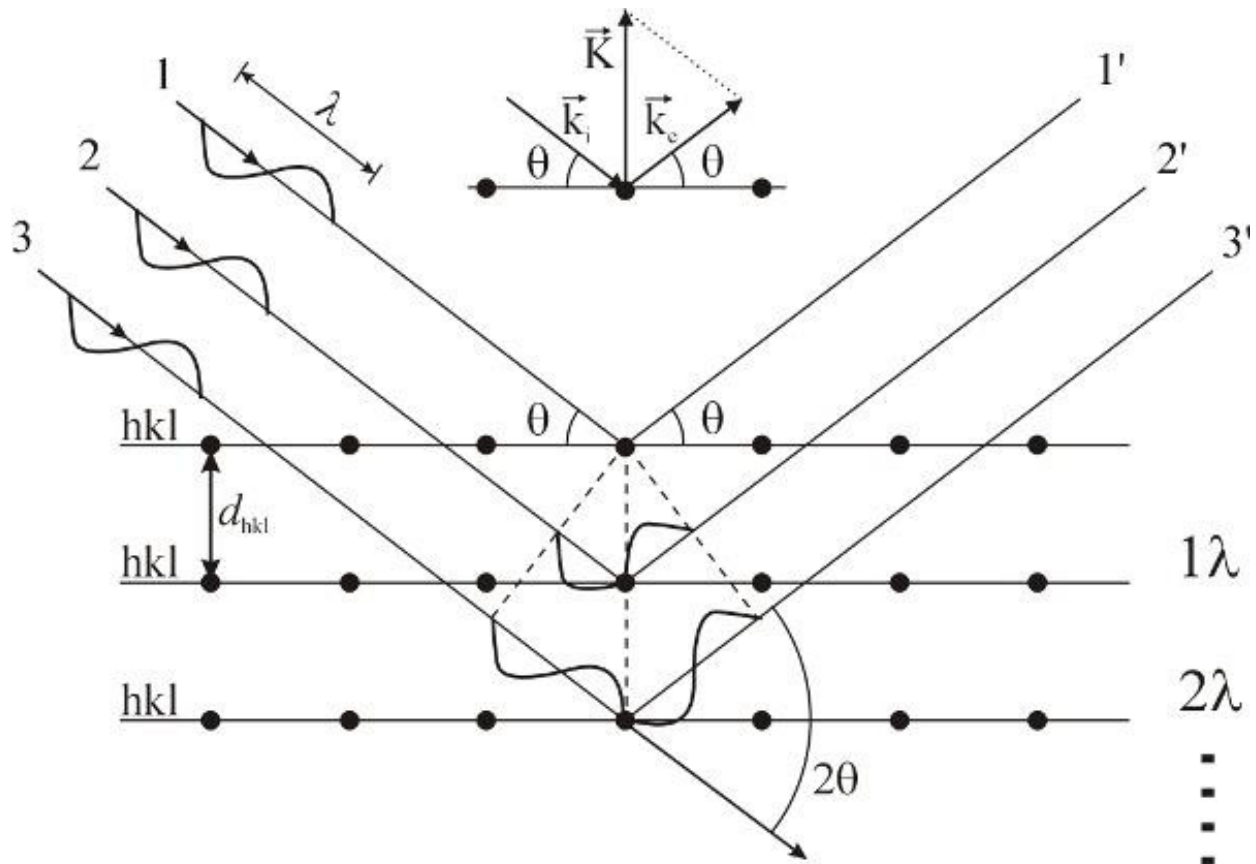


Figure 1.20: X-rays interacting with lattice planes within a crystalline material. As the x-rays hit an appropriate Θ corresponding to a lattice plane as defined by Bragg's law, the x-rays are in phase with each other and through constructive interference, an XRD signal is seen.

with each other and add together constructively. This constructive interference is dictated by Bragg's law:

$$2d\sin\theta = n\lambda \quad (1.13)$$

where d is the distance between lattice planes, n is an integer, and λ is the wavelength of the x-ray beam, which is generally 1.5406\AA due to the copper x-ray source used.⁶⁷ Figure 1.20 is a visual representation of how x-rays interact with lattice planes, resulting in peaks in the XRD spectra. The d value that can be determined through XRD is an important number that represents the lattice spacing. Each crystal structure has its own set of hkl planes which are spaced at exact distances. By evaluating the 2Θ values given in a XRD spectra, the d values can be extracted, and from that, a crystal structure can be found.

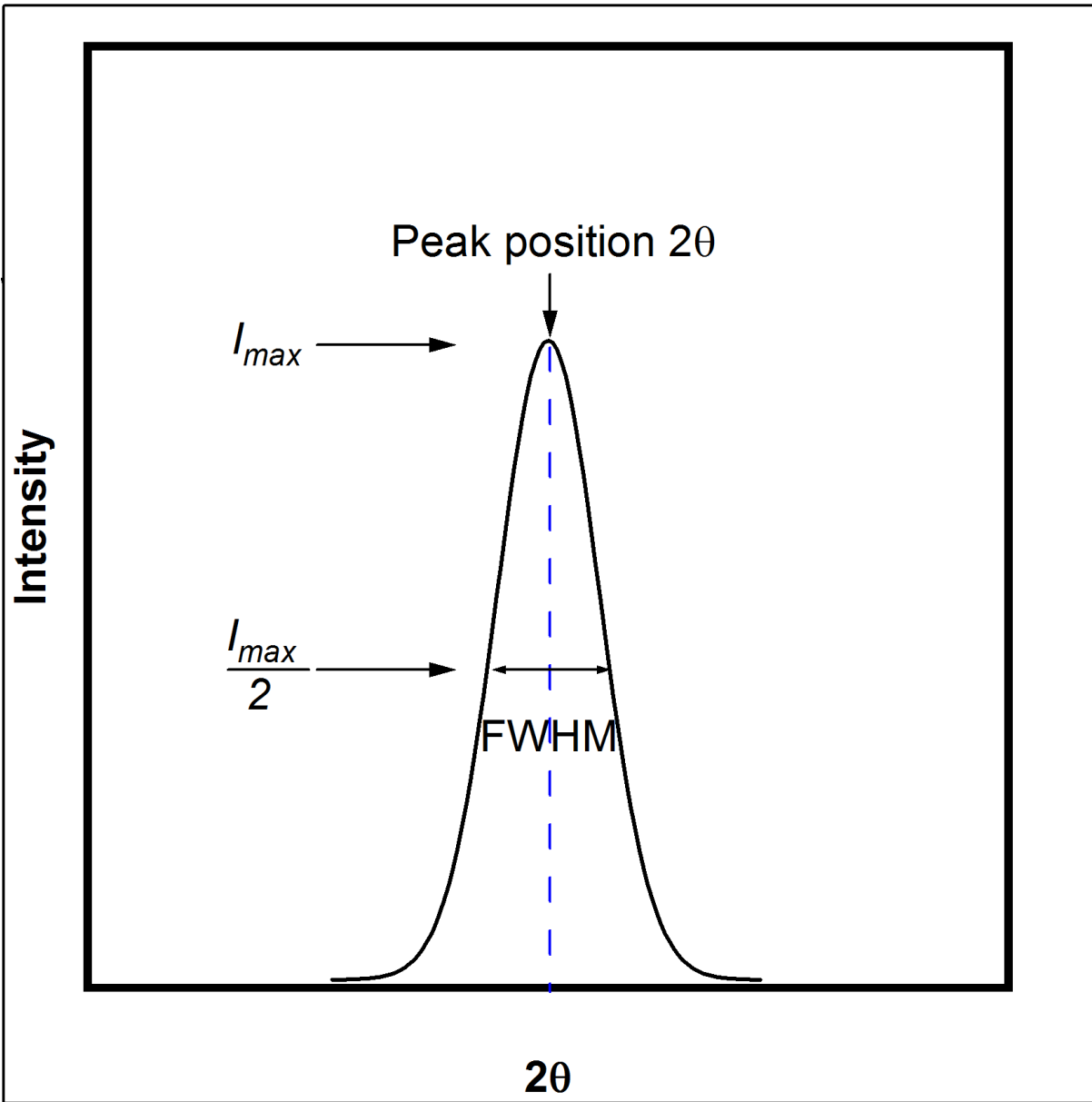


Figure 1.21: Peak in a pXRD spectra, where peak position and the full width half max (FWHM) can be used to determine particle size.

In addition to crystal structure information, pXRD can tell us about size and strain. In NPs, there are not a large enough number of lattice planes in the crystal to allow for perfect destructive interference at angles other than those allowed by Bragg's law. Because of this, information about the average size of the crystallites within a sample can be determined by the Scherrer broadening equation (equation 1.14).⁶⁸

$$L = \frac{\kappa\lambda}{\beta\cos\theta} \quad (1.14)$$

In the Scherrer equation, L represents the crystallite size, K is a unitless shape factor representing the aspect ratio of the particle, λ is the wavelength of the x-ray beam, β is the FWHM less the instrumental broadening in radians, and Θ is the Bragg angle. It can be seen from Figure 1.21 how to determine the FWHM of a peak, as well as the Θ , derived from the peak position.

Although spectral broadening can also be caused by other circumstances besides particle size, including lattice strain, the Scherrer method is a fairly accurate means of determining particle size within the range of 1-50 nm in diameter. In NP synthesis, it is imperative to know the size of the particles as well as the crystal structure. For this reason pXRD is a very powerful technique for NP analysis.

1.6.3 Transmission Electron Microscopy (TEM)

Transmission Electron Microscopy (TEM) is a technique that utilizes a beam of electrons to create a micrograph for the visualization of materials at the near-atomic level. Unlike regular light microscopy, TEM transmits electrons through the sample, and the interaction of that transmission results in the images seen in TEM. Both methods are limited to the wavelength of electromagnetic radiation used, with the wavelength of the electrons being much shorter, and therefore able to achieve significantly better resolution, allowing for imaging on the order of angstroms.

In TEM, heavy atoms with a large number of electrons will interact more strongly with the electron beam than lighter atoms. As a result, atoms such as hydrogen and carbon are generally not seen, though atoms such as gold display great contrast using TEM imaging. The image is a result of unscattered electrons transmitting through the sample, giving rise to a shadow image. Due to the resolution of the TEM being on the order of angstroms, NPs can be imaged, and often lattice planes can also be seen. The actual resolution of the image for TEM, d, is determined by the half aperture angle in radians, α (usually around 10^{-2} radians), and the accelerating voltage, V. The equation is given below:

$$d = \frac{0.753}{\alpha V^{1/2}} \quad (1.15)$$

At an accelerating voltage of 100,000 volts, the resolution is 2.4 Å, while at the higher voltage 250,000 volts, the resolution is down to 1.5 Å. This allows for the sizes, size

distributions, and somethings even the lattice spacings of NPs to be determined. The NPs synthesized in this dissertation were on the order of 3.6 nm, making any other microscopy technique other than TEM impossible for imaging at the single particle level. From TEM analysis, confirmation of size, size distribution, crystallinity, and confirmation of crystal structure was achieved.

1.6.4 Nuclear Magnetic Resonance (NMR)

Nuclear Magnetic Resonance (NMR) is an element specific technique where samples are placed within a magnetic field in order to deduce information about the intrinsic spin of the nuclei within. In order for an atomic nucleus to possess a non-zero spin, and therefore be NMR active, there cannot be an equal number of protons to neutrons in the given element. The nuclear spin, given the designation I , is zero if the number of neutrons and protons are both even. If the atomic mass is odd, the spin will have a half-integer value. If both the protons and neutrons have odd numbers, the element will have a spin with an integer value. Therefore, while ^{12}C is not NMR active, ^{13}C is, as the sum of the protons and neutrons are an odd numerical value. When NMR active nuclei are spinning, they generate a local magnetic field, making them atomic magnets themselves. Normally the spins within a sample are randomly oriented, however, when those atomic magnets are introduced to an external magnetic field, the spins will have $2I+1$ orientations. That is to say, if a nuclei has a $\frac{1}{2}$ spin value, there will be two possible orientations for the spin, with respect to the magnetic field. These orientations represent atomic alignment with or against the external magnetic field, referred to as the lower energy α -spin state, and the higher energy β -spin state, respectively. The splitting of the two states by the external magnetic field, B_0 , can be seen visually in Figure 1.22. The larger the magnetic field that is applied to a nucleus, the greater the splitting between those states, and therefore, the sharper the NMR peaks become, leading to better resolution.⁶⁹

The information received from NMR spectroscopy is how atoms of a given element interact with the applied magnetic field, *ie*, how strongly they “feel” the magnetic field. The strength at which different atoms within a compound experience the magnetic field depends upon how strongly the atom is shielded by electron density. As the electrons around an atom interact with the magnetic field, they induce a local magnetic field at that point, effectively shielding the nucleus from some of the external magnetic field. The result of electronic shielding

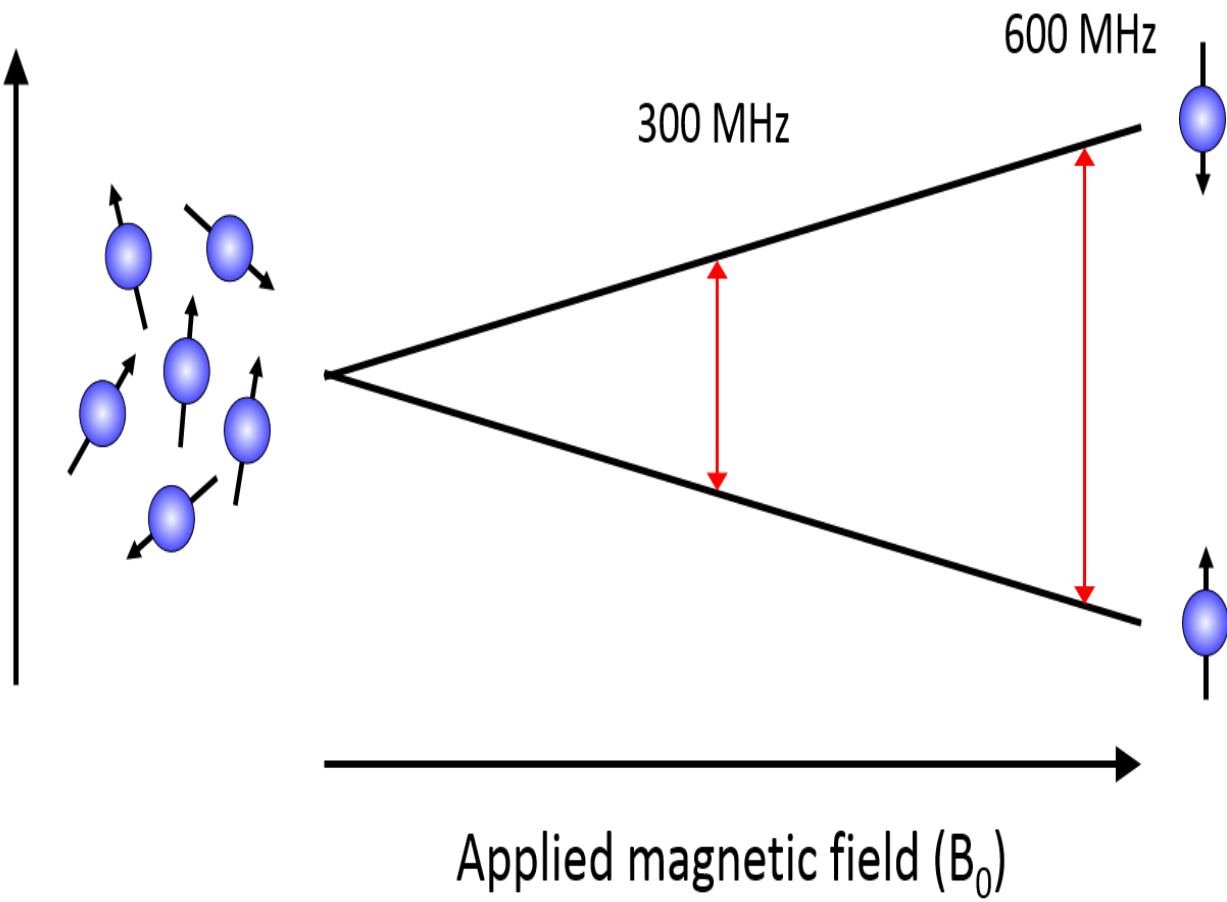


Figure 1.22: Splitting of the spin states induced by an applied magnetic field, the basis behind Nuclear Magnetic Resonance (NMR).

is that the nuclei do not feel the full effect of the magnetic field, but rather what is known as the effective magnetic field, given by:

$$B_{\text{effective}} = B_{\text{applied}} - B_{\text{local}} \quad (1.16)$$

The larger the electron density surrounding an atom, the smaller the effective magnetic field.

This can be seen in ^1H NMR spectroscopy, where protons attached to less electronegative atoms display a chemical shift further upfield in comparison to more shielded neighbors; for example, characteristic chemical shifts for methyl group hydrogens are seen at ~ 1.2 ppm, while protons attached to more electronegative atoms, such as in benzene, are shifted further downfield, at ~ 7 ppm, because of less shielding. Because of the effect of shielding on the position of NMR peaks, structural information can be determined through the use of NMR spectroscopy. In addition to

this, NMR spectroscopy is quite a powerful analytical technique, especially considering that many different factors influence the NMR signal.⁷⁰

Generally NMR is done in the solution state, as it is far easier to allow for the anisotropic tumbling of molecules and ensemble relaxation averaging, which gives cleaner spectra compared to analyzing solid samples. Often, however, samples are not soluble enough in solution to allow for solution NMR to be used. Additionally, if a low abundance nucleus, such as ¹³C, need to be analyzed, large amounts of sample need to be solubilized to avoid incredibly long signal averaging times. There are also circumstances when information about a compound in a particular environment is desired, such as chemical bonding environments for solid state materials, where solvating the complex would distort or destroy the chemical interactions of interest, making solution NMR undesirable. Solid state NMR (ssNMR) is a technique that is often used in NP analysis in order to combat solubility issues as well as to probe the chemical environment of the samples in the solid state. In ssNMR, solid samples are packed into zirconia rotors and spun at incredibly fast speeds, typically anywhere between 5.60 kHz. In general, solid NMR peaks are significantly broader than those found in solution NMR. This is due to interactions that are generally averaged out of solution spectrum as a result of the freedom of rotation resulting in rapid tumbling of molecules within the solution. In order to remove the effects of some of the interactions that cannot be averaged out, magic angle spinning is used. Magic angle spinning refers to a technique where the sample is spun at a canted angle, specifically 54.74°, with respects to the magnetic field. The terminology stems from the effects that magic angle spinning removes or suppresses which are the chemical shift anisotropy, a change in the chemical shift as a result of changes in orientation of a molecule with respect to the magnetic field, and heteronuclear and homonuclear dipolar coupling, which are caused by a partial alignment of spins with each other instead of with the field.⁷⁰

In this dissertation, ¹³C ssNMR spectra are collected for hexadecylamine (HDA) and acetylacetone (acac) passivated Eu:Y₂O₃ NPs. The investigation of the NMR spectra gave important information about the exact composition of the surface molecules of the as-prepared samples, as well as how the surface molecules were appended in the solid state. The use of ssNMR was essential, not only to get accurate information about how the surface molecules oriented on the NP in the solid state, but also due to solubility concerns with the NPs in most organic and aqueous solvents, making solution state NMR experiments infeasible.

CHAPTER 2

LIGAND-PASSIVATED EU:Y₂O₃ NANOCRYSTALS AS A PHOSPHOR FOR WHITE LIGHT EMITTING DIODES

Eu(III)-doped Y₂O₃ nanocrystals are prepared by microwave synthetic methods as spherical 6.4 ± 1.5 nm nanocrystals with a cubic crystal structure. The surface of the nanocrystal is passivated by acac and HDA on the Y exposed facet of the nanocrystal. The presence of acac on the nanocrystal surface gives rise to a strong $S_0 \rightarrow S_1 (\pi \rightarrow \pi^*, \text{acac})$ and $\text{acac} \rightarrow \text{Ln}^{3+}$ ligand to metal charge transfer (LMCT) transitions at 270 and 370 nm, respectively, in the Eu:Y₂O₃ nanocrystal. Excitation into the $S_0 \rightarrow S_1 (\pi \rightarrow \pi^*)$ or $\text{acac} \rightarrow \text{Ln}^{3+}$ LMCT transition leads to the production of white light emission arising from efficient intramolecular energy transfer to the Y₂O₃ oxygen vacancies and the Eu(III) Judd-Ofelt f-f transitions. The acac passivant is thermally stable below 400 °C, and its presence is evidenced by UV-vis absorption, FT-IR, and NMR measurements. The presence of the low-lying acac electronic levels allows UV LED pumping of the solid phosphor, leading to high quantum efficiency (~19%) when pumped at 370 nm, high-quality white light color rendering (CIE coordinates 0.33 and 0.35), a high scotopic-to-photopic ratio (S/P = 2.21), and thermal stability. In a LED lighting package luminosities of 100 lm W⁻¹ were obtained, which are competitive with current commercial lighting technology. The use of the passivant to funnel energy to the lanthanide emitter via a molecular antenna effect represents a new paradigm for designing phosphors for LED-pumped white light.

2.1 Introduction

The use of single-component white light phosphors pumped by high-efficiency UV LEDs, which operate in the wavelength range of 350-420 nm, represent a promising approach for lowcost, next-generation solid-state lighting, owing to their high efficiency in converting electrical energy to light, long duration and lifetime, good reliability and safety, easy maintenance, low energy consumption, and environmental advantages over currently employed mercury-based compact fluorescent lamps (CFLs).⁷¹⁻⁷⁴ High-efficiency LEDs pumping a phosphor are commonly employed in a variety of lighting applications from backlit LCD's to flashlights to, more recently, room lighting, as the luminous efficiency has increased from 5 to

150 lm W⁻¹ for commercial LED based available solid-state lighting.⁷²⁻⁷⁴ Many of these phosphors utilize blue LEDs (450-470 nm) to pump a YAG phosphor, which produces the characteristic blue/yellow color typical of modern LED flashlights. The blue color arises from the LED source, while the yellow is due to the downconversion YAG phosphor. The development of new white phosphors that exhibit lighting more characteristic of an incandescent source without the intense blue of the pumped LED is critical for applications in the household environment. Unfortunately, most phosphors have been optimized for 254 nm pumping in order to be used in compact fluorescent lighting (CFLs) and not the energies available for UV-LEDs (350-370 nm). While CFLs are already being utilized, the concern of Hg-based lighting and the potential cost savings due to lower energy usage and lower operating temperature of an LED-based lighting technology hold promise for LED-pumped white phosphor lighting technology.

The efficiency of LED-pumped phosphor-based lighting technology is directly dependent on the optical properties of the phosphors (optical cross section, radiative quantum yield) and the ability for the phosphor to nonradiatively downconvert excitation energy through energy transfer to the desired emissive state. To achieve more efficient LED-pumped phosphors, semiconductor quantum dots have been employed, due to their broad band excitation and size-dependent color,^{11, 75} as well as rare-earth (RE)-based phosphors in oxide, nitride, sulfide, and oxysulfide host lattices. The use of RE phosphors for lighting has gained attention, due to the reduced environmental toxicity concerns for RE phosphors;⁷⁶ however, RE phosphors in lanthanide sulfides are unstable toward degradation, RE phosphors in lanthanide nitrides lack cost-effective production methods, and RE phosphors in lanthanide oxysulfides have a poor optical cross section for excitation at energies lower than 300 nm.^{13, 77} Lanthanide oxide nanocrystals have been prepared in the literature by combustion, hydrothermal, and lyothermal methods but generally require long reaction times to produce dispersed nanocrystal powders.^{32, 78-80} The highest quality phosphors to date have been prepared by lyothermal techniques utilizing oleic acid as a ligand.⁸⁰ To realize the potential of white LEDs for solid-state lighting, the development of optimized phosphors that produce white light directly when pumped with commercial LEDs that operate between 350 and 420 nm is required. In addition, the LED-based lighting technology developed from the white phosphor must approach 100 lm W⁻¹ to be competitive with current CFL technology.⁷⁴

Rare-earth phosphors, in particular Eu:Y₂O₃ and derivatives of Eu(acac)₃, are well-known red downconversion phosphors used in commercial lighting and display technology, as well as recently in organic light emitting diodes (OLEDs).^{81, 82} These phosphors exhibit RE ion concentration dependent downconversion to the Eu(III) center by direct pumping of the O_{2p} → Eu_{4f} (III) charge transfer (CT) band and higher lying f-f levels at $\lambda > 250$ nm; however, the phosphors cannot be efficiently pumped with commercial UV-LED sources which operate below 300 nm, due to the fact the low-lying f-f Judd Ofelt (J-O) transitions for Eu³⁺ have small optical absorption cross sections. Various oxide hosts, as well as activator ion inclusion (Bi³⁺, Zr⁴⁺), have been investigated to improve the optical cross section for Eu(III) pumping, with limited success.⁸³ Research efforts have shown that nanoscale Eu:Y₂O₃ can shift and broaden the absorption band,⁸⁴ which can improve the direct excitation by UV-LEDs, but unfortunately the nanocrystals still lack a large spectral cross section in the appropriate spectral range for efficient pumping of the phosphor by a UV-LED.

In analogy to the photosynthetic reaction center,⁸⁵ one approach that has not attracted attention in the RE-doped oxide phosphor literature is the use of a passivating ligand on a nanocrystal as a molecular antenna for enhancing the optical cross section for absorption of the exciting LED energy. In RE diketonate complexes such as Ln(acac)₃ (Ln is a lanthanide ion), direct pumping of the diketonate ligand electronic levels leads to improved downconversion to the RE emitter via intramolecular energy transfer from the diketonate S₀ → S₁ π → π* transition or the low-energy ligand to metal charge transfer (LMCT) O_{acac} → Ln(III) transition at $\lambda \sim 370$ nm to the J-O levels of the RE ion.^{62, 86-93} The intramolecular energy transfer from the ligand to the lanthanide, which is often termed a molecular antenna effect, has been widely exploited in lanthanide coordination compounds, with the highest reported quantum efficiency for Eu(III)-(tta)₃(DBSO)₂ being $\phi_{em} \approx 85\%$.^{91, 93-95}

The use of a molecular antenna to improve the cross section for optical pumping of a nanophosphor by passivation of a Eu:Y₂O₃ nanocrystal by a diketonate ligand such as acetylacetone (acac) should allow direct UV-LED pumping of the nanophosphor though improved intramolecular energy transfer to the Eu³⁺ RE emitter. In this paper, microwave (MW) reaction methods are employed to prepare 6.4 ± 1.5 nm spherical acac-passivated Eu(III)-doped Y₂O₃ nanocrystals. The concentration-dependent optical properties for acac-Eu:Y₂O₃ nanocrystals doped from 0% to 18% Eu(III) and phosphor efficiency are reported. The isolated

nanocrystals from the MW method exhibit a cubic structure with evidence for ligand-induced face-specific faceting. The microwave-assisted reaction has several unique advantages over convective heating: namely, selective activation of the target precursor to initiate nucleation and subsequent growth, short reaction times, and reproducibility from batch to batch.^{47-49, 54} The Eu:Y₂O₃ nanocrystals are prepared in a 2.45 GHz MW cavity operating at 300 W in <15 min directly from the Ln(acac)₃ salts in hexadecylamine without the requirement of a cosolvent as previously reported.⁸⁰ Evidence for a thermally stable (below 400 °C) acac passivation layer on the Eu:Y₂O₃ nanocrystal is provided by FT-IR and ¹³C solid-state NMR measurements.

The acac-passivated Eu:Y₂O₃ nanocrystals are observed to exhibit a strong S₀ → S₁ acac π → π* transition at 270 nm and the LMCT O_{acac} → Ln(III) (Ln = Y, Eu) at 370 nm. The presence of the 370 nm O_{acac} → Ln(III) CT band is ideal for overlap with a UV-LED and is shown to produce white light with good color rendition (CIE coordinates of 0.33 and 0.35), high solid-state quantum efficiency for white light ($\phi_{em} \approx 19\%$), and high luminosity (100 lm W⁻¹ at 3.3 V). The efficiency of the phosphor is concentration dependent. The white light exhibits a high S/P ratio (2.20), making the light source desirable for room-lighting applications.⁹⁶ The white light is generated from emission from a combination of localized Y₂O₃ oxygen defect levels and Eu(III) J-O transitions in the nanophosphor. The efficient production of white light from the acac-passivated Eu:Y₂O₃ nanophosphor implies that further tuning of the passivation ligand singlet and triplet levels can allow efficient UV-LED pumped phosphors to be designed that utilize ligand-based energy funneling via a molecular antenna effect for solid-state lighting applications.

2.2 Experimental Section

2.2.1 Synthesis of Eu:Y₂O₃ (0%, 2%, 9%, 11%, 18%) Nanocrystals

Eu:Y₂O₃ (nanocrystals passivated by 2,4.pentadione (acac) were prepared by microwave-induced decomposition of yttrium(III) 2,4. pentanedionate hydrate (Alfa Aesar, 99.9%) and europium(III) 2,4. pentanedionate hydrate (Alfa Aesar, 99.9%) in a CEM Discover Microwave (MW) operating under single mode, continuous power at 2.45 GHz. The CEM MW cavity was commercially modified by CEM with a Teflon insert to allow sustainable heating at 300 °C. A glass microwave reactor vessel containing yttrium(III) 2,4.pentanedionate hydrate (0.193 g, 0.5 mmol), europium(III) 2,4.pentanedionate hydrate (0% (0 g), 2% (0.0045 g), 9% (0.01125 g),

11% (0.0225 g), 18% (0.03375 g)), and 1-hexadecylamine (HDA, 0.971 g, 4 mmol) was heated to 120 °C under vacuum for 30 min. The MW vessel was inserted into the MW cavity and heated at 300 W to 240 °C for 15 min. The solution was cooled to 50 °C, and the Eu:Y₂O₃ nanocrystals were precipitated by addition of toluene (~5 mL) followed by MeOH (~5 mL). The product was isolated for centrifugation, washed four times using toluene/MeOH, and dried under vacuum overnight. The isolated sample is tan in color and can be dispersed in toluene.

2.2.2 Measurements

TGA (thermogravimetric analysis) data were recorded on a TA SDT Q600 instrument. FT-IR spectra were measured on a Perkin-Elmer Spectrum GX system in KBr. The FT-IR spectra on samples that had been annealed at 20, 200, 300, 400, and 500 °C were conducted on individual samples that were premixed with KBr (1.33 mg of Eu:Y₂O₃ with 100 mg of KBr) and then thermally annealed prior to pressing the pellet. The thermal annealing of individual samples allows quantitative analysis of the FT-IR spectral intensity changes.

Elemental composition analysis was performed by X-ray fluorescence for Y and Eu. The measurements were carried out on an Oxford Instruments ED₂₀₀₀ X-ray fluorescence spectrometer with a Cu K α source. The concentrations were measured for Eu at 5.8 and 14.9 keV, corresponding to the L α and K α lines respectively. All of the measurements were performed by complete dissolution of the solid samples in 90% HNO₃, then the solutions were heated until clear, at which point all excess NO_x had been driven off. The samples were diluted to a volume of 3 mL using 2% HNO₃. In order to generate a calibration curve for the molar concentration of Eu, an appropriate amount of EuCl₂ was dissolved in 2% HNO₃ to make a 1000 ppm standard, which was then further diluted to get 800, 600, 400, 200, 100, 50, and 20 ppm solutions. The calibration curve for Y was generated by using a commercially prepared 1000 ppm elemental standard in 2% HNO₃, which was then diluted in the same fashion as above.

Solid-state ¹³C{¹H} CP-MAS NMR experiments were performed on a Varian Unity/Inova 11.75 T spectrometer with a Chemagnetics triple-resonance probe. The probe was tuned to 500.3 MHz for ¹H and 125.8 MHz for ¹³C, and the third channel was not used. Measurements of Y(acac)₃ by ¹³C{¹H} CP-MAS spectra were acquired in a 4 mm probe at 12 kHz using ¹H decoupling, ramped cross-polarization (CP), an acquisition time of 50 ms, a recycling delay of 2 s, a 90° pulse length of 5 μ s, and a 1 ms contact time. Measurements of the

Y_2O_3 and Eu: Y_2O_3 nanocrystal by $^{13}\text{C}\{^1\text{H}\}$ CP-MAS spectra were acquired in a 2.5 mm probe at 15 kHz using ^1H decoupling, ramped cross-polarization (CP), an acquisition time of 20 ms, a recycling delay of 4 s, a 90° pulse length of 5 μs , and a 1 ms contact time.

Structural characterization was performed using powder X-ray diffraction (pXRD) recorded on a Rigaku DMAX 300 Ultima III Powder X-ray diffractometer (using Cu K α $\lambda = 1.5418 \text{ \AA}$ radiation). Size, size dispersity, morphology, and structure were analyzed by TEM using a JEOL-2010 microscope operated at 200 kV. The samples were dispersed on holey carbon grids (400 mesh) from a toluene solution. Size and size dispersity were extracted by analysis of 17 TEM images representing 443 nanocrystals.

Fluorescence spectra were recorded at room temperature using a Spex Fluorolog II equipped with 0.22 m double monochromators (Spex 1680) and a 450 W Hg lamp. Selective excitation spectra for the Eu(III) $^7\text{F}_0 \rightarrow ^5\text{D}_0$ was performed at room temperature by excitation using the output of a dye laser containing Rhodamine 590 and Rhodamine 610 pumped by a NdYAG laser. The photoluminescence was collected at 90°, analyzed using a 0.25 m monochromator (slit 1.5 mm, 1180 grooves/mm) coupled to a Hamamatsu R928 photomultiplier tube, and recorded through an oscilloscope interfaced with a computer.

Absolute solid-state quantum yields were measured on the powdered samples following literature procedures⁹⁷ using a Spex Fluorolog 2 equipped with 250 mm double monochromators in which is mounted a 4.2 cm diameter integrating sphere (Labsphere). The excitation source consists of a NIST-calibrated Hg lamp. The number of photons emitted from the phosphor is integrated from 380 to 780 nm to calculate the emission quantum yield. Measurement of the diffuse scattered light at 90° from the excitation pathway was carried out in accordance with the technical bulletin from Jobin-Horiba. Spectra of the scattered light were recorded with and without the sample in the sphere. Integration of the area beneath the excitation peak is proportional to the total number of incident photons for the first spectrum and to the number of nonabsorbed photons for the second spectrum. The difference between these two is the number of absorbed photons. Integrating the area under the fluorescence peak from the second spectrum gives the emitted photons. By definition, the fluorescence quantum yield is the number of emitted photons divided by the number of absorbed photons. Use of a NIST-calibrated Hg lamp coupled to the integrating sphere allows accurate measurement of the light flux (photons), integrating sphere response function, and the phosphor quantum yield following lamp excitation.

The measurement is validated by comparison to the solid-state quantum yield standard, sodium salicylate.

Fabrication of a prototype solid-state lighting device was prepared by removal of the LED lens (0.4 mm from the wire bond or reflective cavity) from a commercial 370 nm excitation LED (TH-UV365GG, 365/370 m) and coating the exposed LED surface with the phosphor dissolved in cyanoacrylate (Super Glue). The phosphor is deposited as a thin film onto the LED surface and prepared by mixing 0.1 g of Eu:Y₂O₃ with 0.30-0.4 g of Super Glue. The device was operated at 3.0 V. The values for CIE coordinates (Commission Internationale de l'eclairage), the color-coordinated temperature (CCT), the S/P (scotopic-to-photopic) ratio, and the luminous efficiency were obtained as described in the literature.^{72, 74, 98, 99}

2.3 Results

2.3.1 Characterization of Eu:Y₂O₃

The synthesis of Eu(III)-doped Y₂O₃ nanocrystals prepared by microwave (MW)-assisted thermal decomposition of Eu(acac)₃ and Y(acac)₃ at 240 °C (300 W) in hexadecylamine (HDA), a non-MW-absorbing, nonhydrolytic solvent, produces spherical 6.4 ± 1.5 nm Eu:Y₂O₃ nanocrystals with a tail in the distribution toward larger particles, as shown for the 2% Eu:Y₂O₃ nanocrystal (Figure 2.1; larger images and several micrographs are available in Figures 2.2, 2.3, and 2.4). The distribution was measured over 433 nanoparticles. The well-dispersed spherical morphology nanocrystal distribution is consistent with Ostwald ripening growth behavior under the experimental conditions. The reactions are complete within 15 min. The nanocrystals are doped at 0% (Y₂O₃), 2.3% (2% Eu:Y₂O₃), 8.6% (9% Eu:Y₂O₃), 11.4% (11% Eu:Y₂O₃), and 17.6% (18% Eu:Y₂O₃) Eu(III) by control of the initial reaction stoichiometry, as verified by X-ray fluorescence analysis of the samples.

Structural characterization of the isolated Eu:Y₂O₃ nanocrystal is achieved by measurement of the pXRD and TEM electron diffraction (Figure 2.5). The pXRD pattern in Figure 2.5 for the Eu:Y₂O₃ nanocrystal can be indexed to a cubic structure (JCPDS card 43.1036) with well-defined (222), (123), (400), (440), (145), (622), and (662) diffraction peaks. Comparison of the observed pXRD intensities to the bulk standard card reveals the (123) and (145) diffraction intensities are enhanced in the nanocrystal relative to a bulk powder.

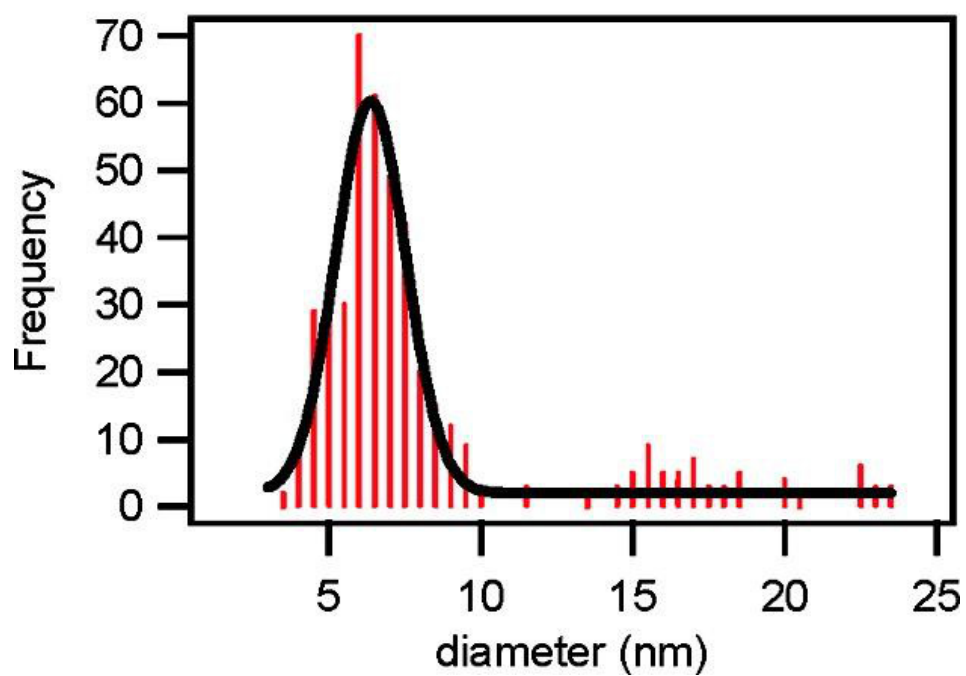
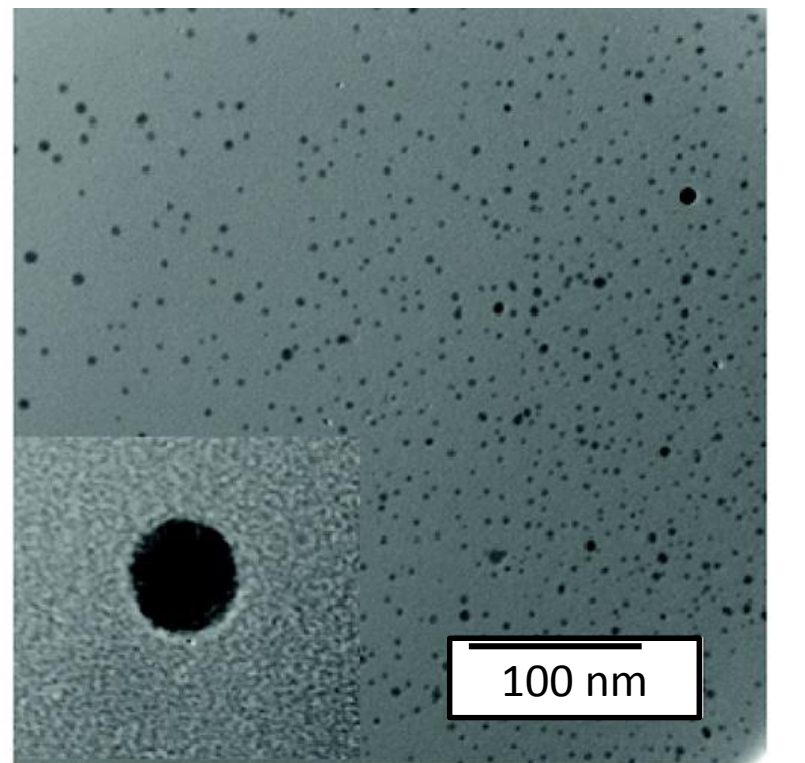


Figure 2.1: (top) TEM micrograph of 6.4 ± 1.5 nm Eu (2%): Y_2O_3 imaged at 200 keV (250 000 \times) on a 400 mesh amorphous carbon grid (scale bar 100 nm). Inset: image of a single Eu: Y_2O_3 nanocrystal at 1 500 000 \times magnification. (bottom) Size distribution of Eu(2%): Y_2O_3 measured over 433 particles in the TEM.

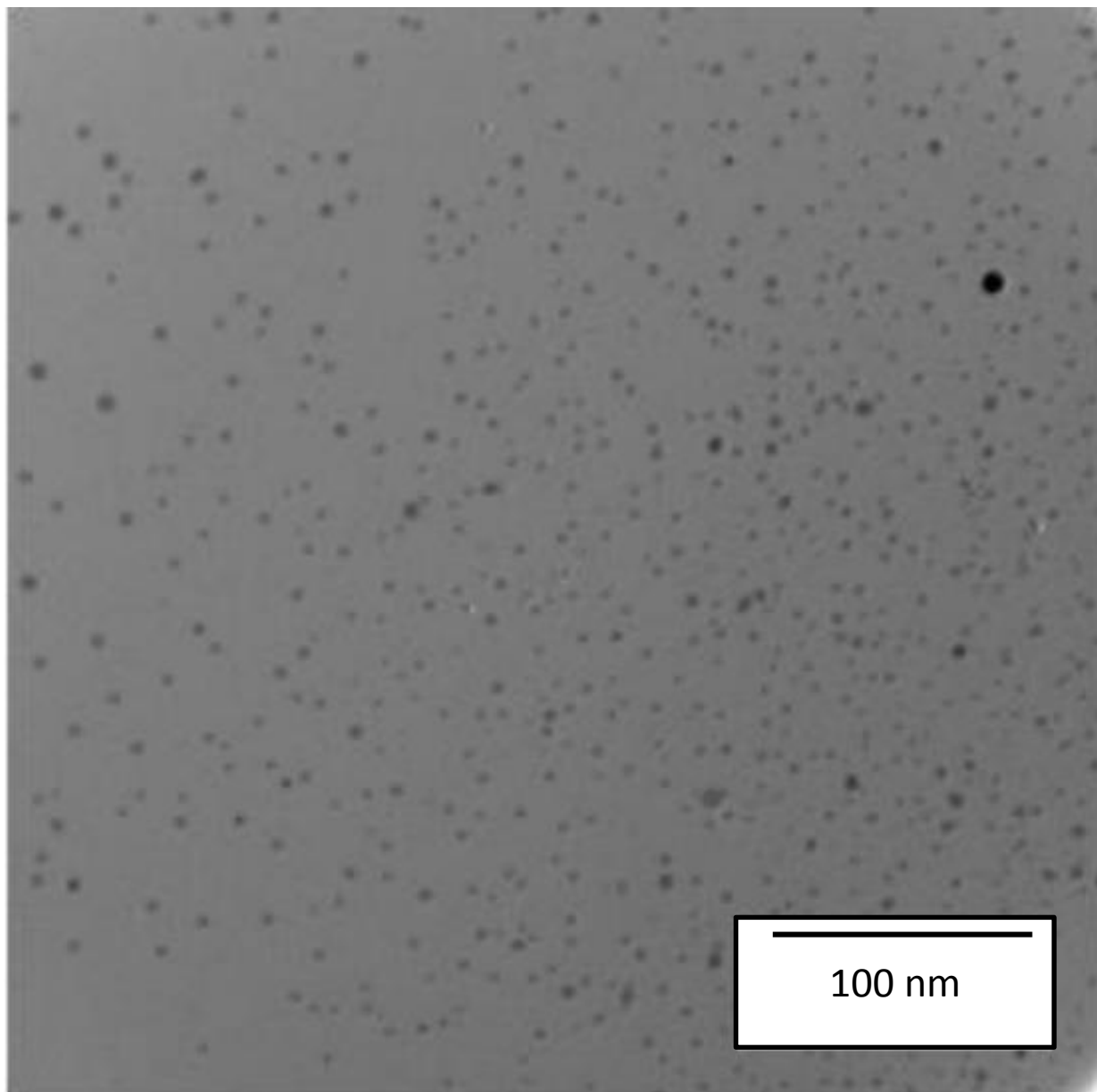


Figure 2.2: Selected TEM micrograph area showing the dominant features observed for the solvent dispersion of Eu(2%):Y₂O₃ on 400 mesh amorphous carbon grid operating at 250keV.

Confirmation of the pXRD cubic phase assignment is provided by the TEM electron diffraction pattern in Figure 2.5 (inset), where the (222) and (440) diffractions are clearly observed. The enhancement of the (123) and (145) diffractions in the pXRD is believed to reflect ligand control over the nanocrystal faceting during growth due to the strong coordination of acac to an oxygen-rich facet of the core nanocrystal or coordination of acac via the oxygen to a Y-rich

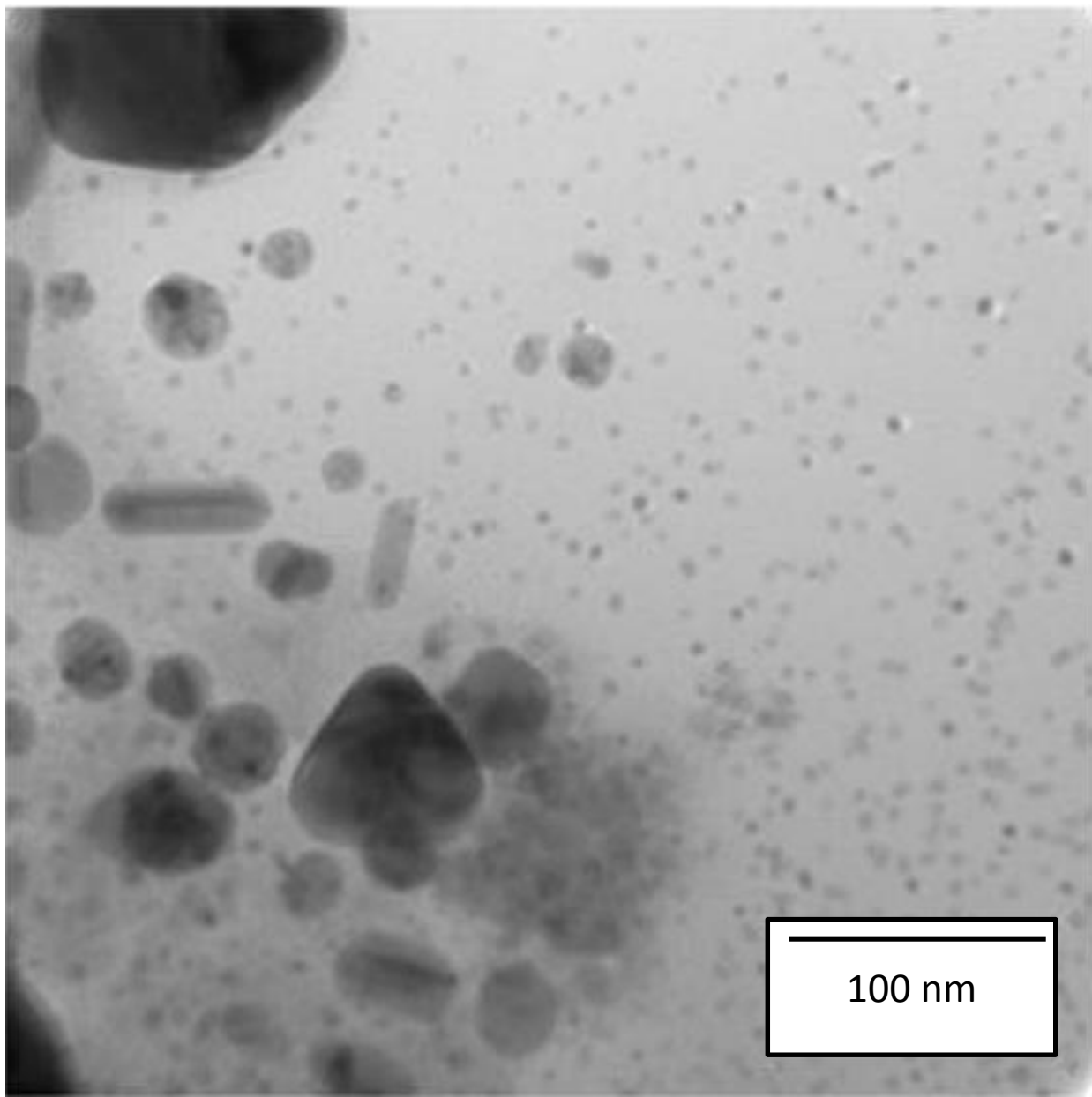


Figure 2.3: Selected TEM micrograph area showing the larger nanoparticles observed for the solvent dispersion of Eu(2%):Y₂O₃ on 400 mesh amorphous carbon grid operating at 250keV.

facet of the core nanocrystal (Figure 2.6). Selective face adsorption of ligands is known to influence nanocrystal growth in CdSe quantum dots.⁹⁸ Observation of the normally weak (123) and (145) pXRD features has been observed previously in the pXRD of Y₂O₃ and Eu₂O₃ nanocrystals passivated with oleic acid.^{80, 100}.

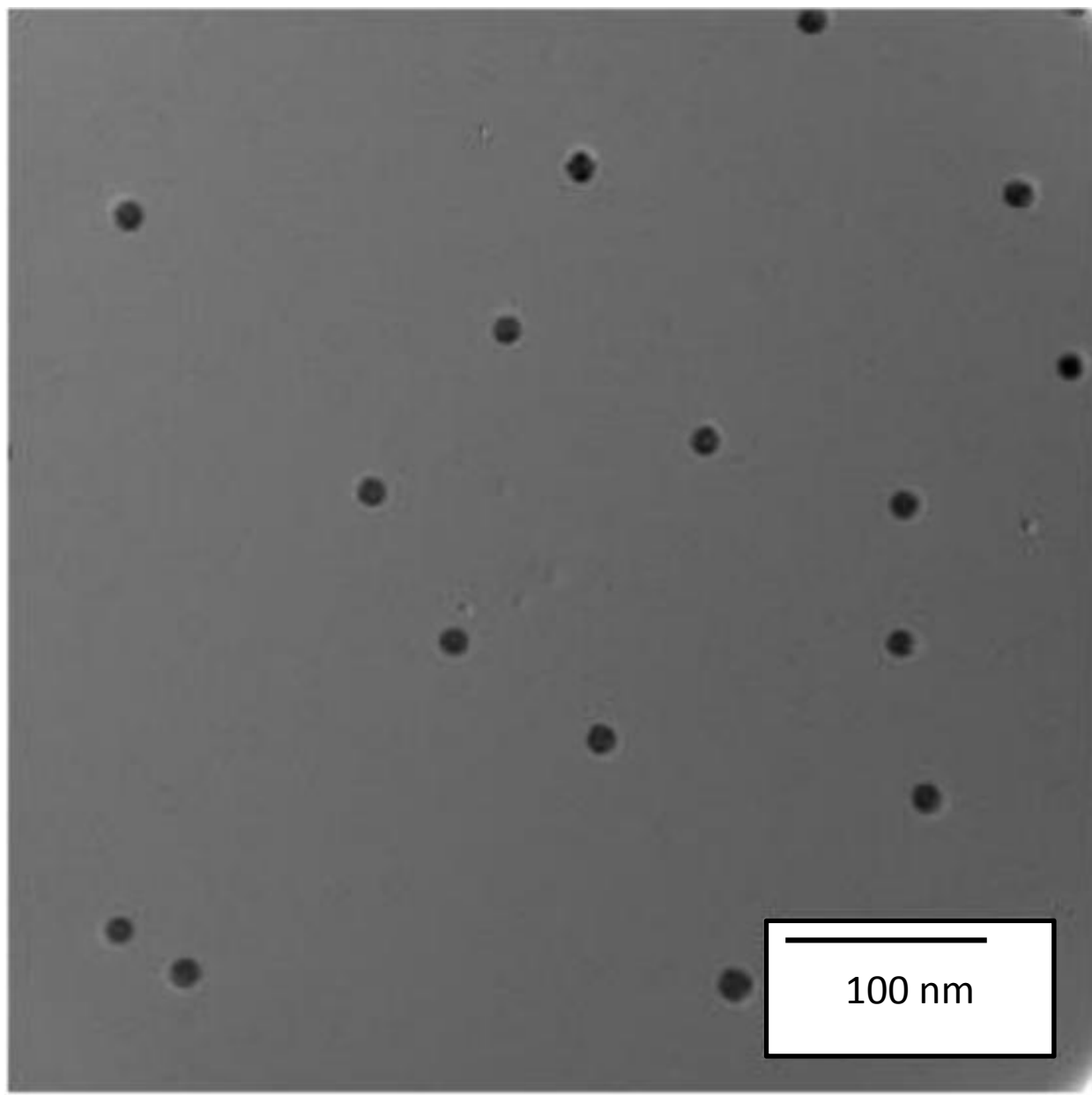


Figure 2.4: Selected TEM micrograph area exhibiting 15 nm particles in the solvent dispersion of Eu(2%):Y₂O₃ on 400 mesh amorphous carbon grid operating at 250keV.

2.3.2 Surface Passivation Layer of Eu:Y₂O₃

The nanophosphor surface passivation can be analyzed by analysis of the FT-IR (Figure 2.7A) and ¹³C{¹H} CP-MAS NMR (Figure 2.8B). In the FT-IR spectra of acac-Eu (2%):Y₂O₃, the IR vibration at 565 cm⁻¹ is assignable to the Y-O vibration for Y₂O₃, which occurs at a frequency identical with the IR-active optical phonon in cubic Y₂O₃, confirming formation of the

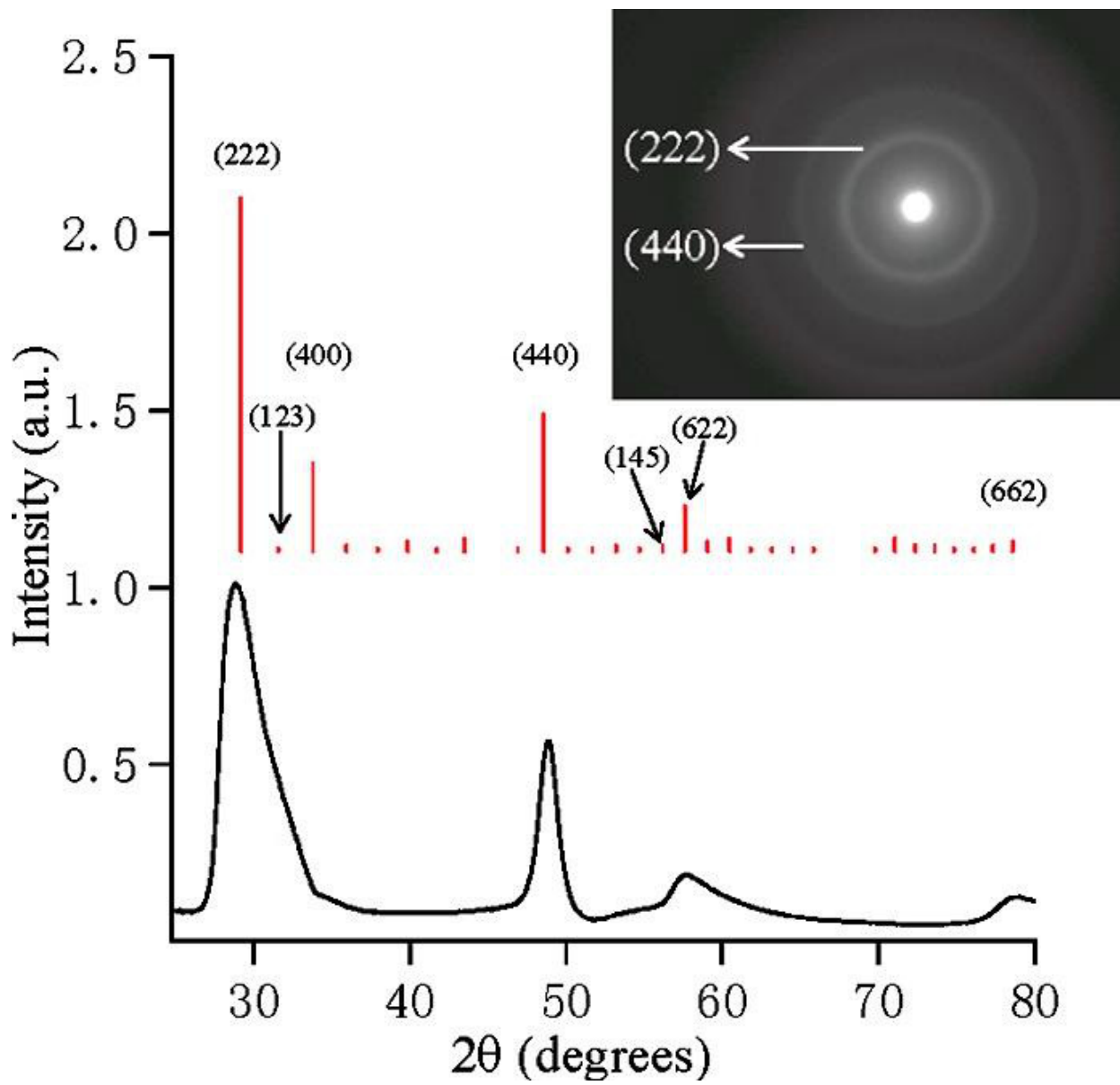


Figure 2.5: pXRD spectra of Eu(2%):Y₂O₃ in comparison to the standard card for the cubic phase of Y₂O₃ (JCPDS 43-1036). Inset: TEM-electron diffraction pattern with plane assignments for the Eu:Y₂O₃ nanocrystal.

cubic lattice.¹⁰¹ The surface passivant exhibits IR vibrations between 700 and 3000 cm⁻¹. Although the acac and HDA absorptions strongly overlap, evidence for both HDA and acac binding is provided by comparison to the FT-IR spectra of Y(acac)₃, Eu(acac)₃, Eu:Y₂O₃, and HDA (Figure 2.8).

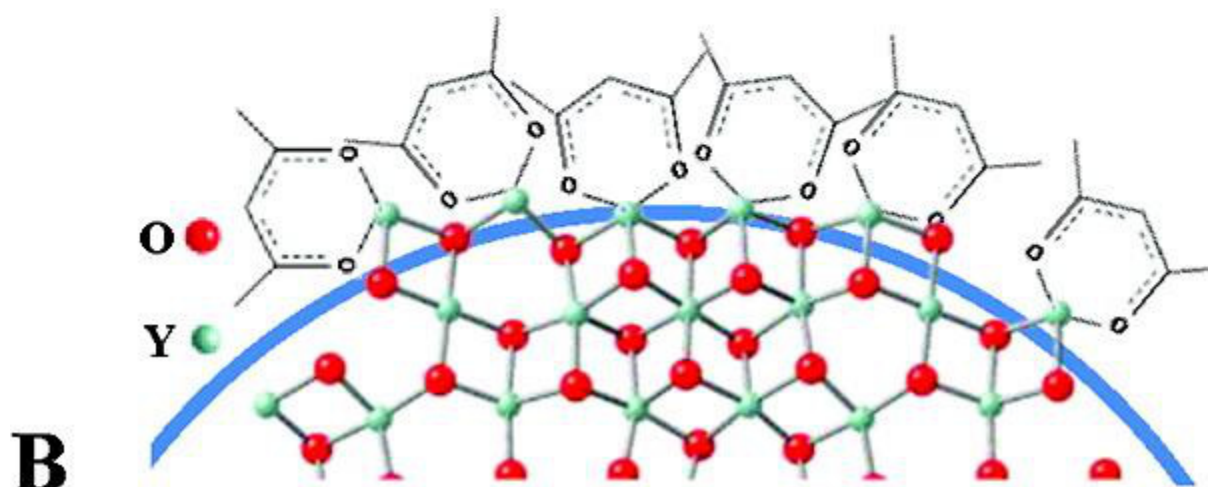
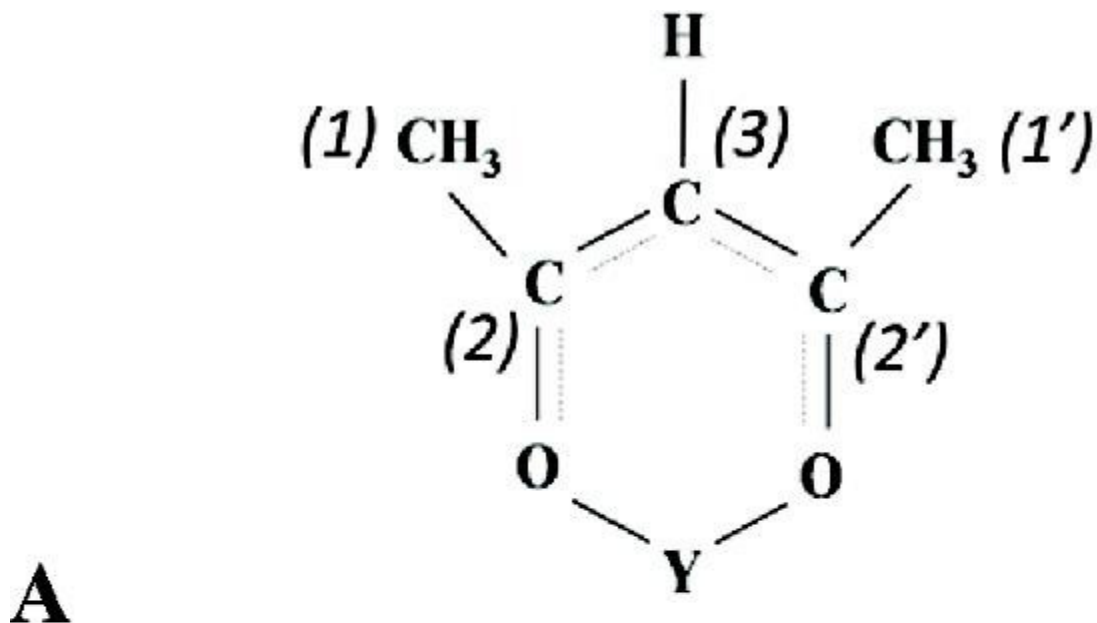


Figure 2.6: (A) Type A bridging bidentate coordination of acac to yttrium. The numbers in parentheses label the carbons as a reference. (B) Proposed octahedral coordination of acac to the (222) lattice plane of Eu:Y₂O₃ in the cubic crystal structure (JCPDS card 43-1036).

In the FT-IR spectra of the Eu(2%):Y₂O₃ nanocrystals in Figure 2.8A, the vibration at 659 cm⁻¹ can be assigned as an acac skeletal deformation mode, the 1025 cm⁻¹ mode is assigned to a -CH₃ rocking mode (P_x) on the acac, and symmetric and antisymmetric acac vibrations for the v(C=C,C=O) can be assigned at 1403 and 1525 cm⁻¹, respectively. The Δv(C=C, C=O) value of 122 cm⁻¹ is typical for a nonbridging bidentate type A coordination of the acac to the metal center, as shown in Figure 2.6A.¹⁰² The presence of HDA as a passivant is confirmed by the

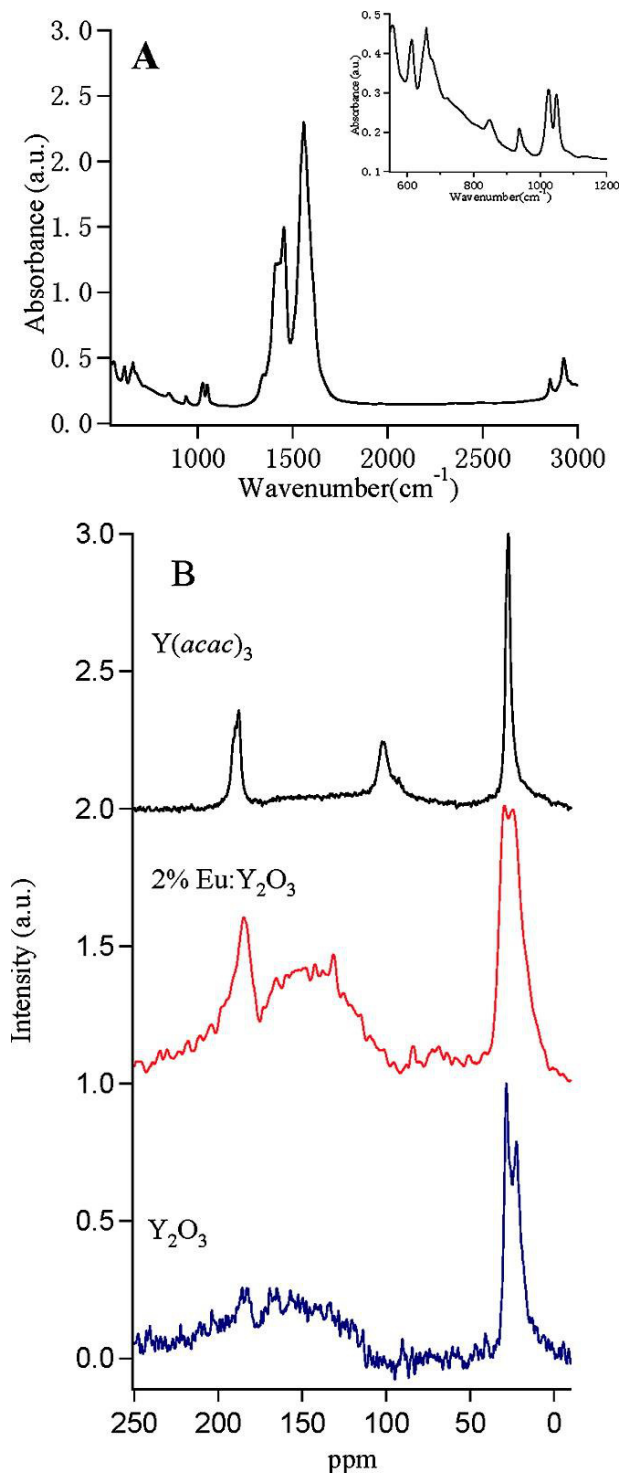


Figure 2.7: Surface passivation layer characterization data for 6.4 ± 1.5 nm acac-passivated Eu:Y₂O₃ nanocrystals: (A) FT-IR spectra of Eu:Y₂O₃ illustrating mid-frequency IR data and (in the inset) low-frequency IR data; (B) $^{13}\text{C}\{^1\text{H}\}$ CP-MAS spectra for Y(acac)₃ (black), acac-Eu:Y₂O₃ (red), and acac-Y₂O₃ (blue).

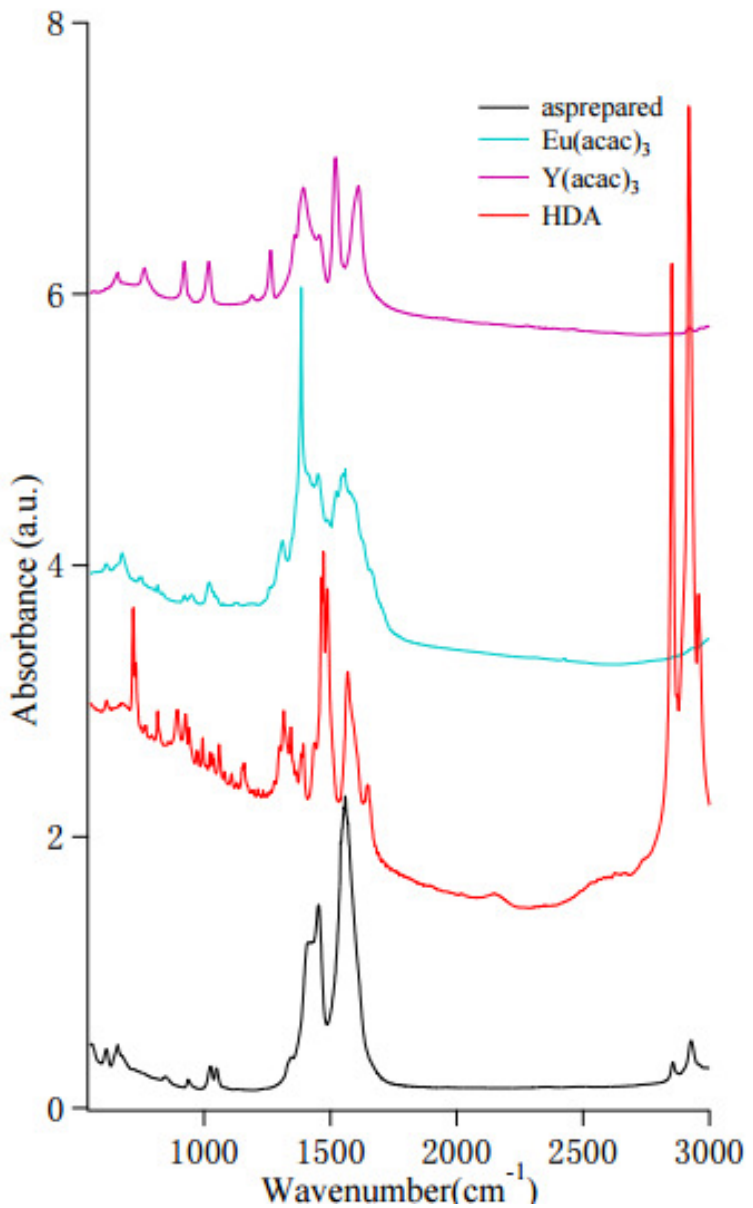


Figure 2.8: FT-IR spectra of KBr pellets containing Y(acac)₃, Eu(acac)₃, HDA, and Eu(2%):Y₂O₃.

observation of the -CH₂ symmetric and asymmetric stretches at $\nu_s(\text{-CH}_2)$ 2854 cm^{-1} , and $\nu_{\text{as}}(\text{-CH}_2)$ 2925 cm^{-1} , which arise at identical frequencies for HDA surface passivation in CdSe QDs.¹⁰³ The HDA -CH₂ deformation mode at 1471 cm^{-1} , which is much weaker than the stretch, overlaps the acac IR absorption and cannot be definitively assigned. From the intensity of the $\nu_s(\text{-CH}_2)$ and $\nu_{\text{as}}(\text{CH}_2)$ stretch to the acac $\nu(\text{C=C,C=O})$, the HDA is a minor passivant of the isolated nanocrystal. The FT-IR data for HDA, Y(acac)₃, Eu(acac)₃, and acac-Eu:Y₂O₃ are collated and

Table 2.1: Experimental FT-IR data and assignments for samples collected in KBr pellets.

IR vibration (cm ⁻¹)	HDA ¹⁰³	Y(acac) ₃ ¹⁰²	Eu(acac) ₃ ¹⁰²
659			
676		v((C-CH ₃)+ring deformation)	
722	CH ₂ ROCK;P ₁		
847	P ₁₃		C-H
937	P _X		
1026	C-C-C		
	SKELETAL; S _X		
1050	S _X		CH ₃
1344	W _X		
1410	COO ⁻ sym stretching	δ(CH ₃)	
1453		δ(CH ₃)+ v(C-C)	δ(CH ₃)+ v(C-C)
1560	N-H		C=O

assigned in Table 2.1.

The experimental results indicating acac and HDA binding to the nanocrystal surface are further supported by solid-state ¹³C¹H} CP-MAS NMR measurements on the acac-Y₂O₃ and acac-Eu(2%):Y₂O₃ nanocrystals by comparison to Y(acac)₃ in Figure 2.8. No measurements were carried out on Eu(acac)₃ or the higher doped samples of acac-Eu:Y₂O₃, due to the large paramagnetic broadening and lanthanide shift observed for Eu(III) coordination complexes that result in loss of the NMR signal.¹⁰⁴

The ¹³C NMR spectrum for Y(acac)₃ exhibits identifiable acac features for type A coordination¹⁰⁵ at 24.8 ppm (¹³C(1,1') for the CH₃ on acac), 191.3 ppm (¹³C(2,2') for the C=O in acac), and 100.5 ppm (¹³C(3) for the >C in acac). The numbering of the carbons of acac refers to Figure 2.6. The solid-state ¹³C NMR for Y₂O₃ shows ¹³C NMR features consistent with acac and HDA, as evidenced by a set of sharp features at 19, 23, and 29 ppm and a broad feature between 100 and 160 ppm. The feature at 23 ppm is assigned as the ¹³C(1,1') for the -CH₃ on acac, the 29

ppm feature is assigned to the -CH₂ units on HDA,¹⁰⁶ and the feature at 19 ppm is assigned as the -CH₃ group in HDA. The broad feature arises from a superposition of the ¹³C on acac at positions 2,2' and 3 for the ligand. The line broadening of the ¹³C(2,2' and 3) reflects the restricted rotational freedom for the bound acac centers and possible contributions from a distribution of binding motifs. The observation of the sharp feature for the ¹³C(1,1') position is due to the free rotation of the -CH₃ group in the acac ligand. Similar observations of extreme line broadening following ligand passivation of a nanocrystal have been reported.¹⁰⁶

The intensity of the features cannot be used to assign the composition of the passivation layer, since the solid-state measurement is a ¹³C{¹H} CP-MAS NMR experiment where the intensity of the CP-MAS experiment will be influenced by a combination of ¹³C population, cross-polarization time, rise time, and proton pool distance and availability.¹⁰⁷ Although predicting the concentration of the acac to HDA is not achievable, it is clear the HDA concentration is substantially lower than that of the acac, since the HDA has more ¹³C and a larger proton pool; however, the acac to HDA signal is smaller. The NMR results, therefore, are in agreement with the IR data, suggesting HDA and acac passivate the nanocrystal surface, with acac being the dominate passivant.

The ¹³C NMR for Eu(2%):Y₂O₃ exhibits features at 24.4, 29.6, 140 (broad), and 185 ppm. The features at 24.4 and 29.6 ppm can be assigned to the -¹³CH₂ on HDA and the -¹³CH₃(1,1') on acac, respectively. The -¹³CH₃ HDA feature at 19 ppm is absent, most likely due to broadening of the NMR features obscuring the peak. The broadening of the NMR feature is due to the restricted rotation of the acac and HDA passivant shell on the nanocrystal surface.¹⁰⁶ The most notable spectral change is the change of the broad, featureless peak in the 100-160 ppm region observed in Y₂O₃. In the Eu:Y₂O₃ NMR, a sharp feature at 185 ppm is observed, as well as a sharpening of the broad feature (center position at 140 ppm). The changes in the ¹³C NMR spectra reflect contributions from a paramagnetic shift and dipolar broadening due to the presence of the Eu(III) ion.¹⁰⁴ Eu(III) diketonate agents are routinely employed as lanthanide shift reagents, and the peak shift is distance and concentration dependent.¹⁰⁴ In the case of the Eu:Y₂O₃ sample, the shift will be complicated by the fact that the Eu-acac distances represent an ensemble across the 16 nm nanocrystal and possible variable bonding motifs. In the solid-state NMR the 185 ppm peak arises from ¹³C(2,2',>C=O) for acac. In Y(acac)₃ the ¹³C(2,2',>C=O) peak is observed at 191 ppm. The small shift for the C=O is expected, due to the dipolar effect of

the lanthanide shift reagent and long contact distances at the low doping concentration. The narrowing of the feature reflects a change in the relaxation rate due to changes in the CP-MAS matching conditions. No attempt was made to further optimize the CP conditions, due to the corroboration of the IR and NMR results. The broad feature from 100 to 160 ppm (center at 140 ppm) is therefore assigned to the $^{13}\text{C}(3,3',>\text{C})$ group on acac, which is broadened due to restricted rotation, and $^{13}\text{C}(2,2',>\text{C}=\text{O})$ on acac not in the vicinity of the Eu(III) ion.

Although the NMR data are broadened by the binding of acac and HDA to the nanophosphor surface, the data support a model in which HDA and acac are bound to the nanocrystal surface in a type A confirmation. The number of acac groups per Y (or Eu) ions at the nanocrystal facet will be equal to 1 or more in order to accommodate the typical >6 coordination number observed for passivation of Ln(III) ions.⁹³ Further insight into the structure at the surface cannot be determined from the structural, vibrational, and NMR results. Experimental observation of acac acting as a passivating ligand has been previously reported in PZT (lead zirconate titanate) nanocrystals prepared from metal acac precursors in nonhydrolytic solvents.¹⁰⁸

2.3.3 Optical Properties of Eu:Y₂O₃

In Eu³⁺ doped into bulk yttria no visible absorption features below 300 nm are observed; however, visible emission is observed from the Eu(III) J-O transitions that are efficiently populated following excitation into the yttria excitonic levels ($\text{O}_{2\text{p}} \rightarrow \text{Y}$), the Eu(III) CT ($\text{O}_{2\text{p}} \rightarrow \text{Eu}$), or the higher lying f-f levels of Eu(III). In Eu(III), the optically observed Judd-Ofelt (J-O) transitions can be assigned as electric dipole and magnetic dipole allowed Eu(III) $^5\text{D}_0 \rightarrow ^7\text{F}_J$ ($J = 1,4$) transitions. The observed electric dipole transitions are the $^5\text{D}_0 \rightarrow ^7\text{F}_J$ ($J = 2,4$) for Eu(III), where $J = 3$ is weak and $J = 2, 4$ are strong. The $^5\text{D}_0 \rightarrow ^7\text{F}_1$ line is a magnetic dipole transition allowed by selection rules of $J = 0, \pm 1$. Doping Eu(III) into bulk Y₂O₃ results in two possible sites of occupation, namely a site with inversion symmetry and a site with no inversion symmetry. The $^5\text{D}_0 \rightarrow ^7\text{F}_2$ electronically allowed transition gains intensity relative to the $^5\text{D}_0 \rightarrow ^7\text{F}_1$ transition when Eu(III) ions occupy a site without inversion symmetry.^{87, 88}

The population of the Eu(III) J-O levels following excitation into the higher lying electronic states occurs by intramolecular energy transfer via nonradiative paths.⁹² The efficiency of the downconversion process is concentration dependent and is known to be impacted by Eu-

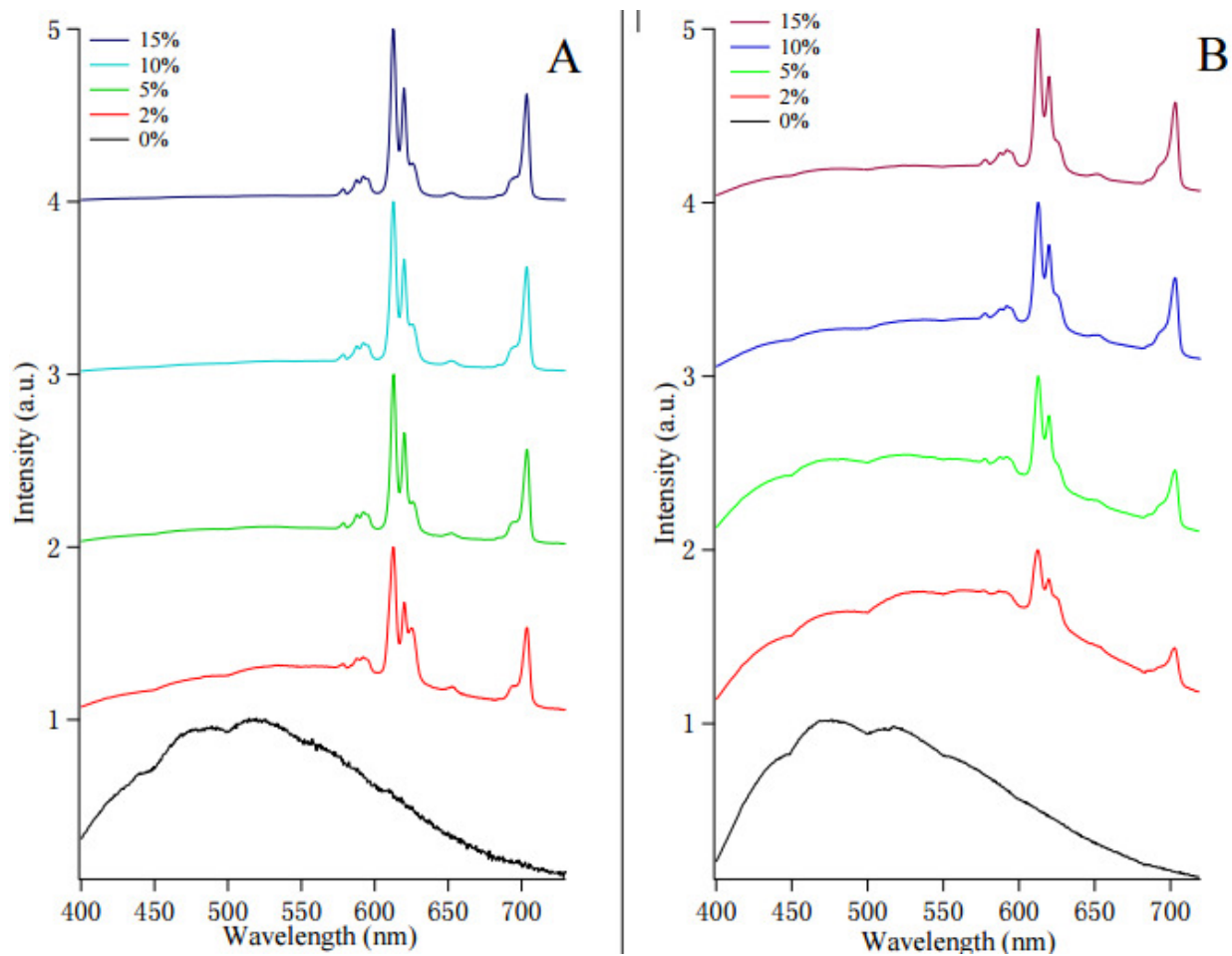


Figure 2.9: The wavelength dependent powder PL spectra of 0%, 2%, 5%, 10%, and 15% Eu:Y₂O₃ excited at A) $\lambda_{\text{ex}}=270 \text{ nm}$, and B) $\lambda_{\text{ex}}=370 \text{ nm}$.

Eu deactivation pathways at high Eu concentrations.⁹⁰ The observed intensities of the J-O transitions in Eu:Y₂O₃ nanocrystals will be influenced by the crystal lattice, the passivating ligand, the RE ion concentration, and the symmetry and site of doping of the Eu(III) guest ion.

The acac-Eu:Y₂O₃ nanocrystals in this study exhibit low energy absorptions due to the presence of the $S_0 \rightarrow S_1 \pi \rightarrow \pi^*$ acac and acac to lanthanide LMCT transitions present in these materials. Due to the presence of these ligand-based transitions, the acac-Eu:Y₂O₃ nanocrystals can be pumped at energies lower than 300 nm, and through intramolecular energy transfer populate the J-O levels of Eu(III). Optical data for 0%, 2%, 9%, 11%, and 18% Eu-doped Y₂O₃ are provided in Figures 2.9 (photoluminescence) and 2.10 (photoluminescence excitation). Representative optical data (absorption, photoluminescence (PL), and photoluminescence excitation (PLE)) for the Eu (2%):Y₂O₃ nanocrystals are shown in Figure 2.11.

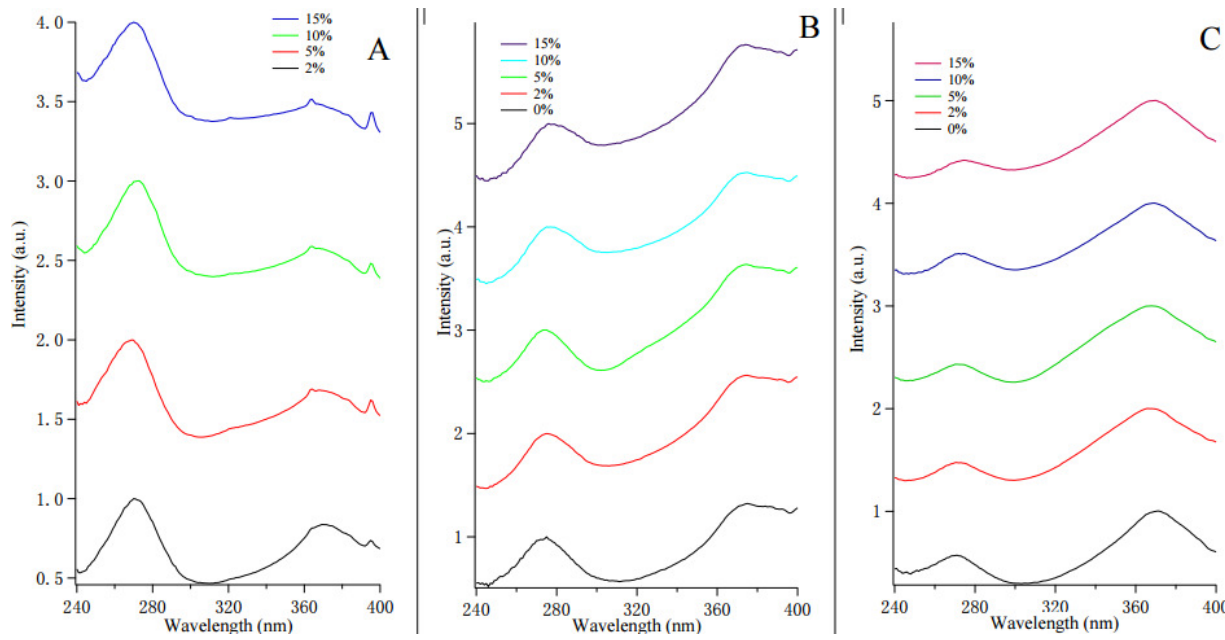


Figure 2.10: Wavelength dependent powder PLE spectra monitored at A) $\lambda_{\text{em}}=611 \text{ nm}$, B) $\lambda_{\text{em}}=520 \text{ nm}$, and C) $\lambda_{\text{em}}=430 \text{ nm}$ for 0%, 2%, 5%, 10%, and 15% doped Eu:Y₂O₃.

Absorption. The solution-phase optical absorption spectrum in CH₃CN for the Eu (2%):Y₂O₃ nanocrystal compared to those of Eu(acac)₃ and Y(acac)₃ is shown in Figure 2.11A. The absorption band observed at 270 nm is assignable to the S₀ \rightarrow S₁ $\pi \rightarrow \pi^*$ molecular orbital transition for acac by comparison to literature values^{87, 88} and the RE acac coordination compounds in Figure 2.11A. It is known that the energy of the S₀ \rightarrow S₁ $\pi \rightarrow \pi^*$ acac transition is not strongly influenced by the lanthanide ion.^{87, 88} The lower energy tail arises from scattering due to the low solubility of the nanocrystals. The observation of the S₀ \rightarrow S₁ $\pi \rightarrow \pi^*$ acac transition is consistent with the presence of acac bound to the nanocrystal surface. The expected higher energy $\sim 210 \text{ nm}$ Y₂O₃ band gap absorption (O_{2p} \rightarrow Y_{5s}, Eg(Y₂O₃) = 6.0 eV), charge transfer transition O_{2p} \rightarrow Eu_{4f} at 250 nm, and Eu(III) f-f allowed transitions occurring at 394 nm (⁷F₀ \rightarrow ⁵L₆) and 465 nm (⁷F₀ \rightarrow ⁵D₂) are not resolved in the solution absorption spectrum.^{15, 78}

Photoluminescence. Photoluminescence (PL) spectra for the Eu(2%):Y₂O₃ sample are shown in Figure 2.11B excited into the energy of the O_{2p} \rightarrow Eu_{4f} CT transition at 250 nm,⁷⁸ the acac S₀ \rightarrow S₁ $\pi \rightarrow \pi^*$ transition at 270 nm,⁸⁶ the O_(acac) \rightarrow Ln(III) LMCT transition at 370 nm,⁸⁶ and directly into the Eu(III) ⁷F₀ \rightarrow ⁵L₆ transition at 394 nm. The concentration-dependent PL behavior is shown in Figures 2.9A (270 nm) and 2.9B (370 nm).

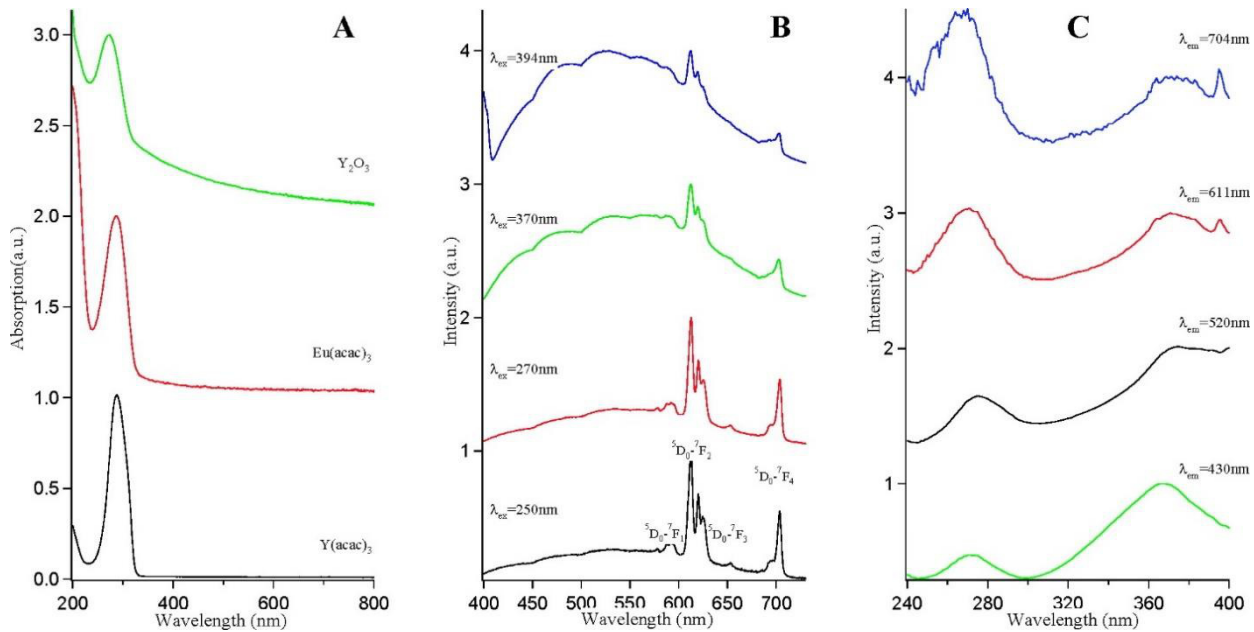


Figure 2.11: (A) Solution UV-vis absorption spectra in CH_3CN of acac-Eu:Y₂O₃, $\text{Eu}(\text{acac})_3$, and $\text{Y}(\text{acac})_3$. (B) Solid-state photoluminescence (PL) spectra (298 K, λ_{ex} 250, 270, 370, and 394 nm) of acac-Eu:Y₂O₃. (C) Solid-state photoluminescence excitation (PLE) spectra (295 K, λ_{em} 430, 520, 611, 704 nm) of acac-Eu:Y₂O₃.

For all excitations, the observed PL spectra in Figure 2.11B consist of a set of sharp features characteristic of Eu(III) f-f allowed Judd-Ofelt (J-O) $^5\text{D}_0 \rightarrow ^7\text{F}_J$ ($J = 1.4$) transitions between 580 and 710 nm overlapped by a broad PL feature centered at 520 nm (range 400-700 nm). The intensities of the $^5\text{D}_0 \rightarrow ^7\text{F}_J$ transitions increase relative to the Y₂O₃ defect as the Eu(III) doping concentration increases (Figure 2.9). The broad feature in the PL spectra centered at 520 nm is assigned to Y₂O₃ oxygen defect PL on the basis of cathodoluminescence measurements carried out on bulk Y₂O₃.^{109, 110} The features in the broad band can be assigned as arising from PL from oxygen vacancies ($V_{\text{O}} \approx 430$ nm),¹⁰⁹ and recombination centers associated with nearest-neighbor Y- (III)-O²⁻ donor-acceptor pairs ($D-\text{A}_{\text{Y}-\text{O}(1)} \sim 653$ nm)^{109, 110} as well as non-nearest-neighbor donor-acceptor pairs for Y(III) and O²⁻ ($D-\text{A}_{\text{Y}-\text{O}(2)}$ at ~ 480 , 520, and 590 nm).^{109, 110} The sharp features are assigned to the J-O $^5\text{D}_0 \rightarrow ^7\text{F}_J$ ($J = 1.4$) Eu(III) transitions and are labeled in Figure 2.11B. In the PL data the $^5\text{D}_0 \rightarrow ^7\text{F}_2$ line is the strongest, indicating the emissive Eu(II) center occupies a site without inversion symmetry. The Eu(III) electric dipole broadens relative to a bulk sample, as shown by the line width of the $^5\text{D}_0 \rightarrow ^7\text{F}_2$ transition in the nanocrystal of 0.018 eV vs that in bulk of 0.009 eV (Figure 2.12).

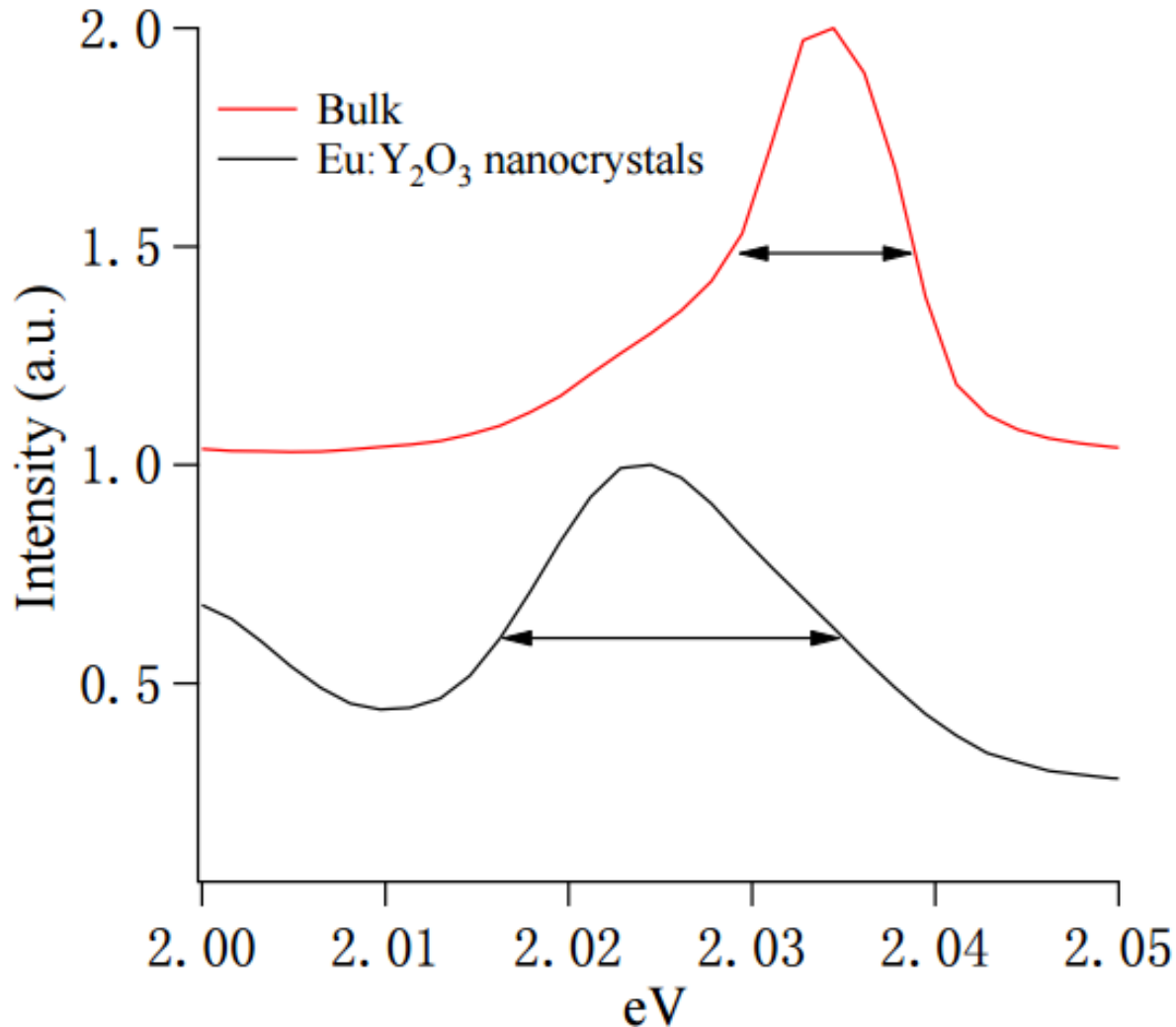


Figure 2.12: Photoluminescence measurement at $\lambda_{\text{ex}} = 270$ nm showing spectral broadening of the ${}^5\text{D}_0 \rightarrow {}^7\text{F}_2$ transition in bulk and nanocrystal Eu(2%):Y₂O₃.

The wavelength dependence of the PL spectra for the Eu:Y₂O₃ in Figure 2.11B is telling with respect to the intramolecular energy transfer cascade from the initial absorption of incident light by the CT ($\text{O}_{2\text{p}} \rightarrow \text{Eu}_{4\text{f}}$) and $\text{S}_0 \rightarrow \text{S}_1 (\pi \rightarrow \pi^*, \text{acac})$ in the UV or the LMCT transition from acac to the Ln(III) ions to the emissive Eu(III) dopant sites. Excitation into the $\text{O}_{2\text{p}} \rightarrow \text{Eu}_{4\text{f}}$ CT transition at 250 nm or the acac $\pi \rightarrow \pi^*$ transition at 270 nm leads to the efficient population of the J-O ${}^5\text{D}_0 \rightarrow {}^7\text{F}_J$ transitions for Eu(III) with minimal population of the Y₂O₃ defect levels. The efficient relaxation from the initially populated S₁ state or CT state to the Eu(II) f-f levels

indicates that the intersystem crossing to the acac T₁ and subsequent nonradiative relaxation to the Eu(III) J-O levels arise from an efficient phonon-assisted process.

The concentration-dependent absolute solid-state quantum efficiencies (ϕ_{em}) measured in an integrating sphere for the acac-Eu:Y₂O₃ pumped at 270 nm are 1% for Eu (0%), 7% for Eu (2%), 12% for Eu (9%), 9% for Eu (11%), and 8% for Eu (18%). The concentration-dependent quantum efficiency is typical of Eu(III) self-quenching arising at higher concentrations and the depopulation of the C₂ Eu(III) site by the S₆ (C_{3i}) site, which has been shown to reduce the quantum efficiency in bulk materials at higher Eu concentration.⁹⁰

Excitation into the O_{acac} → Y(III) LMCT transition at 370 nm or directly into the Eu(III) ⁷F₀ → ⁵L₆ transition at 394 nm results in an increased contribution from the Y₂O₃ oxygen defect energy levels and the production of a white light phosphor spectrum. The quantum efficiencies for acac-Eu:Y₂O₃ pumped at 370 nm of 11% Eu (0%), 14% Eu (2%), 19% Eu (9%), 13% Eu (11%), and 10% Eu (18%) show a smaller concentration dependence, indicating population of the Y defect levels does not efficiently populate the Eu(III) f-f J-O levels due to the inefficient energetic or phonon coupling of the defect levels in Y₂O₃ to the J-O levels in Eu(III) or due to formation of a trapped excitonic state at the defect centers in the lattice. The increased intensity of the defects for optical pumping at 394 nm is more surprising and likely reflects the competition between direct population of the vacancy levels and the low optical cross section Eu(III) f-f levels. Further insight into the energy funneling mechanism to the Eu(III) center can be gained by inspection of the wavelength-dependent photoluminescence excitation spectra.

Photoluminescence Excitation. Photoluminescence excitation (PLE) spectra monitored at selected wavelengths can provide spectral evidence of the excited state partitioning between the Y₂O₃ defect and Eu(III) J-O levels following initial excitation. The wavelength-dependent PLE data for the 2% Eu:Y₂O₃ nanocrystal is shown in Figure 2.11C monitored at the energy of the ⁵D₀ → ⁷F₂ Eu(III) transition at 611 nm, the ⁵D₀ → ⁷F₄ Eu(III) transition at 704 nm, the V_o defect at 430 nm, and the DA_{Y-O(1)} defect at 520 nm. The PLE spectra exhibits two broad PLE features centered at 270 and 370 nm regardless of the monitoring energy. The PLE feature observed at 270 nm can be assigned to the acac S₀ → S₁ π → π* transition, as observed in the solution absorption spectra (Figure 2.11A). The PLE feature at 370 nm can be assigned to the acac O_{acac} → Y(III) LMCT transition by comparison to the absorption features reported for Ln(acac)₃ coordination complexes.⁸⁶ Monitoring at 611 and 704 nm, which correspond to the Eu(III) J-O

transitions, results in the additional observation of the Eu(III) $^7F_0 \rightarrow ^5L_6$ level at 394 nm.¹¹¹ The recorded PLE spectra in Figure 2.11C are notable for several reasons in comparison to the PLE reported for either bulk¹⁶ or nanocrystalline Eu:Y₂O₃:⁷⁸ (i) the appearance of PLE features at 270 and 370 nm, (ii) the PLE feature at 270 nm increasing in intensity relative to the feature at 370 nm as the monitoring wavelength for the PLE spectra is shifted to the red, and (iii) the lack of a 250 nm transition for the O_{2p} \rightarrow Eu_{4f} CT transition. The strong PLE features observed at energies consistent with the presence of acac passivation indicate that the Ln-acac passivant can efficiently absorb and transfer energy to the Eu(III) centers. The lack of a 250 nm transition in the PLE can be attributed to the lower cross section for absorption of the O_{2p} \rightarrow Eu(III)_{4f} CT transition in comparison to the optical cross section for the acac electronic transitions.

The appearance of the Eu(III) $^7F_0 \rightarrow ^5L_6$ is not surprising when the J-O level is probed, but the appearance of the LMCT and S₀ \rightarrow S₁ $\pi \rightarrow \pi^*$ transition associated with acac passivation of the nanocrystal surface is somewhat surprising and suggests direct excitation into the $\pi\text{-}\pi^*$ acac transition results in efficient energy transfer to the Eu(III) centers in the host lattice via a phonon-assisted process or Eu-Eu pair activation leading to excitation of one Eu(III) emissive center to a high-lying level and depopulation of the other Eu(III) pair ion.⁵⁴ Although the results suggest that energy transfer from the high-lying acac transitions is efficient in these materials, the initial excited-state population partitions into a phonon-assisted relaxation into the Eu(III) J-O levels and separately can be trapped by the internal lattice defects. The defect levels are believed to represent local defect radiative trap centers and due to site trapping exhibit poor energy transfer to the Eu J-O levels. Cross population from the defects to the J-O levels appears to be inefficient, reflecting the large separation distance between the defect and Eu(III) center at low doping concentrations. Excitation into the lower energy O_{acac} \rightarrow Ln(III) leads primarily to the population of the Y₂O₃ defect energy levels, implying that the energy gap between the LMCT transition and the Eu(III) J-O levels does not allow efficient depopulation, since the process is anticipated to be a random walk process following a dipole-dipole exchange mechanism. In Eu(acac)₃ poor population of the Eu J-O levels was similarly observed to arise from a competition with the LMCT levels, leading to vibrational relaxation via nonradiative pathways.^{87, 88, 90} On the basis of the optical results, a simplified schematic for the energy relaxation pathway to the Eu(III) center is shown in Figure 2.13. The relative intensity of the

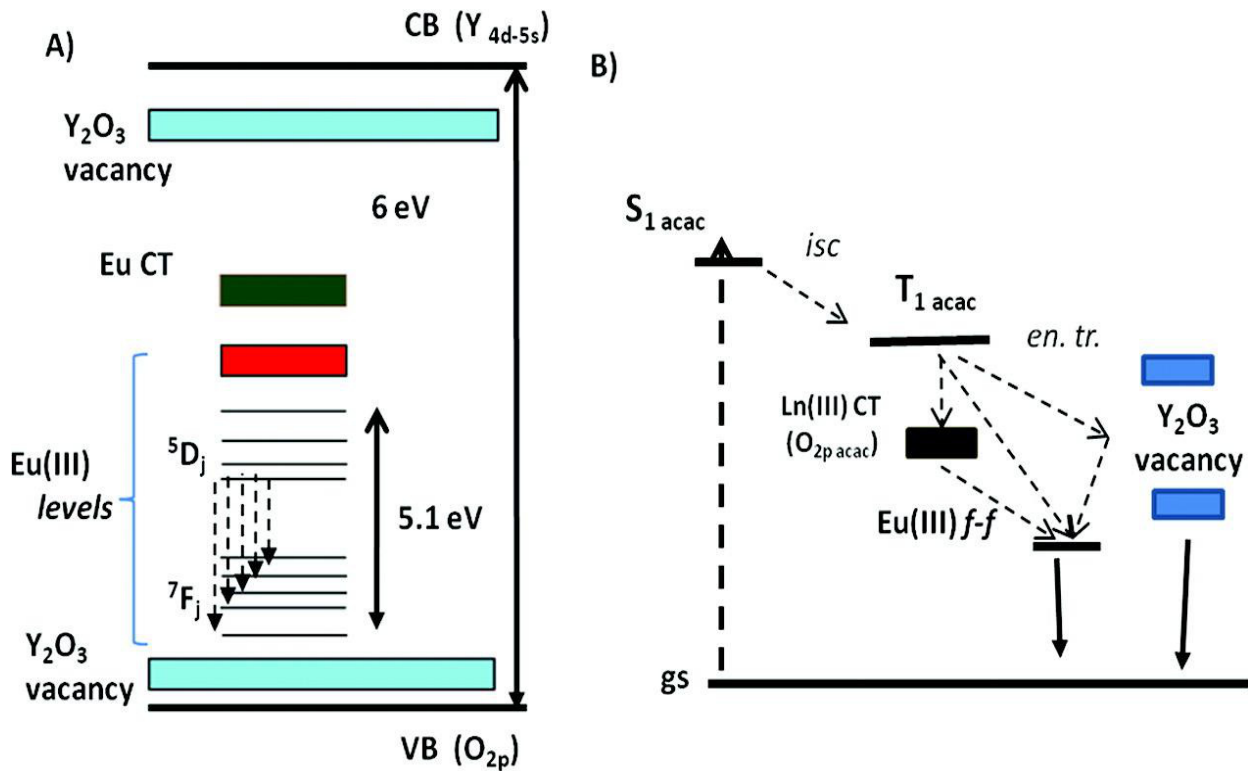


Figure 2.13: (A) Schematic energy level diagram and (B) relaxation pathways for efficient downconversion to the Eu(III) J-O transitions and Y_2O_3 defect levels in the acac–Eu: Y_2O_3 nanocrystals.

optical features feature in Figure 2.11 can be understood in terms of the energy relaxation pathway in Figure 2.13, due to differences in efficiency for energy transfer from the initially populated acac electronic levels to the lower energy electronic levels in the Y_2O_3 defects and Eu(III) dopant centers.

2.3.4 Evidence of the Presence of Surface and Core Eu(III) Sites in the Eu: Y_2O_3 Nanocrystal

In nanocrystal samples of Eu: Y_2O_3 , the intensity and energy of the parity-forbidden Eu(III) $^7F_0 \rightarrow ^5D_0$ transition is often used as a sensitive probe of the Eu(III) site.¹¹² In a bulk sample of Y_2O_3 , the Eu(III) center can occupy either a C_2 or a S_6 symmetry site. Eu(III) ions occupying the C_2 site leads to the parity-forbidden $^7F_0 \rightarrow ^5D_0$ transition becoming partially allowed and in nanocrystals is observed to split reflecting contributions from Eu(III) centers occupying a surface and core site in the nanocrystal.¹¹² In Figure 2.14, the PLE spectrum for the

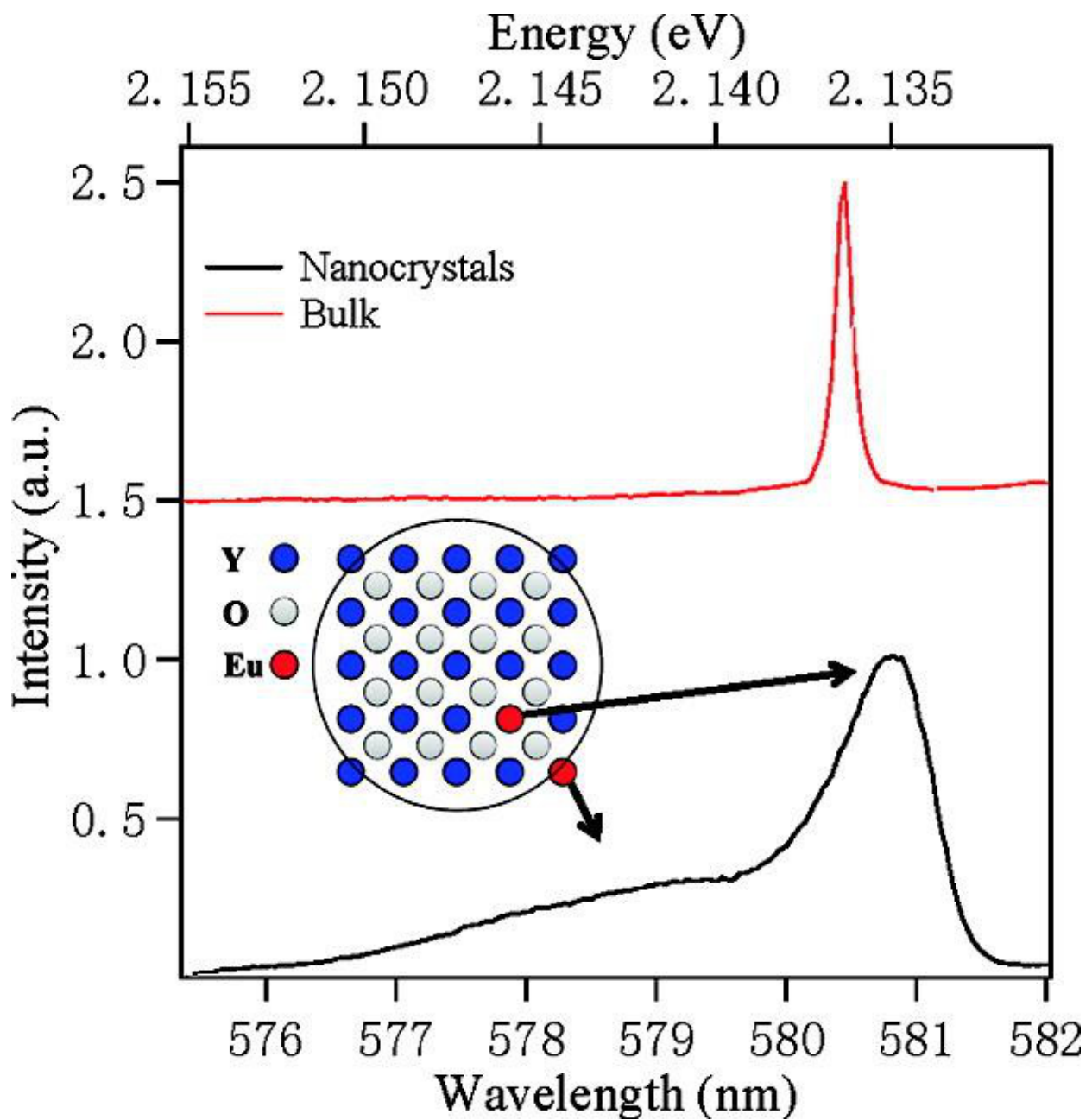


Figure 2.14: High-resolution PLE spectra for Eu (2%):Y₂O₃ and bulk Eu:Y₂O₃ sample monitored at λ_{em} 611 nm in order to probe the $^7\text{F}_0 \rightarrow ^5\text{D}_0$ J-O transition for the Eu(III) C₂ symmetry occupation in the Y₂O₃ host lattice.

parity-forbidden $^7\text{F}_0 \rightarrow ^5\text{D}_0$ transition monitored at 611 nm ($^5\text{D}_0 \rightarrow ^7\text{F}_2$ Eu(III) transition) is shown for the Eu:Y₂O₃ nanocrystal compared to that of a bulk sample. The bulk sample is prepared by sintering the nanocrystal sample at 1000 °C for 2 h. The PLE spectrum for the bulk Eu:Y₂O₃ sample exhibits a single Gaussian transition centered at 580.4 nm, while the nanocrystal

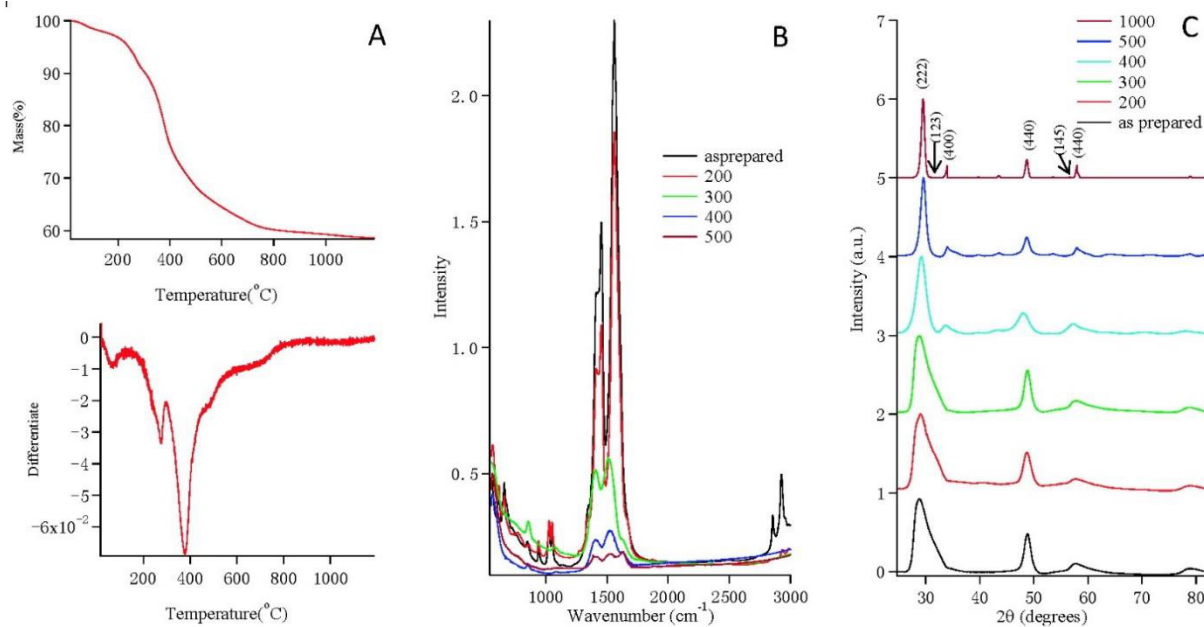


Figure 2.15: Thermal response for the Eu(2%):Y₂O₃ nanocrystal during thermolysis from 20 to 1000 °C: (A) thermogravimetric analysis (TGA) data and first differential of TGA experimental data; (B) temperature-dependent FT-IR spectra; (C) temperature-dependent pXRD spectra.

exhibits a Gaussian transition at 580.8 nm and a weak transition at 578.9 nm. The similarity in energy of the ⁷F₀ → ⁵D₀ parity forbidden transition for the bulk and nanocrystal samples is consistent with the assignment of the Eu(III) ion occupying a Y(III) C₂ symmetry site as a substitutional element in the Y₂O₃ cubic host lattice. The ⁷F₀ → ⁵D₀ transition at 580.8 nm in the nanocrystal sample is assigned to Eu(III) ions occupying a core substitutional site, while the ⁷F₀ → ⁵D₀ transition for Eu(III) at 578.8 nm arises from Eu(III) centers near or at the surface of the nanocrystals, as previously reported.¹¹²

2.3.5 Structural Evolution of Nanocrystals Following Thermal Treatment

In Figure 2.15A, thermogravimetric analysis (TGA) data are shown for the Eu:Y₂O₃ nanocrystal. The changes in the nanocrystal properties following thermal treatment and transformation into a bulk material can provide insight into the stability of the acac passivant layer in the Eu:Y₂O₃ nanocrystal. In the TGA data, a set of sharp transitions is observed at 160, 276, and 379 °C associated with mass losses of ~3, ~6, and ~24%, respectively. Above 379 °C, a continued mass loss of 40% is observed. The mass loss at 160 °C is assigned to solvent loss arising from water or toluene. The transition at 276 °C is assigned to the loss of HDA, as

evidenced by the loss of the -CH₂ and -CH₃ vibrational modes at ~3000 cm⁻¹ in the FT-IR spectra (Figure 2.15B). The transition at 376 °C is assigned to the onset of thermal decomposition of the acac passivating layer on the Eu:Y₂O₃ nanocrystal surface, as confirmed by partial loss of the acac FT-IR transitions at 659, 678, 1453, and 1560 cm⁻¹ (Figure 2.15B). Decomposition of acac with subsequent formation of metal oxides and loss of acetone and acetic acid has been observed in a similar temperature range in acac coordination complexes.³⁰ The mechanism for metal oxide formation in amine solvents has been reported.¹¹³

No structural transition or particle growth is observed in the pXRD following the loss of the HDA passivant at 276 °C (Figure 2.15C). A transformation in the pXRD is observed at the 376 °C transition following acac decomposition. The pXRD narrows, and the complete loss of the (123) and (145) diffraction peaks from the pXRD pattern is observed. The change in the pXRD pattern is consistent with nanocrystal growth by particle to particle fusion as the passivating layer decomposes to form a fresh metal oxide surface. Continued growth of Eu:Y₂O₃ is observed in the pXRD up to 1000 °C.

Confirming the TGA assignments, no change to the PLE and PL spectra are observed below 400 °C. Above 400 °C, the acac π → π * (270 nm) transition and acac CT band (370 nm) disappear in the PLE spectra (Figure 2.16) with a concomitant appearance of the 250 nm lattice CT band typical of bulk Eu:Y₂O₃. Above 400 °C, the reduction in relative intensity of the Eu(III) ⁷F₀ → ⁵D₄ and ⁷F₀ → ⁵L₆ transitions (labeled with an arrow in Figure 2.16A) is noted in the PLE spectra, which is believed to be due to the relative strengthening of the lattice CT band (O_{2p} → Eu_{4f}) as the nanocrystals grow in size. In Figure 2.16B, the PL spectra (λ_{ex} 270 nm) also exhibits a change above 400 °C, with loss of intensity of the Y₂O₃ defect PL, a narrowing of the J-O transitions, and a redistribution of the intensity in the ⁵D₀ → ⁷F₂ Stark-split transitions at 611, 619, and 625 nm. The loss of the defect intensity may reflect the loss of the acac CT transition or changes in Y₂O₃ defect densities in the growing bulk phosphor. The changes in the J-O level as the nanocrystals grow is believed to reflect changes in the core to surface Eu(III) composition with the sintering of the nanocrystal. Consistent with a sintering argument, the PL spectrum of Eu:Y₂O₃ sintered at 1000 °C is directly comparable to that of a bulk phosphor sample.¹⁶ The thermal treatment data indicates that the acac passivation layer is thermally stable below temperatures of 400 °C, which is within the thermal operating range of commercial LED lighting (below 150 °C).

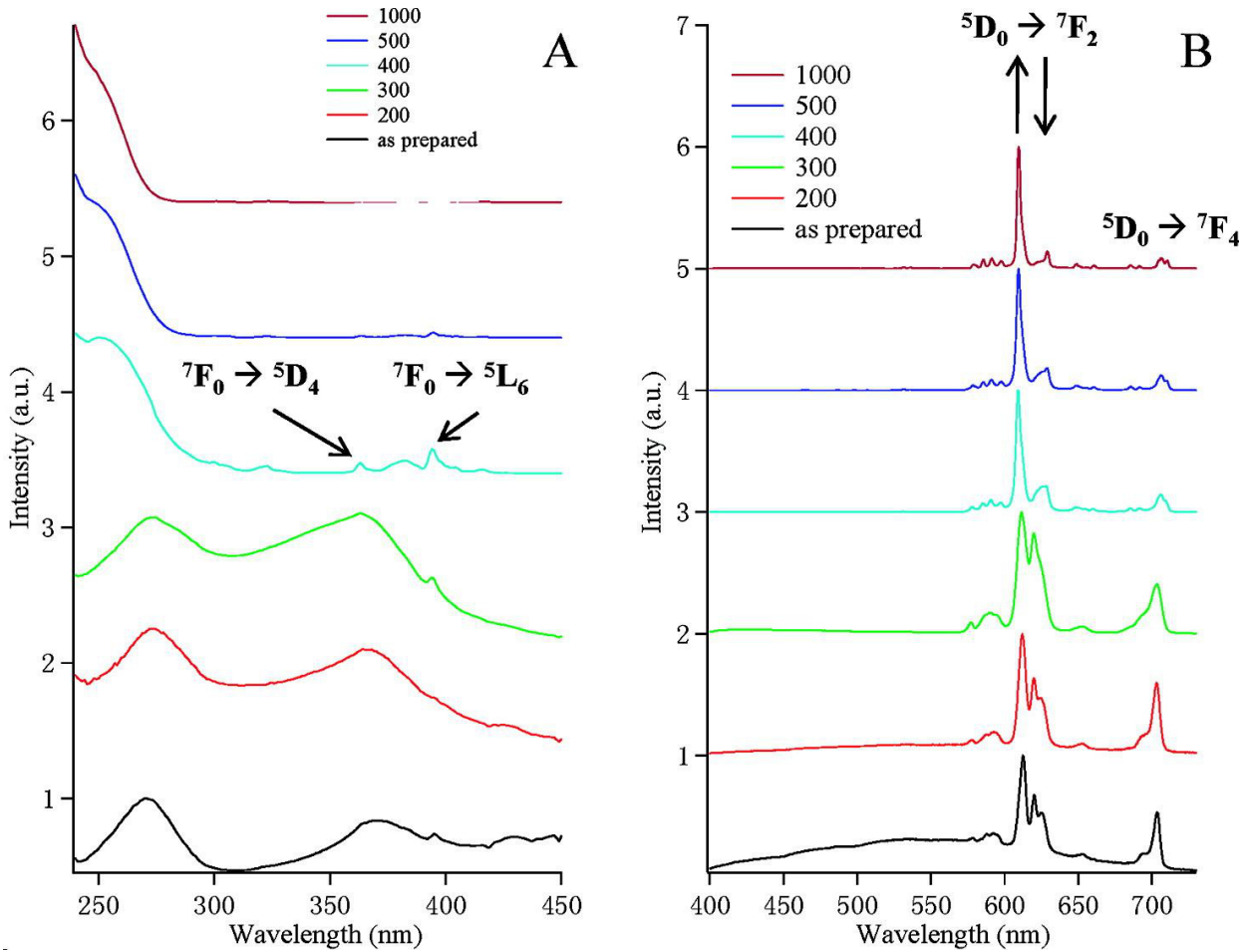


Figure 2.16: Temperature-dependent changes in the optical properties of Eu (2%):Y₂O₃ nanocrystals during thermolysis from 20 to 1000 °C: (A) solid-state photoluminescence excitation spectra monitored at λ_{em} 611 nm; (B) solid-state photoluminescence spectra, λ_{ex} 270 nm.

2.3.6 Application of acac-Eu:Y₂O₃ as a Solid-State Phosphor

Eu:Y₂O₃ is a classic downconversion red phosphor used in lighting and display technologies that can be pumped with UV excitation ($\lambda_{\text{em}}(\text{Hg line})$ 254 nm) into the higher lying O_{2p} to Y_{4d-5s} excitonic level or the Eu(III) CT levels. Nonradiative energy transfer to populate the low-lying Eu(II) J-O levels produce the characteristic red photoluminescence. The lack of electronic transitions with strong optical cross sections for Eu:Y₂O₃ with UV LEDs that exhibit a pump range between 350 and 370 nm limits the use of Eu:Y₂O₃ phosphors in new solid-state

lighting devices. The acac passivation layer on the Eu:Y₂O₃ nanocrystal can overcome this limitation, due to the presence of low-lying LMCT states and the acac $\pi \rightarrow \pi^*$ states that exhibit high optical cross sections in the UV spectral region.

The experimental optical data indicate the highest solid-state quantum efficiency for white light generation is for the Eu (9%): Y₂O₃ nanocrystal pumped at 370 nm with a measured ϕ_{em} value of 18.7%. In comparison to the reported quantum efficiency for nanocrystalline samples of Eu:Y₂O₃ prepared by an alkalide reduction method,¹¹⁴ the highest obtained solid-state quantum yield was $\phi_{em} = 8\%$ pumped at 230 nm, which drops to 2% pumped at 270 nm, and 0% pumped at 370 nm. Although the measured quantum efficiency for the acac-Eu (9%):Y₂O₃ in this study is not at the level of that for the commercial Eu:Y₂O₃ phosphor (90% pumped at 250 nm), the ability to excite the phosphor in the UV (370 nm) and the broad-band white light make the nanophosphor advantageous over the single-color red bulk phosphor when packaged with a UV LED.

In order to generate the quality of the LED phosphor package, a 370 nm LED was coated with the phosphor embedded in cyanoacrylamide and attached to the surface of a declad commercial UV-LED (365/370 nm, 1W), as shown in Figure 2.17B. Measurement of the red/orange (R/O) ratio, the CIE coordinates (Commission Internationale de l'éclairage), the color coordinated temperature (CCT), the S/P (scotopic-to-photopic) ratio, and the luminous efficiency of the device was carried out.⁹² Of these, the S/P ratio and luminous efficiency are important for low-light applications. The R/O is phosphor dependent, while the CIE, S/P, and luminosity are device dependent.

The red/orange (R/O) ratio is a critical phosphor quality control value for the Eu(III)-based phosphors and is calculated by comparing the intensity of the $^5D_0 \rightarrow ^7F_2$ to the $^5D_0 \rightarrow ^7F_1$ J-O transition. The 9% Eu:Y₂O₃ nanocrystal pumped at 370 or 270 nm has an R/O ratio of 10.1 (0.1. In comparison, the R/O ratio for bulk Eu:Y₂O₃ is 6.2, while reported values for non-acac-passivated nanocrystal Eu:Y₂O₃ have reported values ranging from 7 to 9 when pumped at 250 nm.⁸⁰

Figure 2.17 shows the CIE index points for the Eu:Y₂O₃ compositions prepared in the study, along with a photograph of a white light LED formed using the Eu (9%):Y₂O₃ nanocrystal sample (sample C). The CIE coordinates and CCT values for the acac-Eu:Y₂O₃ at 0% (A) is (0.27, 0.32) at 8245 K; 2% (B) is (0.32, 0.36) at 6162 K; 9% (C) is (0.33, 0.35) at 5418 K; 11%

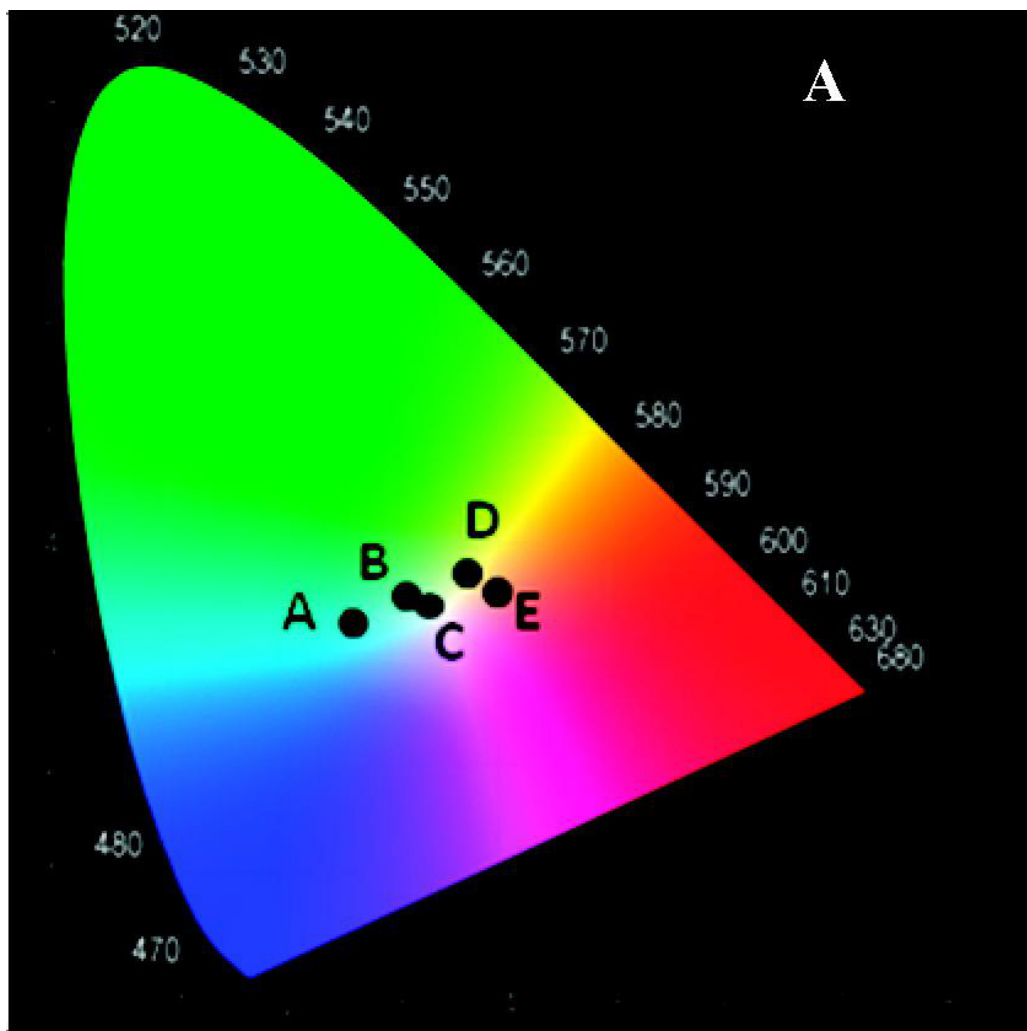


Figure 2.17: (A) CIE coordinates for Eu:Y₂O₃ doped at (A) 0%, (B) 2%, (C) 9%, (D) 11%, and (E) 18% plotted on the CIE1930 chromaticity chart. (B) Images of a LED phosphor assembled from deposition of Eu (9%):Y₂O₃ onto a 370 nm LED operating at 3.0 V.

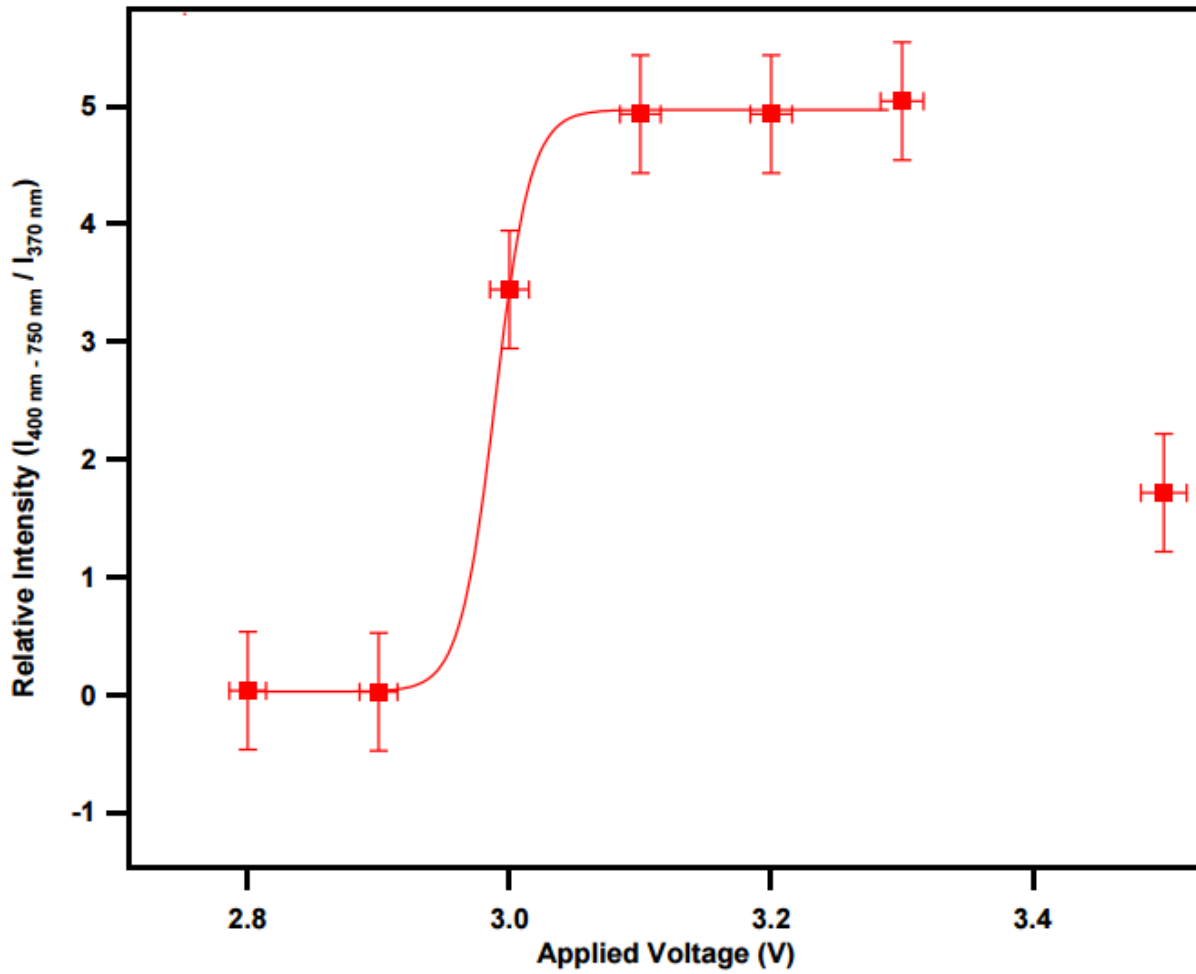


Figure 2.18: Plot of the relative intensity of the white light phosphor versus the applied voltage to the 370 nm LED. The relative intensity is calculated by normalizing the spectra from 400 – 750 nm by the intensity of the LED PL at 370 nm.

(D) is (0.38, 0.38) at 3947 K, and 18% (E) is (0.40, 0.36) at 3364 K. As a comparison, incandescent bulbs have a CCT of 2800 K, cool white fluorescent bulbs have a CCT of 6000 K, and daylight is 4500 K.

The S/P ratio is a measure of the perception of white light by the human eye in a dark environment based upon the rod/cone ratio in the human eye. A low value for the S/P ratio is a leading reason for eye fatigue in solid-state lighting.⁹⁹ The S/P ratio for the acac-Eu:Y₂O₃ samples are 2.73 Eu (0%), 2.10 Eu (2%), 2.20 Eu (9%), 1.83 Eu (11%), and 1.77 Eu (18%). The

S/P ratio for the Eu(III):Y₂O₃ phosphors compares favorably with the S/P ratio for a compact fluorescent light bulb of 2.14.

On the basis of the quantum efficiency, CIE, CCT, and S/P ratio the 9% Eu(III):Y₂O₃ sample produces the highest quality white light and may represent an optimal single-component phosphor for lighting applications using the 370 nm commercial UV-LED. For the phosphor-LED package to be commercially viable, a luminous efficiency of 100 lm W⁻¹ must be achieved. The luminous efficiency (η_L) or luminosity is defined as the amount of light produced for a given device and can be calculated from the luminous flux (ϕ_v) and LED output power (ϕ_e), where $\eta_L = \phi_v/(V_f I_f)$. V_f and I_f are the LED operating voltage and current, respectively, while $\phi_v = \eta_{\text{phosphor}} \phi_e$ (η_{phosphor} is the wavelength conversion efficiency of the phosphor).⁷⁴ Measurement of the luminosity of the LED device resulted in a value of 100 lm W⁻¹ for the 370 nm LED operating at 3.3 V. The white light LED luminosity drops to ~80 lm W⁻¹ at 3.0 V and below 20 lm W⁻¹ at an operating voltage below 3.0 V. A plot of the relative intensity of the white light produced by the device versus applied voltage is plotted in Figure 2.18, where the relative intensity is the intensity of the phosphor between 400 and 750 nm collected by an integrating sphere relative to the LED intensity at 370 nm.

2.4 Conclusion

The optical properties of the isolated acac-passivated Eu:Y₂O₃ nanocrystals indicate the samples are ideal phosphors for application as a single-component white light phosphor pumped by a commercial UV-LED. It is clear that the presence of the acac passivation layer on the Eu:Y₂O₃ nanocrystal surface strongly enhances the optical performance of these white light nanophosphors for applications in UV LED pumped solid-state lighting. The phosphor performance outperforms the compact fluorescent light bulb S/P ratio, CIE index, and CCT values. The strong performance reflects the presence of strong acac $\pi \rightarrow \pi^*$ (270 nm) and O_{acac} \rightarrow Y(III) CT (370 nm) transitions arising from the presence of the acac on the nanocrystal surface. The low-energy CT band is not present in bulk Eu:Y₂O₃ phosphors. The observed highly efficient downconversion from the acac CT band to defect levels and the Eu(III) guest ion energy levels suggests that tailoring the design of the metal acac passivation layer could lead to more efficient white light conversion. Such experiments are currently underway.

The chapter has developed a novel approach to synthesis and phosphor design. While the use of metal acetylacetonate precursors for the preparation of metal oxide nanocrystals and thin films is not novel,^{101, 115} the observation of the formation of an acac passivation layer that efficiently transfers energy via a molecular antenna from the ligand passivation shell to the Eu(III) J-O levels in Eu:Y₂O₃ and the Y defect levels to produce white light with good color rendition has not been reported. The Eu:Y₂O₃ nanocrystals prepared in a microwave reactor by thermal decomposition of the metal acetylacetonate (M(acac)₃) salts in a nonhydrolytic, actively passivating solvent allows rapid preparation (15 min) and isolation of the Eu:Y₂O₃ nanocrystal. The size of the isolated phosphor nanocrystal is not observed to be influenced by reaction concentrations in the MW. It is believed the rapid formation of the nanocrystals reflects the use of MW dielectric heating of the lanthanide coordination compound in a non-MW-absorbing HDA solvent. The rate of reaction in the MW is far faster than in the traditional hydrothermal methods, which require 12 h⁷⁸ or hot injection methods, where reaction times of 1 h have been reported.⁸⁰ Confirmation of the surface passivation by acac was provided by optical absorption, PLE, ¹³C{¹H} CPMAS NMR, and FT-IR analysis.

CHAPTER 3

MICROWAVE SYNTHESIS AND LIGAND MODIFICATION OF OXIDE AND SULFIDE NANOSPINELS

Ternary materials can form as a solid solution with random site occupation or as a line phase where each component occupies a specific crystallographic site. When a ternary phase is grown at the nanoscale, the reaction space for forming a line phase is more complex, as a competition between forming the energetically favorable critical nucleus of the binary phases becomes more favorable leading to the likelihood of forming a solid solution at small sizes. A classical line phase ternary is the AB_2X_4 spinel family, which is easily formed in bulk within a narrow A;B ratio, but has been less explored at the nanoscale when grown by lyothermal routes at or near the critical nuclei size. An efficient synthetic approach to formation of line phase ternary spinel nanocrystals below 4nm is demonstrated by utilizing microwave enhanced thermal decomposition of molecular precursors to allow isolation of a set of high value spinel and thiospinel quantum dots, including ZnB_2O_4 (B = Al or Ga), MgB_2O_4 (B = Al or Ga), and ZnGa_2S_4 to be demonstrated. In the study, the ability to isolate the line phase near the critical size is demonstrated, as well as the ability to selectively ligand exchange the nanospinels to open the potential applications to a wider field.

3.1 Introduction

There is no doubt that ternary materials, which can form as a solid solution or as a line phase, are a class of infinitely tunable materials that are used broadly as optical materials, phosphors, catalysts, triboluminescent materials, or in magnetic applications.^{9, 45, 116-118} A particular class of ternary materials that exhibit line phase behavior and have wide applicability to problems in materials chemistry are the ternary spinel family, AB_2X_4 , which include the oxide and thio spinels. Spinels are very robust, possessing a high degree of thermo-chemical, mechanical, and radiation stability.¹¹⁹ While the synthesis of solid solution ternary materials is described in the literature, the synthesis of ternary line phase nanocrystals is less straightforward.^{120, 121} For nanospinels, only a very few lyothermal routes for the oxides have been reported,^{59, 122} while the thiospinels have not been reported. To date, the spinels have been

made at the nanoscale using solid-state salt reactions, combustion, sol-gel, citrate reduction, and hydrothermal methods,^{9, 10, 45, 120, 123, 124} but many require calcining to achieve the desired phase purity resulting in formation of large (> 100 nm) materials.^{57, 117, 118, 123, 125}

In this chapter, we report a generalizable synthetic methodology that allows formation of ZnAl₂O₄, ZnGa₂O₄, ZnGa₂S₄, MgAl₂O₄, and MgGa₂O₄ nanocrystals in the 2.5–4.5 nm range from simple molecular precursors based on microwave initiated thermal decomposition of acetylacetone (acac) for oxide spinels or dithiocarbamate (dtc) for thiospinels. Investigation of the reaction parameter space for isolation of the pure phases of ZnAl₂O₄ and ZnGa₂O₄ allow a general route to the spinel family to be demonstrated. Mapping of the phase diagram for the solution growth of ZnGa₂O₄ and ZnAl₂O₄ nanospinels shows the reactivity of the M²⁺ vs. M³⁺ ion significantly influences the ability to isolate a pure nanocrystal, consistent with expectations from the bulk phase diagram. In analogy to polymer synthesis, the root of the complexity for ternary nanospinel isolation in the line phase lies in the differences in precursor reaction rates, addition rates to the growing nanocrystal facets for select ions, which may or not be favored,³⁹ and the individual bond strength for the passivating organic layer to facilitate homogenous nucleation. The preparation of a pure line phase for nanocrystals is complicated by nucleation theory and Ostwald's rule of stages.^{29, 49, 126}

To achieve the line phase the synthetic reactions are carried out in a single mode microwave reactor in oleylamine in order to rapidly induce thermal decomposition of the acac (oxide) or dithiocarbamate (sulfide) in a single reaction vessel without the need for hot injection or post reaction treatment to isolate the desired phase. The isolated nanocrystals are passivated by acac and/or oleylamine (OA), depending on the starting materials, but can be routinely ligand exchanged using NOBF₄ to provide materials with a desired passivating group at the surface for further material applications. The methods are scalable, batch to batch reproducible, can be converted to a MW flow reactor⁴⁸ and utilize low-cost precursors that allow isolation of the targeted ternary phase materials by a sustainable approach via a non-complex reaction methodology. It is believed that the approach will allow isolation of a wider range of desired nanomaterials from the known congruent line phase spinels available.

3.2 Experimental Section

3.2.1 Materials

All commercially available reagents and solvents including 2.thenoyltrifluoroacetone (Matrix Scientific, 99%), zinc (II) undecylenate (Spectrum, 98%), zinc diethyldithiocarbamate (Alfa Aesar, 17-19.5% zinc), aluminum (III) 2,4.pentanedionate (Strem Chemicals, 99%), aluminum (III) chloride (Strem Chemicals, 99.99%, anhydrous), gallium (III) 2,4.pentanedionate (Aldrich, 99.99%), gallium (III) chloride (Strem Chemicals, 99.99%, anhydrous), magnesium (II) chloride hexahydrate (J.T. Baker, A.C.S. Reagent, 99%), sodium myristate (Spectrum Chemical, 99%), oleylamine (Aldrich, 70%), NOBF_4 (Alfa Aesar, 98%) were used without further purification. DMF was dried over molecular sieves.

3.2.2 Synthesis of ZnB_2O_4 ($\text{B} = \text{Al}^{3+}$ or Ga^{3+})

ZnB_2O_4 nanospinels passivated by a mixture of acac and oleylamine were prepared by microwave induced decomposition of zinc (II) undecylenate and the appropriate metal (III) acetylacetone complex in oleylamine as the solvent. The ZnGa_2O_4 nanocrystal can also be isolated from gallium chloride resulting in oleylamine passivated nanocrystals.

The thermal decomposition is carried out in a CEM Discover Microwave (MW) operating under single mode, continuous power (300W) at 2.45 GHz. The CEM MW cavity was commercially modified with a Teflon insert to allow sustainable heating at 300°C.

To synthesize the ZnAl_2O_4 , zinc (II) undecylenate (0.108 g, 0.25 mmol), aluminum (III) 2,4.pentanedionate (0.1622 g, 0.5mmol), and oleylamine (OA, 4mL) were sealed in a Pyrex reactor vessel (10 mL) under N_2 . The reactants were sonicated until the solid dissolved (~ 30 min) and heated in the MW at 300W to 280°C for 10 min. The ZnGa_2O_4 nanospinels was synthesized in the same fashion, by substituting gallium (III) 2,4.pentanedionate (0.1835 g, 0.5mmol) as the Ga source.

To isolate the nanospinels, the solution was cooled to 50°C, precipitated by addition of MeOH (~5 mL), isolated by centrifugation, and the supernatant discarded. The process was repeated four times using toluene/EtOH, and the centrifuged pellet dried under vacuum overnight. The isolated sample is white in color and can be redispersed in toluene or chloroform.

3.2.3 Synthesis of MgB₂O₄ (B = Al or Ga)

These materials are prepared analogously to the ZnB₂O₄ analogues using magnesium myristate as the molecular precursor. Magnesium myristate is prepared by adding 20mL of a 0.25 M methanolic solution of MgCl₂·6H₂O dropwise to 2.5 g (10 mmol, 0.05 M) solution of sodium myristate in 200 mL of methanol producing a white precipitate that is collected by vacuum filtration. The precipitate is washed with MeOH four times, and vacuum dried.

The formation of MgAl₂O₄ is accomplished by adding magnesium myristate (0.120 g, 0.25 mmol), aluminum (III) 2,4.pentanedionate (0.1622 g, 0.5mmol), and oleylamine (OA, 4 mL) into a sealed 10mL pyrex microwave reactor vessel under N₂. The reactants were sonicated until the solid dissolved (30 min), inserted into the MW reactor, and heated to 280°C for 10 min at 300 W. The solution was cooled to 50°C, the MgAl₂O₄ nanocrystals precipitated by addition of MeOH (~5 mL), and isolated by centrifugation. The process was repeated four times using toluene/EtOH, and the centrifuged pellet dried under vacuum overnight. The isolated sample is white in color and can be redispersed in toluene or chloroform.

The MgGa₂O₄ nanocrystals was synthesized and isolated in the same fashion, by substituting gallium (III) 2,4.pentanedionate (0.1835 g, 0.5mmol) as the Ga source. The MgGa₂O₄ nanocrystal can also be isolated from gallium chloride resulting in oleylamine passivated nanocrystals. The isolated sample is white in color and can be redispersed in toluene or chloroform.

3.2.4 Synthesis of ZnGa₂S₄

Oleylamine passivated ZnGa₂S₄ was synthesized using a 10 mL pyrex microwave reactor vessel loaded with zinc diethyldithiocarbamate (0.0905 g, 0.25 mmol), gallium (III) chloride (0.088 g, 0.5 mmol), and oleylamine (OA, 4mL). The MW vessel was sealed, and the reactants were stirred until the solid dissolved (~ 30 min). The MW vessel was inserted into the MW cavity and heated to 280°C at 300 W for 10 min. The solution was cooled to 50°C and the ZnGa₂S₄ nanocrystals precipitated by addition of MeOH (~5 mL). The product was isolated by centrifugation, washed four times using toluene/EtOH and dried under vacuum overnight. The isolated sample is white in color and can be dispersed in toluene or chloroform, though less soluble than the oxide nanospins.

3.2.5 Ligand Exchange

Surface exchange of the oleylamine (OA) and/or the mixed oleylamine - acac passivating layer by 2.thenoyltrifluoroacetone (tta) is accomplished by treatment of NOBF_4 in dry DMF followed by exchange. The exchange process is accomplished by treatment of 25 mg of the OA (or OA/acac) passivated nanospinel dispersed in 5 mL hexanes with 5 mL of 0.01 M NOBF_4 in anhydrous DMF under N_2 . The dispersion is allowed to react for 5 min, and the precipitate is collected by centrifugation and washed with acetone (2x). The resultant precipitate is added to 1 ml of anhydrous DMF, 2 mL toluene, and 50 mg of the coordinating ligand (tta) at 60°C under N_2 and stirred until the solution is clear (~ 30 min). The ligand passivated nanospinels are isolated from solution by addition of acetone to induce aggregation of the nanocrystals and collection by centrifugation.

3.2.6 Measurements

Powder X-ray diffraction (pXRD) was recorded on a Rigaku DMAX 300 Ultima III Powder X-ray diffractometer (using $\text{Cu K}\alpha \lambda = 1.5418 \text{ \AA}$ radiation). The pXRD was pattern matched using JADE and the nanospinel size fit using the Scherrer broadening expression. The size was evaluated for the nano oxide spinels by inspection of the (311) and (400) reflection, while the (112) reflection was used for the nano thiospinel.

Transmission electron microscopy measurements for ZnAl_2O_4 , ZnGa_2O_4 , and ZnGa_2S_4 were carried on a Tecnai Osiris operating at 200 kV using either carbon type A (300 mesh) with removable Formvar on Cu grids or ultrathin carbon on copper grids (400 mesh). Energy dispersive x-ray spectroscopy TEM (EDS-TEM) was performed on the Tecnai Osiris for all spinel types and was analyzed using instrumental software. TEM images for MgAl_2O_4 and MgGa_2O_4 were conducted on a JEOL JEM-ARM200cF operating at 200 kV. Image analysis of >100 nanocrystals were used to generate the size distribution curves. Ligand passivation was analyzed by FT-IR and ^1H NMR. FT-IR measurements were measured on powdered samples using a PerkinElmer Spectrum 100 FT-IR Spectrometer equipped with an attenuated total reflectance (ATR) sample chamber consisting of a ZnSe crystal over coated with diamond using a single-bounce configuration. Solution ^1H NMR spectra were recorded in CD_3CN on a Bruker 600 MHz spectrometer ($B_0 = 14.1 \text{ T}$) operating at a frequency of 600.0 MHz and referenced to TMSCl. UV-Vis absorption measurements were recorded on a Varian Cary 50

UV-vis spectrophotometer. Photoluminescence and photoluminescence excitation measurements were recorded on a Varian Cary Eclipse fluorescence spectrophotometer. Absorption, photoluminescence, and photoluminescence excitation spectra were carried out in optical grade acetonitrile for oleylamine passivated spinels, while tta-spinels were dissolved in toluene.

3.3 Results

3.3.1 Synthesis of AB_2O_4 and ZnGa_2S_4 ($\text{A} = \text{Mg or Zn}$; $\text{B} = \text{Al or Ga}$)

Solvent induced thermal decomposition of a metal precursor carried out in a MW reactor leads to the formation of the ternary line phase of ZnAl_2O_4 , ZnGa_2O_4 , MgAl_2O_4 , MgGa_2O_4 and ZnGa_2S_4 as spherical nanospinels when carried out in a 1 : 2 A:B mole ratio of the cations.

The proposed mechanism for formation of AB_2O_4 ($\text{A} = \text{Mg, Zn}$; $\text{B} = \text{Al, Ga}$) nanospinels proceeds via thermal decomposition in oleylamine of the divalent A^{2+} ion coordination complex (Zn undecylenate or Mg myristate) in the presence of the trivalent (B^{3+}) acac or metal chloride salts at a 1:2 mole ratio of A to B, is shown in Figure 3.1A.^{127, 128} Pinna, et. al¹²⁸ and Damm, et. al¹²⁷ proposed that initial nuclei formation occurs through insertion of oleylamine via SN_2 attack of the C_2 carbon ($\text{C}-\text{O}$) of the acac ligand when coordinated to the metal ion. Subsequent elimination of an amide and reaction with the metal chloride salt leads to critical nuclei formation. Subsequent reaction and elimination forms the critical nuclei and growth is then governed by Ostwald mechanisms in accordance with nucleation theory. In the microwave, nucleation followed by rapid depletion of the monomers leads to near critical nanomaterial isolation.

In analogy to the oxide spinel, as shown in Figure 3.1B, the ZnGa_2S_4 thiospinel is formed by thermal decomposition of diethyldithiocarbamate initiated by oleylamine SN_2 attack on the Zn precursor that results in H_2S elimination and formation of the metal sulfide bond, leading to critical nuclei formation of the nano thiospinel. The proposed decomposition pathway is derived from the results of Jung, et. al,¹²⁹ where ZnS nanocrystals were isolated from thermal decomposition of zinc dimethyldithiocarbamate in the presence of octylamine.

The pXRD patterns for the isolated AB_2X_4 samples are shown in Figure 3.2. Experimental pXRD data for the metal chloride grown samples of the oxide spinels is shown in

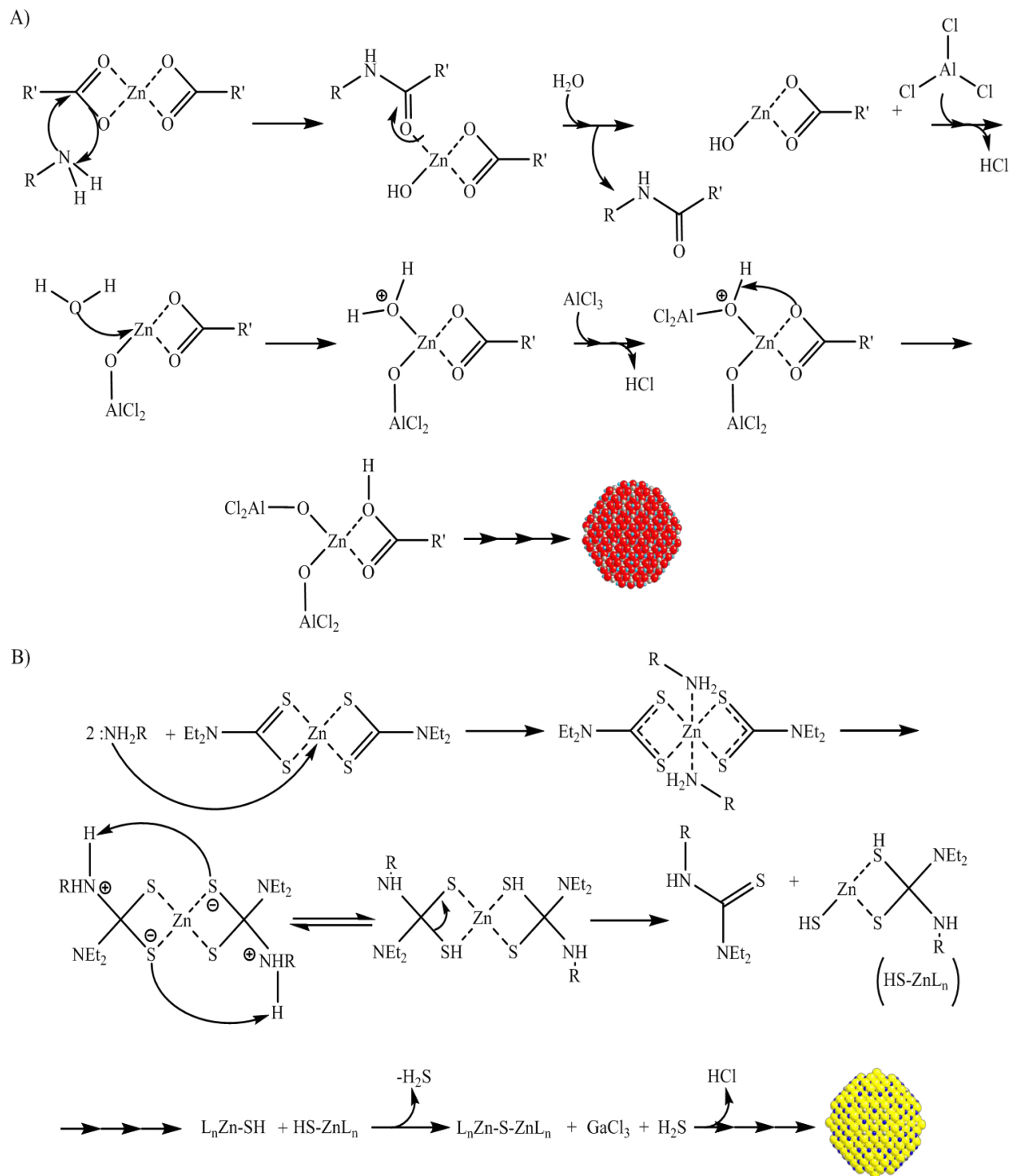


Figure 3.1: Proposed decomposition mechanism for formation of the AB_2X_4 nanospinels from solvent induced thermal de-composition of molecular precursors for A) ZnAl_2O_4 from $\text{Zn}(\text{UND})_2$ and AlCl_3 and B) ZnGa_2S_4 from ZDC and GaCl_3 . The proposed mechanism is believed to be applicable to the analogous AB_2O_4 and AB_2S_4 spinel families.

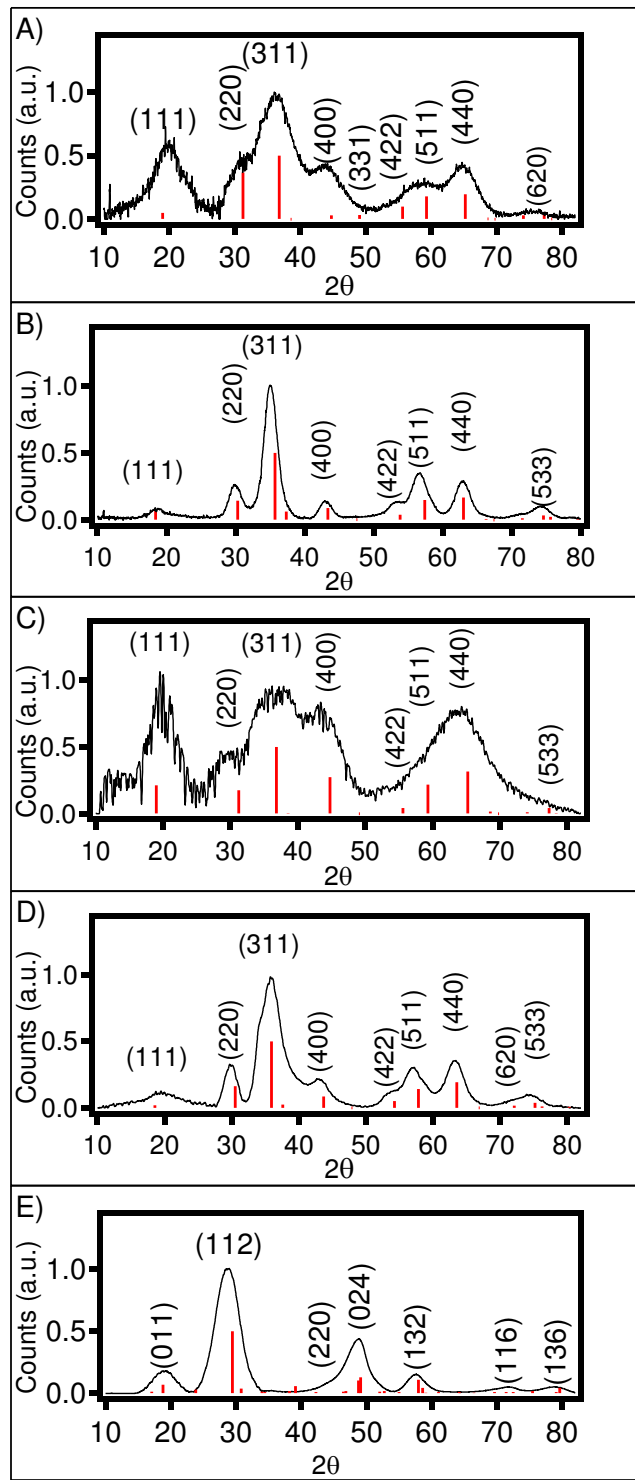


Figure 3.2: pXRD spectra of (A) ZnAl₂O₄ (JCPDS 82-1043), (B) ZnGa₂O₄ (JCPDS 86-0415), (C) MgAl₂O₄ (JCPDS 82-2424), (D) MgGa₂O₄ (JCPDS 89-3082), and (E) ZnGa₂S₄ (JCPDS 40-1462).

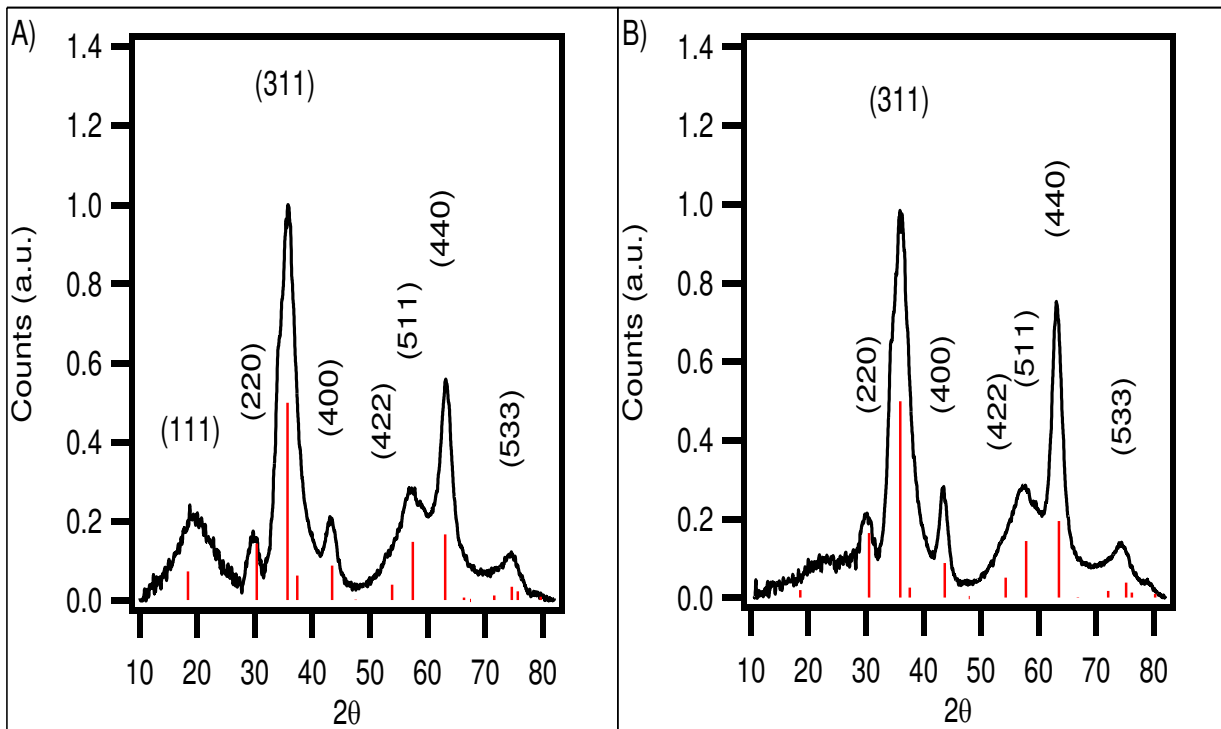


Figure 3.3: pXRD spectra A) ZnGa_2O_4 and B) MgGa_2O_4 made using MCl_3 and Zn(UND)_2 .

Figure 3.3. High resolution TEM images along are shown in Figure 4 and 5, with the low resolution images shown in Figure 3.6. It is important to note that the low contrast for oxides makes image analysis difficult. In Figure 3.2A,B, the pXRD patterns for ZnAl_2O_4 and ZnGa_2O_4 are indexed to the normal spinel with the space group Fd-3m (JCPDS card 82.1043 for ZnAl_2O_4 and JCPDS card 86-0415 for ZnGa_2O_4), while in Figure 3.2C,D, the MgAl_2O_4 , and MgGa_2O_4 are indexed to the spinel with Fd-3m (JCPDS card 82.2424, JCDPS card 89-3082, and JCPDS card 89-3083). Fitting of the pXRD data in Figure 3.2 to the Scherer broadening equation yields sizes of 2.95 nm for ZnAl_2O_4 , 4.3 nm ZnGa_2O_4 for the metal acac precursor; and 2.3 nm for MgAl_2O_4 and 3.6 nm for MgGa_2O_4 . A size of 2.9 nm for ZnGa_2O_4 and 2.8 nm for MgGa_2O_4 is extracted from the pXRD for nanospinels samples prepared from the metal chloride precursor.

Although the nanospinels are low z-number, the low resolution and high resolution TEM images for the ZnAl_2O_4 , ZnGa_2O_4 , MgGa_2O_4 , and ZnGa_2S_4 allow size, size distribution, and lattice fringe analysis. Analysis of the TEM images for AB_2O_4 (Figure 3.4A-E) indicate the as-prepared nanospinels are spherical, are highly crystalline, and exhibit lattice fringes which can be indexed to the appropriate spinel structure. The size distribution for the ZnAl_2O_4 was determined

to be 3.2 ± 0.4 nm, ZnGa_2O_4 was found to be 4.2 ± 0.6 nm, 3.2 ± 0.3 nm for ZnGa_2S_4 , and 3.6 ± 0.4 MgGa_2O_4 . The size of the MgAl_2O_4 can only be estimated to be 2.6 nm since the TEM imaging of the MgAl_2O_4 does not allow accurate distribution analysis.

High resolution TEM images allow lattice fringe analysis confirming the pXRD data interpretation. ZnAl_2O_4 exhibits a lattice spacing of $d = 0.285$ nm assignable to the (220) facet (Figure 3.4A), ZnGa_2O_4 exhibits a lattice spacing of $d = 0.48$ nm assignable to the (111) facet (Figure 3.4B), MgAl_2O_4 exhibits a lattice spacing of $d = 0.292$ nm assignable to the (220) facet (Figure 3.4C) MgGa_2O_4 exhibits a lattice spacing of $d = 0.169$ nm assignable to the (422) facet (Figure 3.4D), and ZnGa_2S_4 with a lattice spacing of 0.30 nm assignable to the (112) facet (Figure 3.4E).

In Figures 3.2 and 3.4, ZnGa_2S_4 is observed to crystallize as spherical nanocrystals in the hexagonal phase for the normal spinel (JCPDS Card 40-1462). The pXRD pattern (Figure 3.1F) can be assigned to the appropriate JCPDS card indicating the single line phase is isolated in the reaction without a post thermal annealing step required to form the desired line phase. No evidence of contamination by the binary phases is observed in the pXRD data. A size of 3.0 nm for ZnGa_2S_4 is extracted from the pXRD, which corresponds to the TEM size of 3.1 ± 0.3 nm in Figure 3.4F. The high resolution TEM confirms the structure assignment for ZnGa_2S_4 with a lattice spacing of 0.30 nm assignable to the (112) facet.

TEM-EDS analysis of the cation ratio for the AB_2X_4 nanospinels is tabulated in Table 1. ICP-MS data, which is accurate to the ppb level, was measured for the ZnAl_2O_4 and ZnGa_2O_4 to validate the EDS data. The A:B mole for ZnAl_2O_4 , ZnGa_2O_4 , and MgAl_2O_4 are in experimental agreement with the theoretical cation ratios of $\sim 1:2$. The MgGa_2O_4 is Ga^{3+} rich, which may indicate Ga surface termination or partial contamination from Ga_2O_3 although the contamination is not observed on the pXRD. ZnGa_2S_4 is observed to be Zn rich, which in analogy to MgGa_2O_4 may imply a Zn surface termination, Ga vacancies, or phase contamination. The pXRD does not support significant phase contamination by the binary phases and therefore is unlikely the cause of the ratio. A recent paper by Khalifah, offers an alternative possibility where at non-stoichiometric ratios of Zn:Ga the formation of ZnGa_2O_4 is observed as intercalation layers within the binary phase crystal lattice.⁵² Similar spinel intercalations into a wurtzite CdSe and ZnSe quantum dot lattice has been reported when M^{3+} ions are doped into the QDs.¹³⁰ The data

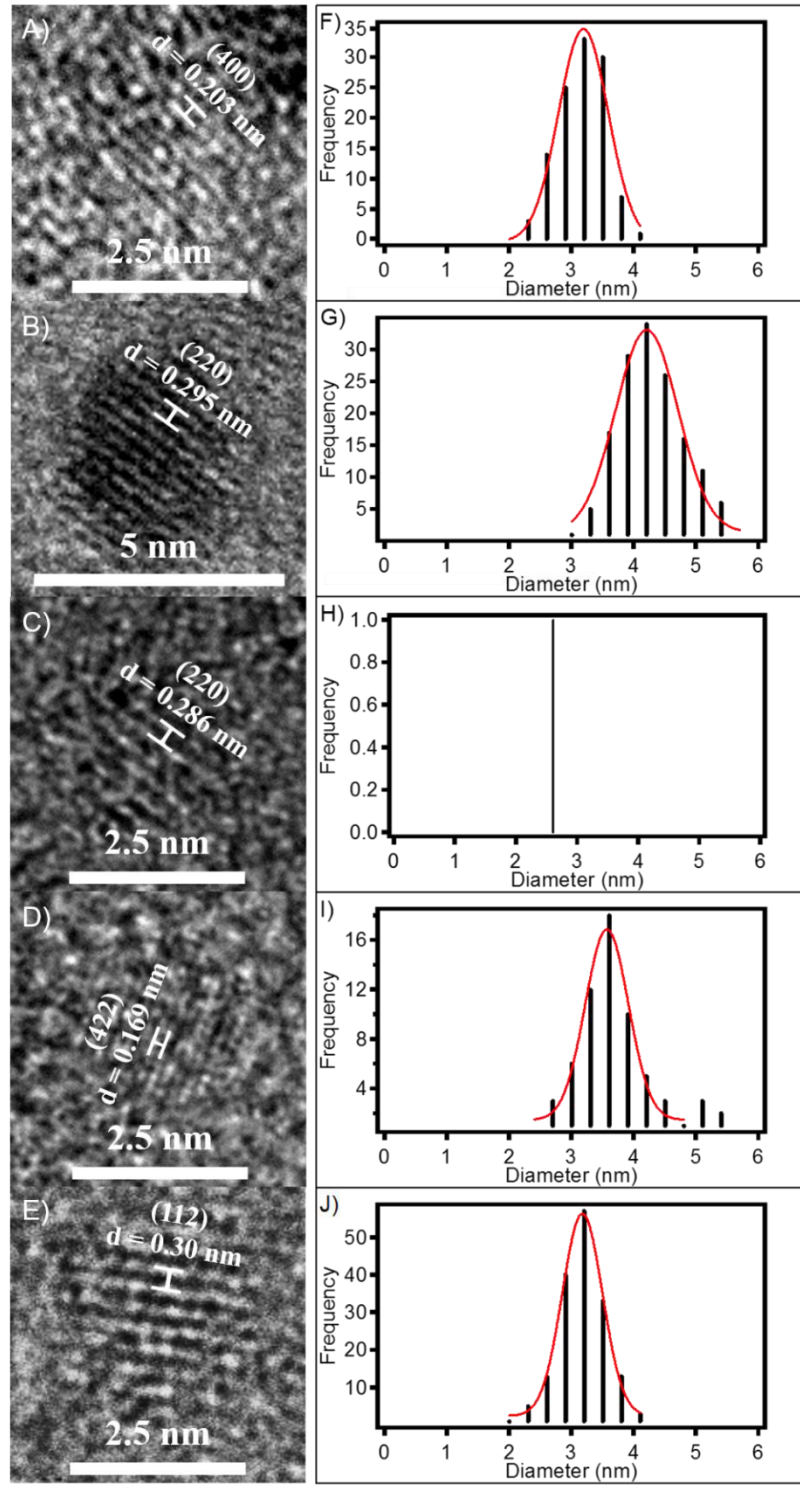


Figure 3.4: Transmission electron microscopy images with indexing of the major facet and size dispersity of A) ZnAl₂O₄, B) ZnGa₂O₄, C) MgAl₂O₄, D) MgGa₂O₄, and E) ZnGa₂S₄. A complete size dispersity graph is not shown for MgAl₂O₄ due to the low TEM cross-section for the sample.

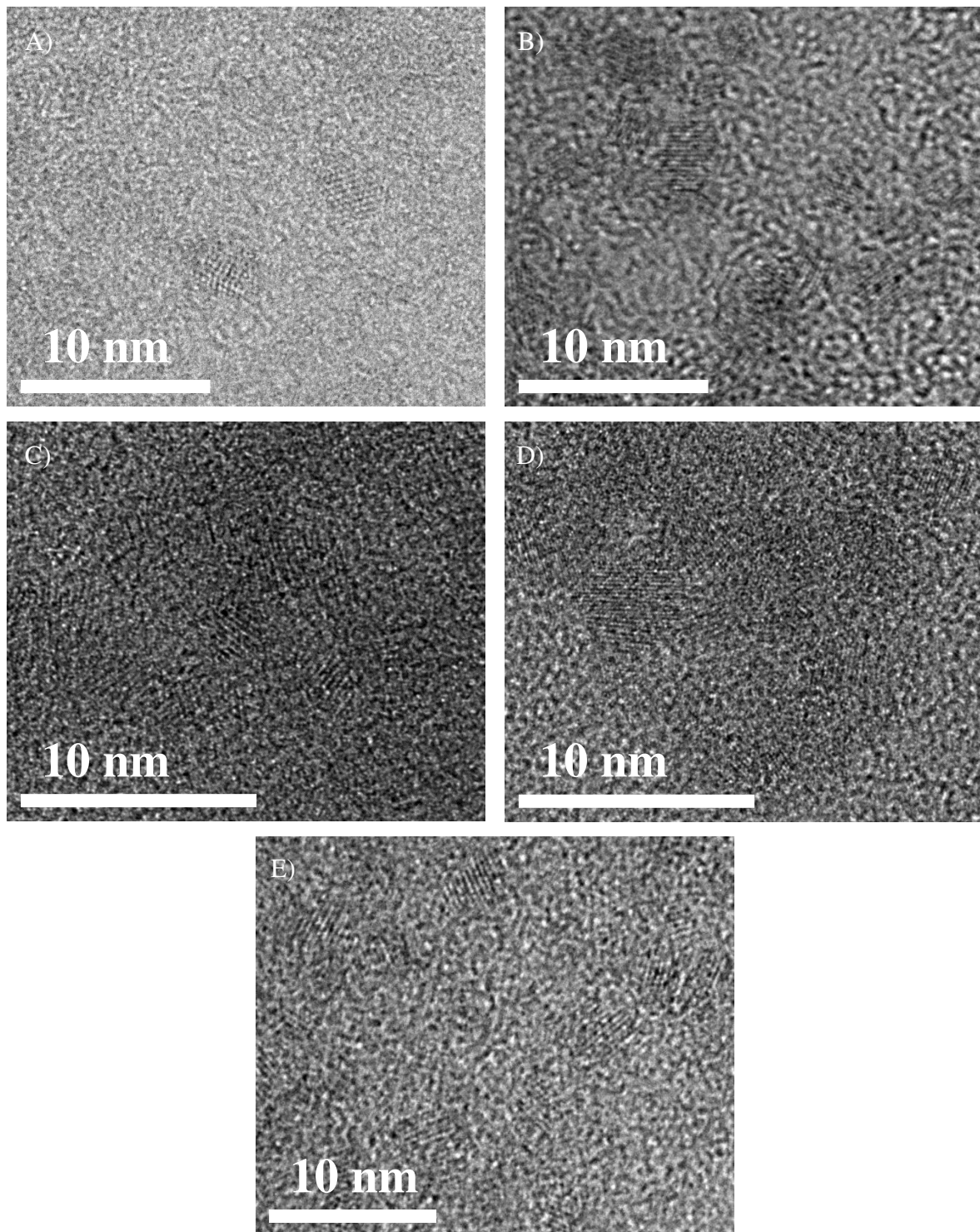


Figure 3.5: High resolution TEM image of A) ZnAl_2O_4 , B) ZnGa_2O_4 , C) MgAl_2O_4 , D) MgGa_2O_4 , and E) ZnGa_2S_4 .

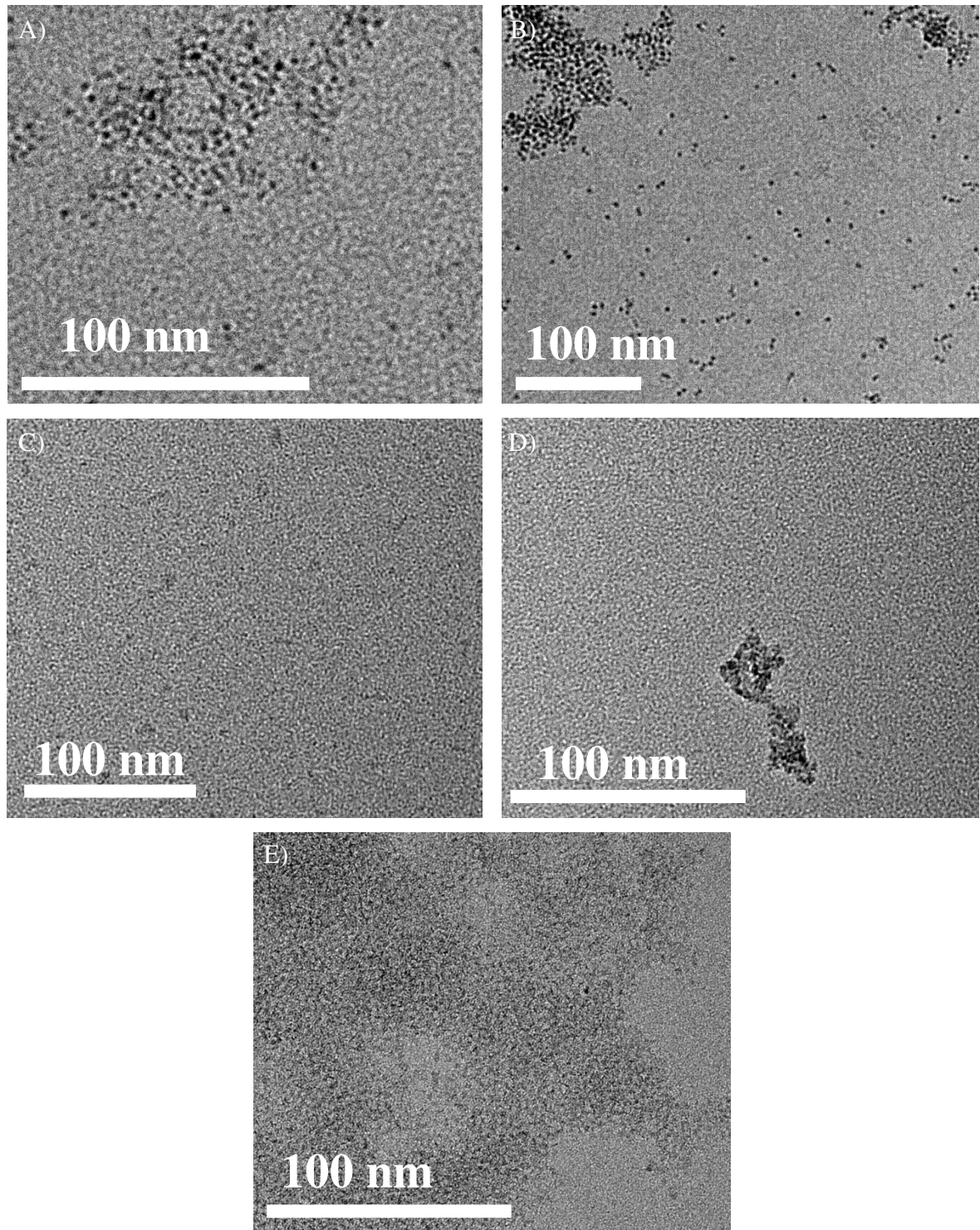


Figure 3.6: Low resolution TEM image of acac grown A) ZnAl_2O_4 , B) ZnGa_2O_4 , C) MgAl_2O_4 , D) MgGa_2O_4 , (E) and ZnGa_2S_4 .

Table 3.1: Structural characteristics of the nanospinels, including sizes, d-spacing, space group, and M²⁺:M³⁺ ratios.

	TEM		pXRD		TEM-EDS M ²⁺ :M ³⁺ ratio		ICP-MS Experimental
	Size	d-spacing	Size	Phase	Theoretical	Experiment	
ZnAl ₂ O ₄	3.2 ± 0.4 nm	0.203 nm (400)	2.95 nm	Fd $\bar{3}$ m	1:2	1:3	1:2.2
ZnGa ₂ O ₄	4.2 ± 0.6 nm	0.295 nm (220)	4.3 nm	Fd $\bar{3}$ m	1:2	1:1.6	1:1.9
MgAl ₂ O ₄	2.6 nm	0.286 nm (220)	2.3 nm	Fd $\bar{3}$ m	1:2	1:2.7	N/A
MgGa ₂ O ₄	3.6 ± 0.4 nm	0.169 nm (422)	3.6 nm	Fd $\bar{3}$ m	1:2	1:3.6	N/A
ZnGa ₂ S ₄	3.2 ± 0.3 nm	0.30 nm (112)	3.0 nm	I $\bar{4}$ 2m	1:2	1:1.2	N/A

in Table 1 and Figures 3.2 and 3.4 can not reject this possibility for ZnGa₂S₄, as the particle size limits the ability to analyze the structural superlattice.

3.3.2 Reaction Phase Space for Formation of ZnB₂O₄ (B = Al or Ga)

In the solid state synthesis of ternary spinels, the line phase AB₂X₄ spinel forms at the exact composition of 1:2 for the A:B ions in a melt reaction. Outside of the concentration of 1:2 for A:B, the resultant product will produce a mixed ce for phase material that often is observed to form as intercalations in the final structure.¹³¹ At the nanoscale, the competitive reaction rates may influence the reaction space.

In Figure 3.7, the evolution of the pXRD pattern as a function of the mole stoichiometry of the initial reaction A:B cation ratio is plotted for ZnAl₂O₄ and ZnGa₂O₄. To interpret the pXRD patterns, there are a few key peaks in the XRDs which indicate the phase composition. The most obvious indication that there is ZnO present is the sharp peaks around 31° (100) and

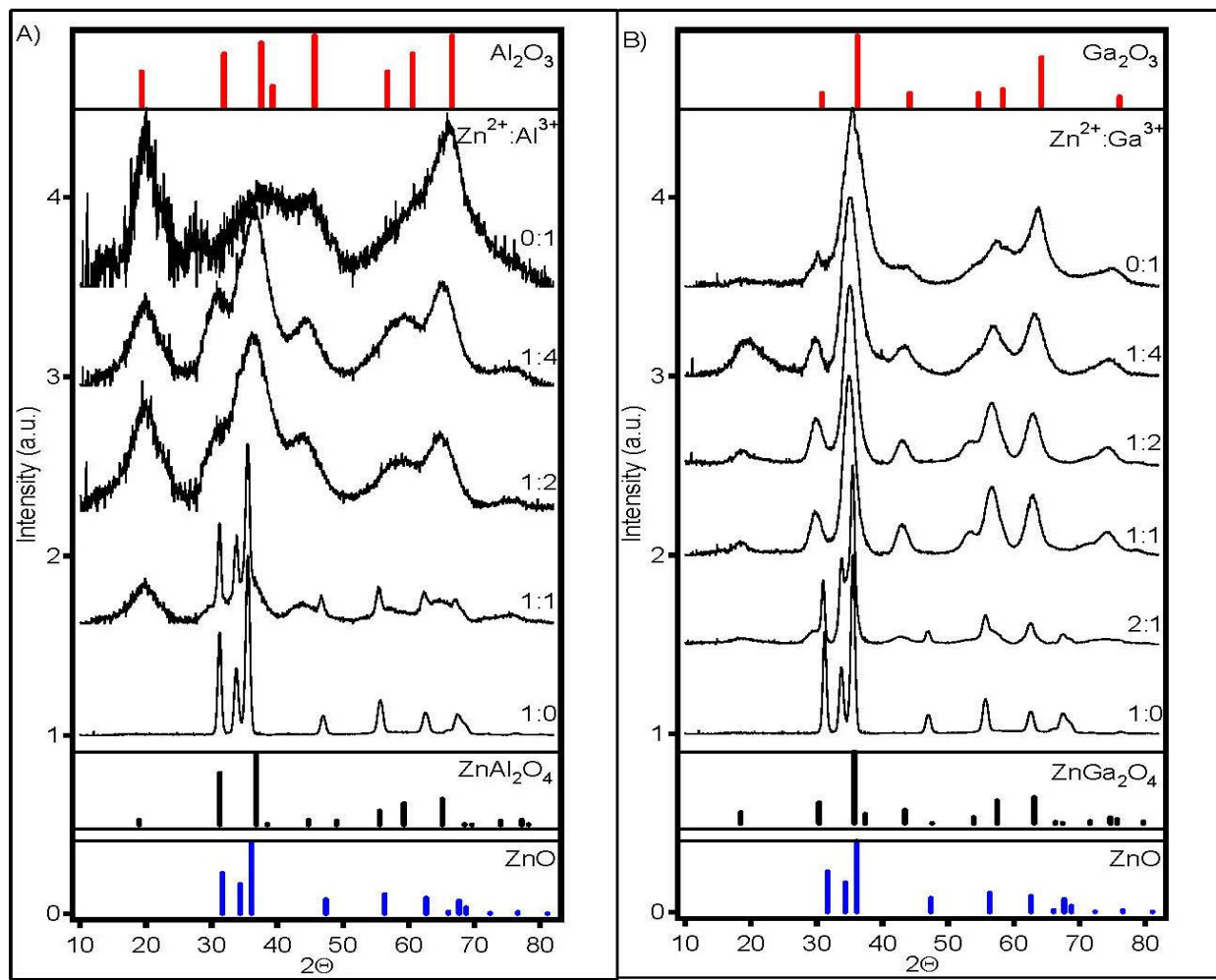


Figure 3.7: pXRD of A) ZnAl₂O₄ and B) ZnGa₂O₄ with different ratios of Zn²⁺ and B³⁺ as well as the XRD diffraction patterns. The inserted XRD diffraction patterns are ZnO (JPCDS 079-0208), ZnAl₂O₄ (JPCDS 82-1043), Al₂O₃ (JPCDS 050-0741), ZnGa₂O₄ (JPCDS 86-0415), and Ga₂O₃ (JPCDS 020-0426).

47° (102). Consistent with these features arising from ZnO, as the Zn²⁺ concentration goes down with increasing Ga³⁺ or Al³⁺ content, the peaks are observed to decrease in intensity. The complete disappearance of these peaks is a good indication that there is no ZnO contamination in the sample. In ZnAl₂O₄ this occurs at 1:2 Zn:Al ratio, while for ZnGa₂O₄ this occurs at 1:1 Zn:Ga. In ZnGa₂O₄, the (111) peak is observed at 18° and is seen in all the patterns with the exception of the 1:0 and 0:1 ratios, which is expected as neither ZnO nor Ga₂O₃ have reflections at that angle. There is a (111) reflection at around 18° for both ZnAl₂O₄ and Al₂O₃, so there is no loss of the (111) peak as in ZnGa₂O₄. There are however, differences in intensity for the

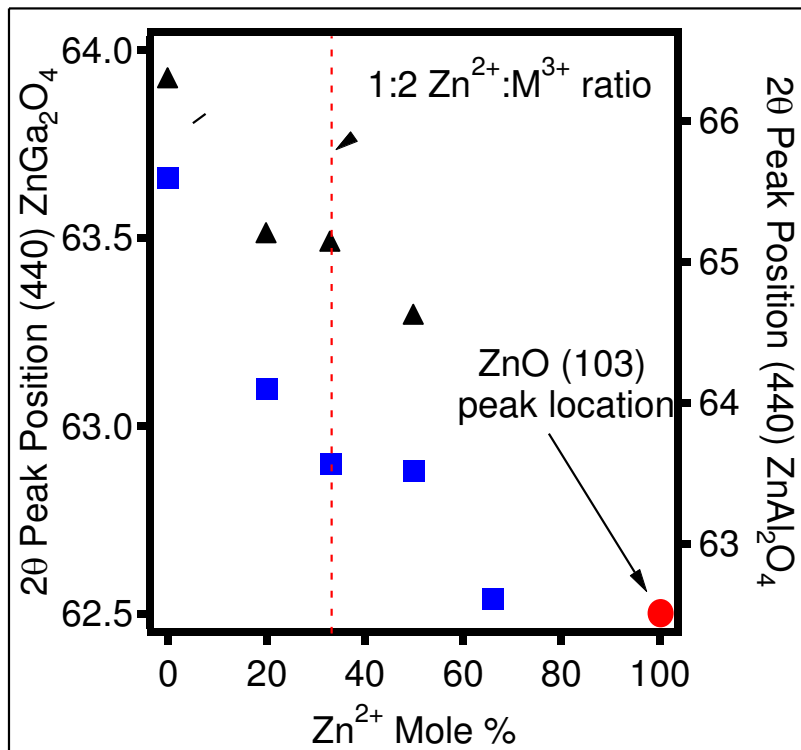


Figure 3.8: (440) peak position shift as a function of Zn²⁺ concentration. The black triangles are ZnAl₂O₄ and the blue squares are the ZnGa₂O₄. The (103) peak for ZnO which is in the same area as the (440) peak is also plotted (red circle).

reflections when going from ZnAl₂O₄ to Al₂O₃. In the XRD card for ZnAl₂O₄, the (111) peak at around 18° and the (440) peak at 65° are much less prominent than the (311) peak at around 37°, while in Al₂O₃, the peak intensity of the (311) reflection drastically decreases. This change in intensity is seen in the powder patterns as the Al³⁺:Zn²⁺ ratio increases, resulting in both the (111) and (440) peaks increasing in intensity relative to the (311) peak, indicative of Al₂O₃ formation. One last indicator of Al₂O₃ formation, as well as lack of ZnAl₂O₄ is the disappearance of the (620) and (533) peaks at about 74° and 77° respectively.

In addition to ZnO peak loss in the pXRD features as the amount of B³⁺ (B = Al, Ga) ion increases, there is also definite shift in the (440) peak in the pXRD, indicating a shift from the cubic ZnB₂O₄ to the cubic B₂O₃ phase. In Figure 3.8, the shifts in the (440) peak for ZnGa₂O₄ and ZnAl₂O₄ is shown. The data exhibits a plateau near the 1:2 mole ratio, indicative of spinel formation. The shift in the (440) peak can be interpreted in terms of Khalifah's findings of intercalation centers of B₂O₃ increasing in the AB₂O₄ nanocrystal resulting in a nearly linear shift

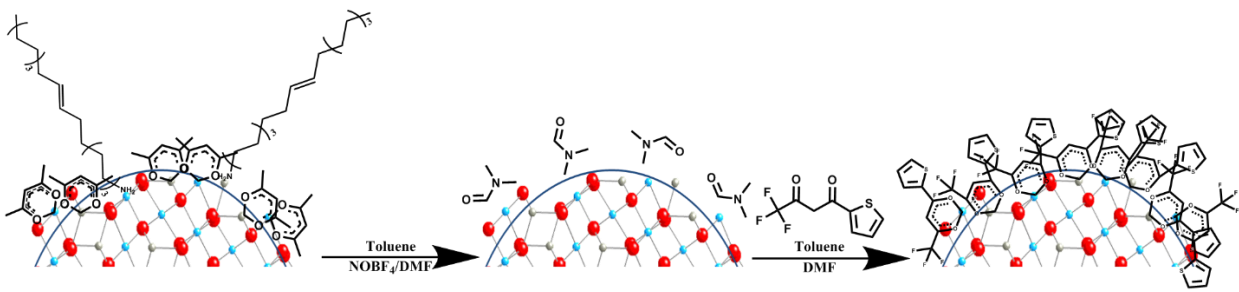


Figure 3.9: NOBF_4 exchange mechanism to replace acac groups passivating the as prepared nanospinels.

in lattice parameter. The lack of clearly defined B_2O_3 features in the pXRD near the absolute stoichiometry further supports this possibility.

Based on the results of the reaction stoichiometry data it appears the spinels are thermodynamically favored at the point of nucleation and for both Zn^{2+} and Ga^{3+} the spinel phase forms even at ratios other than 1:2 $\text{Zn}^{2+}:\text{Ga}^{3+}$. In Figure 3.7A, it is obvious that by decreasing the Al^{3+} content to result in a Zn:Al ratio below 1:2 leads to formation of ZnO . Increasing the Al content up to a 1:4 ratio results in a pXRD pattern that can be indexed to ZnAl_2O_4 , however, intercalation centers of Al_2O_3 are present. For ZnGa_2O_4 formed at a mole ratio between 1:4 to 1:1 A:B ZnGa_2O_4 is formed. ZnO is not observable in the ZnGa_2O_4 reaction until a 2:1 Zn:Ga ratio is used, in effect a 4X excess of Zn^{2+} . The observed difference in reactivity between the Al^{3+} and Ga^{3+} spinels suggests that the ZnGa_2O_4 system is more easily formed, and may account for the larger sizes of the ZnGa_2O_4 and MgGa_2O_4 than the corresponding Al^{3+} derivatives. This result could also help explain why it is so hard to make ZnAl_2S_4 without a large amount of ZnS contamination, unlike the Ga^{3+} derivative, as noted in the experimental section.

3.3.3 Nanospinell Ligand Exchange

The ability to systematically exchange a ligand in a nanocrystal is critical to applications ranging from enhanced energy transport in phosphors to improved cell transfection by $\text{CdSe}@\text{ZnS}$ nanocrystals.^{132, 133} In analogy to controlled ligand exchange on Fe_3O_4 , the isolated nanospinels can be ligand exchanged by treatment with NOBF_4 in DMF to produce a solvated nanocrystal followed by appendage of the desired passivant, as shown in Figure 3.9.¹³⁴ While the approach is applicable to all the AB_2X_4 nanospinels, the discussion is limited to ZnAl_2O_4 and ZnGa_2S_4 . Solution $^1\text{H-NMR}$ analysis of the surface passivation layer on the ZnAl_2O_4 and

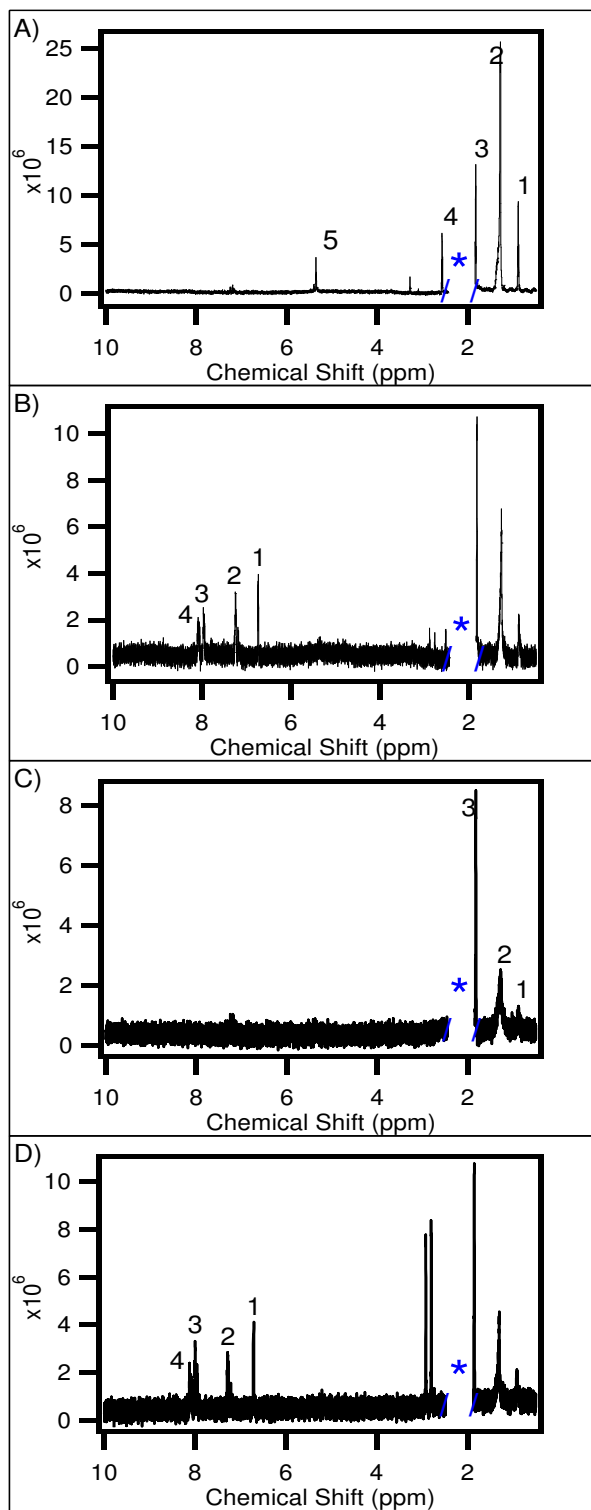


Figure 3.10: ZnAl_2O_4 ^1H NMR spectra of nanocrystals (A) before exchange and (B) after tta exchange. ZnGa_2S_4 ^1H NMR of nanocrystals (C) before exchange and (D) after tta exchange. Samples were dissolved in deuterated acetonitrile.

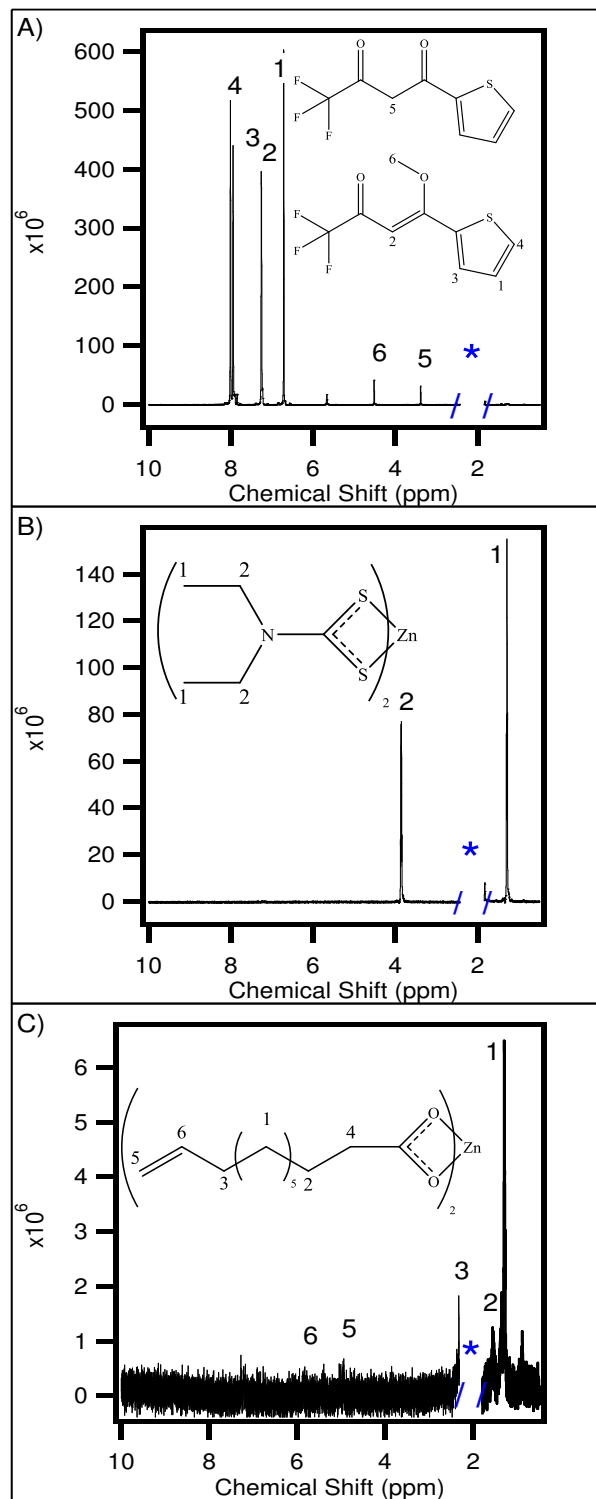


Figure 3.11: ^1H NMR spectra of tta and the starting materials in deuterated acetonitrile at 298K.
A) 2-thenoyltrifluoroacetone, B) Zinc diethyldithiocarbamate, and C) Zinc undecylenate.

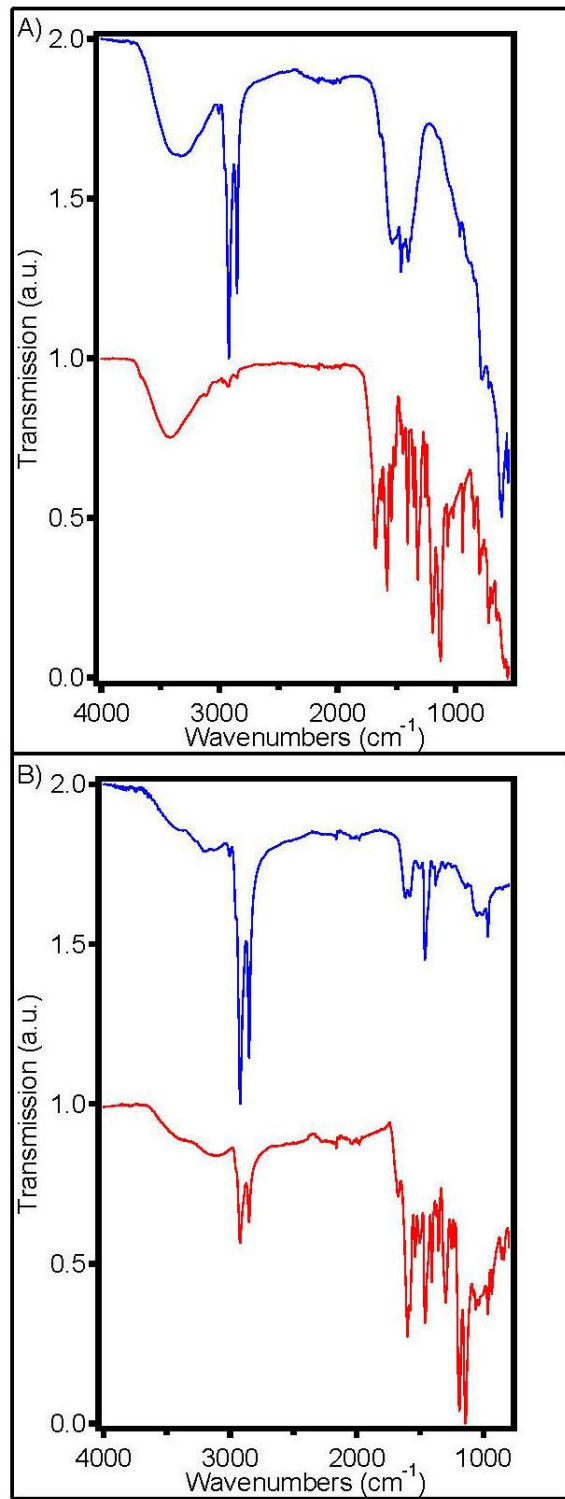


Figure 3.12: IR spectra of A) ZnAl₂O₄ and B) ZnGa₂S₄. As prepared is in blue and after tta exchange in red. The IR was performed on powdered samples using an attenuated total reflectance sample chamber equipped with a ZnSe crystal over coated with diamond.

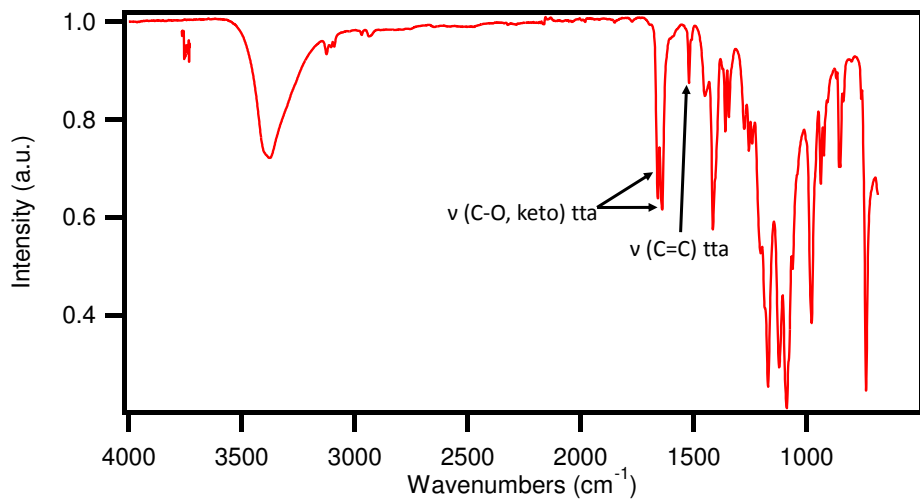


Figure 3.13: IR of tta solid. The IR was performed using an attenuated total reflectance (ATR) sample chamber.

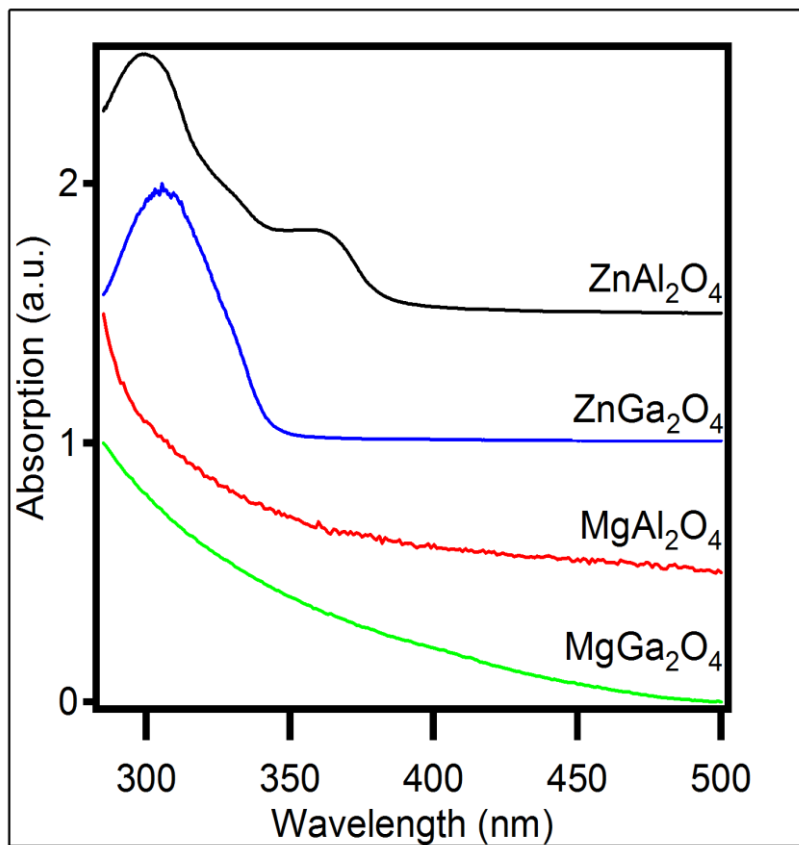


Figure 3.14: Absorption spectra of the nanospinels in toluene. ZnAl_2O_4 is in black, ZnGa_2O_4 is in blue, MgAl_2O_4 in red, MgGa_2O_4 in dark red, and ZnGa_2S_4 in green.

Table 3.2: IR assignments of samples as prepared and after exchange with tta.

ZnAl ₂ O ₄ as prepared (cm ⁻¹)	ZnAl ₂ O ₄ tta (cm ⁻¹)	ZnGa ₂ S ₄ as prepared (cm ⁻¹)	ZnGa ₂ S ₄ tta (cm ⁻¹)	Free tta (cm ⁻¹)	Group
-	-	-	-	3125	-CH ₂ (OA)
3006	-	3005	-	-	=C-H (OA)
2921	-	2921	-	-	-C-H (OA)
2852	-	2581	-	-	-C-H (OA)
-	1679	-	1674	1660	-C=O _{asym} (tta)
-	1630	-	1601	1640	-C=O _{sym} (tta)
1640	-	1615	-	-	-N-H (OA)
1564	-	1584	-	-	-C=C (OA)
1537	-	-	-	-	-C=O (AA)
-	1520	-	1505	1520	-C=C (tta)
1465	-	1464	-	-	-C-H (OA)
-	1446	-	1463	1450	Thiophene -C=C _{asym} (tta)
-	1406	-	1409	1415	Thiophene -C=C _{sym} (tta)
1403	-	-	-	-	-C=C (AA)
1379	-	1377	-	-	-C-H (OA)
-	1258	-	1252	1256	-C-F (tta)
-	1196	-	1191	1171	-C-S (tta)
-	1128	-	1142	1122	-C-CF (tta)
965	-	966	-	-	=C-H (OA)
-	844	-	841	854	-C-S (tta)
720	-	721	-	-	-C-H (OA)

Table 3.3: Optical properties of the nanospinels, including theoretical band gap, the singlet of acac, and vacancies.

	Band gap	$^1\pi-\pi^*$ (acac)	Band gap edge	Vacancies
ZnAl ₂ O ₄	3.8 eV	280 nm	335 nm (3.7 eV)	360 nm (3.4 eV)
ZnGa ₂ O ₄	4.4 eV	280 nm	341 nm (3.6 eV)	N/A
MgAl ₂ O ₄	7.8 eV	280 nm	N/A	N/A
MgGa ₂ O ₄	6.0 eV	280 nm	N/A	N/A
ZnGa ₂ S ₄	3.6 eV	N/A	325 nm (3.8 eV)	N/A

ZnGa₂S₄ as-prepared and following ligand exchange is shown in Figure 3.10, with the ¹H NMR spectra for the ligands shown in Figure 3.11. For solution ¹H NMR, the nanospinels were dispersed in CD₃CN to avoid overlap of the features of interest. The solution NMR data in Figure 3.10 shows the presence of oleylamine and acac for metal acac prepared nanospinels, while only oleylamine (OA) is evidenced as the passivating ligand for metal chloride based reactions. The acac is observed in the NMR spectra at ~10% coverage for ZnAl₂O₄. Oleylamine passivated ZnAl₂O₄ and ZnGa₂S₄ gives rise to ¹H signatures at 0.88 ppm (t, OA, -CH₃), 1.25.1.4 ppm (mm, OA, -CH₂), 1.83 ppm (quintet, OA, CH₂ second from N), 2.33 ppm (s, toluene, CH₃), 2.57 ppm (t, OA, -CH₂ next to N), and 5.35 ppm (t, OA, carbonyl H's). The most characteristic NMR signature for OA is the peak at 5.35 ppm for the double bond. No evidence of undecylenate in the oxide or diethyldithiocarbamate in the sulfides is observed in the NMR data. Solvent impurities are observed in the spectra around 2ppm (*). The results can be confirmed by inspection of the FT-IR data in Figure 3.12. The IR for the ligand tta is shown in Figure 3.13 and a compiled list of IR assignments is available in Table 3.2.

In Figure 3.10B, the ¹H NMR data demonstrates the exchange of the initial passivant by 2.thenoyltrifluoroacetone (tta). Following ligand exchange the nanospinel no longer exhibit the acac double bond at 5.35 ppm confirming complete exchange. Characteristic NMR features for tta are observed at 6.74 ppm (s, tta, C=CH), 7.19 ppm (d, tta, thiophene ring H, in the center),

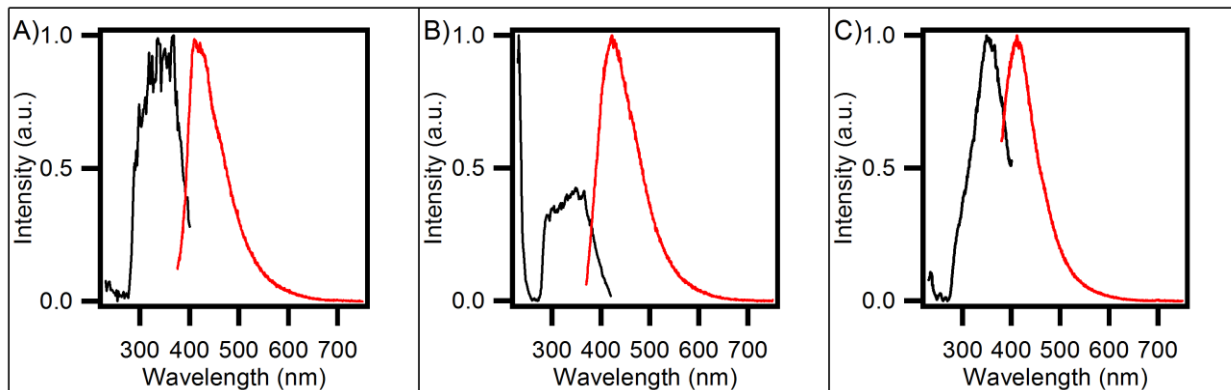


Figure 3.15: Excitation (black) monitored at 420 nm and emission (red) spectra excited at 350 nm in toluene before and after tta exchange. As prepared A) ZnAl₂O₄, C) ZnGa₂O₄, C) ZnGa₂S₄, and tta exchanged D) ZnAl₂O₄, E) ZnGa₂O₄, and ZnGa₂S₄.

7.26 ppm (m, toluene, phenyl H's), 7.96 ppm (s, tta, thiophene ring H, on the bottom), and 8.08 ppm (s, tta, thiophene ring H, closest to sulfide) for both the oxide and thiospinel sample.

3.3.4 Optical Properties of AB₂O₄ (A = Mg or Zn; B = Al or Ga) and ZnGa₂S₄ nanospinels

The oxide and thiospinels are ideal optical hosts for phosphor applications, with absorptions in the near UV reflecting their large bandgap semiconducting behavior.^{117, 122, 135} The optical properties for oleylamine passivated AB₂X₄ nanospinels measured by UV-Vis absorption are provided in Figure 3.14 and tabulated in Table 3. The absorption data for ZnAl₂O₄ exhibits an absorption feature for the acac ${}^1\pi - {}^1\pi^*$ at 305 nm and the bandgap absorption feature is observed at 300 nm (line extrapolated down to give a band gap edge of 325 nm, 3.81 eV) and a peak at 360 nm which has been assigned to V_O defects. The observed absorption peak is consistent with the reported bandgap for ZnAl₂O₄ of 3.8 eV indicating no confinement is observed consistent with the Bohr radius being below 3 nm. Likewise, bandgap absorption are observed for ZnGa₂O₄ and ZnGa₂S₄. The bandgap for MgAl₂O₄, MgGa₂O₄ is beyond the wavelength range of the measurement. The photoluminescence for the ZnAl₂O₄, ZnGa₂O₄, and ZnGa₂S₄, shown in Figure 3.15, when excited at 350 nm results in a PL feature at 422 nm assignable to defect emission in these samples. No photoluminescence is observed for MgAl₂O₄ and MgGa₂O₄.

3.4 Conclusion

Nanocrystals are finding applications in a wide variety of technologies, with development of more complex structures limited only by the imagination. The chapter extends the available nanocrystal materials to AB_2X_4 oxide spinels and thiospinels by demonstrating the ability to prepare pure ternary phases near the point of nucleation through the use of MW assisted thermal decomposition routes. The direct synthesis of nano thiospinels have not been previously reported to the best of our knowledge.¹³⁶ The materials are demonstrated to be a single phase, spherical, highly crystalline, exhibit narrow size dispersity, and are capable of ligand exchange for use in further applications. The synthetic method versatility is demonstrated for a set of high value materials, including MgAl_2O_4 a potential battery material,¹³⁷ and MgGa_2O_4 that exhibits a very high radiation tolerance, making it a useful component in lasers.¹³⁸

While there is no doubt that the illustration of the simple reliable route for formation of a desired line phase ternary spinel shown herein opens a new category of systems to be explored, the development of MW synthetic routes that allow rapid prototyping of reaction conditions coupled to scalability potential is also important.^{48, 139} Lyothermal methods are proven to be scalable, but do not readily lend themselves to rapid prototyping of new reactions conditions. The MW routes allow a pure ternary line phase to be isolated in a wide range of AB_2X_4 nanospinels. The potential of these materials for applications in magnetism (*i.e.* ferrates) and as optical hosts are currently under investigation.

CHAPTER 4

EU³⁺ DOPED ZNM₂O₄ (M = AL³⁺, GA³⁺) NANOSPINELS, AN EFFICIENT RED PHOSPHOR

This chapter describes the synthesis of Eu(III) doped ZnB₂O₄ (B = Al(III) or Ga(III)) nanospinels with Eu(III) concentrations varying between 1 and 15.6%. The synthesis was achieved through a microwave (MW) synthetic methodology producing 3 nm particles by the thermal decomposition of zinc undecylenate (UND) and a metal 2,4.pentanedionate (B(acac)₃, B = Al³⁺ or Ga³⁺) in oleylamine (OAm). The nanospinels were then ligand exchanged with the β -diketonate, 2.thenoyltrifluoroacetone (tta). Using tta as a ligand on the surface of the particles resulted in soluble materials that could be embedded in lens mimics, such as polymethylmethacrylate (PMMA). Through a Dexter energy transfer mechanism, tta efficiently sensitized the Eu(III) doped within the nanospinels, resulting in red phosphors with intrinsic quantum efficiencies (QEs) and QEs in PMMA as high as 50% when excited in the UV. Optical measurements on the out of batch and tta passivated nanospinels were done to obtain absorption, emission, and lifetime data. The structural properties of the nanospinels were evaluated by ICP-MS, pXRD, TEM, FT-IR, EXAFS, and XANES.

4.1 Introduction

Reducing power consumption in buildings through the use of solid state lighting (SSL) is expected to lead to a savings of >30% for the average consumer.¹⁹ SSL is already highly efficient, up to ten times more efficient than incandescent bulbs and twice as efficient as fluorescent lighting.¹⁴⁰ Unfortunately, most SSL technologies depend on down conversion phosphors that have poor color rendering, are non-miscible in the LED lens materials leading to scattering losses, and cannot be tuned to match current LED emitters in the near UV. The poor color rendering behavior can be traced to poor conversion efficiencies for the red phosphors, resulting in CIE coordinates that are too blue.¹⁴¹

While efficient red phosphors are known, DOE has identified efficient down conversion red phosphors as a priority material, since many of the red phosphors are broad emitters and therefore emit red of the visual rage for the eye.¹⁴² Performance enhancement for red phosphors

can be realized by utilizing nanoscale materials to reduce scattering and by enhancing photon absorption and down conversion to an emissive center through the application of molecular sensitizers. Previous studies by our group have shown 28% quantum efficiencies (QE) can be achieved by utilizing the molecular antenna enhancement in 6 nm Eu:Y₂O₃ nanocrystals passivated by acac,¹³² while results from Lin, et al achieved 6% QE using *tta* as the molecular antenna for 29 nm Eu: YPO₄.¹⁴³ The differences in efficiency for the nanophosphors reflects the energy overlap integral ($\langle J \rangle$) of the ligand states and the distance between the molecular sensitizer and the emissive center as defined by the Dexter mechanism. The Dexter mechanism distance for Ln(III) materials is typically <2 nm.^{20, 60}

The chapter reports a microwave (MW) synthetic methodology to produce 3 nm nanospinel phosphors composed of organically soluble Eu:ZnB₂O₄ (B = Ga or Al) passivated by the molecular antenna sensitizer 2.thenoyltrifluoroacetone (*tta*). The ZnAl₂O₄ spinel represents an earth abundant lattice, which will in turn lower the cost of the material as the host accounts for approximately 90% of the material. Spinel lattices exhibits high chemical, thermal, and radiation stability, making them viable for use in optoelectronic devices. MW reactions for formation of nanocrystals near their nucleation size was reported to occur due to rapid nucleation and monomer depletion within a MW cavity when a non-MW absorbing solvent and vessel are used.⁴⁸

The highest QE red phosphor is achieved for Eu(9.7%):ZnAl₂O₄, and when embedded in a LED lens mimic is 50% with an intrinsic QE calculated from the observed lifetime of 45.9%. The Eu(12.4%):ZnGa₂O₄ QE is 25% for the lens mimic with an intrinsic QE of 39%. The observation that the QE scales linearly with concentration for both samples is consistent with a non-diffusive Perrin energy transfer model via a Dexter mechanism, allowing a volume of quenching to be calculated with a radial dimension of ~ 0.5 nm, or in effect 3 lattice planes or $\sim 73\%$ in ZnAl₂O₄ and 71% in ZnGa₂O₄ of the incorporated Eu(III) ions will be efficiently accessed following excitation of the surface bound *tta* ligand levels. The ratio of the electronic ($^5D_0 \rightarrow ^7F_2$ line) to the magnetic ($^5D_0 \rightarrow ^7F_1$ line) dipole allowed transition, referred to as the red/orange (R/O) ratio in Eu doped materials, max out at 12.1 (9.7% Eu:ZnAl₂O₄) and 11.5 (15.6% Eu:ZnGa₂O₄) for the nanospinel samples, as compared to a bulk Eu:Y₂O₃ phosphor standard which has a value of ~ 6 .¹⁴⁴ The CIE coordinates for the samples are tunable from blue to red dependent on the concentration of Eu(III) and the spinel B-ion. The results demonstrate

that the spinel (AB_2O_4) oxide host represents an ideal host lattice for incorporating the Eu(III) centers, effectively eliminating the requirement for the yttrium component. The demonstration of high performance in the alternative spinel lattice coupled to use of molecular antenna sensitizers points towards a viable approach to improve efficiency, use earth abundant hosts, and maximize device output.

4.2 Experimental Section

4.2.1 Materials

All commercially available reagents and solvents, including 2.thenoyltrifluoroacetone (Matrix Scientific, 99%), Zinc (II) Undecylenate (Spectrum, 98%), Aluminum (III) 2,4.pentanedionate (Strem Chemicals, 99%), Gallium (III) 2,4.pentanedionate (Aldrich, 99.99%), Europium (III) 2,4.pentanedionate hydrate (Alfa Aesar, 99.9%), Oleylamine (Aldrich, 70%), Nitrosium tetrafluoroborate (Alfar Aesar, 98%), N,N-Dimethylformamide (Sigma Aldrich, ≥99.8%) were used without further purification with the exception of dimethylforamide (DMF). DMF was dried over molecular sieves.

4.2.2 Synthesis of Eu: ZnB_2O_4 (B = Al³⁺ or Ga³⁺, 1%, 2.5%, 5%, 7.5%, 10%, 12.5% Eu) Nanocrystals

Nanocrystals passivated by 2,4.pentanedione (*acac*) were prepared by microwave induced decomposition of zinc undecylenate ($\text{Zn}(\text{UND})_2$) with aluminum (III) 2,4.pentanedionate ($\text{Al}(\text{acac})_3$) or gallium (III) 2,4.pentanedionate ($\text{Ga}(\text{acac})_3$) and europium (III) 2,4.pentanedionate ($\text{Eu}(\text{acac})_3$) dissolved in oleylamine (OAm) using a CEM Discover Microwave (MW) operating under single mode, continuous power at 2.45 GHz. The CEM MW cavity was commercially modified by CEM with a Teflon insert to allow sustainable heating at 300°C. To synthesize Eu: ZnAl_2O_4 , a glass microwave reactor vessel loaded with $\text{Zn}(\text{UND})_2$ (0.108 g, 0.25 mmol), $\text{Eu}(\text{acac})_3$ (1% (0.0024 g), 2.5% (0.0061 g), 5% (0.0121 g), 7.5% (0.0182 g), 10% (0.0243 g), 12.5% (0.0304 g)), $\text{Al}(\text{acac})_3$ (1% Eu (0.1605 g), 2.5% Eu (0.1581 g), 5% Eu (0.154 g), 7.5% Eu (0.150 g), 10% Eu (0.1459 g), 12.5% Eu (0.1419 g)), and OAm (4mL). The MW vessel was sealed, and the reactants were sonicated until the solid dissolved, approximately 30 min. The MW vessel was then inserted into the MW cavity and heated at 300 W to 280°C then held at that temperature for 5 min. The solution was cooled to 50°C and the Eu: ZnAl_2O_4

nanocrystals were precipitated by addition of MeOH (~5 mL). The product was isolated by centrifugation, washed four times using toluene/EtOH and then dried under vacuum overnight. The isolated sample is white in color and can be dispersed in toluene or chloroform. Eu:ZnGa₂O₄ was synthesized in the same fashion, though using Ga(acac)₃ (1.2% Eu (0.1814 g), 2.1% Eu (0.1787 g), 5.4% Eu (0.174 g), 8.7% Eu (0.1695 g), 12.4% Eu (0.1649 g), 15.6% Eu (0.1603 g)). Elemental composition analysis was performed using ICP-MS for Zn, Al, Ga, and Eu.

4.2.3 Ligand Exchange Protocol

Ligand exchange of the OAm by 2.thenoyltrifluoroacetone (*tta*) is accomplished through the use of nitrosium tetrafluoroborate (NOBF₄) to assist ligand place exchange reactions, as described previously.¹³⁴ The exchange is accomplished by treatment of 25 mg of the nanospinel dispersed in 5 mL toluene with 5 mL of 0.01 M NOBF₄ in dry DMF under N₂. The dispersion is allowed to react for 5 min, and the precipitate is collected by centrifugation and washed with acetone (2x). The resultant precipitate is added to a stirring mixture containing 1 ml of dry DMF, 2 mL toluene, and 50 mg of *tta*. The dispersion was heated to 60°C until the solution is clear (~30 min). The *tta* passivated nanospinel is isolated from solution by addition of acetone and collection by centrifugation. The resultant nanospinels are soluble in toluene.

Ligand passivation was analyzed by FT-IR measured on powdered samples using a PerkinElmer Spectrum 100 FT-IR Spectrometer equipped with an attenuated total reflectance (ATR) sample chamber consisting of a ZnSe crystal over coated with diamond using a single-bounce configuration.

4.2.4 X-ray Powder Diffraction

Structural characterization was performed using powder X-ray diffraction (pXRD) recorded on a Rigaku DMAX 300 Ultima III Powder X-ray diffractometer (using Cu K α $\lambda = 1.5418 \text{ \AA}$ radiation). The pXRD was patterned matched using JADE and the nanospinel size fit using the Scherrer broadening expression. The size was evaluated by inspection of the (220) and (311) reflections.

4.2.5 Transmission Electron Microscopy

Size, size dispersity, morphology, and structure were analyzed by Transmission electron microscopy (TEM). TEM measurements were carried on a Tecnai Osiris operating at 200 kV using either carbon type A (300 mesh) with removable Formvar on Cu grids or graphene films deposited on lacey carbon grids (300 mesh). Image analysis of >100 nanocrystals were used to generate the size distribution curves.

4.2.6 X-ray Absorption Near Edge (XANES) and X-ray Absorption Fine Structure (XAES)

Characterization of the local electronic and atomic structure of the materials was performed by synchrotron based x-ray absorption fine structure spectroscopy (XAES) measurements. The XAFS spectra were acquired at the bend magnet beamline X19A at the National Synchrotron Radiation Light Source, Brookhaven National Laboratory. A double crystal Si(111) monochromator was used and detuned by 40-50% for reduction of harmonics. Three ion gas chambers were used to record in transmission mode the incident (filled with N₂), transmitted (filled with Ar/He), and reference (filled with Ar/He) beam. A metal foil was placed after the second ion chamber for energy calibration purposes. All measurements were performed in transmission mode.

XAFS data processing and analysis was done using the IFEFFIT suite of programs.¹⁴⁵ Initial estimates of the threshold energy values (E₀) were obtained via the inflection point in the normalized absorption edges. A Kaiser-Bessel window was applied to a selected k-range to obtain the Fourier transformed extended XAFS (EXAFS) data. The k-space data was weighted by k³ and Fourier transformed between 2.9 Å⁻¹. In general, the quality of the EXAFS data precludes rigorous fitting of the data outside of the 1st shell, but inspection of the data is useful in understanding the structure of the doped materials.

4.2.7 Optical Measurements

Solution absorption spectra were obtained using a Varian Cary 50 UV-vis spectrophotometer. Solution photoluminescence measurements were carried out on a Varian Cary Eclipse fluorescence spectrophotometer. Relative solution QEs were obtained by comparing to a reference standard quinine standard (Eu(tta)₃phen, Φ = 0.365 in EtOH) according to literature procedures.¹⁴⁶ Absolute QEs were measured on phosphors embedded in PMMA as a lens mimic

for the LED phosphor using the De Mello method equipped with an integrating sphere incorporated into a spectrofluorimeter (FLS980, Edinburgh Instruments).¹⁴⁷ A long pass 374 nm filter was used for emission measurements.¹⁴⁸ The lens mimics were prepared in a silicon mold by dissolving 0.01g of Eu:ZnB₂O₄ into 0.1 g of PMMA in acetone and allowing the acetone to evaporate.

Lifetimes measurements were measured using a Nd-YAG laser pumped at 366nm coupled to a photo-multiplier tube, and recorded through an oscilloscope interfaced with a computer. The decay data was fit to a single exponential decay using a non-linear regression analysis.

4.3 Results

4.3.1 Synthesis of Eu:ZnB₂O₄ (B = Al, Ga)

MW assisted synthesis of acac passivated 3 nm Eu(III):ZnB₂O₄ nanocrystals was achieved by the reaction of the appropriate metal (B³⁺ = Al or Ga) acac salt and zinc undecylenate as the A²⁺ ion. Doping levels of 1%, 2.5% 4.7%, 7.5%, 9.7%, and 12.7% Eu(III) ZnAl₂O₄ and 1.2%, 2.1%, 5.4%, 8.7%, 12.4%, and 15.6% Eu(III) for ZnGa₂O₄ were confirmed by ICP-MS analysis of the samples. Despite using the same mole quantities for doping Eu(III) in both ZnAl₂O₄ and ZnGa₂O₄, ZnGa₂O₄ ended up with greater Eu(III) concentrations. Calculations from the TEM-EDS were also performed on the spinels with the highest Eu(III) content. Microwave enhanced lyothermal routes to narrow dispersity nanocrystals has been reported to produce <4 nm spinels due to rapid nucleation and monomer depletion when the reactions are carried out in a non-MW absorbing solvent or vessel.

In Figure 4.1A-B, the pXRD data confirm isolation in the pure line phase ZnB₂O₄ nanocrystals, with no evidence of the binary phases in the diffraction data. The Eu:ZnB₂O₄nanospinel crystallizes in the Fd-3m group (JCPDS card 74.1138 for ZnAl₂O₄ and JCPDS card 86-0415 for ZnGa₂O₄). Only experimental data for the 12.7% Eu:ZnAl₂O₄ and 15.6% Eu:ZnGa₂O₄ samples are shown in Figure 4.1; pXRD data for the other doping levels is in Figure 4.2. The pXRD diffraction linewidth was fit to the Scherrer broadening equation for the (220) for ZnAl₂O₄ and the (311) for ZnGa₂O₄ to extract nanospinel sizes. Sizes of 3.05 nm, 2.58 nm, 2.6 nm, 2.7 nm, 2.88 nm, and 2.74 nm for 1.0%, 2.5% 4.7%, 7.5%, 9.7%, and 12.7% Eu(III)

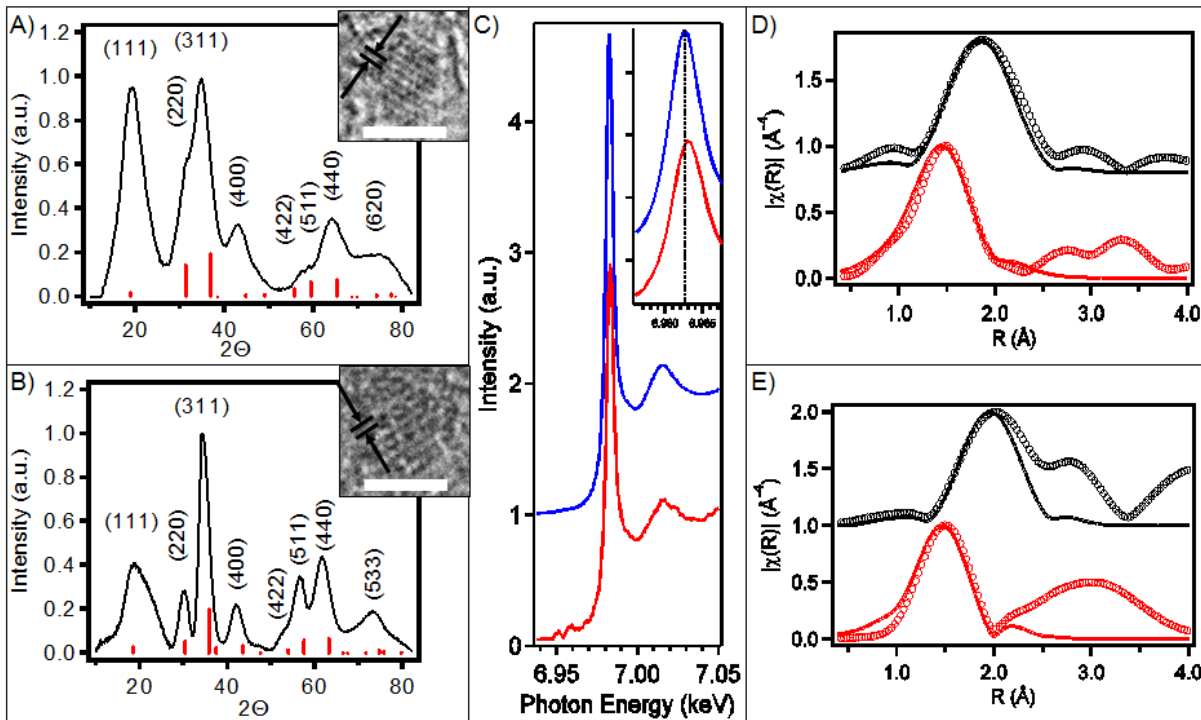


Figure 4.1: pXRDs of A) 12.7% Eu(III) ZnAl₂O₄ (inset: TEM image of a single particle with lattice spacing of 0.285 nm corresponding to the (220) lattice plane) and B) 15.6% Eu(III) ZnGa₂O₄ (inset: TEM image of a single particle with lattice spacing of 0.295 nm corresponding to the (220) lattice plane). TEM scale bar is 2.5 nm. C) Eu L3-edge XANES data for 12.7% Eu:ZnAl₂O₄ (blue) and 15.6% Eu:ZnGa₂O₄ (red). The inset expands the region of the white line to make the spectral shift between samples more observable. EXAFS data (Zn in red and Eu in black) for D) 12.7% Eu:ZnAl₂O₄ and E) 15.6% Eu:ZnGa₂O₄. For both (D) and (E) the open circles represent the data points and the solid lines are the 1st coordination shell fit.

ZnAl₂O₄. Sizes of 3.87 nm, 3.72 nm, 3.55 nm, 3.38 nm, 3.48 nm, and 3.06 nm are measured for the 1.2%, 2.1%, 5.4%, 8.7%, 12.4%, and 15.6% Eu(III) for ZnGa₂O₄ respectively.

A high resolution TEM image of a single particle of the 12.7% ZnAl₂O₄ and 15.6% Eu:ZnGa₂O₄ samples are shown in Figure 4.1A and 1B respectively (inset). The isolated nanocrystals are spherical in shape with well-defined lattice fringes. The TEM sizes for 12.7% Eu:ZnAl₂O₄ is 2.8 ± 0.25 nm and 2.95 ± 0.35 for the 15.6% Eu:ZnGa₂O₄ were in good agreement with the Scherrer broadening values extracted from pXRD. Lattice fringe analysis of the high resolution TEM images shows (220) faceting for both ZnAl₂O₄ and ZnGa₂O₄ consistent with a d-spacing of 0.285 nm in ZnAl₂O₄ and 0.295 nm in ZnGa₂O₄. Full micrographs of the high resolution TEMs with size distributions and corresponding TEM-EDS plots for the 12.7% Eu ZnAl₂O₄ and 15.6 % ZnGa₂O₄ samples are shown in Figure 4.3, 4.4, 4.5, and 4.6. ZnB₂O₄ (B

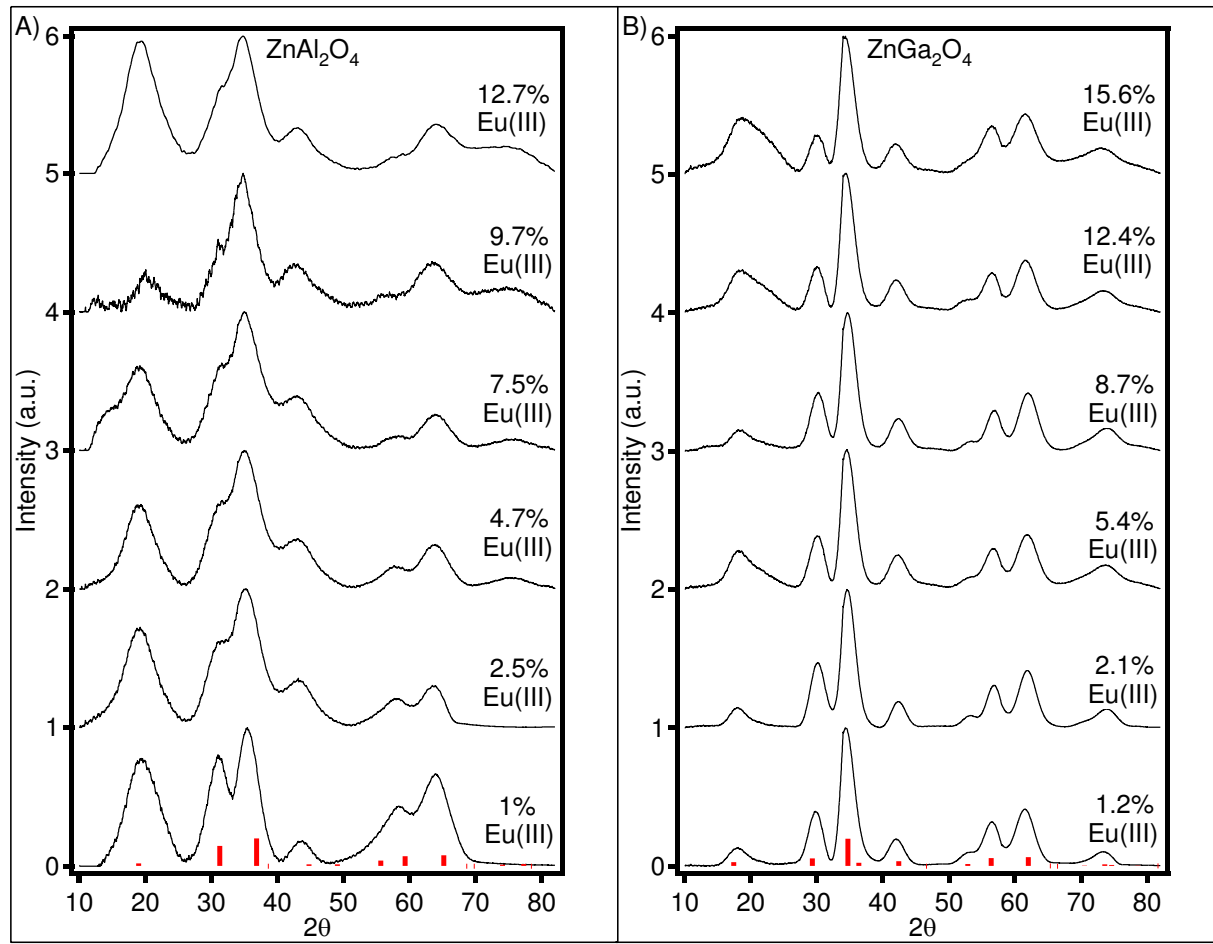


Figure 4.2: pXRD at different Eu(III) concentrations in A) ZnAl_2O_4 and B) ZnGa_2O_4 .

= Al, Ga) has the normal spinel crystal structure. The A-site is occupied by the Zn^{2+} ion on a tetrahedral site (ionic radius = 74 pm) and the Al^{3+} or Ga^{3+} ions occupy the octahedral (Oh) B-site (radius: 67 pm - Al^{3+} , 76 pm - Ga^{3+}). The Eu(III) ion radius is 109 pm for an Oh site occupation.

In Figure 4.1C, the XANES for the Eu L₃-edge for 12.7% Eu: ZnAl_2O_4 and 15.6% Eu: ZnGa_2O_4 is shown. In Figure 4.1C, the L₃-edge XANES data (formally a $2\text{p}3/2 \rightarrow 5\text{d}$ transition) shows a large white line at ~6.983 eV with a less pronounced feature at higher energy. The spectra, when compared to Eu(III) in a silicate glass indicates no clustering of Eu(III) occurs, likely reflecting the substitutional occupation for the B³⁺. Comparison of the results to the reported data for Eu in CaAl_2O_4 , where Eu(II) and Eu(III) is observed, allows definitive evidence of a single oxidation state for the Eu doping with B-site occupation.¹⁴⁹ The XANES white line feature can therefore be assigned to a Eu(III) center sitting on an Oh site in the

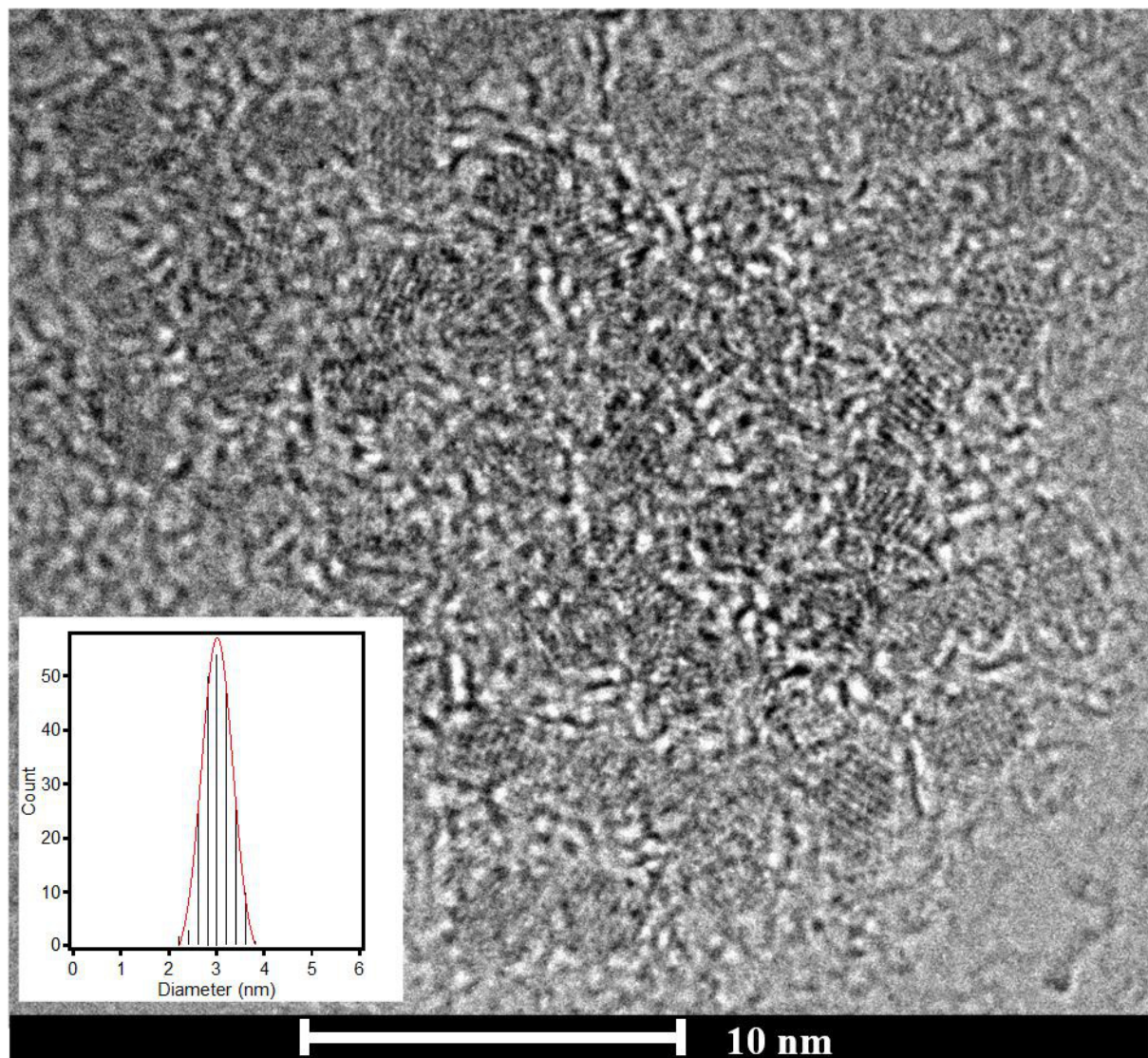


Figure 4.3: High resolution TEM of 12.5% Eu ZnAl₂O₄. The samples were dissolved in toluene and deposited on a graphene grids. The samples were baked under high vacuum at 130°C for at least 8 hours. The TEMs were obtained using a Tecnai Osiris operating at 200 kV. The size distribution plot is included as an inset.

Eu:ZnAl₂O₄ and Eu:ZnGa₂O₄. The Oh site is the B site in the spinel. Closer inspection of the Eu L₃ edge data reveals that the Eu:ZnGa₂O₄ exhibits a spectral shift by ~ 1eV relative to the L₃ edge in Eu:ZnAl₂O₄ (see inset of Figure 4.1C). The small shift may arise from symmetry breaking or disorder at the Eu Oh site in the Ga spinel. Similar observations have been made for the shift in the W L₃ edge in CaWO₄.¹⁵⁰ The disorder likely reflects the size difference for Al vs

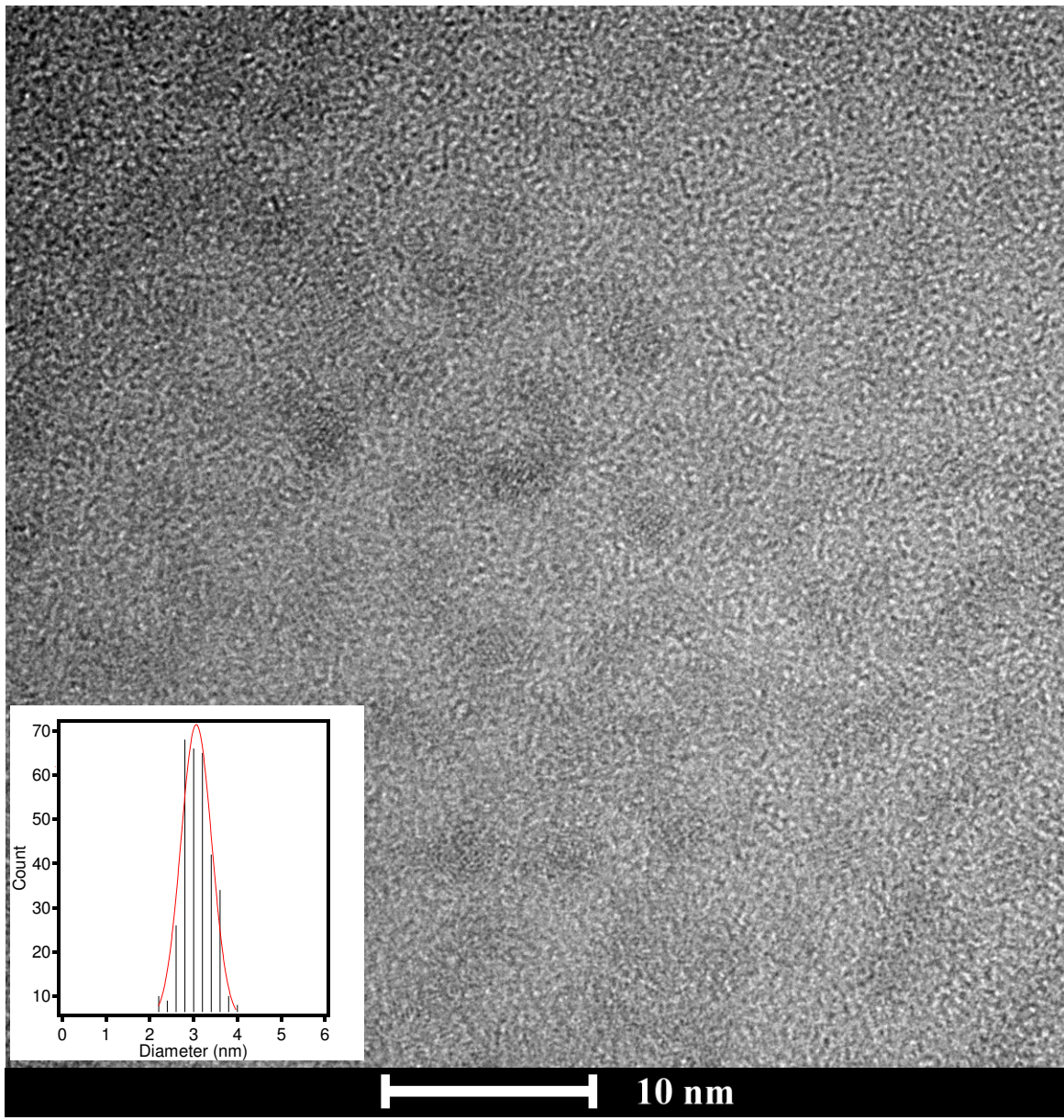


Figure 4.4: High resolution TEM of 15.6% Eu ZnGa₂O₄. The samples were dissolved in toluene and deposited on a Ted Pella carbon type A (300 mesh) Cu grid with removable Formvar. The samples were baked under high vacuum at 130°C for at least 8 hours. The images were obtained using a Tecnai Osiris operating at 200 kV. The size distribution plot is included as an inset.

Ga compared to the substitutional Eu(III) ion. Consistent with the agreement of disorder, the rounding of the second has been interpreted as distortion of the Eu (III) site symmetry in Eu(II) doped silicate glasses. Zn K-edge XANES data, Figure 4.7 also supports a degree of distortion in

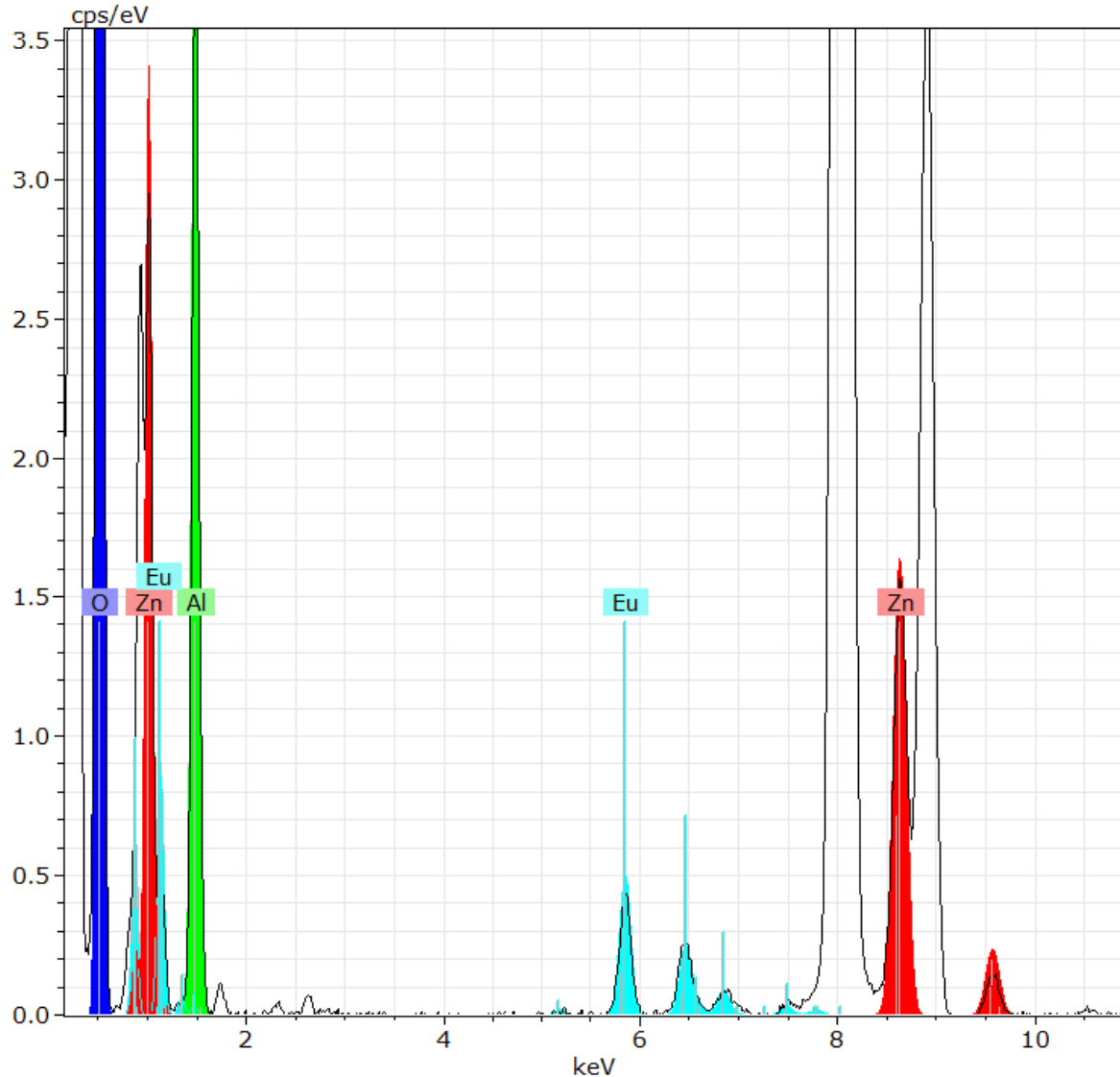


Figure 4.5: TEM-EDS of 12.7% (measured by ICP-MS) Eu ZnAl₂O₄. The TEM-EDS was obtained using a Tecnai Osiris operating at 200 kV. The measured amounts results in a structure of ZnAl_{1.5}Eu_{0.25}O₄.

the Ga samples as several features in the spectra are severely suppressed relative to the Al sample.

Figure 4.1D-E shows the Eu-L₃ and Zn K-edge EXAFS data for both 12.7% Eu:ZnAl₂O₄ and 15.6% Eu:ZnGa₂O₄. The 1st scattering contribution in the Eu L₃-edge and Zn K-edge EXAFS data shown in Figure 4.1D-E can be assigned to Eu-O and Zn-O with bond lengths of R ~ 2.4 Å and 2.0 Å, respectively. While the derived Zn-O bond lengths are consistent with those found in the undoped ZnB₂O₄ lattice, the Eu-O bond lengths are consistent with the Eu-O bond

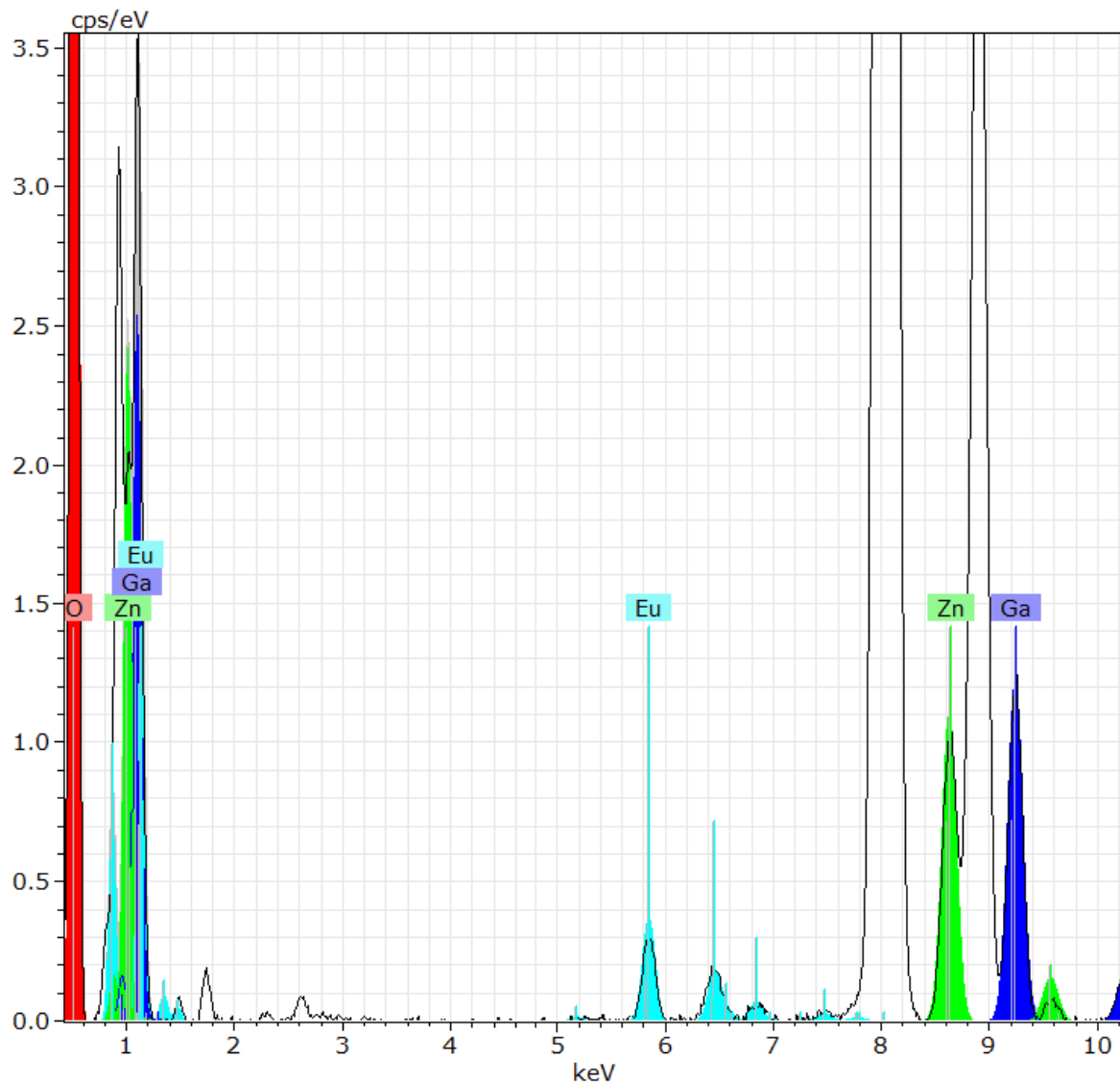


Figure 4.6: TEM-EDS of 15.6% (measured by ICP-MS) Eu ZnGa₂O₄. The TEM-EDS was obtained using a Tecnai Osiris operating at 200 kV. The measured amounts results in a structure of ZnGa_{1.2}Eu_{0.27}O₄.

lengths found in Eu₂O₃. Fitting of the data allows the assignment of six oxygen atoms in the 1st shell around the Eu center thus confirming an Oh B-site for Eu substitution into the spinel for both Eu:ZnAl₂O₄ and Eu:ZnGa₂O₄. The 1st shell fits for both edges are summarized in Table 4.1 (as the data was not of high enough quality, we were not able to successfully fit 2nd shell data). As the expected Eu-O bond length in Eu₂O₃ is 2.43 Å, the EXAFS results support a local

Table 4.1: EXAFS fitting results for 12.7% Eu:ZnAl₂O₄ and 15.6% Eu:ZnAl₂O₄

	12.7% Eu:ZnAl ₂ O ₄			
	R (Å)	σ (Å ²)	ΔE (eV)	R-factor
Zn-O	1.97(3)	0.011(7)	1.3(5)	0.01
Eu-O	2.38(8)	0.006(2)	4.6(5.4)	0.02
	15.6% Eu:ZnGa ₂ O ₄			
	R (Å)	σ (Å ²)	ΔE (eV)	R-factor
Zn-O	1.99(3)	0.001(3)	-0.8(3.7)	0.03
Eu-O	2.45(4)	0.001(4)	7.5(3.0)	0.05

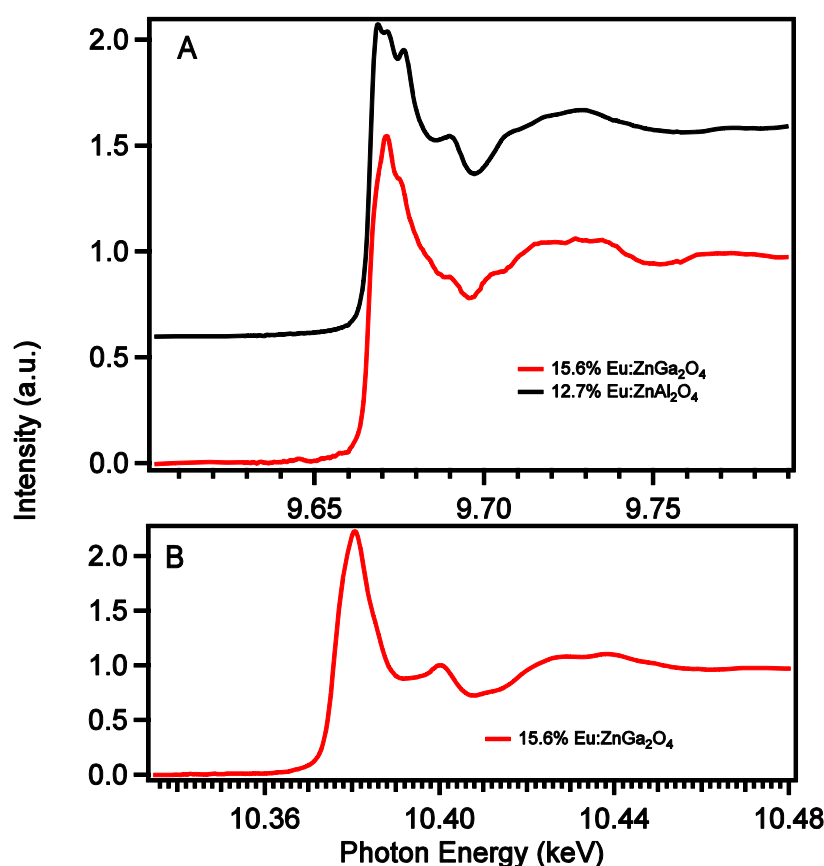


Figure 4.7: XANES of Eu(III) doped ZnAl₂O₄ and ZnGa₂O₄ at the (A) Zn and (B) Ga K-edges.

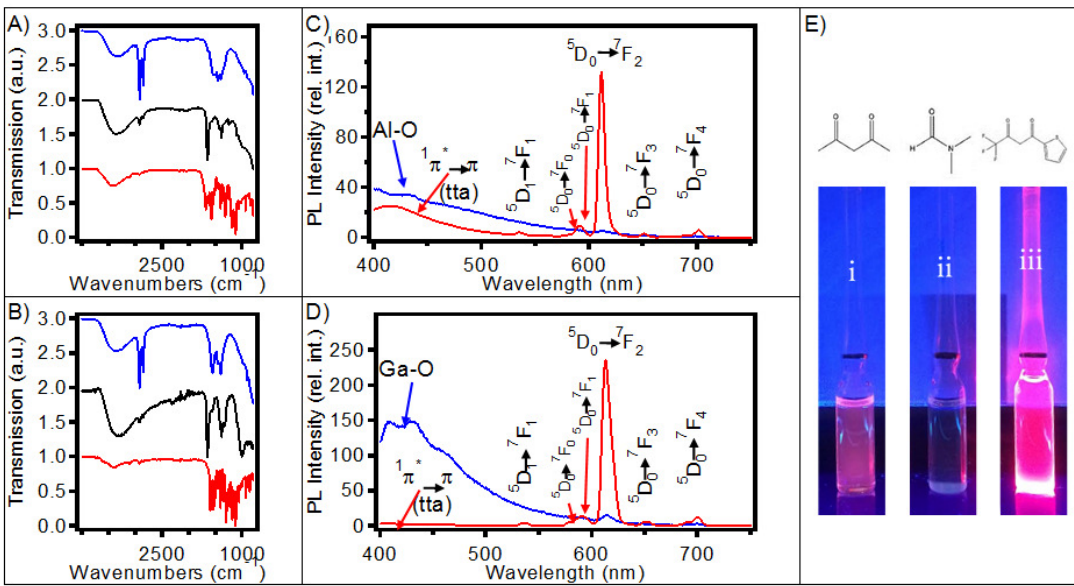


Figure 4.8: Normalized IR spectra of A) 12.7% Eu:ZnAl₂O₄ and B) 15.6% Eu:ZnGa₂O₄ (blue = acac, black = NOBF₄, red = tta). PL spectra of doped nanospinels before (blue) and after (red) tta exchange, C) 12.7% Eu:ZnAl₂O₄ and D) 15.6% Eu:ZnGa₂O₄. E) Luminescence of 1 x 10⁻⁹ M Eu_{0.20}ZnAl_{1.80}O₄ in toluene under 364 nm excitation when passivated by i) acac, ii) DMF, and iii) tta.

distortion in the Ga samples, with Eu-O bond lengths close to the values expected for Eu₂O₃, an unexpected result as the unit cell volume for the ZnB₂O₄ material is much smaller than Eu₂O₃.

4.3.2 Optical Properties of Eu:ZnB₂O₄ (B=Al, Ga)

Molecular sensitization of the Eu(III) emissive center by the ligand tta, which has a low lying $\pi \rightarrow \pi^*$ transition, has been demonstrated in molecular and nanomaterials.¹⁴³ Evidence of NOBF₄ mediated place exchange of acac and OAm by tta is provided by analysis of the FT-IR data (Figure 4.8A and 4.8B). The Eu:ZnB₂O₄ acac passivated nanospinels exhibit the symmetric and anti-symmetric *acac* vibrations for the v(C=C, C=O) at 1408 and 1566 cm⁻¹ respectively. The observation of -CH₂ symmetric and asymmetric stretches at v_s(-CH₂) = 2856 cm⁻¹, and v_{as}(-CH₂) = 2925 cm⁻¹ confirm co-passivation by OAm. Similar observations were reported for growth of Y₂O₃ from Y(acac)₃ in hexadecylamine.¹³² After treatment of the nanospinel with NOBF₄ in DMF the loss of the methyl, methylene, and acac peaks concomitant with the appearance of a peak at 1652 cm⁻¹ for vco DMF confirms removal of the initial mixed acac / tta passivation layer. There is no evidence of N-O vibrations at 2100-2200 cm⁻¹ or B-F at 1084 cm⁻¹,

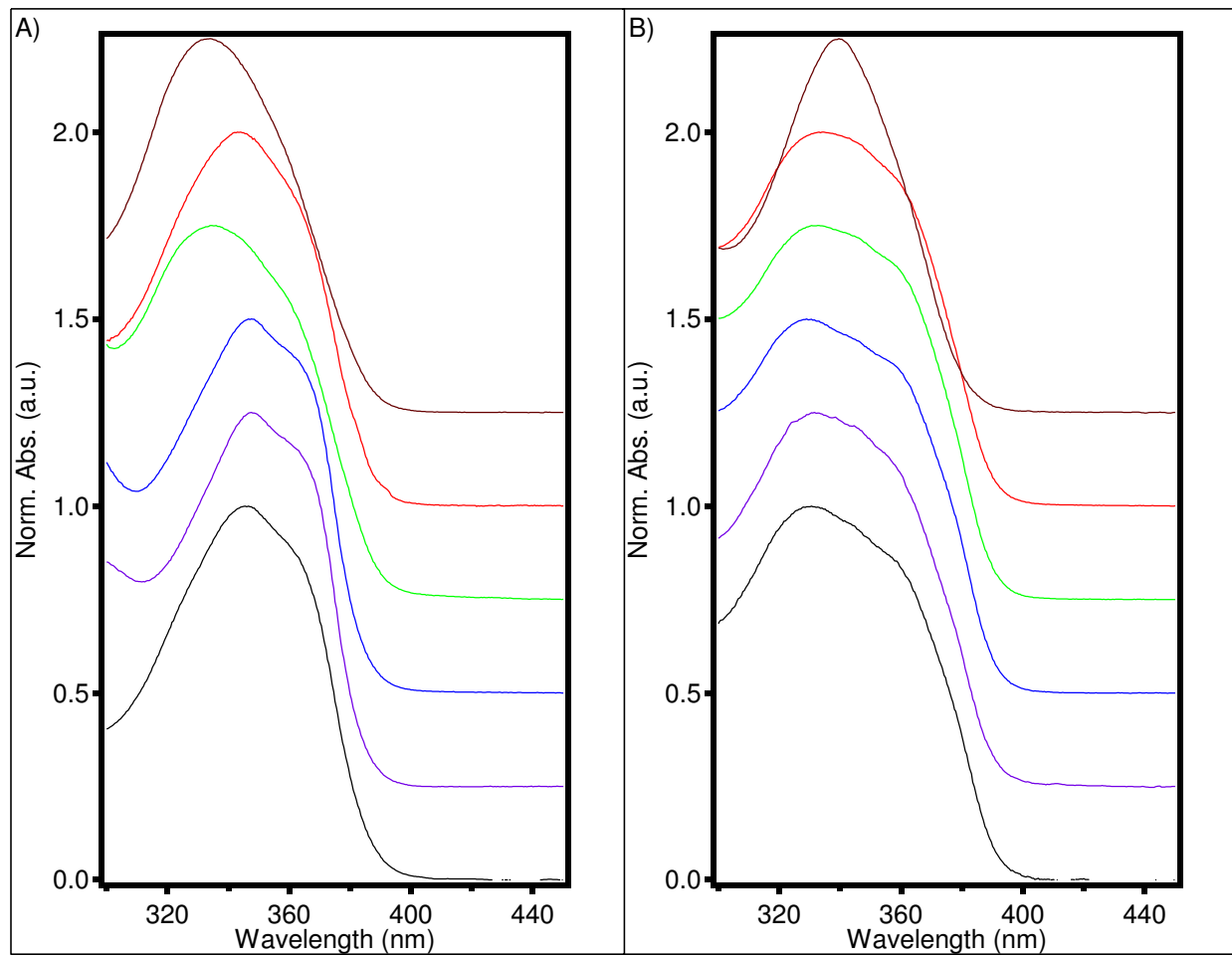


Figure 4.9: Absorption spectra of tta exchanged Eu(III) doped A) ZnAl_2O_4 (1% in black, 2.5% in purple, 4.7% in blue, 7.5% in green, 9.7% in red, and 12.7% in dark red) and B) ZnGa_2O_4 (1% in black, 2.5% in purple, 5% in blue, 8.7% in green, 12.4% in red, and 15.6% in dark red).

which was seen by Murray et. al.¹³⁴ Addition of tta results in the appearance of a feature at 1540 cm^{-1} which arises from the C=C and 1578 cm^{-1} for the enol C-O bond indicating M-O coordination of tta to the nanocrystal surface. Consistent with M-O coordination, the keto C=O vibration observed in unbound tta is not observed and the C=C peak is shifted from 1600 cm^{-1} to 1540 cm^{-1} . Similar shifts were reported for the C-O vibration following acac coordination to Y_2O_3 nanocrystals.¹³²

Further confirmation of tta exchange is evidenced in the optical absorption spectra of the tta passivated samples (Figure 4.9). Prior to exchange, the acac $^1\pi \rightarrow ^1\pi^*$ absorption is visible at 290 nm, as reported in the previous study of acac passivated Eu: Y_2O_3 .¹³² After the tta exchange,

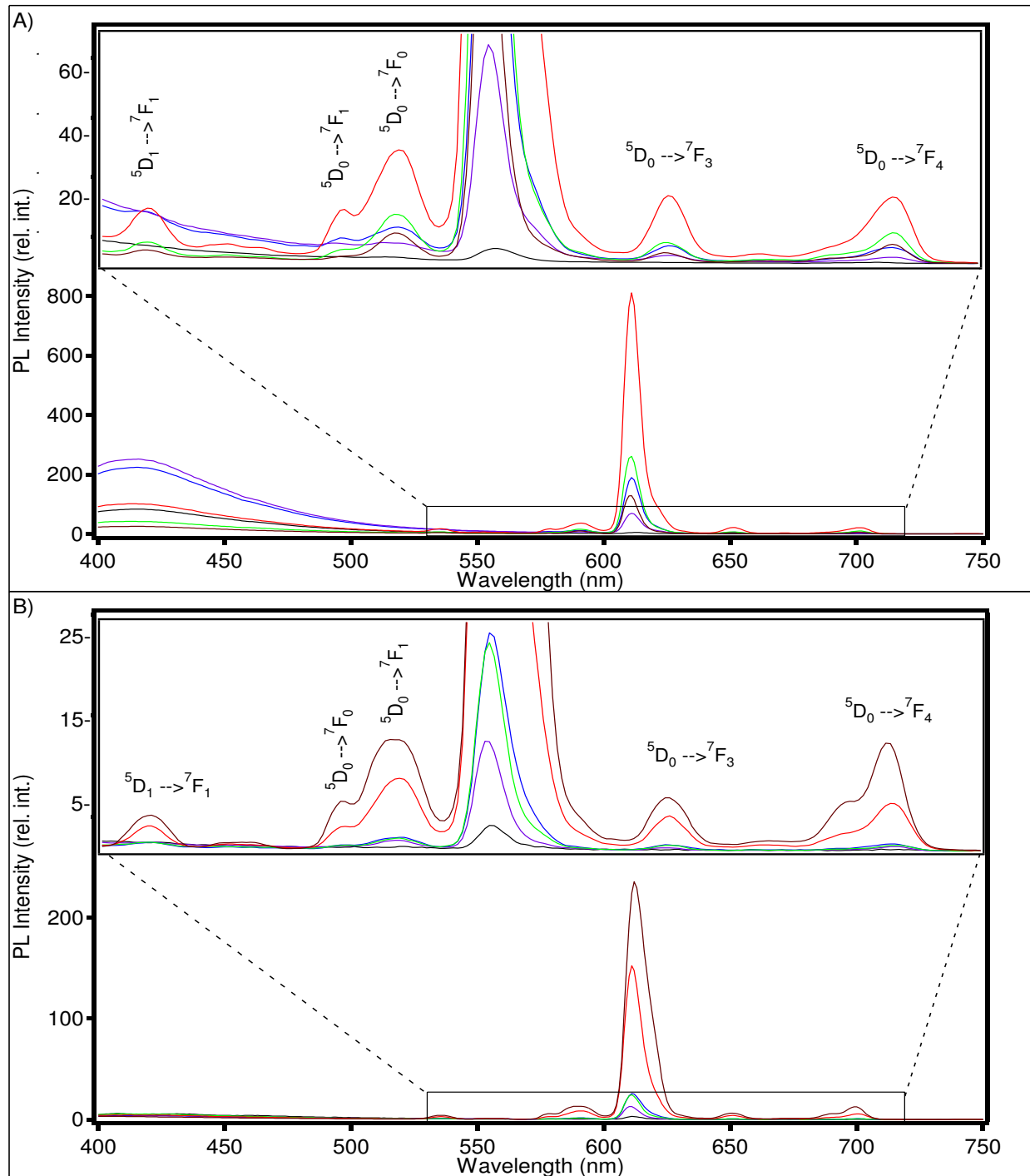


Figure 4. 10: Photoluminescence spectra of tta passivated samples with different concentrations of Eu(III) doped in **A**) ZnAl₂O₄ (1% in black, 2.5% in purple, 4.7% in blue, 7.5% in green, 9.7% in red, and 12.7% in dark red) and **B**) ZnGa₂O₄ (1% in black, 2.5% in purple, 5% in blue, 8.7% in green, 12.4% in red, and 15.6% in dark red). The samples were dissolved in toluene and the PL spectra collected at room temperature.

the absorption feature at 340 nm can be assigned as the $^1\pi \rightarrow \pi^*$ transition for tta. The spectra exhibits a shoulder at lower energy, which may arise from changes to the local coordination environment differences for tta-Zn, tta-Al, and tta-Eu. The spectral features evolve with Eu(III) concentration (Figure 4.9). The absorption spectra of the samples containing the highest concentration of Eu(III) for the Eu:ZnB₂O₄ nanospinels are similar to the absorption of Eu(tta)₃(phen).¹⁵¹ Changes in the spinel lattice with increasing lattice disorder may change the β -diketonate absorption properties, as suggested by Serafin et al.⁸⁷ who has suggested the absorption energy and shape for β -diketonates is highly dependent on ligand resonance conditions. The changes in the absorption spectra therefore may reflect lattice reconstruction at the nanospinel surface with increasing Eu(III) ion incorporation at the B-site. Lattice disorder with increasing Eu content was inferred from interpretation of the XANES and EXAFS data in Figure 4.1, but cannot be considered conclusive with respect to the absorption changes.

The absorption spectra for the Eu doped samples when passivated with acac show a strong $^1\pi \rightarrow \pi^*$ absorption feature at 300 nm for the acac in both samples. The band gap energies are estimated to be 3.6 eV for ZnAl₂O₄ and 3.7 eV for ZnGa₂O₄. The bandgap energies reported in the literature for the lattices are 3.8 eV in ZnAl₂O₄ and 4.1 eV for ZnGa₂O₄.¹⁵² For the ZnAl₂O₄ sample, a defect feature associated with oxygen vacancies at the nanospinel surface is observed at 360 nm.¹⁵² In ZnGa₂O₄ no Ga-O oxygen defect absorption feature is observed. Ligand exchange for tta results in a loss of the defect absorption feature in ZnAl₂O₄ and the appearance of a broad transition centered at 340nm, which can be assigned to the tta $^1\pi \rightarrow \pi^*$ transition.

The PL properties of 12.7% Eu:ZnAl₂O₄ and 15.6% Eu:ZnGa₂O₄ samples passivated by acac (blue) or tta (red) are plotted in Figure 4.8A and Figure 4.8B respectively. The impact of tta passivation on the PL spectra is evidenced by the dramatic change in the solution emissivity and color following tta exchange onto the nanospinel surface (Figure 4.8E). Eu(III) concentration dependent absorption (Figure 4.9) and PL (Figure 4.10) spectra are shown for the nanospinel samples.

The observed PL for the nanospinel samples passivated by acac excited at $\lambda_{ex} = 340$ nm can be assigned to emission from the self-activation centers (traps) of the type octahedral B–O groups (B = Al³⁺ or Ga³⁺, Al → O and Ga → O, $\lambda = 380$ -450 nm).¹⁵³ In ZnGa₂O₄, weak Eu(III) emission is also evident in Figure 4.10D for the $^5D_0 \rightarrow ^7F_4$ J-O level. The self-activation centers

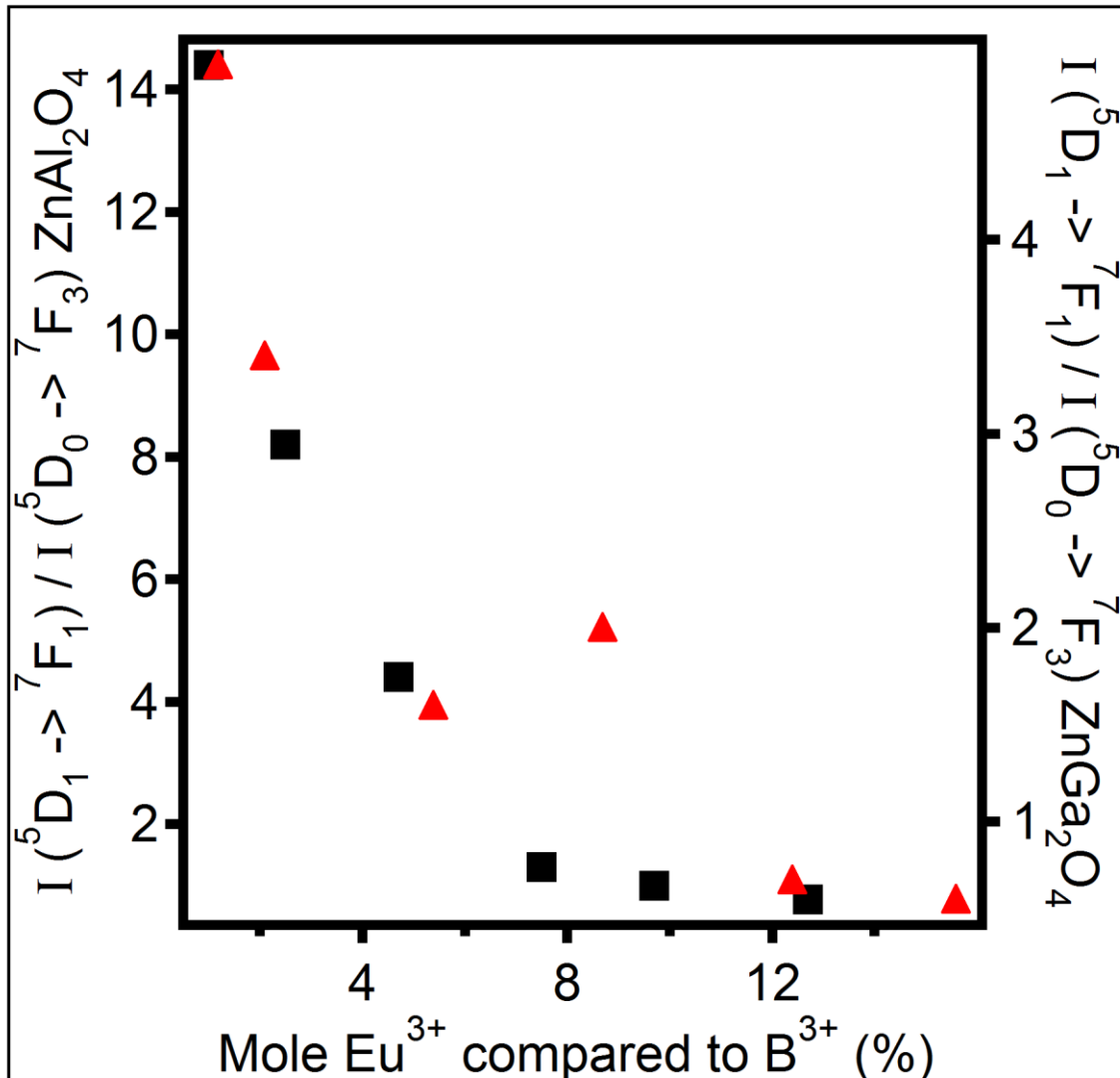


Figure 4.11: Ratio of the integrated intensities of the ${}^5D_1 \rightarrow {}^7F_1$ line to the ${}^5D_0 \rightarrow {}^7F_3$. Higher ratios generally indicate that there are longer Eu-Eu distances.

are attributed to the oxygen vacancies and produce donor states at the Fermi level leading to a broad structured emission profile reflecting the distribution of energies for the vacancy centers. The weak (Eu:ZnGa₂O₄) or non-existent (Eu:ZnAl₂O₄) Eu(III) emission for the samples following excitation into the bandgap reflects the poor energy overlap between the spinel energy levels and the Eu(III) 5D_0 levels.

Following tta exchange, there are significant changes to the observed PL spectra. Excitation at $\lambda_{ex} = 340$ nm leads to population of the tta ${}^1\pi \rightarrow \pi^*$ transition and strong Eu(III) J-O ${}^5D_0 \rightarrow {}^7F_j$ line emission is observed. The PL of the Eu:ZnAl₂O₄ has a fairly significant

Table 4.2: The sensitization efficiency and QEs (Φ) in solution, in a PMMA matrix, and intrinsic

Eu ³⁺		Eu:ZnAl ₂ O ₄	
(%)	Φ_{soln} (Eu ³⁺)	τ_1 (μs)	Φ_{PMMA} (total)
1	0.07 ± 0.03	489 ± 5	0.05 ± 0.00
2.5	0.10 ± 0.06	519 ± 5	0.19 ± 0.01
4.7	0.14 ± 0.08	520 ± 5	0.21 ± 0.01
7.5	0.16 ± 0.05	510 ± 5	0.41 ± 0.02
9.7	0.28 ± 0.08	509 ± 5	0.50 ± 0.03
12.7	0.07 ± 0.01	525 ± 5	0.11 ± 0.01

Eu ³⁺		Eu:ZnGa ₂ O ₄	
(%)	Φ_{soln} (Eu ³⁺)	τ_1 (μs)	Φ_{PMMA} (total)
1.2	0.03 ± 0.00	491 ± 5	0.05 ± 0.00
2.1	0.01 ± 0.00	514 ± 5	0.20 ± 0.01
5.4	0.05 ± 0.00	539 ± 5	0.20 ± 0.01
8.7	0.08 ± 0.01	497 ± 5	0.21 ± 0.01
12.4	0.15 ± 0.01	511 ± 5	0.25 ± 0.01
15.6	0.14 ± 0.02	592 ± 6	0.04 ± 0.00

emission from the tta ligand centered transition leading to emission in the blue region, while ZnGa₂O₄ shows very little emission in the blue. The more efficient population of the Eu(III) J-O levels in the Eu:ZnGa₂O₄ may reflect differences in surface termination leading to differences in tta surface densities, the impact of the size resulting in more tta per unit volume, or potentially differences in Eu(III) distribution between core and surface leading to modification of the energy transfer efficiencies from tta to Eu(III). It was noted that increasing Eu(III) concentrations lead to smaller nanospinels. The small size of the nanospinels results in larger surface to volume ratios,

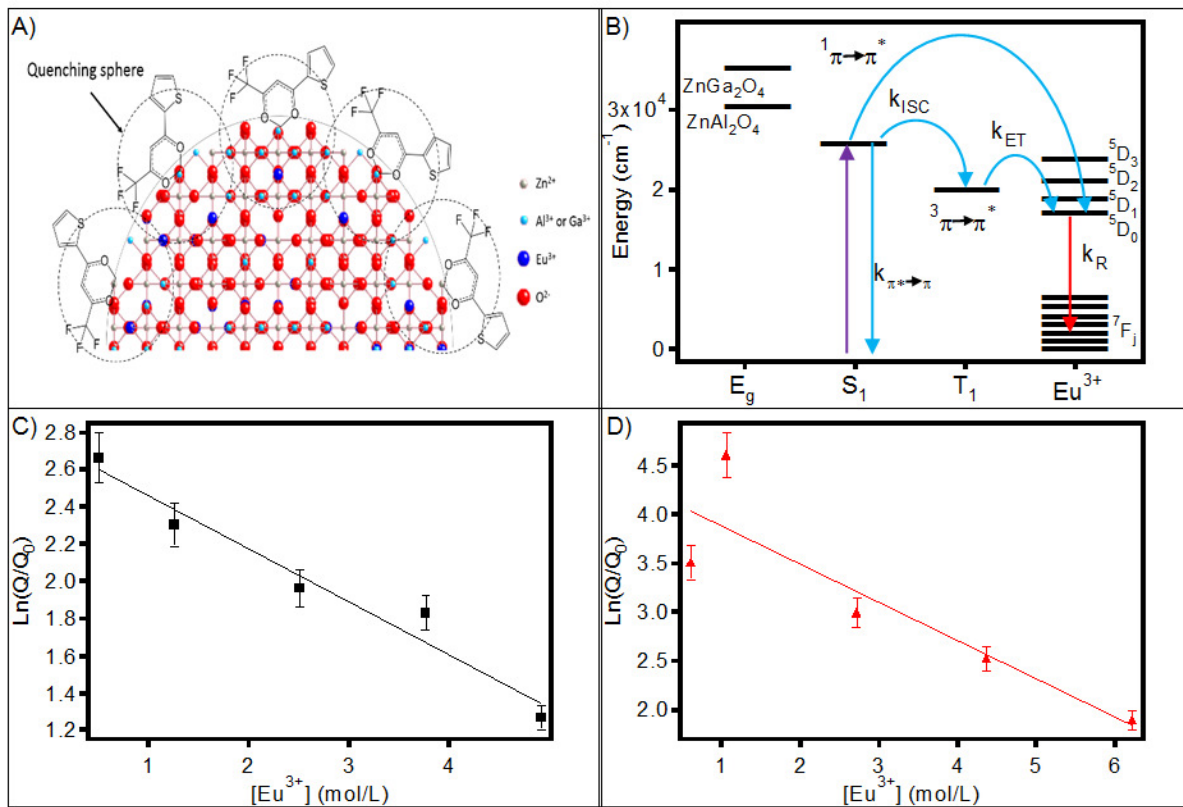


Figure 4.12: A) tta passivated Eu(III) doped ZnB_2O_4 crystal lattice (3 nm) showing the approximate range of the quenching spheres according to a Dexter mechanism. B) Energy level diagram indicating the singlet and triplet levels for tta relative to the Judd-Olfelt allowed transition in Eu(III) and the spinel band gaps. Perrin plot of A) ZnAl_2O_4 (radius of quenching = 0.48 ± 0.02 nm) and B) ZnGa_2O_4 (radius of quenching = 0.54 ± 0.03 nm).

which in turn can lead to a large number of tta ligands on the surface relative to the amount of Eu(III) per particle.

In the PL for the tta exchanged nanospins, the most intense feature is the electronically allowed $^5\text{D}_0 \rightarrow ^7\text{F}_2$. The $^5\text{D}_1 \rightarrow ^7\text{F}_1$ is observed weakly in the spectra, as well as the $^5\text{D}_0 \rightarrow ^7\text{F}_1$ magnetically allowed J-O transition. The weakness of the magnetically allowed transition is consistent with the assignment of the Eu(III) center occupying an asymmetric site, as suggested by the XAS data (Figure 4.1).¹⁵⁴ The $^5\text{D}_1 \rightarrow ^7\text{F}_1$ peak is seen in the PL spectra for all the samples. The $^5\text{D}_1 \rightarrow ^7\text{F}_1$ is typically not observed in Eu(III) spectra and is only observed when the Eu-Eu ions are not nearest neighbors, as would be observed if Eu was not clustering within the lattice.¹⁵⁵ In Eu(III) complexes dispersed in a polymer, it is observed that the ratio of the $^5\text{D}_1$

$\rightarrow ^7F_1$ to $^5D_0 \rightarrow ^7F_3$ decreases as the concentration of the Eu(III) ion increases, which is correlated to the Eu-Eu contact distance.¹⁵⁵ In the spinel samples, it is observed that the ratio of $^5D_1 \rightarrow ^7F_1$ to $^5D_0 \rightarrow ^7F_3$ also decreases with increasing Eu concentration, which reflects the growing Eu-Eu interactions in the nanospinels samples, Figure 4.10 and 4.11. The XAS data can be interpreted as supporting this conclusion, as an additional absorption feature arises in the XANES spectra if clustering of the Eu ions is present.¹⁵⁰

The internal QEs (Φ_{soln}), the excited state lifetimes for the $^5D_0 \rightarrow ^7F_2$ transition, and the absolute QE of the nanospinels in PMMA are compiled in Table 4.2. The internal QEs (Φ_{soln}) are QEs for the Eu(III) J-O levels from 530 to 710 nm, measured relative to Eu(tta)₃phen, while the intrinsic QE ($\Phi_{\text{intrinsic}}$) is extracted from the lifetime and PL spectral profile.¹⁴³ Inspection of Table 4.2 shows the excited state lifetimes for the Eu(III) site are nearly independent of concentration; however the observed Eu(III) QE is dependent on Eu(III) concentration. The experimental lifetime is consistent with measured Eu(III) decay behavior for Eu(III) ions occupying an octahedral site within a host lattice.¹⁵⁶

The QE for the Eu(III) line increases linearly with Eu(III) concentration for the spinel dissolved in solution and in PMMA. The linear increase is consistent with the predicted energy transfer coupling mechanism between the tta ligand excited states and the Eu(III) J-O levels, as shown in Figure 4.12A-B. The maximum observed QE in solution is $\Phi_{\text{soln}} = 27.7\%$ at a doping level of 9.7% Eu for ZnAl₂O₄ and $\Phi_{\text{soln}} = 14.6\%$ for 12.4% Eu in ZnGa₂O₄. The QE in PMMA is $\Phi_{\text{PMMA}} = 50.0\%$ at 9.7% Eu for ZnAl₂O₄ and $\Phi_{\text{PMMA}} = 25.3\%$ for 12.4% Eu in ZnGa₂O₄. Contributions from self-quenching appear for the highest Eu(III) concentrations in both cases. The Eu(III) concentration dependent PL behavior is plotted in Figure 4.13. The intensity of the $^1\pi \rightarrow \pi^*(\text{tta})$ emission relative to the Eu(III) $^5D_0 \rightarrow ^7F_2$ line is plotted in Figure 4.13A, with values tabulated in Table 4.3. The plot exhibits a sigmoidal intensity dependence with increasing Eu(III) line emission as the Eu(III) content is increased for both Eu:ZnAl₂O₄ and Eu:ZnGa₂O₄. For Eu:ZnAl₂O₄, the ratios are below 1 due to the contribution from the tta ligand emission. Figure 4.13B shows the Eu(III) concentration dependent intrinsic quantum yield, where a near linear dependence is observed over the experimental concentration range. The observation of a high QE at concentrations at or above 10% is surprising, as typically self-quenching in material is observed near 6% due to close Eu-Eu distances.^{132, 157} The observation likely reflects the lack of Eu-Eu pair formation in the spinel lattice, as compared to Y₂O₃.

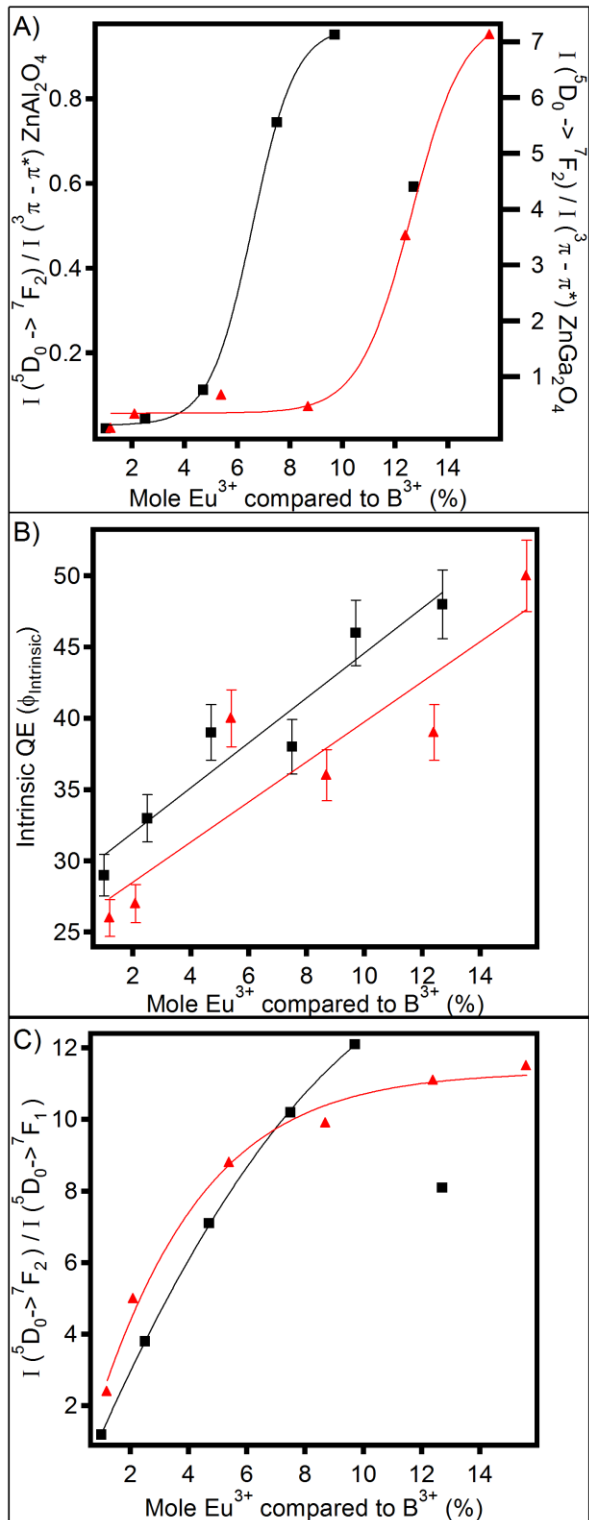


Figure 4.13: A) Ratio Eu³⁺ emission versus tta emission ($I_{612\text{nm}}/I_{420\text{nm}}$) Eu³⁺ doped ZnAl₂O₄ and ZnGa₂O₄ as a function of concentration. B) Intrinsic QE of the Eu³⁺ emission in the spinels as a function of Eu³⁺ concentration. C) Red orange ($I_{612\text{nm}}/I_{580\text{nm}}$) ratio of Eu³⁺ doped ZnAl₂O₄ and ZnGa₂O₄ as a function of concentration. ZnAl₂O₄ is in black and ZnGa₂O₄ in red.

In addition to the change in QE for the Eu(III) J-O lines, the ratio of the magnetic ($^5D_0 \rightarrow ^7F_1$) to electronic ($^5D_0 \rightarrow ^7F_1$) dipole allowed transition is observed to change with dopant level and the B ion in the spinel. In Figure 4.13C the R/O ratio ($I(^5D_0 \rightarrow ^7F_2) / I(^5D_0 \rightarrow ^7F_1)$) for the samples is plotted, with values tabulated in Table 4.3. The ratio exhibits a non-linear response with increasing concentration of Eu(III). The change in R/O ratios likely reflects the Judd-Ofelt selection rules, where loss of site symmetry results in increased intensity from the electronically allowed transition. The loss of site symmetry is consistent with the findings in the XAS data in Figure 4.1, and therefore can be interpreted as reflecting the lattice strain induced by incorporation of the larger Eu(III) ion onto the B-site in the spinel. Strain effects for Eu(III) in a host lattice has been shown to produce an increase in the electric dipole component ($^5D_0 \rightarrow ^7F_2$) and a decrease in the magnetic dipole component ($^5D_0 \rightarrow ^7F_1$).¹⁵⁸ Alternatively, the R/O ratio changes may be influenced by the decrease in particle size with increasing Eu(III) content, resulting in optical broadening which is often invoked to explain the optical differences from bulk to nano in phosphors.¹⁵⁹

4.3.3 Molecular Energy Sensitization of Eu(III) Centers

The observed increased Eu(III) QE and Eu line emission relative to the B-O self-activation PL following tta exchange reflects improved energy transfer from the $^1\pi \rightarrow ^1\pi^*$ excited state on the tta to the Eu(III) emissive centers, as shown in Figure 4.13. Alternatively, population of the triplet level and transfer from the triplet to the 5D_0 energy level of the Eu(III) center may occur, with the difference of energy between the two dictating the efficiency of energy transfer, as postulated by Crosby, et al.⁹⁴ The difference in energy between the triplet of tta and the 5D_0 level of Eu(III) is 0.6 eV. The most favorable difference in energy between the donor and acceptor is 0.3eV for Eu³⁺ according to Latva's empirical rule,⁶³ indicating that improvements in energy transfer can be made to this model.

The transfer of energy from the ligand to the Eu(III) center and between centers is governed by a Dexter mechanism and will involve direct transfer between the centers through a resonant process, or can involve energy hopping. For Eu(III) doped nano-oxides, the efficiency of molecular antenna sensitized emission will scale as the number of molecular antenna bound to the nanoparticle surface increases and the separation distance between the sensitizer and the

Table 4.3: Intrinsic QEs ($\Phi_{\text{intrinsic}}$), sensitization, R/O Ratios, and intensity ratio of Eu³⁺/tta.

Eu ³⁺		Eu:ZnAl ₂ O ₄		
(%)	$\Phi_{\text{intrinsic}}$ (Eu ³⁺)	η_{sens}	R/O	$I_{\text{Eu(III)}}/I_{\text{tta}}$
1	0.29 ± 0.03	0.24	1.2	0.02
2.5	0.33 ± 0.03	0.30	3.8	0.05
4.7	0.39 ± 0.04	0.36	7.1	0.1
7.5	0.38 ± 0.04	0.42	10.2	0.7
9.7	0.46 ± 0.05	0.61	12.1	1.0
12.7	0.48 ± 0.05	0.15	8.1	0.6

Eu ³⁺		Eu:ZnGa ₂ O ₄		
(%)	$\Phi_{\text{intrinsic}}$ (Eu ³⁺)	η_{sens}	R/O	$I_{\text{Eu(III)}}/I_{\text{tta}}$
1.2	0.26 ± 0.03	0.12	2.4	0.08
2.1	0.27 ± 0.03	0.04	5.0	0.3
5.4	0.40 ± 0.04	0.13	8.8	0.7
8.7	0.36 ± 0.04	0.22	9.9	0.5
12.4	0.39 ± 0.04	0.38	11.1	3.5
15.6	0.50 ± 0.05	0.28	11.5	7.1

incorporated Eu(III) emissive centers decreases. In molecular analogues, it has been observed that the efficiency of sensitization of the Judd-Olfelt allowed $^5D_0 \rightarrow ^7F_j$ Eu(III) f-f transitions will vary as the energy difference of the ligand triplet $\pi-\pi^*$ energy level and the 5D_i Eu(III) levels, as defined by the $\langle J \rangle$ overlap integral. Ligand passivation of the nanophosphors has the added advantage of producing materials that are soluble, reducing the scattering losses inherently observed in traditional synthesized phosphors embedded in the lens matrix.¹⁵⁵

Taking into account the small changes in size with Eu(III) doping and the Dexter mechanism for energy transfer, the observed concentration dependent PL data can be interpreted

within the Dexter energy transfer theory using a non-diffusional Perrin model to treat the change in distance from *tta* to Eu(III) as a function of concentration.^{20, 21, 160} As shown in Figure 4.12A, in a non-diffusional model, the quenching can be defined over a fixed volume with respect to the absorber, in this case *tta*, and the emitter, which for the phosphor is the Eu(III) center. The distance of quenching will be influenced by the lattice parameters of the spinel.

Assuming a non-diffusional limit, the intensity of Eu(III) emission will scale as a function of the concentration of Eu, such that

$$\ln \left(\frac{Q}{Q_0} \right) = -VN_A[\text{Eu}] \quad (4.1)$$

where Q is the QE of the sample, Q_0 is taken to be 1, V is the volume of the quenching sphere, N_A is Avogadro's number, and [Eu] is the concentration of Eu(III) in mol/L. If quenching is assumed to be 100% efficient within a given radius from the center of the *tta* molecule to the center of the Eu(III) emissive center, a quenching sphere can be extracted by plotting the intensity ratio, $\ln(Q/Q_0)$, vs Eu(III) concentration, as shown in Figure 4.12. The plot is referred to as a Perrin plot and the slope is equal to $-N_A V$, or the quenching volume. The use of the spherical model is analogous to the idea of R_0 (50% quenching radius) in diffusional resonance energy transfer models.¹⁶¹

The measured radius for quenching for ZnAl_2O_4 and ZnGa_2O_4 is 0.48 ± 0.02 nm and 0.54 ± 0.03 nm respectively. The value of ~ 0.5 nm is consistent with reported literature R_0 values for Dexter energy transfer.^{20, 162} By conversion of the radius to lattice planes, Eu(III) ions within 3 lattice planes of the surface are efficiently pumped (>100% energy transfer) leading to $\sim 70\%$ of the total particle volume containing Eu(III) sites being directly accessible. Hopping within the lattice or less efficient transfer to deeper sites can also occur in the system, leading to the improved phosphor performance.

The difference in quenching radii for the ZnB_2O_4 (B= Al, Ga) lattice will reflect differences in the sensitization efficiency for the lattices. The sensitization efficiency (η_{sens}) for resonant energy transfer from *tta* to Eu(III) energy transfer can be calculated from the intrinsic QE for Eu(III) emission, since

$$\Phi_{\text{intrnsic}} = \eta_{\text{sens}} \Phi_{\text{Eu}} \quad (4.2)$$

where η_{sens} is the sensitization efficiency, and $\Phi_{\text{Eu}} = \tau_{\text{obs}} / \tau_r$. To solve for the intrinsic QE the radiative lifetime for the Eu(III) center is calculated using eqn 4.3

$$k_R = A_{(\text{MD},0)} n^3 (I_{\text{tot}}/I_{\text{MD}}) \quad (4.3)$$

where $A_{MD,0}$ is the Einstein spontaneous emission coefficient for the magnetic dipole transition ($^5D_0 \rightarrow ^7F_1$) in vacuum (determined to be 14.65 s^{-1} by Werts et al.), n is the refractive index of the solvent (toluene $n = 1.49$), and I_{tot} and I_{MD} are the integrated intensities of the total Eu(III) emission spectra and the $^5D_0 \rightarrow ^7F_1$ emission, respectively. From the data in Table 4.2, the intrinsic QE for the samples can be evaluated using eqns 4.1, 4.2, and 4.3, and are compiled in Table 4.3. The intrinsic QE for Eu(III) emission in the ZnB_2O_4 host lattice is a measure of the molecular sensitization by the tta molecular antenna. The experimental results show an increase in intrinsic QE with increasing Eu(III) concentration. The highest intrinsic QE is for the 12.7% Eu(III) in ZnAl_2O_4 with $\Phi_{\text{em}} = 48\%$ and for the 15.6% Eu(III) in ZnGa_2O_4 with a value of $\Phi_{\text{em}} = 50.0\%$. The observed internal and intrinsic QE for the Eu: ZnB_2O_4 nanospinels are higher than previously reported for tta exchanged YPO_4 particles, where a solution QE of 0.7 % and an intrinsic QE of 26 % was reported.¹⁴³ The calculated sensitization value of the Eu(III) by the tta molecular sensitizer (Table 4.3) exhibits a maximum value of $\eta_{\text{sens}} = 0.61$ for 9.7% Eu: ZnAl_2O_4 and $\eta_{\text{sens}} = 0.38$ for 12.4% Eu: ZnGa_2O_4 . The difference in sensitization ratios is consistent with the observed difference in quenching radii. Since the observed energy transfer sensitization and radius of quenching is consistent with literature reports the significant improvement in total phosphor QE in these samples likely reflects the smaller nanospinel sizes, as loss pathways are significant for materials larger than the critical distance.¹⁶³ It is possible that the difference in observed QE for the Al vs Ga samples may also reflect lattice hardness, as proposed by Seshadri, et al,¹⁶⁴ since the phonon frequency for ZnAl_2O_4 is higher than ZnGa_2O_4 .¹⁶⁵ Therefore the experimental observation is consistent with the Seshadri model; however the disorder of the Eu within the lattice site observed by XAS may play a larger role in defining the QE.

4.3.4 CIE Coordinates

A critical performance parameter for a down conversion phosphor is the position in the CIE coordinate. The CIE xy values equate to the actual coordinates of the perceived color on the CIE diagram with x and y axes. A white phosphor will have a CIE coordinate of 0.33, 0.33. In Figure 4.14, the Eu(III) concentration dependent optical coordinates are plotted on the CIE diagram and emissivity for simulated LED lenses for all Eu(III) concentrations in both ZnAl_2O_4 and ZnGa_2O_4

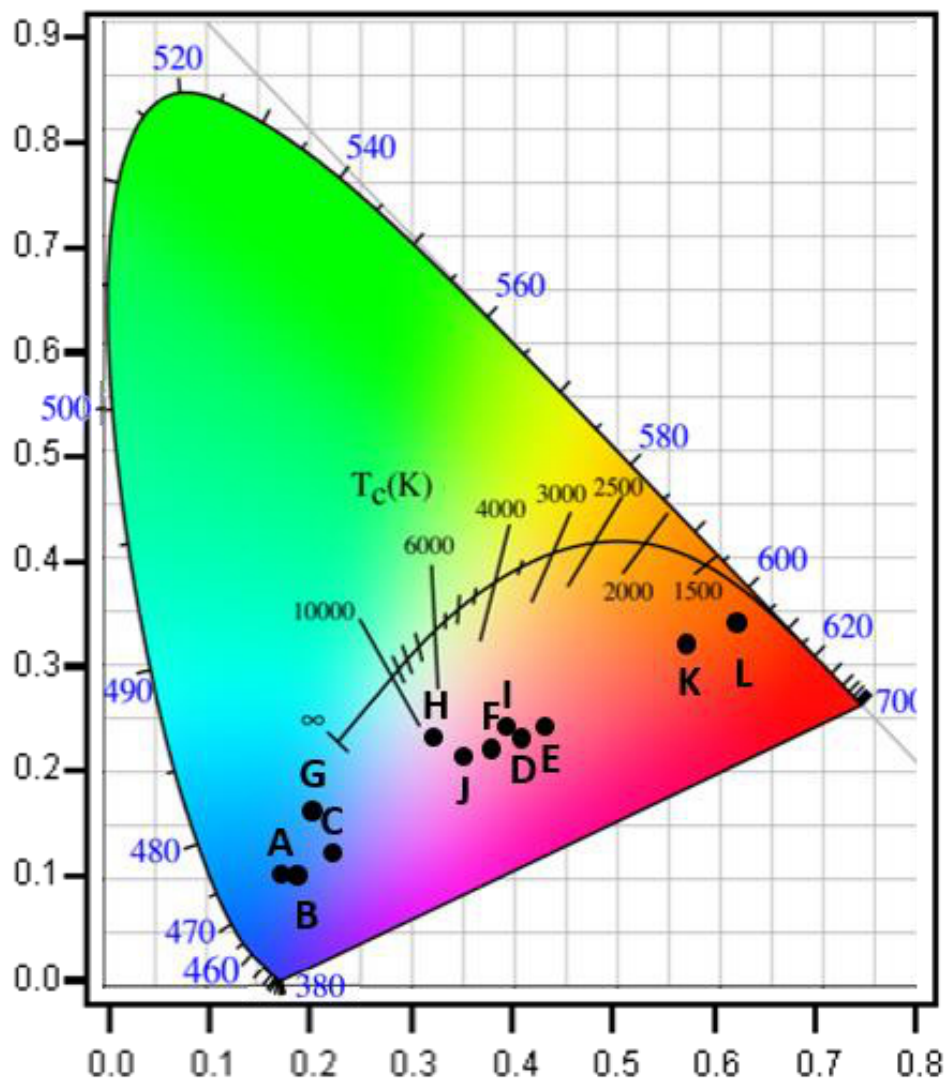


Figure 4.14: CIE diagram above for all the doped spinel samples with the solids excited at 364 nm embedded in a PMMA below. Eu doped ZnAl_2O_4 are represented by letters A-F, where A is 1% Eu: ZnAl_2O_4 and F is 12.7% Eu: ZnAl_2O_4 . Eu: ZnGa_2O_4 are represented by G-L where G is 1.2% Eu: ZnGa_2O_4 , and L is 15.6% Eu: ZnGa_2O_4 .

Table 4.4: CIE coordinates for tta exchanged Eu: ZnAl_2O_4 and Eu: ZnGa_2O_4 .

Host	% Eu ³⁺	Tristimulus values			CIE coordinates	
		X	Y	Z	x	y
ZnAl_2O_4	1	5192	2696	23581	0.16	0.09
	2.5	5679	2831	22922	0.18	0.09
	4.7	9456	4789	29529	0.22	0.11
	7.5	5731	3092	5436	0.40	0.22
	9.7	8321	4448	6596	0.43	0.23
	12.7	4731	2599	5188	0.38	0.21
ZnGa_2O_4	1.2	139	105	449	0.20	0.15
	2.1	518	355	750	0.32	0.22
	5.4	651	377	624	0.39	0.23
	8.7	717	414	916	0.35	0.20
	12.4	3922	2096	843	0.57	0.30
	15.6	6873	3621	574	0.62	0.33

is shown. The CIE coordinates are listed in Table 4.4. Increasing Eu(III) content results in a clear shift to red in the CIE diagram.

4.4 Conclusion

The preparation of Eu(III) doped nanospinels passivated by tta and grown near the critical nucleation size (2.4 nm) lead to enhanced molecular sensitization of the Eu(III) centers. Further ligand optimization may allow higher QEs to be realized. The synthesis of a 3 nm nanospinel leads to efficient energy transfer from the tta ligand shell excited states to the Eu(III) centers via the Dexter energy transfer process resulting in nearly 70% efficient pumping of the incorporated centers. Incorporating Eu(III) into the octahedral B-site for the nanospinel ZnB_2O_4 (B= Al(III) or Ga(III)) passivated by tta produces a highly efficient red down conversion

phosphor. The spinel represents an earth abundant host lattice that is thermally and oxidatively stable and allows the Eu ion to be incorporated to higher concentration without self-quenching. The distorted Oh site in the spinel lattice, evidenced in the XAS and optical data optimizes the red/orange ratio in these materials at higher Eu content leading to better overall performance. The QE for the phosphor reaches a value of ~50% in ZnGa₂O₄ with a red/orange ratio of 11. Similar results are observed for the ZnAl₂O₄ sample. Continued improvement of SSL devices requires high QE, a narrow emission linewidth (5.25 nm), tunability, thermal stability, and low cost.

CHAPTER 5

MOLECULAR SENSITIZATION OF RARE EARTH PHOSPHOR EMISSION IN METAL OXIDE NANOCRYSTALS

A systematic study of β -diketonate passivated nanophosphors was completed to look at the factors that contribute to color quality and quantum efficiency. Terbium and Europium were doped into two different host lattices (Y_2O_3 and ZnAl_2O_4) to gage the effects of dopant site and defect density on the optical properties of the rare earth ions, while a variety of different β -diketonates were used to test the factors that contribute to energy transfer efficiency. It was found that increased dopant site distortions lead to improved color quality in both Tb(III) and Eu(III) doped systems. This can be clearly seen in the ZnAl_2O_4 samples, where the dopants replace Al(III) in the lattice, which has a very small ionic radius compared to yttrium and the rare earth ions ($\text{Al}^{3+} = 0.54 \text{ \AA}$; $\text{Y}^{3+} = 0.96 \text{ \AA}$; $\text{Eu}^{3+} = 0.95 \text{ \AA}$; $\text{Tb}^{3+} = 0.92 \text{ \AA}$). The ZnAl_2O_4 lattice shows significantly more dopant induced site symmetry distortions, resulting in pure red and green emission from the nanophosphors as a result of the relaxation of the selection rules. In addition, the energy transfer efficiencies were tested as a function of intersystem crossing efficiency, triplet to lanthanide excited state energy difference, and the symmetry of the ligands themselves. The study shows that all three factors greatly influence the efficiency of energy transfer, and therefore the quantum efficiency of the nanophosphors themselves. The highest quantum efficiency for the Tb(III) doped systems was found using 1,1,1,5,5-Hexafluoro-2,4-pentanedione (hfacac), while 2-thenoyltrifluoroacetone (tta) resulted in the highest quantum efficiencies in Eu(III) nanophosphors.

5.1 Introduction

Solid state lighting has progressed rapidly to meet the demands of the evolving energy conundrum by producing high efficiency down conversion phosphors that simulate white light when pumped by a LED source.² While LED technology has improved dramatically, the available phosphors for producing white light are still based upon technology from decades ago. The traditional approach to down conversion phosphors relies on rare earth (RE) ions as the emitters in phosphor technology.^{82, 166} While RE(III) and RE(II) based down conversion

phosphors have been known for decades in bulk oxide materials, a desire to prepare these materials as nanocrystals to reduce scattering, improve color quality by substitutional doping onto non-centrosymmetric lattice sites, develop earth abundant host lattices to replace Y_2O_3 , and use passivants that increase miscibility is driving a revitalization of the field. Furthermore, the passivants can act as molecular sensitizers to enhance quantum efficiency as well as allow excitation by UV and blue LEDs.^{11, 143}

In this chapter, the passivant ligand dependent efficiency of molecular sensitization of Eu(III) and Tb(III) incorporated into spherical ZnAl_2O_4 and Y_2O_3 nanocrystals passivated by a selection of β -diketonate ligands is investigated. The lanthanide loading level is 10% for the 2.85 nm (ZnAl_2O_4) and 4.2 nm (Y_2O_3). A series of symmetric and asymmetric β -diketonate ligands with $^1\pi \rightarrow \pi^*$ energy levels between 3.22 eV (385 nm, 2.thenoyltrifluoroacetone (tta)) and 4.09eV (303 nm, 1,1,1.Trifluoroacetylacetone (tfacac)) were investigated. The ligand dependent study to assess the optimal $\pi \rightarrow \pi^*$ energy levels in order to efficiently populate Tb^{3+} and Eu^{3+} emissive centers incorporated into ZnAl_2O_4 and Y_2O_3 host nanocrystals is carried out on identical samples isolated from a single reaction batch. The nanocrystal host is ligand exchanged with the desired β -diketonate in order to allow direct comparison of the optical performance between samples without introducing sample variability between reactions. Correlation of the RE emission quantum yield, excited state lifetimes, and the spectral profile as a function of the energy for the $\pi \rightarrow \pi^*$ levels in the β -diketonate ligand are reported.

The results indicate that highest Φ_{em} for Eu(III) is 35% for tta passivated ZnAl_2O_4 , while a value of 17% in tta passivated Y_2O_3 is observed. The difference in ZnAl_2O_4 and Y_2O_3 is believed to reflect site disorder and self-quenching in the Y_2O_3 sample, as previously reported. In Tb(III), the optimum efficiency is observed for hfacac with a Φ_{em} of 25% in ZnAl_2O_4 and 16% in Y_2O_3 . The experimental observation of very different Φ_{em} for tfacac and hfacac, which have identical $^3\pi \rightarrow \pi^*$ levels, but markedly different $^1\pi \rightarrow \pi^*$ energy levels indicate that intersystem crossing efficiency of the ligand, as influenced by the triplet to singlet energy difference, is critical. The results are in good agreement with predictions from Dexter models for energy transfer from the appended molecular antenna to the RE³⁺ emitter ions embedded in the host lattice, as well as the earlier reported findings in molecular compounds of Tb^{3+} and Eu^{3+} complexed with modified pyridine chelates, where both the $\pi \rightarrow \pi^*$ energy level and the triplet to singlet energy difference is crucial in choosing the molecular sensitizer.⁶³

The study shows that the emission of rare earth (RE) ions doped into a nanocrystal will depend on the RE site symmetry, its location within the host (surface/core), host lattice composition, and can be affected by non-radiative pathways.^{10, 167} Investigation by our group and others has demonstrated that the singlet state of the passivant can be excited directly, which following intersystem crossing to the triplet state, directly populates the RE emitter.^{143, 168, 169} Although several researchers have suggested that selection of the passivating group can enhance the nanophosphor performance in analogy to the enhancement of quantum efficiencies for molecular compounds containing RE ions, no systematic study has been reported.^{143, 169, 170} The relaxation process is both energy and distance dependent as described within the Dexter mechanism.²⁰ By systematic ligand exchange of the nanocrystal phosphors doped by Eu(III) and Tb(III), the quantum efficiency, color purity, and optimal ligand energies can be defined to produce a high efficiency down conversion phosphor. The improved efficiency in 3 nm ZnAl₂O₄ nanocrystals compared to the traditional Y₂O₃ host is traceable to the lower surface defect densities in the nanospinel, formation of a non-centrosymmetric site for the RE(III) ion leading to better R/O levels, and the higher phonon frequency for M-O vibrational modes making this earth abundant lattice a potentially important replacement host for new down conversion solid state lighting phosphors.

5.2 Experimental Section

5.2.1 Materials

All commercially available reagents and solvents, with the exception of dimethylformamide (DMF) were used without further purification. DMF was dried over molecular sieves. The passivating ligands are 2.thenoyltrifluoroacetone (tta, Matrix Scientific, 99%), 2,4.pentanedione (acac, Alfa Aesar, 99%), 6,6,7,7,8,8,8-heptafluoro-2,2.dimethyl-3,5.octanedione (fod, Oakwood Chemicals, 98%), 2,2,6,6-Tetramethyl-3,5.heptanedione (tmhd, Alfa Aesar, 99%), 1,1,1.Trifluoroacetylacetone (tfacac, Oakwood Chemicals, 98%), 1,1,1,5,5,5.Hexafluoro-2,4.pentanedione (hfacac, Alfa Aesar, 98+%Zinc (II) Undecylenate (Spectrum, 98%), Oleylamine (Aldrich, 70%), Hexadecylamine (Aldrich, 90%), NOBF₄ (Alfa Aesar, 98%). The metals are Aluminum (III) 2,4.pentanedionate (Strem Chemicals, 99%), Yttrium (III) 2,4.pentanedionate (Aldrich, 99.99%), Europium (III) 2,4.pentanedionate hydrate (Alfa Aesar, 99.9%), and terbium (III) 2,4.pentanedionate hydrate (Alfa Aesar, 99.9%).

5.2.2 Synthesis of Nanocrystals

Doped ZnAl₂O₄ nanocrystals passivated by 2,4.pentadione (*acac*) were prepared by microwave induced decomposition of zinc (II) undecylenate (Zn(UND)₂), aluminum (III) 2,4.pentanedionate (Al(*acac*)₃) and europium (III) 2,4.pentanedionate hydrate (Eu(*acac*)₃) or terbium (III) 2,4.pentanedionate hydrate (Tb(*acac*)₃) dissolved in oleylamine (OAm) using a CEM Discover Microwave (MW) operating under single mode, continuous power at 2.45 GHz. The CEM MW cavity was commercially modified by CEM with a Teflon insert to allow for sustainable heating at 300°C. To synthesize Eu:ZnAl₂O₄, a glass microwave reactor vessel was loaded with Zn(UND)₂ (0.108 g, 0.25 mmol), Eu(*acac*)₃ (0.0225 g, 0.05 mmol), Al(*acac*)₃ (0.146 g, 0.45 mmol), and OAm (4mL). The MW vessel was sealed, and the reactants were sonicated until the solid dissolved, (approximately 30 min). The MW vessel was then inserted into the MW cavity and heated at 300 W to 280°C for 5 min. The solution was cooled to 50°C and the Eu:ZnAl₂O₄ nanocrystals were precipitated by addition of toluene (~5 mL) followed by MeOH (~5 mL). The product was isolated for centrifugation, washed four times using toluene/EtOH, and dried under vacuum overnight. The isolated sample is white to tan in color and can be dispersed in toluene or chloroform. Tb:ZnAl₂O₄ was made in the same way, except that Terbium (III) 2,4.pentanedionate hydrate (0.0236 g, 0.05 mmol) was used instead of Eu(*acac*)₃. Terbium and europium doped Y₂O₃ weres synthesized using MW heating as well.

For synthesis of RE:Y₂O₃, Yttrium (III) 2,4.pentanedionate (0.193 g Y(*acac*)₃, 0.5 mmol) and Eu(*acac*)₃ (0.0225 g, 0.05 mmol) or Tb(*acac*)₃ (0.0228 g, 0.05 mmol) were added to hexadecylamine (1.932 g HDA, 8 mmol) loaded into a glass MW vial, sealed, and then inserted into the MW cavity and heated at 300 W to 240°C for 15 min. The cleanup procedure was the same as for the ZnAl₂O₄.

5.2.3 Ligand Exchange Protocol

Surface exchange of the passivant layer on the nanocrystal following synthesis by tta, *acac*, fod, hfacac, tfacac, or tmhd is accomplished by treatment of 25 mg of the nanoparticle dispersed in 5 mL toluene with 5 mL of 0.01 M NOBF₄ in anhydrous DMF under N₂. The dispersion is allowed to react for 5min, and the precipitate is collected by centrifugation and washed with acetone (2x). For all the ligands except hfacac, the resultant precipitate is added to a stirring mixture containing 1 ml of anhydrous DMF, 2 mL toluene, and 50 mg of the desired

ligand. The dispersion is then heated to 60°C until the solution is clear (~ 30 min). The passivated nanoparticles are isolated from solution by addition of acetone and collection by centrifugation. Hfacac passivated nanophosphors are soluble in acetone, therefore the stripped particles are dispersed in acetone instead of toluene, then precipitated with distilled water. The resultant nanoparticles are soluble in a variety of organic solvents.

5.2.4 Measurements

Atomic composition was measured using ICP-MS. All the nanophosphor samples were analyzed in 0.44 M HNO₃. Acids, ICPMS standards, and samples were prepared using 18.3 MΩ·cm ultra-high-purity (UHP) water. Optima® (Fisher Scientific, Pittsburg, PA, USA) grade nitric and hydrochloric acid were used for analyte matrix preparation. Analyte blanks of the UHP water, acids, and elemental standards were closely monitored throughout the entire experiment. The accurate molarity of each batch of acid was determined by titrimetric methods. The labware was acid cleaned using reagent grade 8.0 M HNO₃ at sub-boiling temperature (~80 °C). All calibration standards were prepared gravimetrically from high-purity standards (HPS).. Element concentrations were determined using an Agilent 7500cs single collector quadrupole-ICPMS instrument (Agilent Technologies, Santa Clara, CA, USA) equipped with an Octopole Collision/Reaction Cell (CRC). The instrument was operated under hot plasma (1500 W) conditions and in Reaction Mode (H₂ = 4.2 - 4.7 mL min⁻¹). The sample introduction consisted of a nominal 100 μL min⁻¹ self-aspirating concentric Teflon nebulizer, a Scott-type quartz spray chamber, a quartz torch with built-in quartz injector (2.5 mm i.d.), and nickel sampler and skimmer cones (all supplied by Elemental Scientific, Inc., Omaha, NE, USA). The instrument was tuned daily to optimize sensitivity and stability (percentage relative standard deviation (%RSD) ≤1.5%) for ⁷Li+, ²⁴Mg+, ⁵⁹Co+, ⁸⁹Y+, ¹⁴⁰Ce+, and ²⁰⁵Tl+, as well as to optimize the H₂ gas flow. A set of multi-element external calibration standards was used that covered an analyte concentration range of 0.1 to 100 μg L⁻¹.¹⁷¹

Structural characterization was performed using powder X-ray diffraction (pXRD) recorded on a Rigaku DMAX 300 Ultima III Powder X-ray diffractometer (using Cu Kα λ = 1.5418 Å radiation). The size of the nanocrystals were measured by fitting the pXRD pattern to the Scherrer broadening equation.

Size, size dispersity, morphology, and structure were analyzed by TEM using a JEOL-2010 microscope operated at 200 kV. The undoped samples were dispersed on holey carbon grids (400 mesh) from a toluene solution. Image analysis of >100 nanocrystals was used to generate the size distribution curves.

Ligand passivation was analyzed by Fourier transform infrared (FT-IR) measured on powdered samples using a PerkinElmer Spectrum 100 FT-IR Spectrometer equipped with an attenuated total reflectance (ATR) sample chamber consisting of a ZnSe crystal over coated with diamond using a single-bounce configuration.

Optical spectra were obtained in toluene with the exception of hfacac which was measured in acetone in a 1cm³ quartz cuvette under ambient conditions. Absorption was measured on Varian Cary 50 UV-vis spectrophotometer, while photoluminescence ($\lambda_{\text{em}} = 315$ nm (acac, tmhd, tfacac) or 340 nm (hfacac, fod, tta) and photoexcitation (Eu(III): $\lambda_{\text{ex}} = 613$ nm, Tb(III): $\lambda_{\text{ex}} = 544$ nm) were carried out on a Varian Cary Eclipse fluorescence spectrophotometer. Relative quantum yields for the solution were obtained by comparing to a reference standard Eu(tta)₃phen ($\Phi_{\text{em}} = 0.356$ at $\lambda_{\text{ex}} = 360$ nm) using eqn 1.¹⁷²

$$\frac{\Phi_S}{\Phi_R} = \frac{I_S}{I_R} \times \frac{1-10^{-A_R}}{1-10^{-A_S}} \times \frac{\eta_S^2}{\eta_R^2} \quad (5.1)$$

Lifetimes measurements were measured using a Quanta-Ray pulsed Nd-YAG laser pumped at 366nm. The instrument was coupled to a photo-multiplier tube, and decays were recorded through an oscilloscope interfaced with a computer. The data was fit to a single exponential decay using a non-linear regression analysis.

5.3 Results

5.3.1 Nanoparticle Structure

The downshifting nanocrystals RE:ZnAl₂O₄ and RE:Y₂O₃; where RE(III) = Tb³⁺ and Eu³⁺; are doped at 10% RE ion based upon ICP-MS analysis. The nanocrystals are prepared by a microwave enhanced thermal decomposition reaction of a M(acetylacetone)₃ in oleylamine producing spherical and crystalline 3nm RE:ZnAl₂O₄ and 4nm RE:Y₂O₃ as evidenced by TEM imaging and pXRD analysis. The surface passivant from the reaction mixture for the isolated

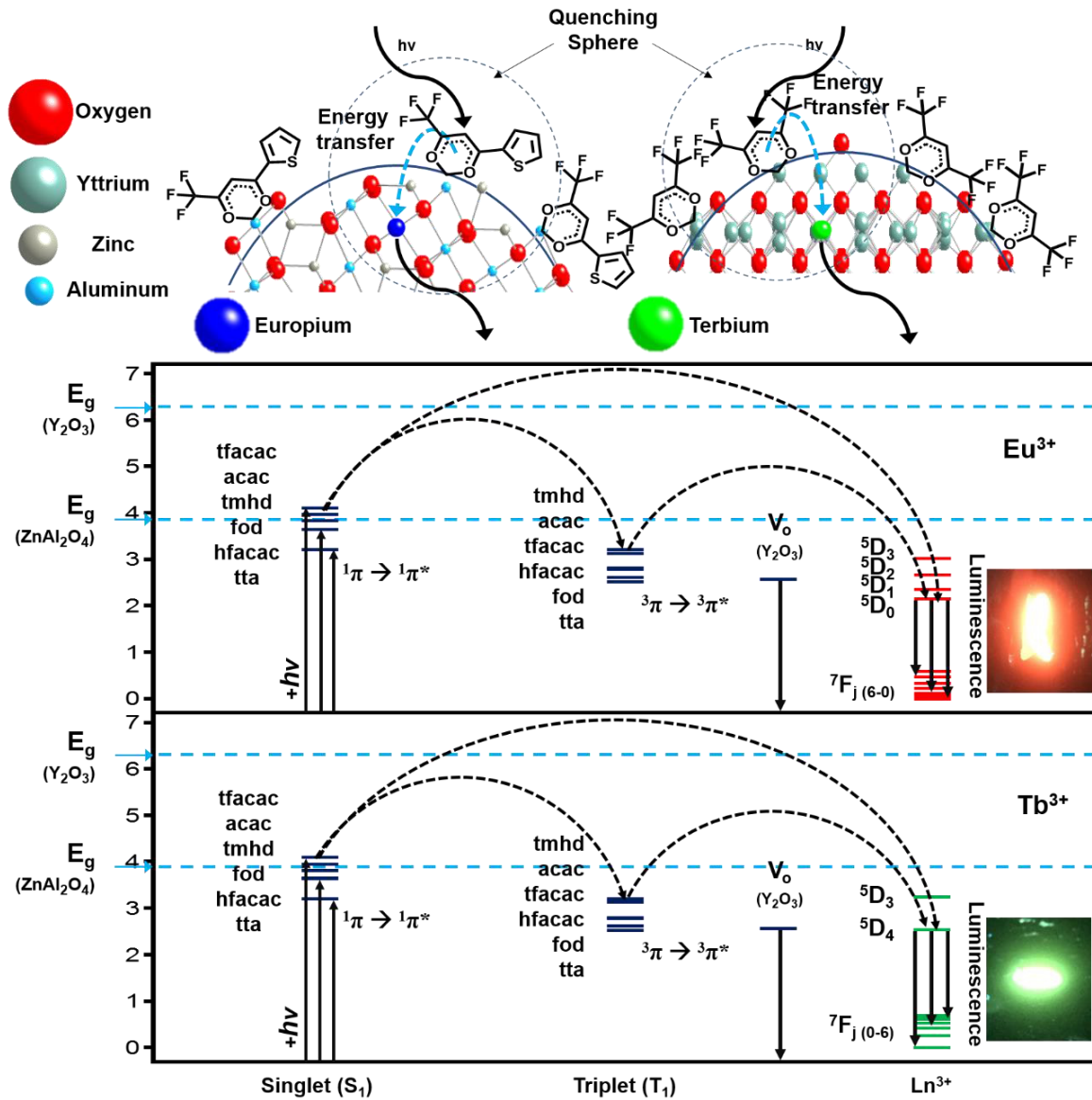


Figure 5.1: A) Lattice structure of lanthanide doped ZnAl₂O₄ and Y₂O₃ with a surface passivation layer of tta and acac respectively. B) Energy level diagram showing the bandgaps of Y₂O₃ and ZnAl₂O₄ (in light blue), the energies of the J-O levels of the Eu³⁺ (in red) and Tb³⁺ (in green) ions, and the singlet and triplet levels of the ligands used in this study (in dark blue).

nanocrystals is a mixture of HDA and acac for Y₂O₃ or OA and acac for ZnAl₂O₄. Ligand exchange for the desired β -diketonate is achieved by treatment of the nanospinel with NOBF₄ / DMF methods to remove the initial surface passivant followed by addition of the desired ligand.¹³⁴

Figure 5.1A shows the crystal structures of nanophosphors with enolate coordination of the β -diketonate thenoyltrifluoroacetone (tta) for Eu:ZnAl₂O₄ and hexafluoroacetylacetone (hfacac) for Tb:Y₂O₃. The enol coordination has been reported for acac coordination to the surface of Y₂O₃,¹¹ and is representative of the binding motifs for the six β -diketonate used in the study. Based on pXRD patterns, ZnAl₂O₄ has a spinel structure with a space group of Fd $\bar{3}$ m (No. 227, O_h⁷) which is four fold degenerate for the Bravais cell, resulting in optical unit cell comprised of eight tetrahedral sites occupied by Zn(II) (a-wyckoff site), and sixteen Al(III) sites with D_{3d} symmetry (d-wyckoff sites). The RE(III) ion occupies the distorted octahedral Al(III) sites based on reported XANES and EXAFS data, as seen in chapter 3. For the RE:ZnAl₂O₄, the differences in ionic radii between Al(III) and the two rare earth ions (Al³⁺ = 0.54 Å; Eu³⁺ = 0.95 Å; Tb³⁺ = 0.92 Å) leads to loss of the inversion center on the site (non-centrosymmetric). The RE:Y₂O₃ is observed to crystallize in the cubic space group Ia $\bar{3}$ (No. 206, T_h⁷) and has a four fold degenerate Bravais cell resulting in an optical cell composed of eight Y(III) sites with S₆ symmetry (a-wyckoff site) and and 24 Y(III) sites with C₂ symmetry (d-wyckoff site). The S₆ site is centrosymmetric, while the C₂ site has no inversion center. The ionic radii for Y(III) is 0.96 Å, which is nearly identical to the RE dopants, resulting in very little distortion at that site.

5.3.2 Nanophosphor Ligand Passivation

The studied β -diketonates involve symmetric (R₁, R₁) and asymmetric (R₁, R₂) structures with differences in their electron withdrawing and electron donating ability, which changes the strength of the enol coordination and the symmetry of the coordination to the metal oxide surface.^{104, 173} Evidence for complete passivant exchange with enol coordination through the oxygen atoms to the Eu:ZnAl₂O₄ and Eu:Y₂O₃ nanocrystal surface is provided by inspection of the v_{C=C} and v_{C=O} β -diketonate modes observed in the FTIR spectra before and after exchange (Figure 5.2). The Tb(III) doped samples exhibit the same FT-IR spectra.

Inspection of Figure 5.2, shows that complete passivant removal is achieved by treatment with NOBF₄. Prior to ligand exchange the contributions characteristic of acac and oleylamine (OA) are observed at the symmetric and anti-symmetric *acac* vibrations for the v_{C=C} at 1408 cm⁻¹ and for the enol v_{C=O} at 1566 cm⁻¹, while OA features are observed for the –CH₂ symmetric and asymmetric stretches at v_s(-CH₂) = 2856 cm⁻¹, and v_{as} (-CH₂) = 2925 cm⁻¹. Following treatment with NOBF₄, the loss of the acac peaks and the appearance of the v_{C=O} for DMF at 1652 cm⁻¹ is

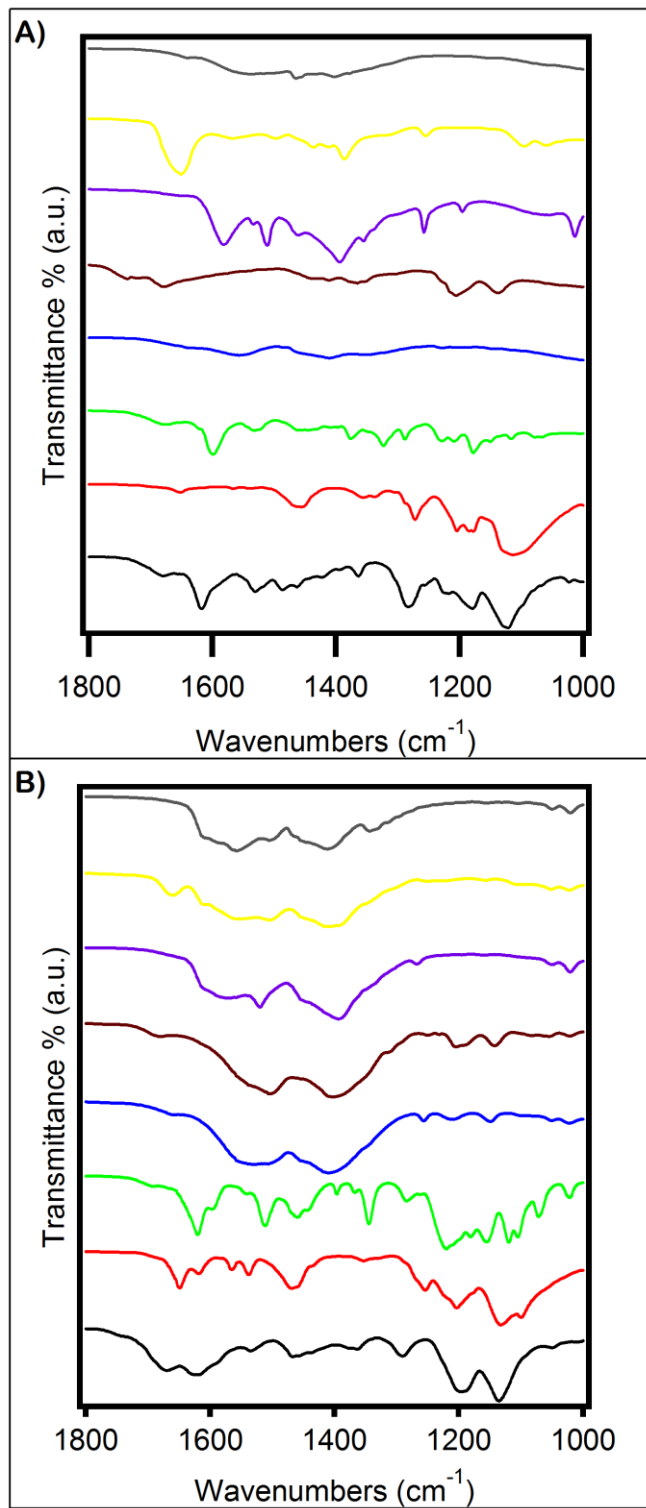


Figure 5.2: IR spectra of A) 10% Eu:Y₂O₃, and B) 10% Tb:Y₂O₃. Ligands are colored the same in each graph (before exchange in grey, NOBF₄ in yellow, tfacac in black, acac in purple, tmhd in blue, fod in green, hfacac in red, and tta in dark red).

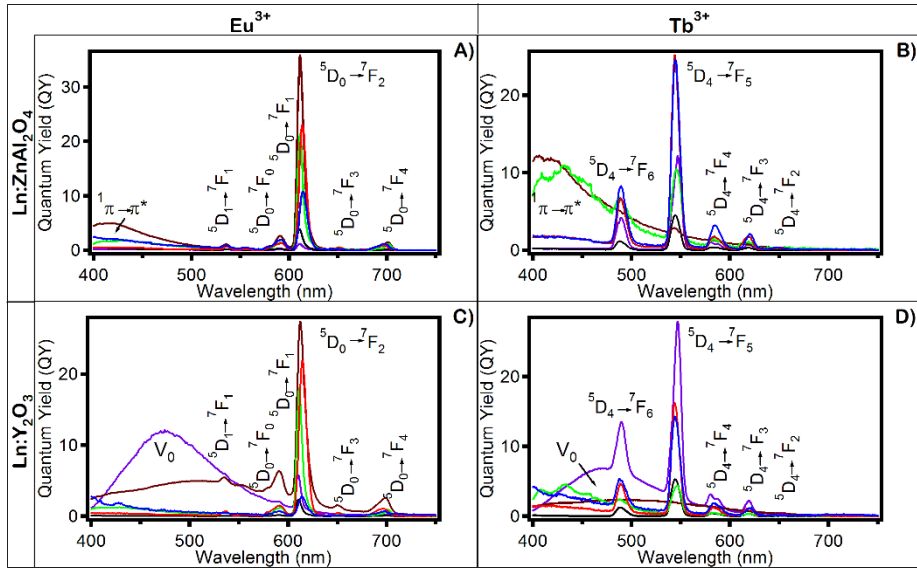


Figure 5.3: PL spectra of ligand passivated, doped nanophosphors A) 10% Eu:ZnAl₂O₄, B) 10% Tb:ZnAl₂O₄, C) 10% Eu:Y₂O₃, and D) 10% Tb:Y₂O₃. Eu(III) doped nanophosphors $\lambda_{\text{ems}} = 614$ nm, Tb(III) doped nanophosphors $\lambda_{\text{ems}} = 544$ nm. Ligands are colored the same in each graph (tfacac in black, acac in purple, tmhd in blue, fod in green, hfacac in red, and tta in dark red). All samples were dissolved in toluene with the exception of samples passivated by hfacac, which were dissolved in acetone.

observed for the DMF-nanospinel. There is no evidence of N-O vibrations at 2100-2200 cm⁻¹ or B-F vibration at 1084 cm⁻¹.¹⁷⁴ Treatment of the DMF-nanospinel with the β -diketonate of choice results in the re-appearance of the signature $\nu_{C=C}$ and enol $\nu_{C=O}$ vibration for the β -diketonate, confirming ligand exchange. Comparison of the exchanged nanocrystal with the original acac sample clearly shows that the $\nu_{C=C}$ and enol $\nu_{C=O}$ vibrations are shifted (Figure 5.2). No evidence for the keto $\nu_{C=O}$ is observed for the β -diketonates indicating the coordination as shown in Figure 5.1A is consistent with the experimental data. In Y₂O₃, the results are the same (Supporting Information), with the HDA peak very close to that of the OA peaks. FT-IR data confirms the complete exchange of the surface occurs by treatment with NOBF₄ with both oxygen atoms bound to a metal coordination of the β -diketonate.

The strength of the metal-oxygen bond formed by coordination of the β -diketonate to the nanocrystal surface is reported to be dependent on the ligand acidity, reflecting Lewis acid-base theory. For the symmetric β -diketonates (acac, tfacac, and fod) the local symmetry of the coordination site is not broken as a resonance form for chelation can be drawn. In the case of the asymmetric β -diketonates (hfacac, tmhd, tta) the local symmetry of the binding site will be

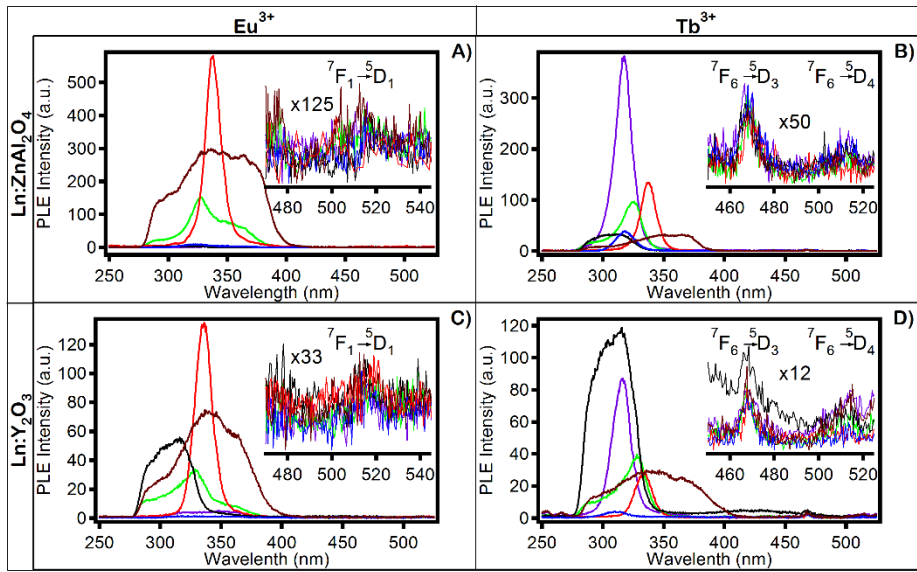


Figure 5.4: Excitation spectra of ligand passivated, doped nanophosphors A) 10% Eu:ZnAl₂O₄, B) 10% Tb:ZnAl₂O₄, C) 10% Eu:Y₂O₃, and D) 10% Tb:Y₂O₃. Ligands are colored the same in each graph (tfacac in black, acac in purple, tmhd in blue, fod in green, hfacac in red, and tta in dark red). Acac, tfacac, and tmhd $\lambda_{\text{exc}} = 315$ nm, tta, fod, and hfacac $\lambda_{\text{exc}} = 340$ nm.

broken, as the C=O and C-O are not equivalent for the polarized structure. The more stable C-O coordination to the nanocrystal surface will occur near the electron withdrawing substituent on the asymmetric β -diketonate and is reflected in the lower frequency vibration relative to the C=O. Thus the binding of the enol form of the β -diketonate to the nanocrystal surface is distinguished by the frequency of the C=O and C-O mode in the FTIR spectra. This is easily seen by considering the symmetric β -diketonates, acac and tmhd passivated nanoparticles that have only electron donating substituents and significantly lower C=O frequencies relative to hfacac. The nanoparticles passivated with asymmetric ligands, tta, tfacac, and fod, which possess both an electron withdrawing and an electron donating group, show a split in the symmetric and asymmetric C=O stretches. The splitting represents the two different resonance forms of the unsymmetrical ligands. Inspection of the assigned lattice C=O vibrations show a shift is observed in the frequency following ligand exchange. The shift reflects the differences in electronegativity of the ligand. Inspection of the structures show that tta, tfacac, hfacac, and fod are all more polarizable than acac and tmhd. Therefore, the more electronegative ligands, (tta, tfacac, hfacac, and fod), result in higher C=O vibrations compared to acac and tmhd. In addition, the asymmetric C-O stretch is also observed in the FTIR data. The C-O mode is strongly shifted

Table 5.1: Lifetimes, quantum efficiencies, and CIE coordinates of the ligand exchanged nanophosphors.

Material	Ligand	τ (μ s)	Φ_{em}	R/O B/G	CIE coordinates	
					x	y
Eu:ZnAl ₂ O ₄	tfacac	474	3.9	5.72	0.51	0.30
	acac	376	1.2	9.28	0.40	0.28
	tmhd	430	10.8	12.48	0.36	0.24
	fod	422	21.5	8.38	0.45	0.26
	hfacac	761	23.1	4.70	0.55	0.31
	tta	503	35.9	10.48	0.60	0.33
Eu:Y ₂ O ₃	tfacac	459	2.4	9.08	0.50	0.31
	acac	494	5.8	8.08	0.20	0.25
	tmhd	498	2.8	5.02	0.20	0.15
	fod	364	18	2.64	0.47	0.27
	hfacac	696	21.9	13.92	0.45	0.26
	tta	489	17.4	6.45	0.40	0.37
Tb:ZnAl ₂ O ₄	tfacac	600	4.5	0.60	0.26	0.48
	acac	869	12.2	0.11	0.29	0.56
	tmhd	713	24.6	0.09	0.27	0.46
	fod	1200	10.5	0.11	0.19	0.19
	hfacac	9.9	25.2	0.30	0.26	0.45
	tta	2.5	2.9	0.29	0.21	0.20
Tb:Y ₂ O ₃	tfacac	1.0	5.3	0.83	.029	0.53
	acac	1030	61	0.90	.022	0.36
	tmhd	910	14.3	0.44	0.23	0.35
	fod	1000	4.4	0.35	0.19	0.18
	hfacac	17.4	16.2	0.68	0.25	0.43
	tta	1.1	2	0.35	0.25	0.29

upon binding to the nanocrystal surface consistent with the enol form dominating the nature of coordination. This is seen particularly in the case of the non-symmetric ligands, which exhibit 2 peaks for the C-O stretch, about 20-30 cm⁻¹ from the free ligand.¹⁷⁵ The lattice structures show insignificant differences in the IR stretches comparatively.

5.3.3 Optical Properties

Studies on rare earth containing molecular compounds have shown that the highest quantum efficiency is achieved when two primary conditions are met: a) the $^3\pi \rightarrow ^3\pi^*$ energy is within 0.3eV for Eu(III) and 0.25 eV in Tb(III), and b) the difference in the $^1\pi \rightarrow ^1\pi^*$ energy and the $^3\pi \rightarrow ^3\pi^*$ energy is most efficient around 0.6 eV.^{63, 92} The efficiency of the down conversion phosphor will therefore dependent on the RE doping concentration, RE energy levels, the distance of the RE from the surface, and the efficiency of energy transfer from the passivating molecular sensitizer to the incorporated RE, which depends on the singlet and triplet energy levels of the passivant.

The inset in Figure 5.1B shows the solution emission for the ligand exchanged 3nm tta-Eu:ZnAl₂O₄ and for a 4nm hfacac-Tb:Y₂O₃ sample following excitation into the ligand $^1\pi \rightarrow \pi^*$ β -diketonate energy level. In Figure 5.3, the emission spectra for the RE:ZnAl₂O₄ and RE:Y₂O₃ samples are plotted, while the excitation spectra are shown in Figure 5.4. The optical data including the Quantum Efficiency (Φ_{em}), the lifetime (τ), and the ratio of J-O forbidden to allowed transition intensity (Eu: R/O, Tb: B/G) for the samples are listed in Table 5.1. The PL spectra in Figure 5.3 is consistent with the energy level diagram in Figure 5.1B, with a significant variance for the Φ_{em} dependent on the ligand singlet and triplet excited state energies. The efficiency of energy transfer to the lanthanide from the molecular passivant will be dependent on the energy levels for the molecular passivant and the distance of the RE from the molecular passivant, as predicted by the Dexter energy transfer mechanism. Additional effects arise from site symmetry reflecting the change in energy population of the magnetic and electronic dipole allowed transitions. Since the population of the separate RE excited state levels occurs via non-radiative pathways which is a phonon dependent event, the intensity of the emission is dependent on the transfer efficiency and the energy spread between the levels, which is effected by the lattice hardness or phonon frequency for the host lattice.¹⁶⁴

Prior to ligand exchange in the PL spectra for the nanocrystals weak RE emission is observed and the spectra is composed primarily of $^1\pi \rightarrow \pi^*$ fluorescence from the β -diketonate passivant in both ZnAl₂O₄ and Y₂O₃. In addition to the $^1\pi \rightarrow \pi^*$ fluorescence from the β -diketonate passivant, the Y₂O₃ samples also exhibit emission from a low lying oxygen vacancy (V_O), as reported previously for Eu:Y₂O₃.¹¹ Following ligand exchange of the nanocrystals, the emission spectra is composed of the same contributions, but the intensity of the $^1\pi \rightarrow \pi^*$ transition is reduced relative to the RE lines. For the Eu(III) samples the $^5D_0 \rightarrow ^7F_2$ transition is the most intense producing a red emission, while for Tb(III) the $^5D_4 \rightarrow ^7F_5$ transition dominates producing a green emission. The linewidth for the *f-f* transitions in the Y₂O₃ sample is broader. In the nanocrystal samples the intensity of the ligand to RE emission lines varies strongly with the ligand in both the Tb(III) and Eu(III) cases. The most intense contribution to the observed excitation spectra in Figure 5.4 is the ligand $\pi \rightarrow \pi^*$ transition, although the RE lines are observable to the red of the ligand centered transitions and can be assigned to f-f transition levels for the RE(III) ions. The lanthanide transitions are nearly three orders of magnitude less intense. Direct excitation into the $^7F_1 \rightarrow ^5D_1$ (Eu) $^7F_6 \rightarrow ^5D_3$ (Tb) result in weak line emission for the RE ions (data not shown).

The observed spectral profile for the RE:ZnAl₂O₄ and RE:Y₂O₃ samples in Figure 5.3 can be assigned the $^5D_0 \rightarrow ^7F_J$ transitions for Eu(III) and $^5D_4 \rightarrow ^7F_J$ transitions for Tb(III) following from the Judd-Olfelt (J-O) rules. The pseudo-quadrupolar $^5D_0 \rightarrow ^7F_2$ electronic dipole transition in Eu(III) is considered hypersensitive. For Tb(III), the J-O pseudo-hypersensitive line is the magnetic dipole allowed transition ($^5D_4 \rightarrow ^7F_5$) at 544 nm. The J-O rules predict the strongest emission for Eu(III) will arise for the red (614 nm) electronic dipole allowed $^5D_0 \rightarrow ^7F_2$ transition when the Eu(III) center occupies a non-centrosymmetric site. The spectra in Figure 5.3 are consistent with the transitions being the predominant RE assigned spectral features in accordance with the J-O rules. In addition, the to J-O lines, the spectra exhibit broad emission to the blue, where the intensity and energy is both ligand dependent and strongly affected by the passivant exchange process.

For Eu:ZnAl₂O₄ (Figure 5.3A), the ligand that resulted in the highest Φ_{em} was found to be tta, while the lowest was tfacac. In Eu:Y₂O₃ (Figure 5.3B), the highest Φ_{em} was found with tta

Table 5.2: Ligand structures and electronic properties.

Ligand structure	Ligand name	Singlet (S ₁)	Triplet (T ₁)	ΔE S ₁ - T ₁	ΔE S ₁ - Ln(III) ⁵ D _n	ΔE T ₁ - Ln(III) ⁵ D _n
	1,1,1-Trifluoroacetylacetone (tfacac)	4.09 eV 303 nm	2.82 eV 440 nm	1.27 eV	Eu = 1.95 eV Tb = 1.55 eV	Eu = 0.68 eV Tb = 0.28 eV
	2,4-pentanedione (acac)	3.97 eV 312 nm	3.14 eV 395 nm	0.83 eV	Eu = 1.83 eV Tb = 1.43 eV	Eu = 1.0 eV Tb = 0.6 eV
	2,2,6,6-Tetramethyl- 3,5-heptanedione (tmhd)	3.84 eV 323 nm	3.22 eV 385 nm	0.62 eV	Eu = 1.7 eV Tb = 1.3 eV	Eu = 1.08 eV Tb = 0.68 eV
	6,6,7,7,8,8,8-heptafluoro-2,2-dimethyl-3,5-octanedione (fod)	3.66 eV 339 nm	2.63 eV 471 nm	1.03 eV	Eu = 1.52 eV Tb = 1.12 eV	Eu = 0.69 eV Tb = 0.09 eV
	1,1,1,5,5,5-Hexafluoro- 2,4-pentanedione (hfacac)	3.65 eV 340 nm	2.79 eV 444 nm	0.86 eV	Eu = 1.51 eV Tb = 1.11 eV	Eu = 0.65 eV Tb = 0.25 eV
	2-thenoyl trifluoroacetone (tta)	3.22 eV 385 nm	2.53 eV 490 nm	0.69 eV	Eu = 1.08 eV Tb = 0.68 eV	Eu = 0.39 eV Tb = -0.01 eV

passivation, and lowest was for acac. In Tb: ZnAl₂O₄ (Figure 5.3C), the highest Φ_{em} is observed for the nanophosphor passivated with hfacac while the lowest is tta. In contrast to the ZnAl₂O₄ samples, Tb:Y₂O₃ (Figure 5.3D) shows the highest Φ_{em} with acac passivation, though the lowest Φ_{em} is still with tta passivation. Interestingly, although the hfacac and fod ligand have identical singlet energy levels, the Φ_{em} for Tb³⁺ is markedly different, while for Eu, the Φ_{ems} are similar. The observation of a different β -diketonate populating the RE energy levels for Tb doping of Y₂O₃ vs. ZnAl₂O₄ is likely due to contributions from population into the V_O levels in Y₂O₃, which has a long lived excited state and can populate the RE lines directly.

The importance of the energy of the triplet level in relation to the RE emitting levels has been investigated in molecular compounds.^{61, 63} The agreed upon mechanism for energy transfer from a molecular sensitizer to a RE ion is through the triplet of the sensitizer, and therefore the difference in energy between the triplet and RE emitting level has a significant impact on the Φ_{em} of luminescent RE ions. In Figure 5.1B, the energy of the electronic transitions for Eu(III), Tb(III), and the singlet and triplet $\pi \rightarrow \pi^*$ passivant energy levels are drawn, along with the oxygen vacancy acceptor level (V_O) for Y₂O₃ ($E_g(V_O) = 2.6$ eV, and the Y₂O₃ and ZnAl₂O₄ band gap energies (E_g) at 6.2 and 3.9 eV, respectively. The triplet and singlet levels of each ligand can be found in Table 5.2.

The trend in the Φ_{em} can be accounted for by consideration of the ligand symmetry or the electronegativity of the β -diketonate, suggesting the energy level of the ligand $\pi \rightarrow \pi^*$ transition is critical, as implied in Figure 5.1B. A plot of the β -diketonate ${}^1\pi \rightarrow \pi^*$ energy levels vs. Φ_{em} is shown for the RE lines in RE:ZnAlO₄ and RE:Y₂O₃ is shown in Figure 5. The contribution from the ligand centered and V_O level are spectrally removed prior to Φ_{em} calculations for the samples by fitting to allow direct comparison of the data. The population of the RE f-f transitions occurs by down conversion energy transfer processes (Figure 5.1B) via a Dexter energy transfer mechanism, reflecting the spin forbidden nature of the ligand to RE energy coupling. The Dexter mechanism is an electron-exchange process that operates efficiently over short distances (< 1nm).^{20, 176} The critical radii for energy transfer, where the probability of energy transfer is 50% often termed the R_o value, is observed to be between 0.1 to 1 nm in RE doped oxides, and has been in chapter 4 in tta-Eu:ZnAl₂O₄ to be 0.5 nm using a Perrin model for non-diffusional energy transfer. The experimental data in Figure 5.5 is in agreement with the most favorable energy gap between the ligand centered ${}^1\pi \rightarrow \pi^*$ in molecular complexes of Tb³⁺ of 0.25 eV and 0.3eV for

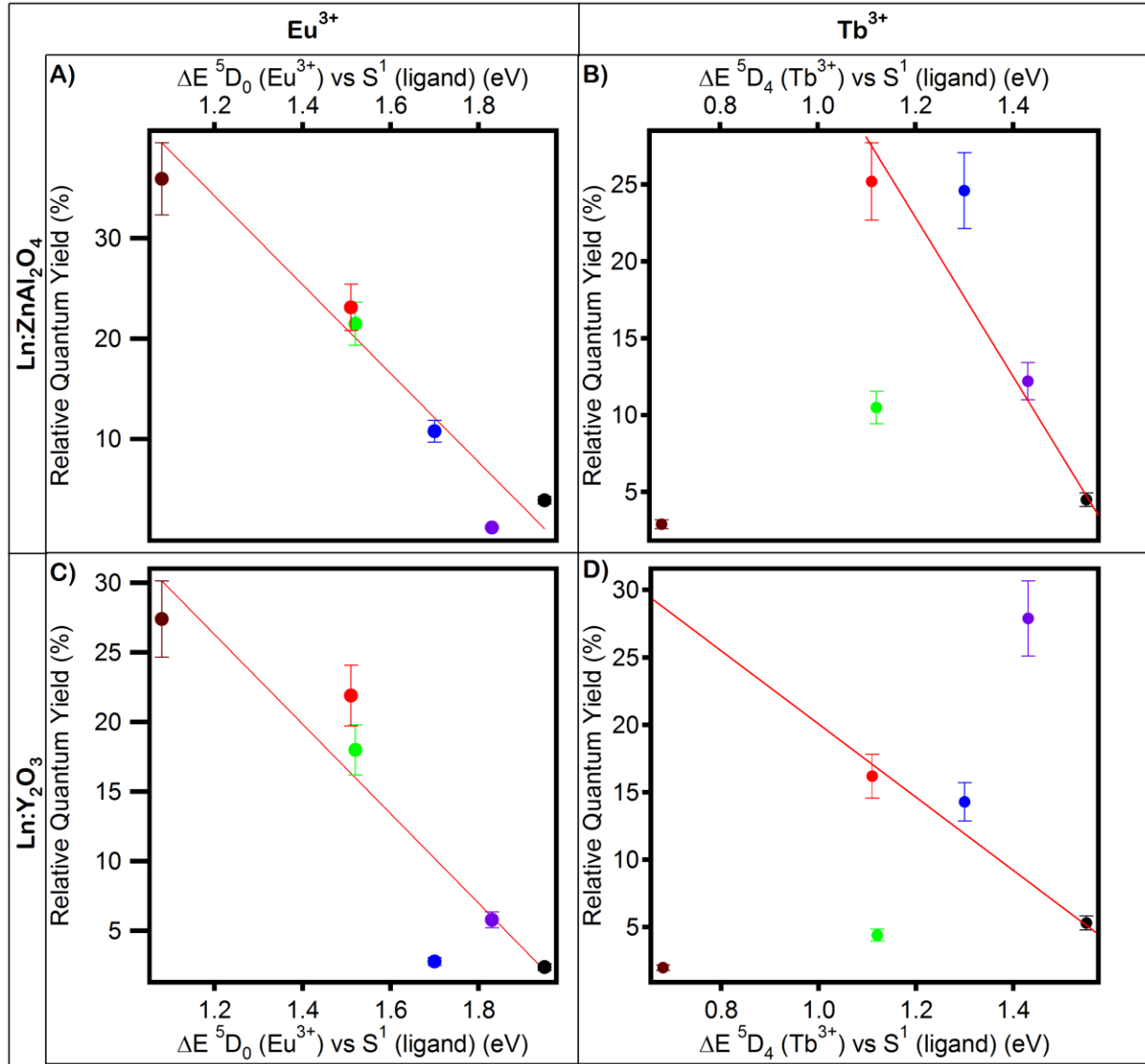


Figure 5.5: Quantum yield of the samples versus the energy difference between the singlet of the ligand and the lowest J-O level (5D_0 in Eu(III) and 5D_4 in Tb(III)). A) 10% Eu:ZnAl₂O₄, B) 10% Tb:ZnAl₂O₄, C) 10% Eu:Y₂O₃, and D) 10% Tb:Y₂O₃. (tfacac in black, acac in purple, tmhd in blue, fod in green, hfacac in red, and tta in dark red).

Eu³⁺, with the highest probability for ligand → RE energy transfer occurring to the outer 2-shells of the nanocrystal. Assuming a stochastic distribution of RE ions doped into the nanocrystal, this amounts to 70% of Eu sites in ZnAl₂O₄ and 58% for Y₂O₃ being efficiently populated by the ligand → RE energy transfer pathway shown in Figure 5.1. Population of the remaining RE ions would primarily occur by excited state hopping between the RE ions.

In molecular RE complexes the efficiency of energy transfer is reduced with increasing energy gap, as predicted by the $\langle J \rangle$ overlap integral. Since the highest probability for population arises from the singlet states, it is anticipated that the efficiency of energy transfer will scale as the singlet. However, since population of the triplet levels occurs, the final transfer requires energetic favorability for the down conversion to be observed. A linear trend is observed for the Φ_{em} with decreasing energy gap for the $^1\pi \rightarrow \pi^*$ level and the allowed RE transition. It is notable that the exception to the trend line occurs for tfacac, where low Φ_{em} are observed in the samples. Inspection of Table 5.2 shows tfacac has nearly the same triplet energy as hfacac, but a very different singlet energy. Tfacac is a prime example of how large differences in singlet to triplet levels are also important, as a decrease in intersystem crossing efficiency results in fewer electrons being able to populate the RE excited states. No significant linear correlation was found between the triplet energy and the Φ_{em} .

Inspection of the lifetime decay for the Eu(III) and Tb(III) emitters in Table 5.1 provides further insight into the RE dopant behavior and the influence of the passivating layer. Typically the lifetime for a RE emitter in a nanocrystal is non-exponential, with contributions arising from the core and surface sites, as well as self-quenching between incorporated emitters.¹⁷⁷ Self-quenching is concentration dependent and will show a loss in Φ_{em} and a shortening of lifetime due to non-diffusional quenching. Between lattices, the observed lifetime will also be influenced by the lattice phonon density. The lifetimes in all samples are reduced relative to the single crystal data. The lifetimes for both lattices and RE dopants are single exponential, indicating the emission most likely occurs from similar lattice sites since earlier studies on nanocrystals have shown multi-exponential decay due to surface and core sites.¹⁷⁸

Nanocrystal samples passivated by hfacac exhibit the longest lifetimes for the Eu(III) samples, while fod produces the longest lifetime for the Tb samples. Since the change in lifetime is a change in the non-radiative path for excited state relaxation, it will be affected by the symmetry breaking within the lattice and surface passivation effects.^{104, 179} Inspection of the Table 5.2 indicates that a strong correlation between the lifetime and the ligand's symmetry and polarizability can be drawn. As a general trend, the lifetime tracks with triplet energies differences, with the longest lifetimes found for ligands that have a favorable ΔE between the triplet state and the main emissive state for the lanthanide ions. However, lifetime are observed to shorten with increasing ligand polarizability, leading to lower than expected lifetimes for those

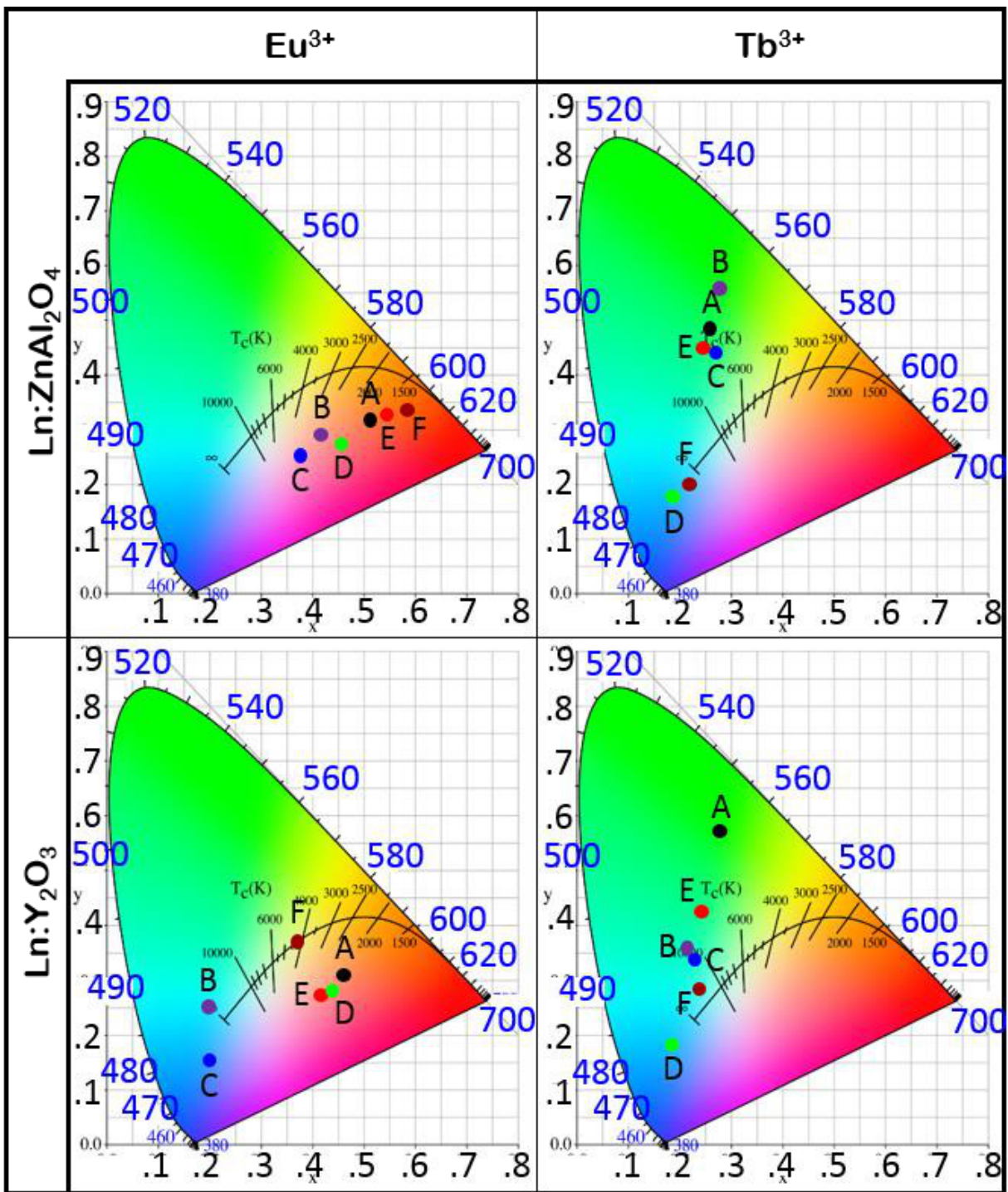


Figure 5.6: CIE coordinate diagram of ligand passivated, doped nanophosphors A) 10% Eu:ZnAl₂O₄, B) 10% Tb:ZnAl₂O₄, C) 10% Eu:Y₂O₃, and D) 10% Tb:Y₂O₃. Eu(III) doped nanophosphors $\lambda_{\text{ems}} = 614$ nm, Tb(III) doped nanophosphors $\lambda_{\text{ems}} = 544$ nm Ligands are colored the same in each graph (tfacac in black, acac in purple, tmhd in blue, fod in green, hfacac in red, and tta in dark red).

samples, especially for tta, which is the most polarizable in the series. The observation of ligand polarizability effects has been reported previously and have been attributed to the strength of the metal-ligand electron phonon coupling, leading to enhanced non-radiative pathways for excited state decay.²⁸ The shortened lifetimes for the asymmetric ligands most likely reflects symmetry breaking leading to enhanced non-radiative rates for relaxation from RE ions that are within the outer-most surface layers. Within the subset of the symmetric ligands, the lifetimes track with the triplet energies.

5.3.4 Color Purity

A plot of the ligand dependent CIE coordinates for the RE doped samples is shown in Figure 5.6, and listed in Table 5.1. The CIE coordinates show that the contribution of ligand emission causes a spread in the CIE coordinate position, which tracks the ligand emission contribution in Figure 5.3. The most pure red downshifting phosphors based on color purity are tta-Eu:ZnAl₂O₄ and tfacac-EuY₂O₃, while the most pure green are acac-Tb:ZnAl₂O₄ and tfacac-Tb:Y₂O₃. If the quantum efficiency and lowest pump wavelength are considered, the best red phosphor would be tta-Eu:ZnAl₂O₄, and the best green phosphor would be hfacac-Tb:ZnAl₂O₄.

In Figure 5.3AC, the hypersensitive $^5D_0 \rightarrow ^7F_2$ transition in Eu(III) is observed to have the strongest intensity for all ligand passivations, consistent with the J-O line prediction of a non-centrosymmetric site for Eu(III). In addition the appearance of the $^5D_0 \rightarrow ^7F_0$ ($J=0$ forbidden transition) as a shoulder in the emission spectra for the Eu(III) sites (Figure 3AC) is a strong indicator of loss of site symmetry for the Eu ion in both the ZnAl₂O₄ and Y₂O₃ lattices. For Tb(III) samples in Figure 5.3CD, the dominant peak is the allowed magnetic transition, $^5D_4 \rightarrow ^7F_5$, which is also considered hypersensitive and has been claimed to be a probe of a non-centrosymmetric Tb site.^{60, 61}

The red/orange (R/O) ratios for Eu(III) and the blue/green (B/G) ratios for Tb(III) are often used as a measure of the site symmetry within the host lattice.⁶⁴ The R/O ratio is the ratio of the integrated intensities of the ratio of $^5D_0 \rightarrow ^7F_2$ to $^5D_0 \rightarrow ^7F_1$ in Eu(III), while the B/G ratio is $^5D_4 \rightarrow ^7F_6$ to $^5D_4 \rightarrow ^7F_5$. In phosphors, the R/O ratios for Eu(III) and the B/G ratios in Tb(III) are critical parameters that impact the CIE coordinates and color purity of the phosphors. Large R/O ratios and small B/G ratios indicate that the RE site is one of low symmetry (without a

center of inversion). For phosphors utilizing Eu(III), the red line is preferred, while for Tb(III) the green line is desirable. Therefore, it is desirable to have RE ions in sites of low symmetry as it improves color purity. In a recent study, the intensity of the hypersenstive line has been reported to be dependent on the surface passivation for Eu(III) NaYF₄, depending on ligand polarizability.²⁸

The values for R/O and B/G are shown in Table 5.1. Comparison of the ligand dependent R/O (and B/G) and Φ_{em} in Table 5.1 shows the highest Φ_{em} and highest R/O ratio are not directly correlated. The observed R/O ratios are highest (most red) for tmhd:ZnAl₂O₄ and fod:Y₂O₃. For Tb(III) the lowest B/G ratios (most green) are for tmhd:ZnAl₂O₄ and for fod:Y₂O₃. In both hosts, the ligand is observed to effect the the R/O and B/G ratios in the nanocrystals. Similar findings have been reported for other nanocrystals hosts for both Tb and Eu. The effect of the passivant was reported to reflect ligand polarizability and the influence on ligand field. In molecular compounds the ligand has also been observed to influence the R/O and B/G ratios. For the limited passivation ligands studied here, the trend is unclear. This may suggest that the passivation layer distorts the RE site near the surface, but one would expect the the energy transfer pathway to likewise be influenced, resulting in the Φ_{em} and the R/O (and B/G) ratios to be correlated, which is not observed.

The magnitude of R/O (and B/G) is different between ZnAl₂O₄ and Y₂O₃. The RE:Y₂O₃ samples have far less favorable R/O and B/G ratios in comparison to RE:ZnAl₂O₄. This behavior for the host lattice is suprising as 75% of the Y sites within Y₂O₃ are non-centrosymmetric (C₂) and 25% are centrosymmetric (S₆) based on the crystal structure, as compared to ZnAl₂O₄ where the Al site is centro-symmetric (D_{3d}). A plausible explanation is that this is due to the difference in ionic radii between the dopant and host cation sites. In Y₂O₃, the RE ions are similar in size to Y(III), resulting in no additional breakage of symmetry. In comparison, Al(III) is significantly smaller than either RE ion, requiring a large distortion in the site to accommodate the dopant. This distortion likely leads to a break in the symmetry for all the sites, and could help explain the differences in R/O and B/G ratios. In Tb doped Y₂O₃ X-ray absorption measurements reported by Soo, et al³⁴ have shown significant disorder for the Tb sites occupying the Y(III) sites in nanomaterials, consistent with the assumption that site disorder may result in the observed enhancement of R/O and B/G ratios in nanocrystals. An alternative explanation may lie in surface relaxation of the nanocrystal, which while not measured for the metal oxide lattices

above, has been reported to occur over two lattice planes in CdSe quantum dots. Since the surface relaxation is influenced by the passivation layer, the contributions from the ligand passivation layer must also be considered. As discussed in the FTIR section, the binding of the asymmetric ligands to the nanocrystal surface will produce a local asymmetry for binding. When the asymmetry is considered, the R/O and B/G ratios exhibit a correlation with the highest R/O and lowest B/G ratios occurring for tta, the ligand with the greatest polarizability differences.

5.4 Conclusion

Nanocrystals that can be excited in the near-visible that exhibit color purity and high quantum efficiencies are important for developing new phosphors for lighting and display technologies. The study clearly shows that the use of ZnAl₂O₄ improves the quantum efficiency and color purity for Eu and Tb emitters relative to doping the common Y₂O₃ lattice, reflecting the enhanced site asymmetry of the RE ion when occupying the smaller Al(III) lattice site. In addition, by careful selection of the surface passivant, the ligand can act as a molecular sensitizer. The observed quantum efficiency scales as both the singlet energy difference and the singlet-triplet gap of the ligand. The highest quantum efficiency occurs in Eu-doped lattices with tta passivation, while hfacac causes the most improvement in the PL quantum efficiency for Tb-doped lattices. This study further distinguishes contributions from ligand induced particle reconstruction and the negative impact of oxygen defect sites in Y₂O₃ that are not present in ZnAl₂O₄. Continued exploration of the ligand dependence and the underlying lattice distortions that lead to improved phosphor properties is an important step in developing next generation host lattices for incorporation into lighting and display technologies.

REFERENCES

1. Intelligent Nanomaterials: Processes, Properties, and Applications. Tiwari, A.; Mishra, A. K.; Kobayashi, H.; Turner, A. P. F., Eds. Scrivener Publishing LLC.: 2012. (accessed 21 FEB 2012 11:00AM EST).
2. Bardsley, N.; Bland, S.; Pattison, L.; Pattison, M.; Stober, K.; Welsh, F.; Yamada, M. Solid-State Lighting Research and Development Multi-Year Program Plan.
http://apps1.eere.energy.gov/buildings/publications/pdfs/ssl/ssl_mypp2014_web.pdf.
3. Navigant Consulting, I., Adoption of Light Emitting Diodes in Common Lighting Applications: Snapshot of 2013 Trends. U.S. Department of Energy, O. o. E. E. a. R. E., Building Technologies Program. Washington, DC: Department of Energy . Ed. 2014.
4. Schubert, E. F., *Light-Emitting Diodes*. Cambridge University Press: United Kingdom, 2003.
5. Zheludev, N., *Nature Photonics* **2007**, 1 (4), 189-192.
6. Akasaki, I., *Journal of Crystal Growth* **2007**, 300 (1), 2-10.
7. Nakamura, S.; Senoh, M.; Mukai, T., *Japanese Journal of Applied Physics Part 2-Letters* **1993**, 32 (1A-B), L8-L11.
8. Inductiveload LED, 5mm, green (en).
9. Farhadi, S.; Panahandehjoo, S., *Appl. Catal. a-Gen.* **2010**, 382 (2), 293-302.
10. Vasile, M.; Vlazan, P.; Avram, N. M., *J. Alloy Compd.* **2010**, 500 (2), 185-189.
11. Dai, Q. L.; Foley, M. E.; Bresheke, C. J.; Lita, A.; Strouse, G. F., *J. Am. Chem. Soc.* **2011**, 133 (39), 15475-15486.
12. Ye, S.; Xiao, F.; Pan, Y. X.; Ma, Y. Y.; Zhang, Q. Y., *Mat. Sci. Eng. R* **2010**, 71 (1), 1-34.
13. Kim, J. S.; Jeon, P. E.; Choi, J. C.; Park, H. L.; Mho, S. I.; Kim, G. C., **2004**.
14. Wang, L.; Liao, N.; Shi, L.; Jia, H.; Du, P.; Xi, Z.; Jin, D., *Electrochemical and Solid-State Letters* **2010**, 13 (6), E7-E9; Muenchhausen, R. E.; Jacobsohn, L. G.; Bennett, B. L.; McKigney, E. A.; Smith, J. F.; Valdez, J. A.; Cooke, D. W., *Journal of Luminescence* **2007**, 126 (2), 838-842; Capobianco, J. A.; Vetrone, F.; D'Alesio, T.; Tessari, G.; Speghini, A.; Bettinelli, M., *Phys. Chem. Chem. Phys.* **2000**, 2 (14), 3203-3207.

15. Guo, H.; Zhang, W.; Lou, L.; Brioude, A.; Mugnier, J., *Thin Solid Films* **2004**, *458* (1–2), 274-280.
16. Wakefield, G.; Holland, E.; Dobson, P. J.; Hutchison, J. L., *Advanced Materials* **2001**, *13* (20), 1557-1560.
17. Goldburt, E. T.; Kulkarni, B.; Bhargava, R. N.; Taylor, J.; Libera, M., *Journal of Luminescence* **1997**, *72-4*, 190-192.
18. Bauer, D.; Diamond, D.; Li, J.; McKittrick, M.; Sandalow, D.; Telleen, P. Critical Materials Strategy. http://energy.gov/sites/prod/files/DOE_CMS2011_FINAL_Full.pdf.
19. Solid State Lighting LED Product Development and Manufacturing R&D Roundtable. <http://energy.gov/sites/prod/files/2014/12/f19/LED%20Product%20Dev%20and%20Mfg%20Roundtable%20Summary.pdf>.
20. Dexter, D. L., *J. Chem. Phys.* **1953**, *21* (5), 836-850.
21. Perrin, F., *C. R. Acad. Sci.* **1924**, *178*, 1978-1980.
22. Feynman, R. P., Presentation by Richard P. Feynman at an American Physical Society meeting at Caltech on December 29, 1959 where he outlined the first outlined the concept of nanotechnology as a topdown technique for making materials and devices at the molecular scale.
23. Taniguchi, N., *Proc. ICPE* **1974**, 5-10; Drexler, K. E., *Engines of Creation: The Coming Era of Nanotechnology*. Anchor; Reprint edition (October 16, 1987): United States of America, 1986.
24. Brus, L. E., *J. Chem. Phys.* **1984**, *80* (9), 4403-4409.
25. Kroto, H.; Heath, J.; Obrien, S.; Curl, R.; Smalley, R., *Nature* **1985**, *318* (6042), 162-163.
26. Du, X.; Li, L.; Zhang, W.; Chen, W.; Cui, Y., *Mater. Res. Bull.* **2015**, *61*, 64-69; Aneesh, P. M.; Krishna, K. M.; Jayaraj, M. K., *J. Electrochem. Soc.* **2009**, *156* (3), K33-K36.
27. Engelsen, D. d.; Harris, P. G.; Ireland, T. G.; Fern, G.; Silver, J., *ECS J. Solid State Sc. Technol.* **2015**, *4* (7), R105-R113.
28. Wawrzynczyk, D.; Bednarkiewicz, A.; Nyk, M.; Strek, W.; Samoc, M., *Journal of Nanoparticle Research* **2013**, *15* (6), 1-11.
29. Washington, A. L.; Foley, M. E.; Cheong, S.; Quffa, L.; Breshike, C. J.; Watt, J.; Tilley, R. D.; Strouse, G. F., *J. Am. Chem. Soc.* **2012**, *134* (41), 17046-17052.

30. Famengo, A.; Anantharaman, S.; Ischia, G.; Causin, V.; Natile, M. M.; Maccato, C.; Tondello, E.; Bertagnolli, H.; Gross, S., *European Journal of Inorganic Chemistry* **2009**, 2009 (33), 5017-5028.
31. Shankar, S. S.; Rai, A.; Ahmad, A.; Sastry, M., *Journal of Colloid and Interface Science* **2004**, 275 (2), 496-502.
32. Song, H.; Chen, B.; Peng, H.; Zhang, J., **2002**.
33. Bhargava, R. N., *Journal of Crystal Growth* **2000**, 214, 926-930; Bhargava, R. N.; Chhabra, V.; Kulkarni, B.; Veliadis, J. V., *Physica Status Solidi B-Basic Research* **1998**, 210 (2), 621-629.
34. Soo, Y. L.; Huang, S. W.; Ming, Z. H.; Kao, Y. H.; Smith, G. C.; Goldburt, E.; Hodel, R.; Kulkarni, B.; Veliadis, J. V. D.; Bhargava, R. N., *Journal of Applied Physics* **1998**, 83 (10), 5404-5409.
35. Bhaviripudi, S.; Mile, E.; Steiner, S. A., III; Zare, A. T.; Dresselhaus, M. S.; Belcher, A. M.; Kong, J., *Journal of the American Chemical Society* **2007**, 129 (6), 1516-+.
36. Shenderova, O. A.; Zhirnov, V. V.; Brenner, D. W., *Critical Reviews in Solid State and Materials Sciences* **2002**, 27 (3-4), 227-356.
37. Ruoff, R.; Malhotra, R.; Huestis, D.; Tse, D.; Lorents, D., *Nature* **1993**, 362 (6416), 140-141; Kulkarni, P.; Jafvert, C., *Abstracts of Papers of the American Chemical Society* **2005**, 229, U933-U933.
38. Chen, K. S.; McGill, S. A.; Xiong, P., *Appl. Phys. Lett.* **2011**, 98 (12), 123110-3.
39. Erwin, S. C.; Zu, L. J.; Haftel, M. I.; Efros, A. L.; Kennedy, T. A.; Norris, D. J., *Nature* **2005**, 436 (7047), 91-94.
40. Horikoshi, S.; Serpone, N., *Microwaves in Nanoparticle Synthesis: Fundamentals and Applications*. Wiley-VCH Verlag GmbH & Co. KGaA: 2013.
41. Nakaso, K.; Han, B.; Ahn, K. H.; Choi, M.; Okuyama, K., *Journal of Aerosol Science* **2003**, 34 (7), 869-881.
42. Behafarid, F.; Cuenya, B. R., *Surface Science* **2012**, 606 (11-12), 908-918.
43. Trewyn, B. G.; Slowing, I. I.; Giri, S.; Chen, H.-T.; Lin, V. S. Y., *Accounts of Chemical Research* **2007**, 40 (9), 846-853; Niederberger, M.; Garnweitner, G., *Chemistry-a European Journal* **2006**, 12 (28), 7282-7302.
44. Panacek, A.; Kvitek, L.; Prucek, R.; Kolar, M.; Vecerova, R.; Pizurova, N.; Sharma, V. K.; Nevecna, T. j.; Zboril, R., *Journal of Physical Chemistry B* **2006**, 110 (33), 16248-16253;

Shankar, S. S.; Rai, A.; Ankamwar, B.; Singh, A.; Ahmad, A.; Sastry, M., *Nature Materials* **2004**, 3 (7), 482-488.

45. Anand, G. T.; Kennedy, L. J.; Aruldoss, U.; Vijaya, J. J., *J. Mol. Struct.* **2015**, 1084, 244-253.
46. Motta, F. V.; Marques, A. P. A.; Li, M. S.; Abreu, M. F. C.; Paskocimas, C. A.; Bomio, M. R. D.; Souza, R. P.; Varela, J. A.; Longo, E., *J. Alloy Compd.* **2013**, 553, 338-342.
47. Washington, A. L.; Strouse, G. F., *Chemistry of Materials* **2009**, 21 (15), 3586-3592.
48. Washington II, A. L.; Strouse, G. F., *J. Am. Chem. Soc.* **2008**, 130 (28), 8916-8922.
49. Lovingood, D. D.; Oyler, R. E.; Strouse, G. F., *J. Am. Chem. Soc.* **2008**, 130 (50), 17004-17011.
50. Tu, W. X.; Lin, H. F., *Chemistry of Materials* **2000**, 12 (2), 564-567; Alcazer, J., *Journal of Combinatorial Chemistry* **2005**, 7 (3), 353-355.
51. Thanh, N. T. K.; Maclean, N.; Mahiddine, S., *Chemical Reviews* **2014**, 114 (15), 7610-7630.
52. Reinert, A. A.; Payne, C.; Wang, L. M.; Ciston, J.; Zhu, Y. M.; Khalifah, P. G., *Inorg. Chem.* **2013**, 52 (15), 8389-8398.
53. Tsao, J. Y.; Crawford, M. H.; Coltrin, M. E.; Fischer, A. J.; Koleske, D. D.; Subramania, G. S.; Wang, G. T.; Wierer, J. J.; Karlicek, R. F., *Adv. Opt. Mater.* **2014**, 2 (9), 809-836; Yu, X. Z.; Wang, H. L.; Pan, D.; Zhao, J. H.; Misuraca, J.; von Molnar, S.; Xiong, P., *Nano Lett.* **2013**, 13 (4), 1572-1577.
54. Gerbec, J. A.; Magana, D.; Washington, A.; Strouse, G. F., *Journal of the American Chemical Society* **2005**, 127 (45), 15791-15800.
55. Zhu, Y.-J.; Chen, F., *Chemical Reviews* **2014**, 114 (12), 6462-6555.
56. Spencer, P. L. Method of Treating Foodstuffs. 1950.
57. Zhao, H.; Dong, Y.; Jiang, P.; Wang, G.; Zhang, J.; Zhang, C., *Chem. Eng. J.* **2015**, 260, 623-630.
58. Xu, X.; Azad, A. K.; Irvine, J. T. S., *Catal. Today* **2013**, 199, 22-26; Podhorodecki, A.; Banski, M.; Misiewicz, J.; Serafinczuk, J.; Gaponenkov, N., *Journal of the Electrochemical Society* **2010**, 157 (6), H628-H632; Seo, S.; Yang, H.; Holloway, P. H., *J. Colloid Interf. Sci.* **2009**, 331 (1), 236-242; Barros, B. S.; Melo, P. S.; Kiminami, R. H. G. A.; Costa, A. C. F. M.; de Sa, G. F.; Alves, S., Jr., *J. Mater. Sci.* **2006**, 41 (15), 4744-4748.

59. Seo, S.; Yang, H.; Holloway, P. H., *J. Lumin.* **2009**, *129* (3), 307-311.
60. Bunzli, J. C. G.; Eliseeva, S. V., Basics of Lanthanide Photophysics. In *Lanthanide Luminescence: Photophysical, Analytical, and Biological Aspects*, Springer: 2011; pp 1-47.
61. Binnemans, K., *Chemical Reviews* **2009**, *109* (9), 4283-4374.
62. Lis, S.; Elbanowski, M.; Mkowska, B.; Hnatejko, Z., *Journal of Photochemistry and Photobiology A: Chemistry* **2002**, *150* (1-3), 233-247.
63. Latva, M.; Takalo, H.; Mukkala, V. M.; Matachescu, C.; Rodriguez-Ubis, J. C.; Kankare, J., *J. Lumin.* **1997**, *75* (2), 149-169.
64. Motta, F. V.; Marques, A. P. A.; Li, M. S.; Abreu, M. F. C.; Paskocimas, C. A.; Bomio, M. R. D.; Souza, R. P.; Varela, J. A.; Longo, E., *Journal of Alloys and Compounds* **2013**, *553*, 338-342.
65. Lothian, G., *Analyst* **1963**, *88* (105), 678-&.
66. Brouwer, A. M., *Pure Appl. Chem.* **2011**, *83* (12), 2213-2228; de Mello, J. C.; Wittmann, H. F.; Friend, R. H., *Adv. Mater.* **1997**, *9* (3), 230-232.
67. Jauncey, G., *Proceedings of the National Academy of Sciences of the United States of America* **1924**, *10*, 57-63.
68. Mcgehee, R.; Renault, J., *Journal of Applied Crystallography* **1972**, *50* (Oct 1), 365-&.
69. Levitt, M. H., *Spin Dynamics: Basics of Nuclear Magnetic Resonance*, 2nd Edition. Wiley: West Sussex, England, 2008; p 740.
70. Duer, M. J., *Solid-State NMR Spectroscopy*. Blackwell Publishing: Malden, MA, 2004.
71. Schubert, E. F.; Kim, J. K., *Science* **2005**, *308* (5726), 1274-1278; Justel, T.; Nikol, H.; Ronda, C., *Angewandte Chemie-International Edition* **1998**, *37* (22), 3085-3103; Xu, X. R.; Su, M. Z., *Luminescence and Luminescent Materials*. Chemical Industry Press Pub. Date :2004-10-01: 2004; Ronda, C. R., *Luminescence: From Theory to Applications*. Wiley-VCH: New York, 2007.
72. Chen, G.; Craven, M.; Kim, A.; Munkholm, A.; Watanabe, S.; Camras, M.; Gotz, W.; Steranka, F., *Phys. Status Solidi A* **2008**, *205* (5), 1086-1092.
73. Kim, H.-s.; Brueckner, E.; Song, J.; Li, Y.; Kim, S.; Lu, C.; Sulkin, J.; Choquette, K.; Huang, Y.; Nuzzo, R. G.; Rogers, J. A., *Proceedings of the National Academy of Sciences* **2011**, *108* (25), 10072-10077.

74. Narukawa, Y.; Ichikawa, M.; Sanga, D.; Sano, M.; Mukai, T., *Journal of Physics D-Applied Physics* **2010**, 43 (35).
75. Bowers, M. J.; McBride, J. R.; Rosenthal, S. J., *J. Am. Chem. Soc.* **2005**, 127 (44), 15378-15379.
76. Shi, M.; Li, F.; Yi, T.; Zhang, D.; Hu, H.; Huang, C., *Inorg. Chem.* **2005**, 44 (24), 8929-8936; Jia, D.; Wang, X.-J., *Optical Materials* **2007**, 30 (3), 375-379; He, X.-H.; Zhu, Y., *Journal of Materials Science* **2008**, 43 (5), 1515-1519.
77. Shur, M. S.; Zukauskas, A., *Proceedings of the IEEE* **2005**, 93 (10), 1691-1703; Kapoor, P. N.; Heroux, D.; Mulukutla, R. S.; Zaikovskii, V.; Klabunde, K. J., *J. Mater. Chem.* **2003**, 13 (2), 410-414; Kim, J. S.; Kang, H. I.; Kim, W. N.; Kim, J. I.; Choi, J. C.; Park, H. L.; Kim, G. C.; Kim, T. W.; Hwang, Y. H.; Mho, S. I.; Jung, M. C.; Han, M., *Appl. Phys. Lett.* **2003**, 82 (13), 2029-2031.
78. Bai, X.; Song, H.; Yu, L.; Yang, L.; Liu, Z.; Pan, G.; Lu, S.; Ren, X.; Lei, Y.; Fan, L., *J. Phys. Chem. B* **2005**, 109 (32), 15236-15242.
79. Yada, M.; Mihara, M.; Mouri, S.; Kuroki, M.; Kijima, T., *Advanced Materials* **2002**, 14 (4), 309-313; Hsu, W. P.; Ronnquist, L.; Matijevic, E., *Langmuir* **1988**, 4 (1), 31-37; Wakefield, G.; Keron, H. A.; Dobson, P. J.; Hutchison, J. L., *Journal of Physics and Chemistry of Solids* **1999**, 60 (4), 503-508; Wang, X.; Sun, X. M.; Yu, D.; Zou, B. S.; Li, Y., *Advanced Materials* **2003**, 15 (17), 1442-1445; Liu, T.; Zhang, Shao; Li, *Langmuir* **2003**, 19 (18), 7569-7572; Cao, Y. C., *J. Am. Chem. Soc.* **2004**, 126 (24), 7456-7457; Si, R.; Zhang, Y.-W.; You, L.-P.; Yan, C.-H., *Angewandte Chemie International Edition* **2005**, 44 (21), 3256-3260; Yu, T.; Joo, J.; Park, Y. I.; Hyeon, T., *Journal of the American Chemical Society* **2006**, 128 (6), 1786-1787.
80. Si, R.; Zhang, Y.-W.; Zhou, H.-P.; Sun, L.-D.; Yan, C.-H., *Chemistry of Materials* **2007**, 19 (1), 18-27.
81. Shin, J. H.; Vandenhoven, G. N.; Polman, A., *Appl. Phys. Lett.* **1995**, 66 (18), 2379-2381; Fujii, M.; Yoshida, M.; Kanzawa, Y.; Hayashi, S.; Yamamoto, K., *Appl. Phys. Lett.* **1997**, 71 (9), 1198-1200; Wang, X.; Li, Y. D., *Chem.-Eur. J.* **2003**, 9 (22), 5627-5635; Wang, X. J.; Gao, M. Y., *J. Mater. Chem.* **2006**, 16 (14), 1360-1365; Patra, C. R.; Alexandra, G.; Patra, S.; Jacob, D. S.; Gedanken, A.; Landau, A.; Gofer, Y., *New J. Chem.* **2005**, 29 (5), 733-739; Mai, H. X.; Zhang, Y. W.; Si, R.; Yan, Z. G.; Sun, L. D.; You, L. P.; Yan, C. H., *J. Am. Chem. Soc.* **2006**, 128 (19), 6426-6436; Rao, R. P.; Devine, D. J., *J. Lumin.* **2000**, 87-9, 1260-1263; Zheng, Y. X.; Liang, Y. J.; Zhang, H. J.; Lin, Q.; Chuan, G.; Wang, S. B., *Mater. Lett.* **2002**, 53 (1-2), 52-56; Kido, J.; Nagai, K.; Okamoto, Y.; Skotheim, T., *Chem. Lett.* **1991**, (7), 1267-1270.
82. Zhu, W. G.; Jiang, Q.; Lu, Z. Y.; Wei, X. Q.; Xie, M. G.; Zou, D. C.; Tsutsui, T., *Thin Solid Films* **2000**, 363 (1-2), 167-169.
83. Hu, L. Y.; Song, H. W.; Pan, G. H.; Yan, B.; Qin, R. F.; Dai, Q. L.; Fan, L. B.; Li, S. W.; Bai, X., *J. Lumin.* **2007**, 127 (2), 371-376; Park, W. J.; Yoon, S. G.; Yoon, D. H., *Journal of*

Electroceramics **2006**, *17* (1), 41-44; Wu, X. Y.; Liang, Y. J.; Chen, R.; Liu, M. Y.; Li, Y. Z., *J. Mater. Sci.* **2011**, *46* (16), 5581-5586; Liu, X.; Lin, C.; Lin, J., **2007**.

84. Shang, C. Y.; Shang, X. H.; Qu, Y. Q.; Li, M. C., *Chem. Phys. Lett.* **2011**, *501* (4-6), 480-484.
85. Steffen, M. A.; Lao, K.; Boxer, S. G., *Science* **1994**, *264* (5160), 810-816; Stowell, M. H. B.; McPhillips, T. M.; Rees, D. C.; Soltis, S. M.; Abresch, E.; Feher, G., *Science* **1997**, *276* (5313), 812-816; Michel, H.; Deisenhofer, J., *Biochemistry* **1988**, *27* (1), 1-7; Thompson, M. A.; Zerner, M. C., *Journal of the American Chemical Society* **1991**, *113* (22), 8210-8215; Marchi, M.; Gehlen, J. N.; Chandler, D.; Newton, M., *Journal of the American Chemical Society* **1993**, *115* (10), 4178-4190.
86. Napier, G. D. R.; Neilson, J. D.; Shepherd, T. M., *Chemical Physics Letters* **1975**, *31* (2), 328-330.
87. Sager, W. F.; Filipescu, N.; Serafin, F. A., *J. Phys. Chem.* **1965**, *69* (4), 1092-1100.
88. Filipescu, N.; Sager, W. F.; Serafin, F. A., *J. Phys. Chem.* **1964**, *68* (11), 3324-3346.
89. Mishra, K. C.; Berkowitz, J. K.; Johnson, K. H.; Schmidt, P. C., *Phys. Rev. B Condens. Matter* **1992**, *45* (19), 10902-10906; Fernandes, José A.; Ferreira, Rute A. S.; Pillinger, M.; Carlos, Luís D.; Gonçalves, Isabel S.; Ribeiro-Claro, Paulo J. A., *European Journal of Inorganic Chemistry* **2004**, *2004* (19), 3913-3919; Mita, Y.; Togashi, M.; Yamamoto, H., *Journal of Luminescence* **2000**, *87*-*89*, 1026-1028; Kutsenko, A. B.; Heber, J.; Kapphan, S. E.; Demirbilek, R.; Zakharchenya, R. I., *physica status solidi (c)* **2005**, *2* (1), 685-688.
90. Tallant, D. R.; Seager, C. H.; Simpson, R. L., *J. Appl. Phys.* **2002**, *91* (7), 4053-4064.
91. Fu, L.-M.; Ai, X.-C.; Li, M.-Y.; Wen, X.-F.; Hao, R.; Wu, Y.-S.; Wang, Y.; Zhang, J.-P., *The Journal of Physical Chemistry A* **2010**, *114* (13), 4494-4500.
92. Sato, S.; Wada, M., *Bulletin of the Chemical Society of Japan* **1970**, *43* (7), 1955-1962.
93. de Sá, G. F.; Malta, O. L.; de Mello Donegá, C.; Simas, A. M.; Longo, R. L.; Santa-Cruz, P. A.; da Silva Jr, E. F., *Coord. Chem. Rev.* **2000**, *196* (1), 165-195.
94. Crosby, G. A.; Whan, R. E.; Alire, R. M., *J. Chem. Phys.* **1961**, *34*, 743.
95. Zhang, H.; Song, H.; Yu, H.; Bai, X.; Li, S.; Pan, G.; Dai, Q.; Wang, T.; Li, W.; Lu, S.; Ren, X.; Zhao, H., *J. Phys. Chem. C* **2007**, *111* (17), 6524-6527.
96. Berman, S. M., *Publications of the Lighting Research Group*. Lawrence Berkeley Laboratory: Berkeley, CA, 1995.

97. Bourhill, G.; Palsson, L. O.; Samuel, I. D. W.; Sage, I. C.; Oswald, I. D. H.; Duignan, J. P., *Chem. Phys. Lett.* **2001**, *336* (3-4), 234-241.
98. Peng, X.; Manna, L.; Yang, W.; Wickham, J.; Scher, E.; Kadavanich, A.; Alivisatos, A. P., *Nature* **2000**, *404* (6773), 59-61.
99. Lita, A.; Washington, A. L.; van de Burgt, L.; Strouse, G. F.; Stiegman, A. E., *Adv. Mater.* **2010**, *22* (36), 3987-3991.
100. Panda, A. B.; GlasPELL, G.; El-Shall, M. S., *The Journal of Physical Chemistry C* **2007**, *111* (5), 1861-1864.
101. Alarcón-Flores, G.; Aguilar-Frutis, M.; García-Hipolito, M.; Guzmán-Mendoza, J.; Canseco, M. A.; Falcony, C., *Journal of Mater. Sci.* **2008**, *43* (10), 3582-3588.
102. Nakamoto, K., *Infrared and Raman Spectra of Inorganic and Coordination Compounds, Part B, Applications in Coordination, Organometallic, and Bioinorganic Chemistry*. Wiley: Hoboken, NJ, 2009; p 424.
103. Meulenberg, R.; Strouse, G., *Journal of Physical Chemistry B* **2001**, *105* (31), 7438-7445.
104. Binnemans, K., *Rare-Earth Beta-Diketonates*. Elsevier: Amsterdam, 2005; Vol. 35.
105. Scolan, E.; Sanchez, C., *Chemistry of Materials* **1998**, *10* (10), 3217-3223.
106. Berrettini, M. G.; Braun, G.; Hu, J. G.; Strouse, G. F., *J. Am. Chem. Soc.* **2004**, *126* (22), 7063-7070.
107. Hartmann, S. R.; Hahn, E. L., *Physical Review* **1962**, *128* (5), 2042-2053.
108. Garnweitner, G.; Hentschel, J.; Antonietti, M.; Niederberger, M., *Chemistry of Materials* **2005**, *17* (18), 4594-4599.
109. Bordun, O. M.; Bordun, I. M., *Ukr. Fiz. Zhurn.* **1998**, *43*, 275-278.
110. Osipov, V. V.; Rasuleva, A. V.; Solomonov, V. I., *Optics and Spectroscopy* **2008**, *105* (4), 524-530.
111. Meyssamy, H.; Riwozki, K.; Kornowski, A.; Naused, S.; Haase, M., *Advanced Materials* **1999**, *11* (10), 840-844.
112. Dai, Q.; Song, H.; Bai, X.; Pan, G.; Lu, S.; Wang, T.; Ren, X.; Zhao, H., *J. Phys. Chem. C* **2007**, *111* (21), 7586-7592.

113. Pinna, N.; Garnweitner, G.; Antonietti, M.; Niederberger, M., *J. Am. Chem. Soc.* **2005**, 127 (15), 5608-5612.
114. Nelson, J. A.; Brant, E. L.; Wagner, M. J., *Chemistry of Materials* **2003**, 15 (3), 688-693.
115. Fauteux, C.; Longtin, R.; Pegna, J.; Therriault, D., *Inorganic Chemistry* **2007**, 46 (26), 11036-11047; Xu, L.; Hu, Y.-L.; Pelligra, C.; Chen, C.-H.; Jin, L.; Huang, H.; Sithambaram, S.; Aindow, M.; Joesten, R.; Suib, S. L., *Chemistry of Materials* **2009**, 21 (13), 2875-2885.
116. Biju, S.; Gopakumar, N.; Bünzli, J. C. G.; Scopelliti, R.; Kim, H. K.; Reddy, M. L. P., *Inorg. Chem.* **2013**, 52 (15), 8750-8758.
117. Huang, I. B.; Chang, Y. S.; Chen, H. L.; Hwang, C. C.; Jian, C. J.; Chen, Y. S.; Tsai, M. T., *Thin Solid Films* **2014**, 570, 451-456.
118. Jamal, E. M. A.; Kumar, D. S.; Anantharaman, M. R., *B. Mater. Sci.* **2011**, 34 (2), 251-259.
119. Raj, S. S.; Gupta, S. K.; Grover, V.; Muthe, K. P.; Natarajan, V.; Tyagi, A. K., *J. Mol. Struct.* **2015**, 1089, 81-85; Hosono, E.; Kudo, T.; Honma, I.; Matsuda, H.; Zhou, H., *Nano Lett.* **2009**, 9 (3), 1045-1051; Bhaduri, S.; Bhaduri, S. B., *Ceram. Int.* **2002**, 28 (2), 153-158; Sainz, M. A.; Mazzoni, A. D.; Aglietti, E. F.; Caballero, A., *Mater. Chem. Phys.* **2004**, 86 (2-3), 399-408.
120. Sakoda, K.; Hirano, M., *Ceram. Int.* **2014**, 40 (10), 15841-15848.
121. Sakoda, K.; Hirano, M., *J. Nanosci. Nanotechno.* **2015**, 15 (8), 6069-6077; Petrova, M. A.; Mikirticheva, G. A.; Novikova, A. S.; Popova, V. F., *J. Mater. Res.* **1997**, 12 (10), 2584-2588.
122. Byun, H. J.; Kim, J. U.; Yang, H., *Nanotechnology* **2009**, 20 (49).
123. Duan, X.; Yu, F.; Wu, Y., *Appl. Surf. Sci.* **2012**, 261, 830-834; Yu, M.; Lin, J.; Zhou, Y. H.; Wang, S. B., *Mater. Lett.* **2002**, 56 (6), 1007-1013.
124. Duan, X.; Liu, J.; Wu, Y.; Yu, F.; Wang, X., *J. Lumin.* **2014**, 153, 361-368; Zhang, Y.; Wu, Z.; Geng, D.; Kang, X. o.; Shang, M.; Li, X.; Lian, H.; Cheng, Z.; Lin, J., *Adv. Funct. Mater.* **2014**, 24 (42), 6581-6593; Du, X.; Li, L.; Zhang, W.; Chen, W.; Cui, Y., *Mater. Res. Bull.* **2015**, 61, 64-69; Kim, J. S.; Kim, T. W.; Kim, S. M.; Park, H. L., *Appl. Phys. Lett.* **2005**, 86 (9); Ohtake, T.; Sonoyama, N.; Sakata, T., *Chem. Phys. Lett.* **2000**, 318 (6), 517-521; Bessiere, A.; Sharma, S. K.; Basavaraju, N.; Priolkar, K. R.; Binet, L.; Viana, B.; Bos, A. J. J.; Maldiney, T.; Richard, C.; Scherman, D.; Gourier, D., *Chem. Mater.* **2014**, 26 (3), 1365-1373; Allix, M.; Chenu, S.; Véron, E.; Poumeyrol, T.; Kouadri-Boudjelthia, E. A.; Alahraché, S.; Porcher, F.; Massiot, D.; Fayon, F., *Chem. Mater.* **2013**, 25 (9), 1600-1606; Yu, R.; Luan, R. X.; Wang, C. F.; Chen, J. T.; Wang, Z. X.; Moon, B. K.; Jeong, J. H., *J. Electrochem. Soc.* **2012**, 159 (5), J188-J192; Yu, R.; Noh, H. M.; Moon, B. K.; Choi, B. C.; Jeong, J. H.; Jang, K.; Yi, S. S.; Jang, J. K., *Mater. Res. Bull.* **2013**, 48 (6), 2154-2158; Kim, J. W.; Kim, Y. J., *J. Nanosci.*

Nanotechno. **2007**, *7* (11), 4065-4068; Miron, I.; Enache, C.; Vasile, M.; Grozescu, I., *Phys. Scripta* **2012**, *T149*; Vasile, M.; Vlazan, P.; Sfirloaga, P.; Grozescu, I.; Avram, N. M.; Rusu, E., *Phys. Scripta* **2009**, *T135*; Zhou, W.; Yang, X.; Huang, L.; Wang, J.; Tang, J.; Liang, H., *Chem-a Eur. J.* **2012**, *18* (17), 5367-5373; Hirano, M.; Sakaida, N., *J. Am. Ceram. Soc.* **2002**, *85* (5), 1145-1150.

125. da Silva, A. A.; Goncalves, A. S.; Davolos, M. R.; Santagneli, S. H., *J. Nanosci. Nanotechno.* **2008**, *8* (11), 5690-5695; Yuan, Y.; Huang, J.; Tu, W.; Huang, S., *J. Alloy Compd.* **2014**, *616*, 461-467.

126. Norberg, N. S.; Parks, G. L.; Salley, G. M.; Gamelin, D. R., *J. Am. Chem. Soc.* **2006**, *128* (40), 13195-13203; Bryan, J. D.; Schwartz, D. A.; Gamelin, D. R., *J. Nanosci. Nanotechno.* **2005**, *5* (9), 1472-1479.

127. Damm, H.; Kelchtermans, A.; Bertha, A.; Van den Broeck, F.; Elen, K.; Martins, J. C.; Carleer, R.; D'Haen, J.; De Dobbelaere, C.; Hadermann, J.; Hardy, A.; Van Bael, M. K., *RSC Adv.* **2013**, *3* (45), 23745-23754.

128. Pinna, N.; Garnweitner, G.; Antonietti, M.; Niederberger, M., *J. Am. Chem. Soc.* **2005**, *127* (15), 5608-5612.

129. Jung, Y. K.; Kim, J. I.; Lee, J. K., *J. Am. Chem. Soc.* **2010**, *132* (1), 178-184.

130. Zheng, W. W.; Singh, K.; Wang, Z. X.; Wright, J. T.; van Tol, J.; Dalal, N. S.; Meulenberg, R. W.; Strouse, G. F., *J. Am. Chem. Soc.* **2012**, *134* (12), 5577-5585.

131. Kimizuka, N.; Isobe, M.; Nakamura, M., *J. Solid State Chem.* **1995**, *116* (1), 170-178.

132. Dai, Q. L.; Foley, M. E.; Breshike, C. J.; Lita, A.; Strouse, G. F., *J. Am. Chem. Soc.* **2011**, *133* (39), 15475-15486.

133. Bradburne, C. E.; Delehanty, J. B.; Gemmill, K. B.; Mei, B. C.; Matoussi, H.; Susumu, K.; Blanco-Canosa, J. B.; Dawson, P. E.; Medintz, I. L., *Bioconjugate Chem.* **2013**, *24* (9), 1570-1583.

134. Dong, A. G.; Ye, X. C.; Chen, J.; Kang, Y. J.; Gordon, T.; Kikkawa, J. M.; Murray, C. B., *J. Am. Chem. Soc.* **2011**, *133* (4), 998-1006.

135. Joos, J. J.; Korthout, K.; Nikitenko, S.; Poelman, D.; Smet, P. F., *Opt. Mater. Express* **2013**, *3* (9), 1338-1350.

136. Ding, P.; Zhang, M.; Xie, Z. L.; Cao, L. H., *J. Nanomat.* **2015**.

137. Blaakmeer, E. S.; Rosciano, F.; van Eck, E. R. H., *J. Phys. Chem. C* **2015**, *119* (14), 7565-7577; Ozawa, N.; Donoue, K.; Yao, T., *Electrochem. Solid St.* **2003**, *6* (6), A106-A108.

138. Shen, T. g. D.; Feng, S.; Tang, M.; Valdez, J. A.; Wang, Y.; Sickafus, K. E., *Appl. Phys. Lett.* **2007**, *90* (26); Suzuki, T.; Murugan, G. S.; Ohishi, Y., *J. Lumin.* **2005**, *113* (3-4), 265-270.
139. Kim, K.-J.; Oleksak, R. P.; Hostetler, E. B.; Peterson, D. A.; Chandran, P.; Schut, D. M.; Paul, B. K.; Herman, G. S.; Chang, C.-H., *Crystal Growth & Design* **2014**, *14* (11), 5349-5355; Taylor, B. R.; Kauzlarich, S. M.; Delgado, G. R.; Lee, H. W. H., *Chemistry of Materials* **1999**, *11* (9), 2493-2500; Kim, K. J.; Oleksak, R. P.; Hostetler, E. B.; Peterson, D. A.; Chandran, P.; Schut, M.; Paul, B. K.; Herman, G. S.; Chang, C. H., *Cryst. Growth Des.* **2014**, *14* (11), 5349-5355; Taylor, B. R.; Kauzlarich, S. M.; Delgado, G. R.; Lee, H. W. H., *Chem. Mater.* **1999**, *11* (9), 2493-2500.
140. Bardsley, N.; Bland, S.; Pattison, L.; Pattison, M.; Stober, K.; Welsh, F.; Yamada, M. Solid-state lighting research and development multi-year program plan http://apps1.eere.energy.gov/buildings/publications/pdfs/ssl/ssl_mypp2014_web.pdf.
141. Zhu, H.; Lin, C. C.; Luo, W.; Shu, S.; Liu, Z.; Liu, Y.; Kong, J.; Ma, E.; Cao, Y.; Liu, R. S.; Chen, X., *Nat. Commun.* **2014**, *5*.
142. Tan, S. T.; Sun, X. W.; Demir, H. V.; DenBaars, S. P., *IEEE Photon. J.* **2012**, *4* (2), 613-619.
143. Chen, J.; Meng, Q.; May, P. S.; Berry, M. T.; Lin, C., *J. Phys. Chem. C* **2013**, *117* (11), 5953-5962.
144. Si, R.; Zhang, Y. W.; Zhou, H. P.; Sun, L. D.; Yan, C. H., *Chem. Mater.* **2007**, *19* (1), 18-27.
145. Ravel, B.; Newville, M., *J. Synchrotron Radiat.* **2005**, *12*, 537-541.
146. Brouwer, A. M., *Pure Appl. Chem.* **2011**, *83* (12), 2213-2228; Nockemann, P.; Beurer, E.; Driesen, K.; Van Deun, R.; Van Hecke, K.; Van Meervelt, L.; Binnemans, K., *Chem. Commun.* **2005**, (34), 4354-4356.
147. de Mello, J. C.; Wittmann, H. F.; Friend, R. H., *Adv. Mater.* **1997**, *9* (3), 230-232.
148. Bourhill, G.; Palsson, L. O.; Samuel, I. D. W.; Sage, I. C.; Oswald, I. D. H.; Duignan, J. P., *Chem. Phys. Lett.* **2001**, *336* (3-4), 234-241.
149. Avci, N.; Korthout, K.; Newton, M. A.; Smet, P. F.; Poelman, D., *Opt. Mater. Express* **2012**, *2* (3), 321-330.
150. Pellicer-Porres, J.; Segura, A.; Martinez-Criado, G.; Rodriguez-Mendoza, U. R.; Lavin, V., *J. Phys. Condens. Matter* **2013**, *25* (2).
151. Wu, S.; Yu, X. O.; Huang, J. T.; Shen, J.; Yan, Q.; Wang, X.; Wu, W. X.; Luo, Y. H.; Wang, K. Y.; Zhang, Q. J., *J. Mater. Chem.* **2008**, *18* (27), 3223-3229.

152. Sampath, S. K.; Cordaro, J. F., *J. Am. Ceram. Soc.* **1998**, 81 (3), 649-654.
153. Jeong, I.; Park, H.; Mho, S., *Solid State Communications* **1998**, 105 (3), 179-183; Motloung, S. V.; Dejene, F. B.; Ntwaeborwa, O. M.; Swart, H. C., *Mater. Res. Express* **2014**, 1 (4), 045029.
154. Choi, Y. I.; Sohn, Y., *Rsc Adv.* **2014**, 4 (78), 41292-41292.
155. Huang, J.; Bekiari, V.; Lianos, P., Enhancement Of Weak Radiative Transitions of Eu³⁺ in Thin Surfactant Films in the Presence of Poly(Methyl Methacrylate). In *Trends in Colloid and Interface Science XV*, Koutsoukos, P., Ed. Springer Berlin Heidelberg: 2001; Vol. 118, Pp 27-29.
156. Yu, R. J.; Wang, C. F.; Chen, J. T.; Wu, Y. K.; Li, H. J.; Ma, H. L., *ECS J. Solid State Sc.* **2014**, 3 (3), R33-R37.
157. Tsai, B. S.; Chang, Y. H.; Chen, Y. C., *J. Mater. Res.* **2004**, 19 (5), 1504-1508.
158. Zhang, F. L.; Hou, Y. H.; Du, C. X.; Wu, Y. J., *Dalton Trans.* **2009**, (36), 7359-7367; Gou, R. H.; Li, G.; Yang, R. D.; Yan, L., *Synth. React. Inorg. M.* **2006**, 36 (4), 365-371; Yin, M.; Zhang, W.; Lou, L.; Xia, S.; Krupa, J. C., *Spectrosc. Lett.* **1998**, 31 (4), 767-778.
159. Capobianco, J.; Vetrone, F.; D'Alesio, T.; Tessari, G.; Speghini, A.; Bettinelli, M., *Phys. Chem. Chem. Phys.* **2000**, 2 (14), 3203-3207.
160. Turro, N. J.; Kochevar, I. E.; Noguchi, Y.; Chow, M. F., *J. Am. Chem. Soc.* **1978**, 100 (10), 3170-3177.
161. van der Meer, B. W.; Coker III, G.; Chen, S. Y., *Resonance Energy Transfer: Theory and Data*. VCH Publishers (Now Wiley-VCH), Inc.: New York, 1994.
162. Monguzzi, A.; Mezyk, J.; Scotognella, F.; Tubino, R.; Meinardi, F., *Phys. Rev. B* **2008**, 78 (19).
163. Andrews, D. L., Resonance Energy Transfer: Theoretical Foundations and Developing Applications. In *Tutorials in Complex Photonic Media*, Noginov, M. A.; Dewar, G.; McCall, M. W.; Zheludev, N. I., Eds. SPIE Press: Washington, 2009; pp 439-470
164. Brögel, J.; DenBaars, S. P.; Seshadri, R., *J. Phys. Chem. C* **2013**, 117 (35), 17955-17959.
165. Lopez, S.; Romero, A.; Rodriguez-Hernandez, P.; Munoz, A., *Physical Review B* **2009**, 79 (21).
166. Shin, J. H.; Vandenhoven, G. N.; Polman, A., *Applied Physics Letters* **1995**, 66 (18), 2379-2381; Fujii, M.; Yoshida, M.; Kanzawa, Y.; Hayashi, S.; Yamamoto, K., *Applied Physics Letters* **1997**, 71 (9), 1198-1200; Wang, X.; Li, Y. D., *Chemistry-a European Journal* **2003**, 9 (22), 5627-5635; Wang, X. J.; Gao, M. Y., *Journal of Materials Chemistry* **2006**, 16 (14), 1360-

- 1365; Zheng, Y. X.; Liang, Y. J.; Zhang, H. J.; Lin, Q.; Chuan, G.; Wang, S. B., *Materials Letters* **2002**, 53 (1-2), 52-56; Patra, C. R.; Alexandra, G.; Patra, S.; Jacob, D. S.; Gedanken, A.; Landau, A.; Gofer, Y., *New Journal of Chemistry* **2005**, 29 (5), 733-739; Mai, H. X.; Zhang, Y. W.; Si, R.; Yan, Z. G.; Sun, L. D.; You, L. P.; Yan, C. H., *Journal of the American Chemical Society* **2006**, 128 (19), 6426-6436; Rao, R. P.; Devine, D. J., *Journal of Luminescence* **2000**, 87-9, 1260-1263; Kido, J.; Nagai, K.; Okamoto, Y.; Skotheim, T., *Chemistry Letters* **1991**, (7), 1267-1270; Kumar, V.; Som, S.; Ntwaeborwa, O. M.; Coetsee, E.; Swart, H. C., *Chemical Engineering Journal* **2014**, 255, 541-552; Han, B.; Zhang, J.; Lu, Y. H., *Russian Journal of Physical Chemistry a* **2014**, 88 (7), 1209-1214; Shaat, S. K. K.; Swart, H. C.; Ntwaeborwa, O. M., *Optical Materials Express* **2012**, 2 (7), 962-968.
167. Werts, M. H. V., *Science Progress* **2005**, 88 (Part 2), 101-131; Murner, H. R.; Chassat, E.; Thummel, R. P.; Bunzli, J. C. G., *Journal of the Chemical Society-Dalton Transactions* **2000**, (16), 2809-2816; Beeby, A.; Clarkson, I. M.; Dickins, R. S.; Faulkner, S.; Parker, D.; Royle, L.; de Sousa, A. S.; Williams, J. A. G.; Woods, M., *Journal of the Chemical Society-Perkin Transactions 2* **1999**, (3), 493-503.
168. Hebbink, G. A.; Grave, L.; Woldering, L. A.; Reinhoudt, D. N.; van Veggel, F. C. J. M., *The Journal of Physical Chemistry A* **2003**, 107 (14), 2483-2491.
169. Cross, A. M.; May, P. S.; van Veggel, F. J. M.; Berry, M. T., *J. Phys. Chem. C* **2010**, 114 (35), 14740-14747.
170. Xiao, Q. B.; Liu, Y. S.; Liu, L. Q.; Li, R. F.; Luo, W. Q.; Chen, X. Y., *J. Phys. Chem. C* **2010**, 114 (20), 9314-9321.
171. Dial, A. R.; Misra, S.; Landing, W. M., *Rapid Communications in Mass Spectrometry* **2015**, 29 (8), 707-718.
172. Filipescu, N.; Mushrush, G. W.; Hurt, C. R.; McAvoy, N., *Nature* **1966**, 211 (5052), 960-961.
173. Chae, W. S.; Kim, K. J., *Bulletin of the Korean Chemical Society* **1994**, 15 (12), 1050-1054.
174. Dong, A. G.; Ye, X. C.; Chen, J.; Kang, Y. J.; Gordon, T.; Kikkawa, J. M.; Murray, C. B., *Journal of the American Chemical Society* **2011**, 133 (4), 998-1006.
175. Nekoei, A.-R.; Tayyari, S. F.; Vakili, M.; Holakoei, S.; Hamidian, A. H.; Sammelson, R. E., *Journal of Molecular Structure* **2009**, 932 (1-3), 112-122.
176. Ma, B.; Djurovich, P. I.; Yousufuddin, M.; Bau, R.; Thompson, M. E., *J. Phys. Chem. C* **2008**, 112 (21), 8022-8031.
177. Fouassier, C.; Saubat, B.; Hagenmuller, P., *Journal of Luminescence* **1981**, 23 (3-4), 405-412.

178. *Handbook on the Physics and Chemistry of Rare Earths, Volume 37: Optical Spectroscopy*. North Holland: The Netherlands, 2007; p 558.
179. Maji, S.; Sundararajan, K.; Viswanathan, K. S., *Spectrochimica Acta Part A: Molecular and Biomolecular Spectroscopy* **2003**, 59 (3), 455-461.

BIOGRAPHICAL SKETCH

EDUCATION

Florida State University **December 2015**

PhD in Materials Chemistry

Thesis: Synthesis of Oxide and Spinel Nanocrystals for use in Solid State Lighting

Thesis Advisor: Prof. Geoffrey F. Strouse

North Georgia College and State University **May 2009**

B.S. in Chemistry

TEACHING EXPERIENCE

Florida State University **2009–2014**

Department of Chemistry and Biochemistry, Organic Chemistry

North Georgia College and State University **2005-2009**

Department of Chemistry, General Chemistry Laboratory

PUBLICATIONS

- 1) Foley, ME; Strouse, GF; Synthesis of Eu³⁺, and Tb³⁺ co-doped ZnAl₂O₄ spinels. In preparation.
- 2) Carnevale, D; Foley, ME; Lochner, E; Strouse, GF; Size and Concentration Dependent Magnetization of Mn²⁺ Doped CdTe Quantum Dots. In preparation.
- 3) Foley, ME; Ashley, B; Carnevale, D; Strouse, GF; Facile Synthesis of CdTe Quantum Dots from the Cluster Li₄[Cd₁₀Te₄(SePh)₁₆]. In preparation.
- 4) Foley, ME; Meulenberg, RW; Carnevale, D; Strouse, GF; Bright Blue and Red Emission from Eu²⁺ and Eu³⁺ Codoped ZnGa₂S₄ Nanophosphors. In preparation.
- 5) Abhyankar, N; Lee, M; Foley, ME; Choi, ES; Strouse, GF; Kroto, H; Dalal, N; Rapid Microwave-Assisted Synthesis and Grain-Size Dependence of Magnetic and Electric Properties in Perovskite-Like Metal-Organic Frameworks. Submitted to the Journal of the American Chemical Society.
- 6) Foley, ME; McBride, JR; Meulenberg, RW; Strouse, GF; Microwave Synthesis and Ligand Modification of Oxide Nanospinels. Submitted to Chemistry of Materials.
- 7) Foley, ME; Strouse, GF; Molecular Sensitization of Rare Earth Phosphor Emission in Metal Oxide Nanocrystals. Submitted to Journal of Physical Chemistry C.
- 8) Foley, ME; McBride, JR; Meulenberg, RW; Strouse, GF; Eu³⁺ Doped ZnM₂O₄ (M = Al³⁺, Ga³⁺) Nanospinels, an efficient Red Phosphor. Accepted to Chemistry of Materials.

- 9) Washington, AL; Foley, ME; Cheong, S; Quffa, L; Breshike, CJ; Watt, J; Tilley, RD; Strouse, GF; Ostwald's Rule of Stages and its Role in CdSe Quantum Dot Crystallization, *J. Am. Chem. Soc.*, **2012**, 134 (41), pp 17046-17052. DOI: 10.1021/ja302964e
- 10) Dai, QL; Foley, ME; Breshike, CJ; Lita, A; Strouse, GF; Ligand-Passivated Eu:Y₂O₃ Nanocrystals as a Phosphor for White Light Emitting Diodes, *J. Am. Chem. Soc.*, **2011**, 133 (39), pp 15475-15486. DOI: 10.1021/ja2039419

MEETINGS

- 1) Synthesis of Phosphors for use in Solid State Lighting, Materials Retreat, Tallahassee, FL, January 2014
- 2) Microwave Synthesis of Nano-Phosphors for use in Solid State Lighting, SWRMACS, Baton Rouge, LA, November 2012.
- 3) Synthesis of ZnSe and CdTe Using Microwave Irradiation, FAME, Orlando, FL, May 2010.

AWARDS

- American Chemical Society (2008-2010)
Society of Chemistry Students (2006-2009), treasurer (2008-2009)
Georgia Hope Scholarship (2004-2008)

EXPERTISE

- Synthesis of quantum dots, nano-oxides, and nanospinels
- Ligand exchange chemistry of nanomaterials
- Powder X-ray Diffraction Analysis
- Optical spectroscopy (UV-Vis, Photoluminescence, lifetime, solid state quantum yields)
- Nuclear Magnetic Resonance (solution, solid state)
- Phosphor coated-LED (pc-LED) material design